Phenomenology of TeV-scale leptoquarks at the large hadron collider: Current status and future prospects

Thesis submitted in partial fulfillment
of the requirements for the degree of

Doctor of Philosophy
in
Computational Natural Sciences

by

Arvind Bhaskar
20172148
arvind.bhaskar@research.iiit.ac.in

International Institute of Information Technology
Hyderabad - 500 032, INDIA
November 2023

International Institute of Information Technology
Hyderabad, India

CERTIFICATE

It is certified that the work contained in this thesis, titled "**Phenomenology of TeV-scale leptoquarks at the large hadron collider: Current status and future prospects**" by **Arvind Bhaskar**, has been carried out under my supervision and is not submitted elsewhere for a degree.

Date

Adviser: Dr. Subhadip Mitra

Dedicated to my parents and sister...

Acknowledgments

I am grateful to many people from whom I got immense support during my PhD journey—it is tough to put it into words.

Let me begin with the one person who made it all happen, the one who gave me this fantastic opportunity, the one who has always been around each time I stumbled or made a silly error; I didn't just learn how to do research; I learned what doing research means. He taught me to learn something, I need to give up my fear of failure or making a mistake. With him, I realized that doing research is not just about publishing papers; it is about venturing into the unknown. He was less of a supervisor and more of a friend or an elder brother who introduced me to some unique books, TV shows, how to write good English, a new way of looking at things, and the zeal to do the best work possible. I can go on, but I am sure I would still be unable to justify his role. I am forever indebted to him for all he taught me in these 5 years and will guide me in the future. He is my mentor, my friend, and a very wise man—Dr. Subhadip Mitra.

In addition to having a mentor, I was fortunate enough to have a co-mentor to whom I could confess my silly doubts, which I was afraid to ask my supervisor. I still remember our first work when he told me not to call him sir and call him "*Tanumoy Da*". He has been another constant in my PhD life. He taught me several hacks to overcome my initial difficulties with the software packages. I learned a lot of tricky physics concepts from him, and he was always too kinda to overlook my idiosyncrasies. I was happy to finally meet him during one of my conferences.

I want to thank Dr Diganta Das. I learned flavour physics and cosmology concepts while attending his classes with him. I have worked with him in one of my publications and want to work with him in the future. I also thank Dr Debottam Das and his PhD student Dr Bibhabasu De from IOP Bhubaneshwar. Working with them taught me concepts such as loop calculations, Higgs Physics, and some interesting BSM models. Debottam sir and Bibhabasu have always been kind and patient and accommodated all my doubts.

Professor Harjinder Singh or fondly known as *Laltu da*. He is a chemist, part physicist, activist, poet, linguist, and any other ist you could imagine. He carries a wealth of knowledge about a wide range of topics and is always eager to inspire young and open minds. I still remember the first talk he gave; his ideas and thoughts were entirely new to me, and I found them odd. Still,

eventually, I realized his way of thinking and his opinions are more logical and make more sense. I was extremely fortunate to be his teaching assistant, and I could learn a bit or two about chemistry. I am lucky to have met him in my PhD life.

I have an aversion to coding and would only do it with a gun to my head. Being a computational program, I thought I would be in a soup. Luckily and thanks to the foresight of my supervisor, I got a fantastic person who was not just good at coding but taught me how to think logically when it came to coding and physics. With him, I learned statistics, a bit about machine learning, and a competitive spirit to read diverse books. His advice has often helped me immensely during the many problems I faced. He is a great friend and a great husband to Asha Chechi. He is Cyrin Neeraj or as I call him "*chetta*".

In the final days of my PhD, I was lucky to spend a considerable amount of my time with Maaz Khan and Jai Bardhan. Both of them are incredibly talented and quirky in a fantastic way. With Maaz, one could be entertained limitlessly over tea, Biryani, or shawarma. He knows a lot about a wide range of topics, such as politics, science fiction, manga, and of course, physics. I wish him the best of luck with his PhD and hope I get to collaborate with him. Even though an MS student, Jai Bardhan was knowledgeable about particle physics, machine learning, and anything about computers. Hanging out with him, I picked up the basics of machine learning and some GenZ lingo. Yash Chaurasia, a MS student and collaborator in our group. He was in charge of the astronomy club and a part of the photography club. We could constantly nag him to set up the telescope if we wanted to look at the stars, moon, and planets. I wish all the good luck to the next batch of MS students in our group—Rishabh, Kushagra, Mihir, Shivangi, Radhikesh, and Mayank.

I thank my other lab mates, like Rohit Modee and Shweta Kumari. They were the first friends I made in IIIT. They were responsible for ensuring I stopped sitting alone in the Library and came to sit with them in the PhD workspace. Shweta is less of a friend and more of a mother and always used to make delicious food in her hostel and bring it to us. Rohit taught me that working smart is sometimes better than working hard. Pradeep Kumar Pal, my fondest memories with him are the countless trips to the vet, taking the campus dogs to the dog park, and arguing with the authorities over dog-related incidents. Since he was in the student parliament, hanging out with him made me semi-famous in college. It got me in the authorities' good books. Vishal Kumar is one of the funny guys in our lab. He taught me it is ok to care less what people think about you. He is mature for his age and knows how to avoid adverse situations. Rakesh sir is a post-doc in IIIT. He is the one person older than me, and I am allowed to feel young around him. He may be a scientist by training but his true calling lies in stand-up comedy. He gave tough life lessons with comic relief.

I would like thank Chandan Bhaiya. I have spent numerous Skype calls with him, asking him my doubts and him explaining them in great detail and often simplifying them. I am looking forward to working with him in the future.

I want to thank Anirudhan Madathil, an MS student from IISER Trivandrum. He is meticulous and organized when it comes to research. Working with him taught me many things.

I have had a sibling relationship with my juniors, and few of them were as good as my younger siblings. I have enjoyed troubling them and hearing them rant about the class work and assignments. Shweta Sahoo, Shreeya Pahune, and Yagya Chaudhary, I hope you do amazing things.

Thanks to two special people, the final PhD days have been memorable and delightful. Gokul Praneetha and Aathira Nair. I would miss annoying Praneetha and her solving her “crises”. With Aathira, I have had some exceptional moments in IIIT. The NBH Biryani sharing, the mango with rotis, studying in the Library. I wish her good luck in her PhD at GWU.

A special thanks and cheers go to Kavita Ma’am and Tui-Tui for the endless cups of tea and homemade brownies.

I thank my friends Syed, Namit, Anubhav, Jahanavi, Deepa, Priti, Ruth, and Sudha. I am sorry for when I was not talking or answering calls. You, people, have constantly supported me and let me vent my frustrations. I want to thank my parents and my sister Ananya for their support and encouragement.

I thank SERB for the financial support. I also thank the organisers of the SERB-Main School 2019 for giving me an opportunity to attend the school.

My PhD life would be incomplete without my dogs, Waffle, Caesar, Oreo, Lily, and many more, and cat tuk-tuk. They were the best stress relievers, and I will miss them a lot.

List of pre-print and peer-reviewed publications

Papers in Refereed Journals

- **Right-handed neutrino pair production via second-generation leptoquarks**.
  Arvind Bhaskar, Yash Chaurasia, Kuldeep Deka, Tanumoy Mandal, Subhadip Mitra, Ananya Mukherjee.
  Physics Letters B **843**, 138039 (2023). DOI:10.1016/j.physletb.2023.138039.
  Arxiv: 2301.11889 [hep-ph]

- **Combined explanation of W-mass, muon $g-2$, $R_{K^{(*)}}$ and $R_{D^{(*)}}$ anomalies in a singlet-triplet scalar leptoquark model**.
  Arvind Bhaskar, Anirudhan A. Madathil, Tanumoy Mandal, Subhadip Mitra.
  Physical Review D **106**, 115009 (2022). DOI:10.1103/PhysRevD.106.115009.
  Arxiv: 2204.09031 [hep-ph]

- **Leptoquark-assisted singlet-mediated di-Higgs production at the LHC**.
  Arvind Bhaskar, Debottam Das, Bibhabasu De, Subhadip Mitra, Aruna Kumar Nayak and Cyrin Neeraj.
  Physics Letters B **833** 137341 (2022). DOI:10.1016/j.physletb.2022.137341.
  Arxiv: 2205.12210 [hep-ph]

- **Improving third-generation leptoquark searches with combined signals and boosted top quarks**.
  Arvind Bhaskar, Tanumoy Mandal, Subhadip Mitra and Mohit Sharma.
  Physical Review D **104**, 075037 (2021). DOI:10.1103/PhysRevD.104.075037.
  ArXiv: 2106.07605 [hep-ph].

- **Precise limits on the charge-$2/3$ U_1 vector leptoquark**.
  Arvind Bhaskar, Diganta Das, Tanumoy Mandal, Subhadip Mitra and Cyrin Neeraj.

Physical Review D **104**, 035016 (2021). DOI:10.1103/PhysRevD.104.035016.
ArXiv: 2101.12069 [hep-ph].

- **Enhancing scalar productions with leptoquarks at the LHC**.
  Arvind Bhaskar, Debottam Das, Bibhabasu De and Subhadip Mitra.
  Physical Review D **102**, 035002 (2020). DOI:10.1103/PhysRevD.102.035002.
  ArXiv: 2002.12571 [hep-ph].

- **Boosting vector leptoquark searches with boosted tops**.
  Arvind Bhaskar, Tanumoy Mandal and Subhadip Mitra.
  Physical Review D **101**, 115015 (2020). DOI:10.1103/PhysRevD.101.115015.
  ArXiv: 2004.01096 [hep-ph].

Papers in Conferences

- **Precise LHC limits on the U_1 leptoquark parameter space**.
  Arvind Bhaskar, Diganta Das, Tanumoy Mandal, Subhadip Mitra and Cyrin Neeraj.
  Proceeding Of Science **398**, 678 (2022). DOI:10.22323/1.398.0678.
  Arxiv: 2110.07638 [hep-ph]

- **LHC bounds on $R_{D^{(*)}}$ motivated Leptoquark Models.**
  Arvind Bhaskar, Diganta Das, Tanumoy Mandal, Subhadip Mitra, Cyrin Neeraj and Swapnil Raz.
  Springer Proceedings in Physics **277**, 103 (2022). DOI:10.1007/978-981-19-2354-8_18.
  Arxiv: 2105.07210 [hep-ph]

Abstract

Despite its successful predictions, the Standard Model (SM) is not a complete theory. There are theoretical issues and experimental observations that it cannot explain. Over the years, experimental measurements of several observables have shown deviations from their SM-predicted values. For instance, the latest measurement of the anomalous magnetic moment of the muon $(g-2)_\mu$ by Fermilab shows a deviation of 4.2σ. There is a discrepancy of 7σ between the SM value and the experimentally observed value of the W boson mass as reported by the CDF collaboration. The SM shows lepton-flavour universality (LFU), i.e., the couplings of leptons to the gauge bosons are flavour independent in the SM. However, the measurements of the leptonic decays of B-mesons at BaBar, Belle, and LHCb indicate some LFU violations. These deviations are popularly referred to as B-anomalies—those seen in the $R_{D^{(*)}}$ and $R_{K^{(*)}}$ observables are some of the well-known examples. Until recently, the experimental values of R_D and R_{D^*} exceeded their SM predictions by 1.4σ and 2.5σ, respectively. On the other hand, the deviations in the R_K and R_{K^*} measurements were smaller than the theoretical predictions by about 3.1σ. The current measurement of R_D still stands 2σ away from the SM, putting the global average of $R_{D^{(*)}}$ (combined) at 3.2σ.

The deviations in the measurement of $(g-2)_\mu$, W boson mass anomaly and the B-anomalies led to numerous beyond the Standard Model (BSM) explanations in the literature. Among these, the most popular ones involve a class of hypothetical particles known as the Leptoquarks (LQs). LQs are scalar (sLQ) or vector (vLQ) bosons that are electromagnetically charged. They are colour triplets with nonzero lepton numbers. They can form various weak representations—singlet, doublet or triplet. They appear in theories such as R-parity violating Supersymmetry, SU(5) Grand Unified Theories, Pati-Salam models, Technicolour models, etc. The LHC has an active LQ-search program. Their connections to the lepton and colour sector make them ideal candidates for resolving the above anomalies. In this thesis, we study the phenomenology of TeV-scale LQs, especially of the models proposed to address the anomalies and investigate their current status. We obtain the latest bounds from low-energy observables and the latest LHC data. Many of these LQ models involve sizable cross-generational LQ-lepton-quark couplings, leading to exotic decay modes of LQs. We estimate the discovery/exclusion prospects of all possible LQs in some interesting or new channels at the high-luminosity LHC (HL-LHC).

Contents

List of Figures

List of Tables

Chapter

1

Introduction

The Standard Model (SM) of particle physics describes the nature around us at a fundamental level. It is a quantum field theory based on the $SU(3)_c \times SU(2)_L \times U(1)_Y$ gauge symmetry. We show the particle contents of the SM in Fig 1.1. The visible matter content of the universe is composed of fermions. There are six flavours of quarks divided into three generations. Each carries a colour charge and a fractional electromagnetic (EM) charge. Similarly, there are three generations of leptons, and each generation contains an electromagnetically charged lepton and a corresponding neutrino.

The SM explains three of the four fundamental forces—strong, weak, and electromagnetic. Gravity is beyond the purview of SM. There are four types of gauge bosons in the SM responsible for particle interactions. The massless gluons mediate the strong force; the weak force is mediated by the massive W and Z bosons and the EM force is mediated by the massless photon. Gauge invariance requires the gauge bosons to be massless. In the SM, the Higgs Mechanism spontaneously breaks the electroweak symmetry ($SU(2)_L \times U(1)_Y$) down to $U(1)_{EM}$ giving masses to the W and Z bosons and the fermions (except for the neutrinos) but keeping the photon massless. Until recently, the sole spinless particle of the SM, the Higgs boson, was missing an experimental verification. In 2012, it was discovered at the Large Hadron Collider (LHC), the giant particle accelerator that currently collides proton beams at the centre of mass energy of 13.6 TeV.

The SM sits at the pinnacle of human intellectual achievements. It is one of the most well-tested theories. Its predictions have been experimentally verified to spectacular degrees of

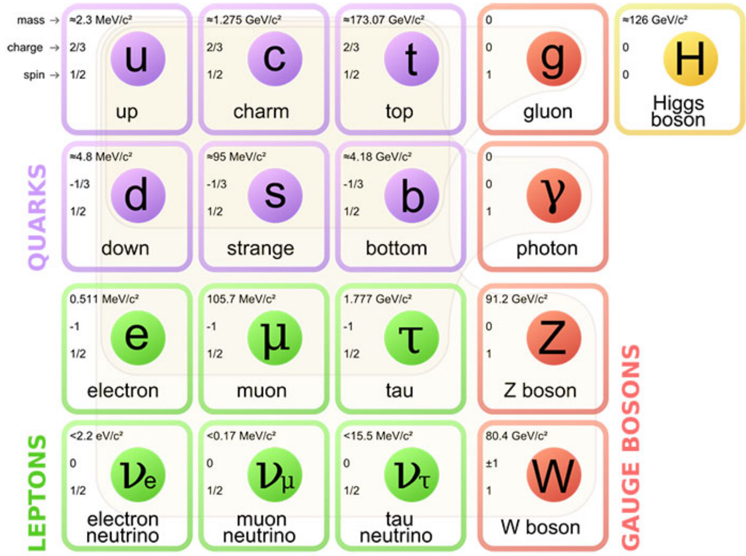

Figure 1.1: Particles in the Standard Model [1]

accuracy. However, we know that it is not the complete theory—it says nothing about gravitational interactions. However, there are more reasons for viewing the SM as an effective theory.

1.1 Shortcomings of the SM

There are both theoretical as well as experimental reasons for not treating the SM as the ultimate theory. We start with some pieces of empirical evidence first.

Neutrino Masses

The neutrinos are massless in the SM. Experimentally, we now know that neutrinos have tiny nonzero masses. The solar neutrino puzzle and the atmospheric neutrino experiments by Raymond Davies were the beginning. These experiments recorded lesser electron neutrinos reaching the earth than what was expected. The results suggested that an electron neutrino can change into a muon neutrino or vice versa as they travel from the sun to the Earth. This transmutation of neutrinos from one flavour to another can be explained by what is known as the neutrino oscillation, provided the neutrinos have nonzero masses. The neutrino oscillations experiments (Super-Kamiokande, IceCube) confirmed this, and now we know that neutrinos have tiny (much smaller than all other SM particles) but nonzero masses.

Dark Matter and Energy

The matter as we see and measure (i.e., the visible matter) makes up only 5% of the observable universe. The rest appears to be in forms, the presence of which can only be inferred through their gravitational interactions. In 1933, when the American astronomer Fritz Zwicky was studying the galaxies of the Coma cluster, he made a strange observation. He discovered that of the entire mass of the cluster required to keep it from escaping its gravitational pull, only 1% of the mass came from the visible stars in those galaxies. Similar studies were later done by numerous people, including Sinclair Smith in 1936 on the velocities of the galaxies in the Virgo cluster, Babcock in 1939 on the rotation of Andromeda galaxy (M31) using optical spectroscopy, and Kahn and Woltjer in 1959 on the velocities of the milky way and M31. These findings led us to conclude that the universe contained some kind of matter with mass but was not visible (i.e., dark matter). In the current cosmological model, the observable universe has about 27% dark matter and 68% dark energy, which is a mysterious form of energy with negative pressure needed to explain the expansion of the universe.

Anomalies in the Low-energy Experiments

Under the electroweak interactions, the three flavours of charged leptons—the electron, the muon, and the tau—behave as copies of each other, modulo their mass differences. In other words, the electroweak gauge bosons couple to the leptons in a flavour-universal manner. (The Higgs field, on the contrary, distinguishes between the different flavours of leptons and gives them different masses.) This principle of lepton flavour universality (LFU) is an important ingredient of the SM. The predictions of the LFU are well tested—the semileptonic decays of heavy hadrons act as excellent probes. However, in the last decade or so, several experiments, such as Babar, Belle, and LHCb, observed some hints of violations of this principle in some decays of the B meson. Such violations indicate the existence of some physics beyond the SM (BSM)[1]. Some significant deviations ($\sim 3\sigma$) were found in the ratios of branching ratios of the semileptonic B-decay processes

[1] Initially the results from these experiments indicated clear deviations from the SM predicted values, but now the deviations have come down. We have shown both cases in the following chapters.

like the tree level decay $b \to c\ell\nu$ or the loop-level process of $b \to s\ell\ell$[2]. Apart from these, recently, the Collider Detector at Fermilab (CDF) reported a precise measurement of the W boson mass. It deviated from the SM value by about 7σ. Similarly, the Muon g-2 experiment at Fermilab earlier reported a 4.2σ discrepancy in the measurement of the anomalous magnetic moment of the muon. We will discuss these anomalies and their possible solutions in detail in later chapters.

Parameters of the Standard Model

On the theoretical side, there are a few issues which the SM cannot resolve. For example, it contains 18 free parameters—the six quark masses, three lepton masses, three independent gauge couplings, three weak mixing angles, and a CP violating phase of the Cabibbo-Kobayashi-Maskawa (CKM) matrix, the electro-weak symmetry breaking scale (vev) and the Higgs mass—that need to be determined from experiments. Once the values of these parameters are determined, the SM agrees very well with the data from other experiments. However, the fact remains that the SM cannot explain this large set of parameters with some fundamental principles.

Hierarchy Problems

There are two types of hierarchies in the SM that are problematic. One is the gauge hierarchy problem. It comes from the vast difference between the energy scales of the weak interactions and gravity. There is another way to see this problem. The mass ($\sim$ vev) of the observed Higgs boson is $\mathcal{O}(100)$ GeV, many orders of magnitude smaller than the highest scale in the theory [the Planck scale 10^{19} GeV or the Grand Unified Theory scale 10^{16} GeV]. However, the higher-order quantum corrections are expected to take the Higgs mass to the highest scale. Since that does not happen, there must be a very high degree of cancellation within the higher-order corrections. This unnatural fine-tuning creates a strong motivation to look for a better explanation. The second hierarchy problem is called the fermion-mass hierarchy. It refers to the wide spectrum of fermion masses (even if we ignore the tiny neutrino masses, the mass of the electron is 0.5 MeV, which is negligible compared to the 172 GeV top mass) even though all fermions get their masses from the Higgs mechanism. The SM offers no explanation for this.

[2]In the latest update from the LHCb, the deviations in this process have come down.

Unification

The SM describes the strong, weak and electromagnetic interactions, but the interactions do not unify in the sense that their coupling constants do not merge into a single coupling. Though not really a limitation but the unification of interactions is a common theme of physics and we look for possibilities where a single gauge interaction at very high energies gives rise to these different interactions. This is the motivation for the Grand Unified Theories (GUTs).

In the last few decades, a large number of BSM theories have been hypothesized to address one or more limitations of the SM. In this thesis, however, we do not look at these hypotheses, rather we look at the phenomenology of a class of hypothetical particles that appears in many of these models. We consider the case of TeV-scale Leptoquarks.

1.2 Leptoquarks

Leptoquarks (LQs) are a class of colour triplet scalar and vector bosons that carry lepton numbers. They can exist as weak singlets, doublets, or triplets and, like the quarks, carry fractional EM charges. As a result, they can simultaneously couple with quarks and leptons. They are popular in the current literature as candidates for explaining the B and other anomalies observed in low-energy experiments. LQs arise naturally in many BSM theories such as R-parity violating (RPV) Supersymmetry (SUSY) [2], models with quark lepton compositness [3], Pati-Salam model [4], SU(5) or SO(10) GUTs [5], coloured Zee-Babu models [6], and Technicolor models [7], etc. Below, we briefly discuss some of these models.

– **R Parity-violating (RPV) Supersymmetry**: The R parity of a particle is given by $(-1)^{3(B-L)+2S}$, where B, L, and S denote the baryon number, lepton number, and S spin, respectively. R parity is $+1$ for the SM particles and -1 for their superpartners. The conservation of R parity implies that the lightest supersymmetric particle (LSP) cannot decay into SM particles. Thus, it can serve as an ideal candidate for dark matter. If R parity is not conserved then the superparticles can fully decay to SM particles. The RPV models allow terms that couple the squarks to the SM quarks and leptons. In other words, the squarks essentially behave as LQs. (For instance, Ref. [8] obtains bounds on SUSY particles by reinterpreting them as LQs.)

$SU(3) \times SU(2) \times U(1)$	Spin	Symbol	F
$(\bar{3}, 3, 1/3)$	0	S_3	-2
$(3, 2, 7/6)$	0	R_2	0
$(3, 2, 1/6)$	0	$\tilde{R_2}$	0
$(\bar{3}, 1, 4/3)$	0	$\tilde{S_1}$	-2
$(\bar{3}, 1, 1/3)$	0	S_1	-2
$(\bar{3}, 3, 2/3)$	0	$\bar{S_1}$	-2
$(3, 3, 2/3)$	1	U_3	0
$(\bar{3}, 2, 5/6)$	1	V_2	-2
$(\bar{3}, 2, -1/6)$	1	$\tilde{V_2}$	-2
$(3, 1, 5/3)$	1	$\tilde{U_1}$	0
$(3, 1, 2/3)$	1	U_1	0
$(3, 1, -1/3)$	1	$\bar{U_1}$	0

Table 1.1: Possible LQs [9, 10]

- **SU(5) Grand Unified Theories**: GUTs are gauge theories where the strong, weak, and electromagnetic interactions unify and hence can be described by a bigger gauge group. The general idea is to combine the fermions and bosons into a single multiplet, and interactions are mediated via new gauge bosons which carry lepton and baryon numbers. The gauge group like SU(5) proposed by Georgi and Glashow was the first such attempt at the unification of $SU(3)_c \times SU(2)_L \times U(1)_Y$ into a simpler group.

- **Pati-Salam and Composite Models:** There is much similarity between the quark and the lepton sectors in the SM. Both have the same number of generations, and each generation has the same properties as the predecessor except the mass. The Pati-Salam model, based on the gauge group $SU(4) \times SU(2)_L \times SU(2)_R$, proposed the unification of the quarks and leptons into a single representation. It predicts the existence of bosons carrying both baryon and lepton numbers. These exotic particles can be thought of as LQs. In general, in composite models, the quarks and leptons are considered to be composite particles which are composed of some fundamental particles (like Preons). These models also explain the relationship between the baryon and lepton numbers. In these models, it is assumed that the fundamental entities combine to form the first generation of quarks and leptons, and the higher generations are the higher-order excitations of the same system. Leptoquarks naturally arise in such theories. The fundamental particles that combine to form the quark and leptons can also combine to form to LQs.

The LQs have well-defined fermion numbers given as $F = 3B + L$. Thus, LQs can be classified based on their fermion numbers as those with $|F| = 0$ or $|F| = 2$. The LQs with $|F| = 0$ couple with a fermion-fermion pair, whereas the LQs with $|F| = 2$ couple with a fermion-antifermion pair. Since they are colour triplets, they can couple with a quark-quark pair as well, but here, in this thesis, we assume such interaction to be zero to avoid proton decay. We show some LQ interaction Lagrangians based on different fermion numbers below.

1. $S_1 = (\bar{\mathbf{3}}, \mathbf{1}, 1/3)$: $\mathscr{L}_{|F|=2} \supset\ y^{LL}_{1\,ij}\bar{Q}^{C\,i}_{L} S_1 i\sigma^2 L^j_L + y^{RR}_{1\,ij}\bar{u}^{C\,i}_{R} S_1 \ell^j_R + \text{H.c.}$
2. $S_3 = (\bar{\mathbf{3}}, \mathbf{3}, 1/3)$: $\mathscr{L}_{|F|=2} \supset\ y^{LL}_{3\,ij}\bar{Q}^{C\,i,a}_{L} \epsilon^{ab}(\tau^k S^k_3)^{bc} L^{j,c}_L + \text{H.c.}$
3. $R_2 = (\mathbf{3}, \mathbf{2}, 7/6)$: $\mathscr{L}_{|F|=0} \supset\ -y^{RL}_{2\,ij}\bar{u}^i_R R^a_2 \epsilon^{ab} L^{j,b}_L + y^{LR}_{2\,ji}\bar{e}^j_R R^{a\,*}_2 Q^{i,a}_L + \text{h.c.}$
4. $\tilde{R}_2 = (\bar{\mathbf{3}}, \mathbf{2}, 1/6)$: $\mathscr{L}_{|F|=0} \supset\ \tilde{y}^{\overline{LR}}_{2\,ij}\ \bar{d}^i_R \tilde{R}^a_2 \epsilon^{ab} \hat{L}^{j,b}_L + \text{H.c.}$
5. $\tilde{V}_2 = (\bar{\mathbf{3}}, \mathbf{2}, -1/6)$: $\mathscr{L}_{|F|=2} \supset\ \tilde{x}^{\overline{LR}}_{2\,ij}\bar{u}^{C\ i}_R \gamma^\mu \epsilon^{ab} \tilde{V}^b_{2,\mu} \epsilon^{ab} \hat{L}^{j,b}_L + \text{H.c.}$
6. $V_2 = (\bar{\mathbf{3}},\mathbf{2},5/6)$: $\mathscr{L}_{|F|=2} \supset\ x^{RL}_{2\ ij}\ \bar{d}^{Ci}_R \gamma^\mu V^a_{2,\mu} \epsilon^{ab} L^{jb}_L + x^{LR}_{2\ ij}\ \bar{Q}^{Ci,a}_L \gamma^\mu \epsilon^{ab} V^b_{2,\mu} \ell^j_R + \text{H.c.}$
7. $U_1 = (\mathbf{3},\mathbf{1},2/3)$: $\mathscr{L}_{|F|=0} \supset x^{LL}_{1\ ij}\ \bar{Q}^i_L \gamma^\mu U_{1,\mu} L^j_L + x^{RR}_{1\ ij}\ \bar{d}^i_R \gamma^\mu U_{1,\mu} \ell^j_R + \text{H.c.}$

Here, $\bar{Q}^C_L$ denotes the charge conjugated quark doublet, $\bar{d}^C_R$ denotes the charge conjugated down-type quark singlet, $\hat{L}_L$ stands of lepton doublet, i, j stand for generation indices, $a, b = 1, 2$ denote the $SU(2)$ indices, τ^k with $k = 1, 2, 3$ stands for the Pauli matrices. Table. 1.1 shows the list of all the scalar and vector LQs in the literature. The LHC has been actively searching for these BSM particles. We will discuss these searches and the limits obtained from them in the following chapters. In this thesis, we investigate a few LQ models that can contribute to the anomalies in the low-energy experiments and highlight the importance of obtaining precise and competitive bounds on their parameter space from the LHC.

1.3 Plan of the thesis

The thesis is divided into two parts. In the **first part**, we focus on the current status of anomalies-motivated LQ models. We analyse some simple models and obtain the parameter regions favoured by these observables that survive other low-energy bounds. We compare these with all available direct search bounds from the LHC. The parameter regions are constrained further by the indirect limits obtained by recasting the latest high p_T dilepton or monolepton searches in terms of the LQ parameters. We formulate a generic method to obtain these indirect limits. In the **second part** of the thesis, we look at its future prospects.

- In **chapter one**, we present an overview of the main problems with some backgrounds and briefly review the existing literature.

- In **chapter two**, we consider a $U_1 \equiv (\mathbf{3}, \mathbf{1}, 2/3)$ vLQ, known for its ability to fit the $R_{D^{(*)}}$ and $R_{K^{(*)}}$ measurements simultaneously. We identify the effective operators and corresponding coefficients through which the U_1 can contribute to the $R_{D^{(*)}}$ and $R_{K^{(*)}}$ observables. It contributes to $R_{D^{(*)}}$ via its coupling to a third-generation lepton(s) and, second- and third-generation quarks. For $R_{K^{(*)}}$, it has to couple to the second-generation leptons. Keeping these in mind, we make some generic flavour ansatzes and look for the relevant parameter regions that also satisfy the bounds from all relevant low-energy experiments in a systematic manner. In particular, we consider an exhaustive list of single and two-coupling scenarios. After identifying the regions of interest, we estimate the effects of precise direct and indirect LHC limits on them. We recast the latest high-p_T dilepton data to obtain the indirect limits. For this, we systematically combine all the U_1 production modes leading to dilepton final states. The production modes include resonant pair and single production of U_1, nonresonant t-channel U_1 exchange leading to a lepton pair in the final state and its interference with the SM background. We use the χ^2 parameter estimation technique to obtain the (2σ) exclusion bounds on the LQ couplings. The method is generic and can be adapted to scenarios with more-than-one unknown coupling—we illustrate the method in detail. We show that the LHC limits are competitive with the other low-energy bounds and already rule out all single-coupling scenarios. The scenarios with more than one coupling are more promising as there are overlaps between the regions favoured by the anomalies and those allowed by the LHC data. In the $R_{K^{(*)}}$ motivated single coupling scenarios, the restrictions from the LHC indirect limits on the $R_{K^{(*)}}$ favoured regions are much less. Interestingly, even though the direct search limit on U_1 can go up to 2 TeV, we identify lighter than 2 TeV multi-coupling scenarios that can bypass all limits and resolve the anomalies simultaneously.

- In **chapter three**, we investigate an interesting possibility of a simple phenomenological model with two scalar LQs—one a weak-singlet $S_1\left(\overline{\mathbf{3}}, \mathbf{1}, 1/3\right)$ and the other, weak-triplet $S_3\left(\overline{\mathbf{3}}, \mathbf{3}, 1/3\right)$—which can provide a simultaneous explanation for the discrepancies in $(g-2)_\mu$, W boson mass, $R_{D^{(*)}}$ and $R_{K^{(*)}}$ observables. We discuss an economical solution that requires minimal new couplings without any fine-tuning and is testable at the LHC. Considering all relevant bounds, we show that the LQs can be as light as ~ 1.5 TeV. By demanding that all new couplings remain within the perturbative limit, we also obtain an upper value of the LQ-mass scale.

- In **chapter four**, we provide a status update on these models in the light of the latest measurements of the $R_{K^{(*)}}$ and $R_{D^{(*)}}$ observables by the LHCb Collaboration.

- In **chapter five**, we investigate the discovery/exclusion prospects of TeV scale sLQs or vLQs decaying dominantly to a top quark and a charged lepton. Such LQs would form an exotic resonance system of a boosted top quark and a high-p_T lepton. We make an exhaustive list of the LQs which can give the desired final states. We introduce simple phenomenological parametrisations suitable for bottom-up/experimental studies and explicitly map them to all possible sLQ and vLQ models. In our collider analyses, we define our signal inclusively, allowing us to combine events from the LQ pair and single production processes. Such combinations have the potential to enhance the reach of an experiment significantly. At higher mass values, LQ single productions become more important than the pair production process due to the lesser phase space suppression. At the same time, the contribution of the single production process scales as λ^2 (λ being the LQ-q-ℓ coupling) and thus, becomes significant if λ is not negligible. The single production of LQs along with a lepton and a jet can give us the same final state ($qq\ell\ell$) as the pair production. We propose a search strategy of selecting events with at least one hadronically decaying top quark and two same-flavour opposite-sign leptons. For decays involving the τ lepton, the selection criteria are adapted suitably to reflect that a τ decays hadronically most of the time. We interpret the 2σ and 5σ significance contours in terms of LQ masses and new couplings. We identify interesting signal-signal interference effects that lead to noticeable differences in the LHC reaches depending on the weak representation of the LQs.

- In **chapter six**, we focus on an interesting possibility where LQs decay to produce right-handed neutrinos (RHNs) and quarks. There are no direct experimental constraints on the LQ couplings with quarks and RHNs. If RHNs are lighter than the LQs (possible within the inverse seesaw framework), they can be produced copiously via LQs. The LQ-mediated production of RHNs has never been searched for in experiments. We consider all possible LQs that dominantly couple to quarks and RHNs. For a conservative estimate of the prospects of this channel, we consider the quarks to be second-generation ones, except in the cases of the doublet LQs, where one component of the doublets gains coupling with the first and third-generation quarks through Cabibbo-Kobayashi-Maskawa quark mixing. There are two possible production processes for the RHNs—they can come from LQ decays or they can be directly pair produced in the quark fusion channel by a t-channel LQ exchange. The production from LQ decays is more important if the LQs are not very heavy, whereas the t-channel process contributes more if the LQs are heavy and the coupling λ is of order one. For the same reason as explained above, we combine events from different processes producing RHN pairs and jets, leading to mono and (opposite-sign) dilepton final states. We analyse these channels and estimate the HL-LHC discovery and exclusion reaches.

- In **the final chapter**, we present a summary of our studies, offer our conclusions and point to some future directions.

Part I

Anomalies-motivated leptoquark models

Chapter 2

Simultaneous explanations of the anomalies with the U_1 leptoquark

Several experiments, such as BaBar, Belle (I and II), and LHCb, reported discrepancies between their measurements of some decays of the B meson from the SM values. These discrepancies, popularly known as the 'B-anomalies', attracted a lot of attention in the literature as they hinted towards a violation of the Lepton Flavour Universality (LFU) principle, which is a prediction of the SM. (In this chapter, we describe the anomalies as they were till Summer 2022. We discuss the changes due to the latest updates in Chapter 4.) The LFU requires the coupling of the gauge bosons to the leptons to be flavour blind. Hence, any LFU violation would suggest the presence of some physics beyond the SM (BSM).

Two of the most notable B-anomalies were in seen the $R_{D^{(*)}}$ and $R_{K^{(*)}}$ observables. A TeV-scale charge-2/3 vector LQ, U_1 is an ideal candidate to explain these anomalies simultaneously. In this chapter, we investigate the U_1 solutions in detail. We obtain parameter regions where the U_1 models can explain anomalies without violating any flavour bounds. In these solutions, generally, one or more new couplings become large to resolve the anomalies. Such large couplings can be constrained from the LHC data. We inspect the direct search bounds on the U_1 solutions and obtain bounds from the latest LHC high-p_T dilepton data. To obtain precise limits, one must systematically combine all the production modes of U_1, which lead to dilepton final states. Finally, we show how a TeV-scale LQ can simultaneously explain the $R_{D^{(*)}}$ and $R_{K^{(*)}}$ anomalies and satisfy bounds from LHC and other relevant flavour observables.

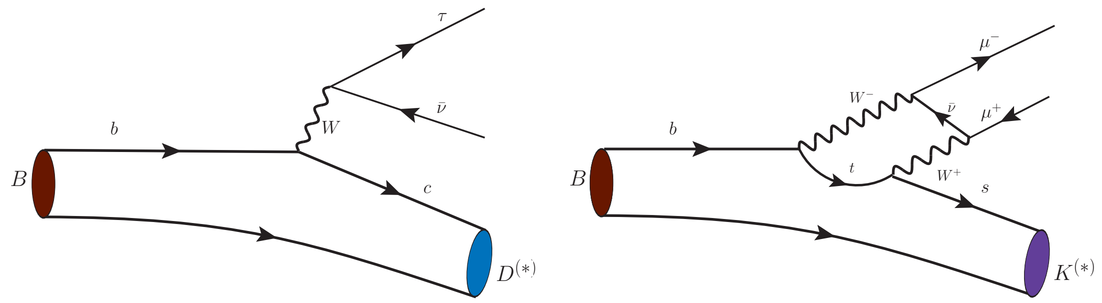

(a) (b)

Figure 2.1: We show (a) the tree level SM contribution to the $B \to D^{(*)}\tau\,\bar{\nu}$ decay and (b) the SM contribution at the loop level to the $B \to K^{(*)}\mu^+\mu^-$ decays decay.

2.1 Flavour anomalies

2.1.1 $R_{D^{(*)}}$ observables

The $R_{D^{(*)}}$ observables are defined as,

$$R_{D^{(*)}} = \frac{\mathscr{B}(B \to D^{(*)}\tau\,\bar{\nu})}{\mathscr{B}(B \to D^{(*)}\hat{\ell}\,\bar{\nu})} \tag{2.1}$$

where $\mathscr{B}$ is the branching ratio, $\hat{\ell}$ are the light leptons. The average value of $R_{D^{(*)}}$ as reported by the BaBar, Belle, and LHCb experiments is $(R_{D^{(*)}})_{Exp} = 0.340 \pm 0.027$ [11–15]. This is about 3.1σ away from the value predicted by the SM, $(R_{D^{(*)}})_{SM} = 0.258 \pm 0.005$. In the SM, it comes from a charged current-mediated semi-leptonic decay of the b quark to a charm quark and leptons ($b \to c\tau\,\bar{\nu}$) at the tree level (see Fig 2.1a). The Lagrangian for the $b \to c\tau\,\bar{\nu}$ transition in the SM is given as

$$\mathscr{L}_{\text{SM}} = -\frac{4G_F}{\sqrt{2}} V_{cb}\; \mathscr{O}_{V_L} = -\frac{4G_F}{\sqrt{2}} V_{cb}\; [\bar{c}\gamma^\mu P_L b]\big[\bar{\tau}\gamma_\mu P_L \nu_\tau\big]\,. \tag{2.2}$$

There can be new physics contributions to the $b \to c\tau\,\bar{\nu}$ transition in the form of four-fermion operators. The most general form of the Lagrangian can be written as [16]

$$\mathscr{L} \supset -\frac{4G_F}{\sqrt{2}} V_{cb}\big[\big(1 + \mathscr{C}_{V_L}\big)\mathscr{O}_{V_L} + \mathscr{C}_{V_R}\mathscr{O}_{V_R} + \mathscr{C}_{S_L}\mathscr{O}_{S_L} + \mathscr{C}_{S_R}\mathscr{O}_{S_R} + \mathscr{C}_{T_L}\mathscr{O}_{T_L}\big]\,, \tag{2.3}$$

where the Wilson coefficient corresponding to an operator $\mathscr{O}_i$ is denoted as $\mathscr{C}_i$. The operators have three different Lorentz structures:

- Vector: $\left[\begin{array}{lcl} \mathscr{O}_{V_L} & = & [\bar{c}\gamma^\mu P_L b]\big[\bar{\tau}\gamma_\mu P_L \nu\big] \\ \\ \mathscr{O}_{V_R} & = & [\bar{c}\gamma^\mu P_R b]\big[\bar{\tau}\gamma_\mu P_L \nu\big] \end{array}\right.$

- Scalar: $\left[\begin{array}{lcl} \mathcal{O}_{S_L} & = & [\bar{c} P_L b][\bar{\tau} P_L \nu] \\ \\ \mathcal{O}_{S_R} & = & [\bar{c} P_R b][\bar{\tau} P_L \nu] \end{array}\right.$

- Tensor: $\mathcal{O}_{T_L} = [\bar{c}\sigma^{\mu\nu} P_L b]\big[\bar{\tau}\sigma_{\mu\nu} P_L \nu\big].$

Evaluating the operators at the scale $\mu = \mu_b$ we can express the ratios $r_{D^{(*)}} = R_{D^{(*)}}/R^{\rm SM}_{D^{(*)}}$ in terms of the nonzero Wilson coefficients as [17, 18],

$$\begin{aligned} r_D \equiv \frac{R_D}{R_D^{\rm SM}} \approx & \left|1 + \mathcal{C}_{V_L}^{NP} + \mathcal{C}_{V_R}^{NP}\right|^2 + 1.02 \left|\mathcal{C}_{S_L}^{NP} + \mathcal{C}_{S_R}^{NP}\right|^2 + 0.90 \left|\mathcal{C}_{T_L}^{NP}\right|^2 \\ & + 1.49 \,\mathrm{Re}\Big[(1 + \mathcal{C}_{V_L}^{NP} + \mathcal{C}_{V_R}^{NP})(\mathcal{C}_{S_L}^{NP*} + \mathcal{C}_{S_R}^{NP*})\Big] \\ & + 1.14 \,\mathrm{Re}\Big[(1 + \mathcal{C}_{V_L}^{NP} + \mathcal{C}_{V_R}^{NP})(\mathcal{C}_{T_L}^{NP*})\Big], \end{aligned} \tag{2.4}$$

$$\begin{aligned} r_{D^*} \equiv \frac{R_{D^*}}{R_{D^*}^{\rm SM}} \approx & \left|1 + \mathcal{C}_{V_L}^{NP}\right|^2 + \left|\mathcal{C}_{V_R}^{NP}\right|^2 + 0.04 \left|\mathcal{C}_{S_L}^{NP} - \mathcal{C}_{S_R}^{NP}\right|^2 + 16.07 \left|\mathcal{C}_{T_L}^{NP}\right|^2 \\ & - 1.81 \,\mathrm{Re}\Big[(1 + \mathcal{C}_{V_L}^{NP})\mathcal{C}_{V_R}^{NP*}\Big] + 0.11 \,\mathrm{Re}\Big[(1 + \mathcal{C}_{V_L}^{NP} - \mathcal{C}_{V_R}^{NP})(\mathcal{C}_{S_L}^{NP*} - \mathcal{C}_{S_R}^{NP*})\Big] \\ & - 5.12 \,\mathrm{Re}\Big[(1 + \mathcal{C}_{V_L}^{NP})\mathcal{C}_{T_L}^{NP*}\Big] + 6.66 \,\mathrm{Re}\Big[\mathcal{C}_{V_R}^{NP}\mathcal{C}_{T_L}^{NP*}\Big]. \end{aligned} \tag{2.5}$$

Here, $\mathcal{C}_X^{NP}$ (with $X = V_L, V_R, S_L, S_R, T_L$) are the Wilson coefficients corresponding to the new-physics contributions.

The extra operators also contribute to some other observables in the $\bar{B} \to D^* \tau^- \bar{\nu}_\tau$ decay like the longitudinal polarization of D^* or the τ polarisation. The D^* polarisation is generally expressed as a fraction:

$$F_L(D^*) = \frac{\Gamma(\bar{B} \to D_L^* \tau \bar{\nu})}{\Gamma(\bar{B} \to D^* \tau \bar{\nu})} = \frac{\Gamma(\bar{B} \to D_L^* \tau \bar{\nu})}{\Gamma(\bar{B} \to D_T^* \tau \bar{\nu}) + \Gamma(\bar{B} \to D_L^* \tau \bar{\nu})}, \tag{2.6}$$

where D_L^* and D_T^* denote the longitudinal and transverse modes of the D^* meson, respectively. Like before, we can scale $F_L(D^*)$ with respect to its SM expectation to express it as a ratio [18]:

$$\begin{aligned} f_L(D^*) \equiv \frac{F_L(D^*)}{F_L^{\rm SM}(D^*)} \approx \frac{1}{r_{D^*}} \Big\{ & |1 + \mathcal{C}_{V_L}^{NP} - \mathcal{C}_{V_R}^{NP}|^2 + 0.08\, |\mathcal{C}_{S_L}^{NP} - \mathcal{C}_{S_R}^{NP}|^2 + 7.02\, |\mathcal{C}_{T_L}^{NP}|^2 \\ & + 0.24 \,\mathrm{Re}\Big[(1 + \mathcal{C}_{V_L}^{NP} - \mathcal{C}_{V_R}^{NP})(\mathcal{C}_{S_L}^{NP*} - \mathcal{C}_{S_R}^{NP*})\Big] - 4.37 \,\mathrm{Re}\Big[(1 + \mathcal{C}_{V_L}^{NP} - \mathcal{C}_{V_R}^{NP})(\mathcal{C}_{T_L}^{NP*})\Big]\Big\}. \end{aligned} \tag{2.7}$$

The polarization of the τ lepton in the $\bar{B} \to D^* \tau^- \bar{\nu}_\tau$ decay is expressed by the following ratio,

$$P_\tau(D^*) = \frac{\Gamma^+(D^*) - \Gamma^-(D^*)}{\Gamma^+(D^*) + \Gamma^-(D^*)}, \tag{2.8}$$

where $\Gamma^{\pm}(D^*)$ denotes the D^* decay rate when the emitted τ has helicity equal to $\pm 1/2$. The scaled expression for this observable can be written as [18],

$$\begin{aligned}
p_\tau(D^*) \equiv \frac{P_\tau(D^*)}{P_\tau^{\rm SM}(D^*)} \approx \ & \frac{1}{r_{D^*}}\Big\{|1+\mathscr{C}_{V_L}^{NP}|^2+|\mathscr{C}_{V_L}^{NP}|^2-0.07\,|\mathscr{C}_{S_L}^{NP}-\mathscr{C}_{S_R}^{NP}|^2-1.86\,|\mathscr{C}_{T_L}^{NP}|^2 \\
& -1.77\,\mathrm{Re}\Big[(1+\mathscr{C}_{V_L}^{NP})\mathscr{C}_{V_R}^{NP*}\Big]-0.22\,\mathrm{Re}\Big[(1+\mathscr{C}_{V_L}^{NP}-\mathscr{C}_{V_R}^{NP})(\mathscr{C}_{S_L}^{NP*}-\mathscr{C}_{S_R}^{NP*})\Big] \\
& -3.37\,\mathrm{Re}\Big[(1+\mathscr{C}_{V_L}^{NP})\mathscr{C}_{T_L}^{NP*}\Big]+4.37\,\mathrm{Re}\Big[\mathscr{C}_{V_R}^{NP}\mathscr{C}_{T_L}^{NP*}\Big]\Big\}. \qquad (2.9)
\end{aligned}$$

2.1.2 $R_{K^{(*)}}$ observables

The $R_{K^{(*)}}$ observables are defined as follows,

$$R_{K^{(*)}} = \frac{\mathscr{B}(B\to K^{(*)}\mu^+\mu^-)}{\mathscr{B}(B\to K^{(*)}e^+e^-)}. \qquad (2.10)$$

The LHCb found $R_{K^{(*)}}$ 3.1σ smaller than the SM-predicted value. In the SM, the $b\to s\mu^+\mu^-$ decay occurs through a loop (see Fig. 2.1b). A general Lagrangian for $b\to s\mu^+\mu^-$ transition can be written as [19, 20]

$$\mathscr{L} \supset \frac{4G_F}{\sqrt{2}} V_{tb}V_{ts}^* \sum_{i=9,10,S,P}\left(\mathscr{C}_i\mathscr{O}_i+\mathscr{C}_i'\mathscr{O}_i'\right) \qquad (2.11)$$

where the Wilson coefficients are evaluated at $\mu_{ren}=m_b$. The operators are given by

$$\begin{aligned}
\mathscr{O}_9 &= \frac{\alpha}{4\pi}(\bar{s}_L\gamma_\alpha b_L)(\bar{\mu}\gamma^\alpha\mu), & \mathscr{O}_9' &= \frac{\alpha}{4\pi}(\bar{s}_R\gamma_\alpha b_R)(\bar{\mu}\gamma^\alpha\mu),\\
\mathscr{O}_{10} &= \frac{\alpha}{4\pi}(\bar{s}_L\gamma_\alpha b_L)(\bar{\mu}\gamma^\alpha\gamma_5\mu), & \mathscr{O}_{10}' &= \frac{\alpha}{4\pi}(\bar{s}_R\gamma_\alpha b_R)(\bar{\mu}\gamma^\alpha\gamma_5\mu),\\
\mathscr{O}_S &= \frac{\alpha}{4\pi}(\bar{s}_L b_R)(\bar{\mu}\mu), & \mathscr{O}_S' &= \frac{\alpha}{4\pi}(\bar{s}_R b_L)(\bar{\mu}\mu),\\
\mathscr{O}_P &= \frac{\alpha}{4\pi}(\bar{s}_L b_R)(\bar{\mu}\gamma_5\mu), & \mathscr{O}_P' &= \frac{\alpha}{4\pi}(\bar{s}_R b_L)(\bar{\mu}\gamma_5\mu)
\end{aligned}$$

where α is the fine-structure constant. We show the new physics contributions to the Wilson coefficients in the following sections.

2.2 A promising solution to the anomalies

A TeV scale vector LQ is a suitable candidate to explain these B-anomalies [21–50]. [1] A U_1 vector LQ of charge-2/3 is known to explain the $R_{D^{(*)}}$ and $R_{K^{(*)}}$ anomalies simultaneously [37]. The necessary interactions can be expressed as [9, 10, 76, 77],

$$\mathscr{L} \supset x_{1\,ij}^{LL}\ \bar{Q}^i\gamma_\mu U_1^\mu P_L L^j + x_{1\,ij}^{RR}\ \bar{d}_R^i\gamma_\mu U_1^\mu P_R \ell_R^j + \text{H.c.} \tag{2.12}$$

Here, Q_i and L_j denote the SM left-handed quark and lepton doublets, respectively, and d_R^i and ℓ_R^j are the right-handed down-type quarks and leptons, respectively. The indices $i, j = \{1,\ 2,\ 3\}$ stand for quark and lepton generations, respectively; i.e., $x_{1\,ij}^{LL}$ and $x_{1\,ij}^{RR}$ are 3×3 matrices in flavour space. Though these matrices can be complex in general, we assume them to be real as the LHC is insensitive to their complex natures. The U_1 can explain the $R_{D^{(*)}}$ anomalies at the tree level via the $U_1 b\tau$ and $U_1 c\nu$ couplings,(see Fig. 2.2a). The U_1 can also contribute to the $R_{K^{(*)}}$ at the tree level by the $U_1 s\mu$ and $U_1 b\mu$ couplings (see Fig. 2.2b). Thus, keeping the required couplings in mind, we make the following flavour ansatz:

$$x_1^{LL} = \begin{pmatrix} 0 & 0 & 0 \\ 0 & \lambda_{22}^L & \lambda_{23}^L \\ 0 & \lambda_{32}^L & \lambda_{33}^L \end{pmatrix};\ x_1^{RR} = \begin{pmatrix} 0 & 0 & 0 \\ 0 & \lambda_{22}^R & 0 \\ 0 & \lambda_{32}^R & \lambda_{33}^R \end{pmatrix}. \tag{2.13}$$

The new coupling λ is responsible for the LQ-quark-lepton interaction. For instance, λ_{23}^L stands for the strength of the U_1 interaction with a second generation quark and a third-generation lepton.

In the case of the vLQ U_1, the kinetic term contains an additional term given as [10, 78],

$$\mathscr{L} \supset -\frac{1}{2} U_{1\mu\nu}^\dagger U_1^{\mu\nu} + M_{U_1}^2\ U_{1\mu}^\dagger U_1^\mu - i g_s \kappa\ U_{1\mu}^\dagger T^a U_{1\nu}\ G^{a\mu\nu}, \tag{2.14}$$

where $M_{U_1}^2$ is the mass of U_1. The pair and single production cross sections depend on κ. For our analysis, we consider the benchmark value $\kappa = 0$.

2.3 $R_{D^{(*)}}$ scenarios

From the flavour ansätz in Eq. (2.13), we see that various combinations of the couplings λ_{23}^L, λ_{33}^L, and λ_{33}^R can resolve the $R_{D^{(*)}}$ anomalies. After the necessary Fierz transformations, we find that

[1] See Refs. [51–75] and the references therein for other recent phenomenological studies on LQs.

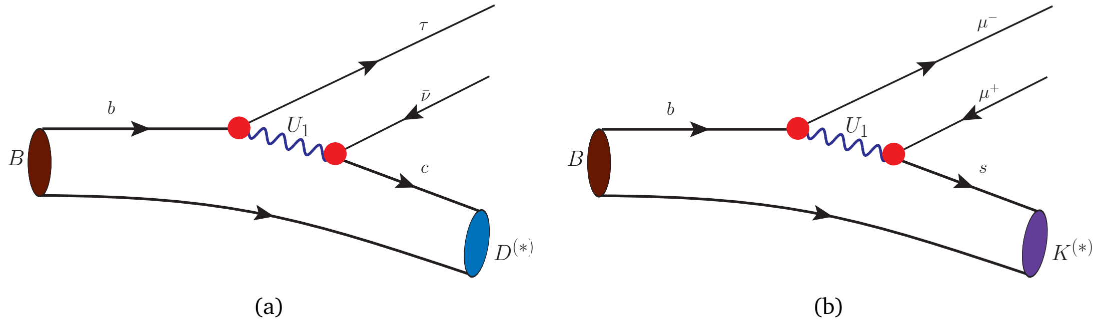

Figure 2.2: The Feynman diagrams representing the U_1 contribution at the tree level to the $B \to D^{(*)}\tau\bar{\nu}$ and $B \to K^{(*)}\mu^+\mu^-$ decays.

the U_1 can contribute only to $\mathcal{O}_{V_L}$ and $\mathcal{O}_{S_L}$, i.e., $\mathcal{C}_{V_R}^{U_1} = \mathcal{C}_{S_R}^{U_1} = \mathcal{C}_{T_R}^{U_1} = 0$ [Eq. (2.3)]. The nonzero Wilson coefficients, $\mathcal{C}_{V_L}$ and $\mathcal{C}_{S_L}$ can be written in terms of the $\bar{c}\nu U_1$ and $\bar{b}\tau U_1$ couplings as,

$$\left.\begin{aligned} \mathcal{C}_{V_L}^{U_1} &= \frac{1}{2\sqrt{2}G_F V_{cb}} \frac{\lambda_{c\nu}^L \left(\lambda_{b\tau}^L\right)^*}{M_{U_1}^2} \\ \mathcal{C}_{S_L}^{U_1} &= -\frac{1}{2\sqrt{2}G_F V_{cb}} \frac{2\lambda_{c\nu}^L \left(\lambda_{b\tau}^R\right)^*}{M_{U_1}^2} \end{aligned}\right\}. \tag{2.15}$$

Thus, the expressions for $R_{D^{(*)}}$ and the related observables (see Section 2.1.1) change as follows,

$$r_D \equiv \frac{R_D}{R_D^{\rm SM}} \approx \left|1+\mathcal{C}_{V_L}^{U_1}\right|^2 + 1.02\,\left|\mathcal{C}_{S_L}^{U_1}\right|^2 + 1.49\,{\rm Re}\left[(1+\mathcal{C}_{V_L}^{U_1})\mathcal{C}_{S_L}^{U_1*}\right], \tag{2.16}$$

$$r_{D^*} \equiv \frac{R_{D^*}}{R_{D^*}^{\rm SM}} \approx \left|1+\mathcal{C}_{V_L}^{U_1}\right|^2 + 0.04\,\left|\mathcal{C}_{S_L}^{U_1}\right|^2 - 0.11\,{\rm Re}\left[(1+\mathcal{C}_{V_L}^{U_1})\mathcal{C}_{S_L}^{U_1*}\right], \tag{2.17}$$

$$f_L(D^*) \equiv \frac{F_L(D^*)}{F_L^{\rm SM}(D^*)} \approx \frac{1}{r_{D^*}}\left\{|1+\mathcal{C}_{V_L}^{U_1}|^2 + 0.08\,|\mathcal{C}_{S_L}^{U_1}|^2 - 0.24\,{\rm Re}\left[(1+\mathcal{C}_{V_L}^{U_1})\mathcal{C}_{S_L}^{U_1*}\right]\right\}, \tag{2.18}$$

$$p_\tau(D^*) \equiv \frac{P_\tau(D^*)}{P_\tau^{\rm SM}(D^*)} \approx \frac{1}{r_{D^*}}\left\{|1+\mathcal{C}_{V_L}^{U_1}|^2 - 0.07\,|\mathcal{C}_{S_L}^{U_1}|^2 + 0.22\,{\rm Re}\left[(1+\mathcal{C}_{V_L}^{U_1})\mathcal{C}_{S_L}^{U_1*}\right]\right\}. \tag{2.19}$$

In addition to this, a nonzero $\mathcal{C}_{V_L}^{U_1}$ and $\mathcal{C}_{S_L}^{U_1}$ would also contribute to leptonic decays $B_c \to \tau\nu$ and $B \to \tau\nu$ as,

$$\mathcal{B}(B_c \to \tau\nu) = \frac{\tau_{B_c} m_{B_c} f_{B_c}^2 G_F^2 |V_{cb}|^2}{8\pi} m_\tau^2 \left(1 - \frac{m_\tau^2}{m_{B_c}^2}\right)^2 \left|1 + \mathcal{C}_{V_L}^{U_1} + \frac{m_{B_c}^2}{m_\tau(m_b+m_c)}\mathcal{C}_{S_L}^{U_1}\right|^2, \tag{2.20}$$

$$\mathcal{B}(B \to \tau\nu) = \mathcal{B}(B \to \tau\nu)_{\rm SM} \left|1 + \mathcal{C}_{V_L}^{U_1} + \frac{m_B^2}{m_\tau(m_b+m_u)}\mathcal{C}_{S_L}^{U_1}\right|^2 \tag{2.21}$$

where τ_{B_c} is the lifetime of the B_c meson, f_{B_c} is its decay constant, and $\mathcal{B}(B \to \tau\nu)_{\rm SM}$ is the branching ratio within the SM. The LEP data put a constraint on the $B_c \to \tau\nu$ branching ratio [79]

Observable	Experimentally Allowed Range	SM Expectation	Ratio	Value
R_D	$0.340 \pm 0.027 \pm 0.013$ [15]	0.299 ± 0.003 [11]	r_D	1.137 ± 0.101
R_{D^*}	$0.295 \pm 0.011 \pm 0.008$ [15]	0.258 ± 0.005 [15]	r_{D^*}	1.144 ± 0.057
$F_L(D^*)$	$0.60 \pm 0.08 \pm 0.035$ [82, 83]	0.46 ± 0.04 [84]	$f_L(D^*)$	1.313 ± 0.198
$P_\tau(D^*)$	$-0.38 \pm 0.51^{+0.21}_{-0.16}$ [85]	-0.497 ± 0.013 [16]	$p_\tau(D^*)$	0.766 ± 1.093
$\mathscr{B}(B \to \tau\nu)$	$< (1.09 \pm 0.24) \times 10^{-4}$ [80]	$(0.812 \pm 0.054) \times 10^{-4}$ [81]		
$\mathscr{B}(B_c \to \tau\nu)$	$< 10\%$ [79]			

Table 2.1: Bounds on the $R_{D^{(*)}}$ scenarios.

as, $\mathscr{B}(B_c \to \tau\nu) < 10\%$. The experimental upper bound on the $B \to \tau\nu$ decay is given as [80] $\mathscr{B}(B \to \tau\nu) < (1.09 \pm 0.24) \times 10^{-4}$, and the corresponding SM branching ratio is estimated to be [81] $\mathscr{B}(B \to \tau\nu)_{\rm SM} = (0.812 \pm 0.054) \times 10^{-4}$. We summarise the bounds on these observables in Table 2.1.

In addition to these, we also consider bounds from the B_s-$\bar{B}_s$ mixing [see Fig. 2.3a] through the effective Hamiltonian,

$$H_{\rm eff} = (\mathscr{C}^{\rm SM}_{box} + \mathscr{C}^{U_1}_{box})(\bar{s}_L \gamma^\alpha b_L)(\bar{s}_L \gamma_\alpha b_L) \tag{2.22}$$

where the SM and U_1 contributions are given as $\mathscr{C}^{\rm SM}_{box}$ and $\mathscr{C}^{U_1}_{box}$ respectively. $\mathscr{C}^{U_1}_{box}$ depends on the new coupling(s) as $\sim \lambda^4$. The expressions are given as,

$$\mathscr{C}^{\rm SM}_{box} = \frac{G_F^2}{4\pi^2}(V_{tb}V_{ts})^2 M_W^2 S_0(x_t), \tag{2.23}$$

$$\mathscr{C}^{U_1}_{box} = \frac{\lambda^4}{8\pi^2 M_{U_1}^2}. \tag{2.24}$$

In Eq. (2.24), we ignore the generation indices and Cabibbo-Kobayashi-Maskawa (CKM) elements as they depend on the scenario we would be considering. The loop function is the Inami-Lim function [86], $S_0(x_t \equiv m_t^2/m_W^2) \sim 2.37$ [87]. The UTfit Collaboration gives the following bounds on the ratio $\mathscr{C}^{U_1}_{box}/\mathscr{C}^{\rm SM}_{box}$ [81]:

$$0.94 < \left| 1 + \frac{\mathscr{C}^{U_1}_{box}}{\mathscr{C}^{\rm SM}_{box}} \right| < 1.29. \tag{2.25}$$

A non-zero $\lambda^L_{b\tau}$ and $\lambda^L_{s\tau}$ can also contribute to another lepton-flavour-universal operator in a log-enhanced manner through an off-shell photon penguin diagram as [see Fig. 2.3b].

$$\mathscr{L} \supset -\frac{4G_F}{\sqrt{2}}\left(V_{tb}V_{ts}^*\right)\mathscr{C}_9^{\rm univ}\mathscr{O}_9^{\rm univ} \tag{2.26}$$

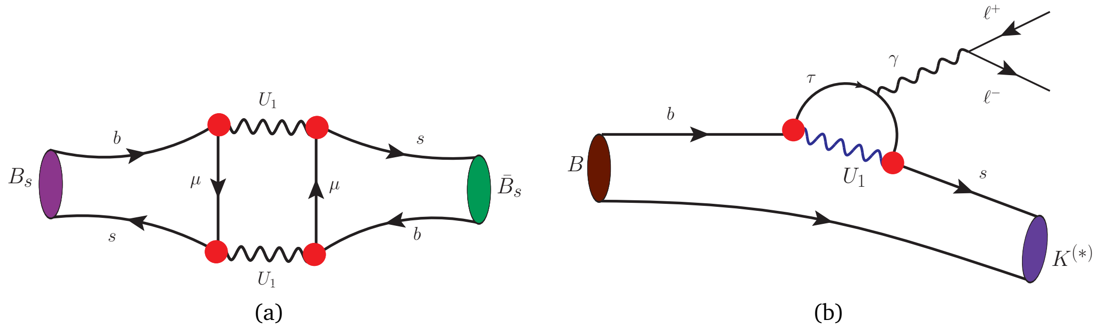

Figure 2.3: (a) The Feynman diagram showing the U_1 contribution to B_s-$\bar{B}_s$ mixing and (b) the U_1-mediated photon penguin diagram contributing to $b \to s\ell^+\ell^-$.

where

$$\mathcal{O}_9^{\rm univ} = \frac{\alpha}{4\pi}(\bar{s}_L\gamma_\alpha b_L)\left(\bar{\ell}\gamma^\alpha\ell\right) \quad \text{and} \quad \mathcal{C}_9^{\rm univ} = -\frac{1}{V_{tb}V_{ts}^*}\frac{\lambda_{s\tau}^L\left(\lambda_{b\tau}^L\right)^*}{3\sqrt{2}G_F M_{U_1}^2}\log(m_b^2/M_{U_1}^2). \tag{2.27}$$

We consider the 2σ limits from the global fits to the $b \to s\mu^+\mu^-$ data [88–90] as $-1.27 \leq \mathcal{C}_9^{\rm univ} \leq -0.51$.

We investigate the U_1 solutions in a bottom-up manner and construct single and multi-coupling U_1 scenarios, which can contribute to the $R_{D^{(*)}}$ anomalies, depending on the couplings we have assumed. We begin with the single coupling scenarios.

■ Scenario RD1A: Here, we set all the $R_{D^{(*)}}$ motivated couplings but λ_{23}^L to zero. This gives us the $\bar{c}\nu U_1$ and $\bar{s}\tau U_1$ interactions. We further assume that the U_1 is aligned with the up-type quarks, i.e., the down-type quark mix via the CKM matrix [91]. This gives us the required $\bar{b}\tau U_1$ coupling of strength $V_{cb}^*\lambda_{23}^L$. Here, V_{cb} is the element in the CKM matrix. The interaction Lagrangian becomes,

$$\begin{aligned}\mathcal{L} &\supset \lambda_{23}^L[\bar{c}_L\gamma_\mu\nu_L + \bar{s}_L\gamma_\mu\tau_L)]U_1^\mu, \\ &= \lambda_{23}^L[\bar{c}_L\gamma_\mu\nu_L + (V_{cd}^*\bar{d}_L + V_{cs}^*\bar{s}_L + V_{cb}^*\bar{b}_L)\gamma_\mu\tau_L)]U_1^\mu\end{aligned} \tag{2.28}$$

giving

$$\mathcal{C}_{V_L}^{RD1A} = \frac{1}{2\sqrt{2}G_F}\frac{\left(\lambda_{23}^L\right)^2}{M_{U_1}^2}, \quad \mathcal{C}_{S_L}^{RD1A} = 0. \tag{2.29}$$

Likewise, the observables, $R_{D^{(*)}}$, $F_L(D^*)$, $P_\tau(D^*)$, and $\mathcal{B}(B_{(c)} \to \tau\nu)$ also receive contributions from the U_1. In Fig. 2.3, the off-shell penguin diagram leads to a log-enhanced lepton-universal contribution to the $b \to s\ell^+\ell^-$ transition [36]:

$$\mathscr{C}_9^{\rm univ} = -\frac{V_{cb}V_{cs}^*}{V_{tb}V_{ts}^*}\frac{\left(\lambda_{23}^L\right)^2}{3\sqrt{2}G_F M_{U_1}^2}\log(m_b^2/M_{U_1}^2). \tag{2.30}$$

This scenario would lead to a nonzero contribution to the B_s-$\bar{B}_s$ mixing coefficient as

$$\mathscr{C}_{box}^{U_1} = \frac{|V_{cb}|^2|V_{cs}|^2(\lambda_{23}^L)^4}{8\pi^2 M_{U_1}^2}. \tag{2.31}$$

In this scenario, the U_1 decays to $c\bar{\nu}$ and $s\tau^+$ with almost 50% BR.

■ Scenario RD1B: In this scenario, we assume only λ_{33}^L to be non-zero. This leads to the $\bar{b}\tau U_1$ and $\bar{t}\nu U_1$ couplings. Here, we assume that U_1 is aligned with the down-type quarks—there is mixing in the up-type quarks. Hence, we obtain the effective $\bar{c}\nu U_1$ coupling as $V_{cb}\lambda_{33}^L$. The interaction Lagrangian is given as,

$$\begin{aligned}\mathscr{L} \supset\ & \lambda_{33}^L[\bar{t}_L\gamma_\mu\nu_L + \bar{b}_L\gamma_\mu\tau_L]U_1^\mu \\ =\ & \lambda_{33}^L[(V_{ub}\bar{u}_L + V_{cb}\bar{c}_L + V_{tb}\bar{t}_L)\gamma_\mu\nu_L) + \bar{b}_L\gamma_\mu\tau_L]U_1^\mu,\end{aligned} \tag{2.32}$$

and the contributions to the Wilson coefficients are given by

$$\mathscr{C}_{V_L}^{RD1B} = \frac{1}{2\sqrt{2}G_F}\frac{\left(\lambda_{33}^L\right)^2}{M_{U_1}^2}, \quad \mathscr{C}_{S_L}^{RD1B} = 0. \tag{2.33}$$

As in the previous scenario, the $R_{D^{(*)}}$, $F_L(D^*)$, $P_\tau(D^*)$, and $\mathscr{B}(B_{(c)} \to \tau\nu)$ observables receive contributions from U_1. The dominant decay modes of U_1 are $U_1 \to t\bar{\nu}$ and $U_1 \to b\tau^+$ with 50% BR each.

In a single coupling scenario with only λ_{33}^R as the non-zero coupling the U_1 would exclusively decay to the $b\tau^+$ final state. However, only λ_{33}^R cannot explain the $R_{D^{(*)}}$ anomalies. Hence, we do not consider it.

We move on to the two-coupling and other multi-coupling scenarios.

■ Scenario RD2A: In this two coupling scenario, we consider λ_{23}^L and λ_{33}^L to be nonzero. Here, we assume U_1 to be aligned with the physical basis of the down-type quarks. Thus, there is mixing in the up-quark sector. The interaction Lagrangian reads as,

$$\begin{aligned}\mathscr{L} \supset\ & [\lambda_{23}^L(\bar{c}_L\gamma_\mu\nu_L + \bar{s}_L\gamma_\mu\tau_L) + \lambda_{33}^L(\bar{t}_L\gamma_\mu\nu_L + \bar{b}_L\gamma_\mu\tau_L)]U_1^\mu \\ =\ & [\lambda_{23}^L(V_{us}\bar{u}_L\gamma_\mu\nu_L + V_{cs}\bar{c}_L\gamma_\mu\nu_L + V_{ts}\bar{t}_L\gamma_\mu\nu_L + \bar{s}_L\gamma_\mu\tau_L) \\ & + \lambda_{33}^L(V_{ub}\bar{u}_L\gamma_\mu\nu_L + V_{cb}\bar{c}_L\gamma_\mu\nu_L + V_{tb}\bar{t}_L\gamma_\mu\nu_L + \bar{b}_L\gamma_\mu\tau_L)]U_1^\mu,\end{aligned} \tag{2.34}$$

Here, $\mathscr{C}_{V_L}^{RD2A}$ is the only nonzero Wilson coefficient, i.e.,

$$\mathscr{C}_{V_L}^{RD2A} = \frac{1}{2\sqrt{2}G_F V_{cb}} \frac{(V_{cs}\lambda_{23}^L + V_{cb}\lambda_{33}^L)\lambda_{33}^L}{M_{U_1}^2}, \qquad \mathscr{C}_{S_L}^{RD2A} = 0. \tag{2.35}$$

In addition to the contribution to the $R_{D^{(*)}}$, $F_L(D^*)$, $P_\tau(D^*)$, and $\mathscr{B}(B_{(c)} \to \tau\nu)$ processes, we consider the lepton flavour-universal contribution

$$\mathscr{C}_9^{\rm univ} = -\frac{1}{V_{tb}V_{ts}^*} \frac{\lambda_{23}^L\lambda_{33}^L}{3\sqrt{2}G_F M_{U_1}^2} \log(m_b^2/M_{U_1}^2). \tag{2.36}$$

In this scenario, the B_s-$\bar{B}_s$ mixing coefficient would receive a contribution from U_1

$$\mathscr{C}_{box}^{U_1} = \frac{\left(\lambda_{23}^L\right)^2\left(\lambda_{33}^L\right)^2}{8\pi^2 M_{U_1}^2}. \tag{2.37}$$

Here, U_1 can decay to $c\bar{\nu}$, $s\tau^+$, $t\bar{\nu}$, and $b\tau^+$ final states with roughly equal BRs.

■ Scenario RD2B: In this scenario, we assume λ_{23}^L and λ_{33}^R are nonzero. The interaction Lagrangian reads as,

$$\begin{aligned}\mathscr{L} &\supset [\lambda_{23}^L(\bar{c}_L\gamma_\mu\nu_L + \bar{s}_L\gamma_\mu\tau_L) + \lambda_{33}^R\bar{b}_R\gamma_\mu\tau_R]U_1^\mu \\ &= [\lambda_{23}^L(V_{us}\bar{u}_L\gamma_\mu\nu_L + V_{cs}\bar{c}_L\gamma_\mu\nu_L + V_{ts}\bar{t}_L\gamma_\mu\nu_L + \bar{s}_L\gamma_\mu\tau_L) + \lambda_{33}^R\bar{b}_R\gamma_\mu\tau_R]U_1^\mu\end{aligned} \tag{2.38}$$

Similar to the previous two-coupling scenario, we assume mixing among the up-type quarks. However in this case, we get a contribution to $\mathscr{C}_{S_L}$:

$$\mathscr{C}_{V_L}^{RD2B} = 0, \quad \mathscr{C}_{S_L}^{RD2B} = -\frac{V_{cs}}{\sqrt{2}G_F V_{cb}} \frac{\lambda_{23}^L\lambda_{33}^R}{M_{U_1}^2}. \tag{2.39}$$

Here, $R_{D^{(*)}}$, $F_L(D^*)$, $P_\tau(D^*)$, and $\mathscr{B}(B_{(c)} \to \tau\nu)$ receive contributions from U_1. The dominant decay modes of U_1 are $U_1 \to c\bar{\nu}$, $U_1 \to s\tau^+$, and $U_1 \to b\tau^+$. Note that even though $\lambda_{33}^L = 0$ in this scenario, a small $\mathscr{C}_{V_L}$ can be generated from effective λ_{33}^L coupling if, instead of up-type quark mixing, one assumes mixing in the down sector (like in Scenario RD1A).

Combinations	Best fit	1σ	2σ	Corresponding scenarios
$\mathcal{C}_9^{U_1} = -\mathcal{C}_{10}^{U_1}$	-0.44	$[-0.52, -0.37]$	$[-0.60, -0.29]$	RK1A, RK1B, RK2A
$\mathcal{C}_S^{U_1} = -\mathcal{C}_P^{U_1}$	-0.0252	$[-0.0378, -0.126]$	$[-0.0588, -0.0042]$	RK2B
$\mathcal{C}_9^{\prime\, U_1} = \mathcal{C}_{10}^{\prime\, U_1}$	$+0.06$	$[-0.18, +0.30]$	$[-0.42, +0.55]$	RK1C, RK1D, RK2D
$\mathcal{C}_S^{\prime\, U_1} = \mathcal{C}_P^{\prime\, U_1}$	-0.0252	$[-0.0378, -0.126]$	$[-0.0588, -0.0042]$	RK2C

Table 2.2: Global fits of combinations of Wilson coefficients relevant in the $R_{K^{(*)}}$ observables [89, 90, 92].

2.4 $R_{K^{(*)}}$ scenarios

We write the U_1 contribution to the Wilson coefficients in terms of the $\bar{b}\mu U_1$ and $\bar{s}\mu U_1$ couplings as,

$$\left.\begin{aligned}
\mathcal{C}_9^{LQ} &= -\mathcal{C}_{10}^{LQ} = \frac{\pi}{\sqrt{2}G_F V_{tb}V_{ts}^*\alpha}\frac{\lambda_{s\mu}^L(\lambda_{b\mu}^L)^*}{M_{U_1}^2} \\
\mathcal{C}_S^{LQ} &= -\mathcal{C}_P^{LQ} = \frac{-\sqrt{2}\pi}{G_F V_{tb}V_{ts}^*\alpha}\frac{\lambda_{s\mu}^L(\lambda_{b\mu}^R)^*}{M_{U_1}^2} \\
\mathcal{C}_9^{\prime\, LQ} &= \mathcal{C}_{10}^{\prime\, LQ} = \frac{\pi}{\sqrt{2}G_F V_{tb}V_{ts}^*\alpha}\frac{\lambda_{s\mu}^R(\lambda_{b\mu}^{R*})}{M_{U_1}^2} \\
\mathcal{C}_S^{\prime\, LQ} &= \mathcal{C}_P^{\prime\, LQ} = \frac{-\sqrt{2}\pi}{G_F V_{tb}V_{ts}^*\alpha}\frac{\lambda_{s\mu}^R(\lambda_{b\mu}^{L*})}{M_{U_1}^2}
\end{aligned}\right\} . \tag{2.40}$$

As we did for the $R_{D^{(*)}}$ scenarios, Here, as well, we consider one and multi-coupling scenarios. The relevant global fits of the Wilson coefficients to the $b \to s\mu^+\mu^-$ data are taken from Refs. [89, 90, 92] and are listed in Table 2.2.

■ <u>Scenario RK1A:</u> In this $R_{K^{(*)}}$ single coupling scenario, we consider only λ_{22}^L to be nonzero. This generates the required $\bar{s}\mu U_1$ coupling. If we assume the U_1 is aligned in the physical up-quark basis, then the required $\bar{b}\mu U_1$ coupling is generated via CKM mixing in the down-quark sector, (similar to Scenario RD1A and Scenario RD1B). The interaction Lagrangian reads as

$$\mathcal{L} \supset \lambda_{22}^L[\bar{c}_L\gamma_\mu\nu_L + (V_{cd}^*\bar{d}_L + V_{cs}^*\bar{s}_L + V_{cb}^*\bar{b}_L)\gamma_\mu\mu_L)]U_1^\mu . \tag{2.41}$$

This Lagrangian contributes to the following coefficients:

$$\mathcal{C}_9^{RK1A} = -\mathcal{C}_{10}^{RK1A} = \frac{\pi V_{cb} V_{cs}^*}{\sqrt{2} G_F V_{tb} V_{ts}^* \alpha} \frac{(\lambda_{22}^L)^2}{M_{U_1}^2}. \tag{2.42}$$

The contribution to the B_s-$\bar{B}_s$ mixing coefficient is given by

$$\mathcal{C}_{box}^{U_1} = \frac{|V_{cb}|^2 |V_{cs}|^2 (\lambda_{22}^L)^4}{8\pi^2 M_{U_1}^2}. \tag{2.43}$$

The dominant decay modes of U_1 in this case are $U_1 \to c\bar{\nu}$ and $U_1 \to s\mu^+$ with almost 50% BR each.

■ Scenario RK1B: In this single-coupling scenario, we assume only λ_{32}^L to be nonzero. The interaction Lagrangian is given by

$$\mathcal{L} \supset \lambda_{32}^L [\bar{t}_L \gamma_\mu \nu_L + (V_{td}^* \bar{d}_L + V_{ts}^* \bar{s}_L + V_{tb}^* \bar{b}_L) \gamma_\mu \mu_L)] U_1^\mu. \tag{2.44}$$

The relevant Wilson coefficients are given by

$$\mathcal{C}_9^{RK1B} = -\mathcal{C}_{10}^{RK1B} = \frac{\pi}{\sqrt{2} G_F \alpha} \frac{(\lambda_{32}^L)^2}{M_{U_1}^2}, \tag{2.45}$$

and the contribution to the B_s-$\bar{B}_s$ mixing coefficient is given as

$$\mathcal{C}_{box}^{U_1} = \frac{|V_{tb}|^2 |V_{ts}|^2 (\lambda_{32}^L)^4}{8\pi^2 M_{U_1}^2}. \tag{2.46}$$

Here, we consider the U_1 to be aligned with the up-type quark sector. Hence, the off-diagonal couplings are generated via mixing amongst the down-type quarks. From the Lagrangian, we can see that the $\bar{s}\mu U_1$ coupling is V_{ts}^*-suppressed. The coupling λ_{32}^L alone, however, cannot explain the $R_K^{(*)}$ anomalies. From Table 2.2, we see that the anomalies need a negative $\mathcal{C}_9$, whereas the r.h.s. of Eq. (2.45) is always positive (even if we consider a complex λ_{32}^L). The dominant decay modes of U_1 in this case are $U_1 \to t\bar{\nu}$ and $U_1 \to b\mu^+$, and they share almost 50% BR each.

■ Scenario RK1C: In this scenario, we assume only λ_{22}^R to be nonzero. The interaction Lagrangian is given by,

$$\mathcal{L} \supset \lambda_{22}^R [(V_{cd} \bar{d}_R + V_{cs} \bar{s}_R + V_{cb} \bar{b}_R) \gamma_\mu \mu_R] U_1^\mu. \tag{2.47}$$

The nonzero Wilson coefficients from Eq. (2.40) are

$$\mathcal{C'}_9^{RK1C} = \mathcal{C'}_{10}^{RK1C} = \frac{\pi V_{cb}^* V_{cs}}{\sqrt{2} G_F V_{tb} V_{ts}^* \alpha} \frac{(\lambda_{22}^R)^2}{M_{U_1}^2}, \tag{2.48}$$

and the contribution to the B_s-$\bar{B}_s$ mixing coefficient is

$$\mathscr{C}^{U_1}_{box} = \frac{|V_{cb}|^2|V_{cs}|^2(\lambda^R_{22})^4}{8\pi^2 M^2_{U_1}}. \tag{2.49}$$

Here, the $\bar{b}\mu U_1$ coupling is V^*_{cb} suppressed. In this scenario, the $U_1 \to s\mu^+$ decay mode has almost 100% BR.

■ <u>Scenario RK1D:</u> We assume λ^R_{32} to be nonzero and the rest of the couplings to be SM-like. The interaction Lagrangian is given by

$$\mathscr{L} \supset \lambda^R_{32}[(V_{td}\bar{d}_R + V_{ts}\bar{s}_R + V_{tb}\bar{b}_R)\gamma_\mu \mu_R]U^\mu_1 \tag{2.50}$$

where the $\bar{s}\mu U_1$ coupling is V_{ts} suppressed. The nonzero Wilson coefficients are

$$\mathscr{C}'^{RK1D}_{9} = \mathscr{C}'^{RK1D}_{10} = \frac{\pi V^*_{tb}V_{ts}}{\sqrt{2}G_F V_{tb}V^*_{ts}\alpha}\frac{(\lambda^R_{32})^2}{M^2_{U_1}}. \tag{2.51}$$

In this scenario, the $U_1 \to b\mu^+$ decay mode is dominant with almost 100% BR. The contribution to the B_s-$\bar{B}_s$ mixing coefficient is given as

$$\mathscr{C}^{U_1}_{box} = \frac{|V_{tb}|^2|V_{ts}|^2(\lambda^R_{32})^4}{8\pi^2 M^2_{U_1}}. \tag{2.52}$$

We now consider the two coupling scenarios relevant to the $R_{K^{(*)}}$ anomalies.

■ <u>Scenario RK2A:</u> In this scenario, we assume the couplings λ^L_{22} and λ^L_{32} to be nonzero. The interaction Lagrangian reads as,

$$\mathscr{L} \supset [\lambda^L_{22}(\bar{c}_L\gamma_\mu \nu_L + \bar{s}_L\gamma_\mu\mu_L) + \lambda^L_{32}(\bar{t}_L\gamma_\mu \nu_L + \bar{b}_L\gamma_\mu\mu_L)]U^\mu_1. \tag{2.53}$$

The dominant contributions to the Wilson coefficients are,

$$\mathscr{C}^{RK2A}_9 = -\mathscr{C}^{RK2A}_{10} \approx \frac{\pi}{\sqrt{2}G_F V_{tb}V^*_{ts}\alpha}\frac{\lambda^L_{22}\lambda^L_{32}}{M^2_{U_1}}. \tag{2.54}$$

Here, we don't show the CKM-suppressed couplings as we already get the dominant required interactions.

The contribution to the B_s-$\bar{B}_s$ mixing coefficient is

$$\mathscr{C}^{U_1}_{box} = \frac{(\lambda^L_{22})^2(\lambda^L_{32})^2}{8\pi^2 M^2_{U_1}}. \tag{2.55}$$

In this scenario, the dominant decay modes for U_1 are $b\mu^+$, $s\mu^+$, $c\bar{\nu}$, and $t\bar{\nu}$.

■ Scenario RK2B: In this scenario, only λ^L_{22} and λ^R_{32} are nonzero. The interaction Lagrangian is given by

$$\mathscr{L} \supset [\lambda^L_{22}(\bar{c}_L\gamma_\mu\nu_L + \bar{s}_L\gamma_\mu\mu_L) + \lambda^R_{32}\bar{b}_R\gamma_\mu\mu_R]U_1^\mu \tag{2.56}$$

The Wilson coefficients getting the dominant contributions are

$$-\mathscr{C}_P^{RK2B} = \mathscr{C}_S^{RK2B} \approx \frac{-\sqrt{2}\pi}{G_F V_{tb}V^*_{ts}\alpha}\frac{\lambda^L_{22}\lambda^R_{32}}{M^2_{U_1}}. \tag{2.57}$$

For this scenario, B_s-$\bar{B}_s$ mixing is not relevant. The dominant decay modes of U_1 are $b\mu^+$, $s\mu^+$, and $c\bar{\nu}$.

■ Scenario RK2C: In this scenario, only λ^R_{22} and λ^L_{32} are nonzero. Ignoring the CKM-suppressed couplings, we get the following interaction Lagrangian:

$$\mathscr{L} \supset [\lambda^R_{22}\bar{s}_R\gamma_\mu\mu_R + \lambda^L_{32}(\bar{t}_L\gamma_\mu\nu_L + \bar{b}_L\gamma_\mu\mu_L)]U_1^\mu \tag{2.58}$$

The Wilson coefficients getting the dominant contributions are

$$\mathscr{C}'^{RK2C}_P = \mathscr{C}'^{RK2C}_S \approx \frac{-\sqrt{2}\pi}{G_F V_{tb}V^*_{ts}\alpha}\frac{\lambda^R_{22}\lambda^L_{32}}{M^2_{U_1}}. \tag{2.59}$$

In this case also B_s-$\bar{B}_s$ mixing is not relevant. The dominant decay modes of U_1 are $b\mu^+$, $s\mu^+$, and $t\bar{\nu}$.

■ Scenario RK2D: Here, we assume λ^R_{22} and λ^R_{32} to be nonzero. We ignore the CKM-suppressed couplings and the interaction Lagrangian reads as

$$\mathscr{L} \supset (\lambda^R_{22}\bar{s}_R\gamma_\mu\mu_R + \lambda^R_{32}\bar{b}_R\gamma_\mu\mu_R)U_1^\mu. \tag{2.60}$$

The Wilson coefficients are

$$\mathscr{C}'^{RK2D}_9 = \mathscr{C}'^{RK2D}_{10} \approx \frac{\pi}{\sqrt{2}G_F V_{tb}V^*_{ts}\alpha}\frac{\lambda^R_{22}\lambda^R_{32}}{M^2_{U_1}}. \tag{2.61}$$

The contribution to the B_s-$\bar{B}_s$ mixing coefficient is given as

$$\mathscr{C}^{U_1}_{box} = \frac{(\lambda^R_{22})^2(\lambda^R_{32})^2}{8\pi^2 M^2_{U_1}}. \tag{2.62}$$

The dominant decay modes of U_1 are $b\mu^+$ and $s\mu^+$.

$R_{D^{(*)}}$ scenarios	$\lambda^L_{c\nu}$	$\lambda^L_{b\tau}$	$\lambda^R_{b\tau}$	$R_{K^{(*)}}$ scenarios	$\lambda^L_{s\mu}$	$\lambda^L_{b\mu}$	$\lambda^R_{s\mu}$	$\lambda^R_{b\mu}$
RD1A	λ^L_{23}	$V^*_{cb}\lambda^L_{23}$	—	RK1A	$V^*_{cs}\lambda^L_{22}$	$V^*_{cb}\lambda^L_{22}$	—	—
RD1B	$V_{cb}\lambda^L_{33}$	λ^L_{33}	—	RK1B	$V^*_{ts}\lambda^L_{32}$	$V^*_{tb}\lambda^L_{32}$	—	—
				RK1C	—	—	$V_{cs}\lambda^R_{22}$	$V_{cb}\lambda^R_{22}$
				RK1D	—	—	$V_{ts}\lambda^R_{32}$	$V_{tb}\lambda^R_{32}$
RD2A	$V_{cs}\lambda^L_{23}+V_{cb}\lambda^L_{33}$	λ^L_{33}	—	RK2A	λ^L_{22}	λ^L_{32}	—	—
RD2B	$V_{cs}\lambda^L_{23}$	—	λ^R_{33}	RK2B	λ^L_{22}	—	—	λ^R_{32}
				RK2C	—	λ^L_{32}	λ^R_{22}	—
				RK2D	—	—	λ^R_{22}	λ^R_{32}
RD3	$V_{cb}\lambda^L_{33}+V_{cs}\lambda^L_{23}$	λ^L_{33}	λ^R_{33}	RK4	λ^L_{22}	λ^L_{32}	λ^R_{22}	λ^R_{32}

Table 2.3: We show the summary of the single and multi-coupling scenarios that contribute to the $R_{D^{(*)}}$ and $R_{K^{(*)}}$ scenarios.

In a similar fashion, one could construct three or four coupling scenarios relevant to the $R_D^{(*)}$ and $R_K^{(*)}$. But we don't show such multi-coupling scenarios as one cannot conclude anything extra from such scenarios. Our analysis of the single coupling scenarios is generic and hence can act as a template to obtain bounds on the multi-coupling scenarios [63, 91]. In Table 2.3, we summarise the various $R_D^{(*)}$ and $R_K^{(*)}$ anomalies motivated single and multi-coupling scenarios.

From the list of single and multi-coupling $R_{D^{(*)}}$ and $R_{K^{(*)}}$-motivated scenarios, they may not appear very different from each other in an effective theory perspective. However, when we study their LHC phenomenologies, they look different. For instance, let us consider the two single-coupling $R_{D^{(*)}}$-scenarios, Scenario RD1A and Scenario RD1B. In both cases, $\mathscr{C}_{V_L}$ receives a nonzero contribution proportional to the square of the unknown new coupling, λ^L_{23} or λ^L_{33}. Hence, from the effective-theory side, both scenarios look essentially the same. However, the dominant decay modes of U_1 in these two scenarios are different—in the first one, they are $U_1 \to c\,\nu$ and $U_1 \to s\tau$, whereas in the second one, they are $U_1 \to t\,\nu$ and $U_1 \to b\tau$. Thus, in the first scenario, U_1 can produce $\not{E}_T$ + jet or τ + jet in the final state, whereas, in the second scenario, it can produce $t + \not{E}_T$ or $\tau + b$ signatures. Moreover, in the first scenario, a U_1 can be produced via c- or s-quark-initiated processes. However, in the second scenario, it is produced by the b-quark-initiated processes. Since the b-quark parton distribution function (PDF) is smaller than the second-generation ones, the U_1 production cross sections would be higher in Scenario RD1A than those in Scenario RD1B. Hence, one needs to analyse the LHC bounds for the scenarios differently.

2.5 Bounds from the LHC

As explained earlier, it is important to consider the bounds from LHC as those are competitive with the low-energy ones. The bounds from the LHC are of two kinds—direct and indirect. First, we list the latest direct bounds from the LHC:

- Pair-produced scalar LQs decaying to a light quark and a neutrino with $\mathscr{B}$ unity can be excluded up to 980 GeV. A scalar LQ decaying to a b-quark and a neutrino with a 100% branching ratio can be excluded up to 1100 GeV [93].

- A scalar LQ decaying to a b-quark and a neutrino with a 100% branching ratio can be excluded up to 1100 GeV [93]. The ATLAS experiment searched for scalar LQs decaying to the following final states, μc, μ + a light quark, and μb [94].

- Assuming the extra gauge coupling $\kappa = 0$ (we follow the same convention as [78]), a recent LQ pair production search at the CMS detector has excluded vLQs with masses below 1460 GeV for $\mathscr{B}(\mathrm{LQ} \to t\,\nu) = 1$ [93].

- For a vLQ decaying to a light quark and a neutrino with 100% BR, the mass exclusion limit is at 1410 GeV. In the case where it decays to a bottom quark and a neutrino, the limit goes to 1475 GeV.

- If the vLQ decays to a top quark + a neutrino and a bottom quark + τ with equal BRs, then the mass points below 1115 GeV are excluded. For $\kappa = 1$, the limits go up [93].

We also include the scalar searches as we recast scalar searches for better limits on U_1 than ones from vLQs. These direct limits, however, do not provide the entire picture. Thus, we systematically combine these direct bounds with the indirect limits to obtain the most precise limits on the U_1 parameter space. We show that these limits are competitive with the bounds from the flavour data. The indirect bounds are obtained by recasting the latest LHC high p_T dilepton and monolepton data in terms of the model parameters. However, in [91], one finds that the bounds from the dilepton searches are more restricting as compared to the monolepton searches. Hence, here we consider the indirect limits from the dilepton searches. We consider the latest ditau and dimuon search data. There are four modes of production that can give us the desired dilepton final states.

	Integrated Luminosity [fb^{-1}]	Scalar LQ Mass [GeV]	Vector LQ, $\kappa = 0$ Mass [GeV]	Vector LQ, $\kappa = 1$ Mass [GeV]
LQ $\to t\,\nu$ ($\mathcal{B} = 1.0$) [93, 95]	35.9 (36.1)	1020 (992)	1460	1780
LQ $\to q\,\nu$ ($\mathcal{B} = 1.0$) [93]	35.9	980	1410	1790
LQ $\to b\,\nu$ ($\mathcal{B} = 1.0$) [93, 95]	35.9 (36.1)	1100 (968)	1475	1810
LQ $\to b\tau\ /t\,\nu$($\mathcal{B} = 0.5$) [96]	137	950	1290	1650
LQ $\to b\tau$ ($\mathcal{B} = 1.0$) [95] $*$	(36.1)	(1000)	–	–
LQ $\to \mu j$ ($\mathcal{B} = 1.0$) [94] $*$	(139)	(1733)	–	–
LQ $\to \mu c$ ($\mathcal{B} = 1.0$) [94]	(139)	(1680)	–	–
LQ $\to \mu b$ ($\mathcal{B} = 1.0$) [94] $*$	(139)	(1721)	–	–

Table 2.4: Summary of LQ mass exclusion limits from recent direct searches by the CMS (ATLAS) Collaboration.

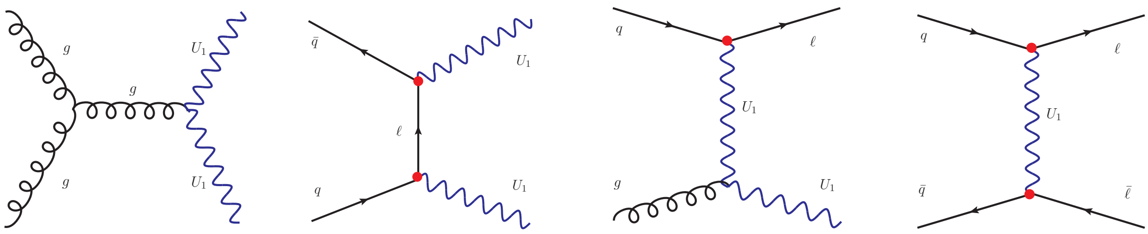

(a) (b) (c) (d)

Figure 2.4: We show diagrams for the various production modes of the U_1. (a) Gluon initiated pair production process. (b) quark initiated pair production process. (c) quark and gluon initiated single production process. (d) Nonresonant production of U_1. The $q\ell U_1$ coupling denoted by λ is marked in red colour.

2.6 Production modes and decays

We investigate the possible LHC signatures of the scenarios we constructed in the previous section. We discuss various modes of LQ production and decay to the desired final states. The U_1 can be produced resonantly (i.e., near on-shell) in pairs (see Fig. 2.4a and 2.4a) or singly along with a lepton (see Fig. 2.4c). They can also be produced non-resonantly through a t-channel U_1 exchange as shown in Fig. 2.4d.

Pair production

In this production mode, a pair of resonant LQs are produced which subsequently decay to quarks and leptons, thus leading to dijet and dilepton in the final state. Consider Scenario RD1A, where only λ^L_{23} is nonzero. Thus, the main decay modes of U_1 are $s\tau$ and $c\nu$ with roughly equal (about 50%) BRs. We have ignored the CKM-suppressed effective couplings in the discussions on the LHC phenomenology of U_1 as they do not play any important role. Thus, here the pair production of U_1 leads to the following final states:

$$pp \to \left\{ \begin{array}{lcccl} U_1U_1 & \to & s\tau\, s\tau & \equiv & \tau\tau + 2j \\ U_1U_1 & \to & s\tau\, c\nu & \equiv & \tau + \not{E}_T + 2j \\ U_1U_1 & \to & c\nu\, c\nu & \equiv & \not{E}_T + 2j \end{array} \right\} \tag{2.63}$$

where j denotes a light jet or a b-jet. Here, the second channel has a cross section almost two times that of the other two channels due to combinatorics. However, this channel is not fully reconstructible due to the presence of the missing energy. As a result, both the first and second channels have comparable sensitivities. The sensitivity of the third channel ($\not{E}_T + 2j$) is poor as there are two neutrinos in the final state. So far, these channels with cross-generation couplings have not been used in any LQ search at the LHC.

Next, we consider the Scenario RD1B. Here, only λ^L_{33} is nonzero. Here, $U_1 \to t\nu$ and $U_1 \to b\tau$ are the main decay modes of U_1 with roughly equal (about 50%) BRs. Thus, the pair production of U_1 mostly leads to the following final states:

$$pp \to \left\{ \begin{array}{lcccl} U_1U_1 & \to & b\tau\, b\tau & \equiv & \tau\tau + 2j \\ U_1U_1 & \to & b\tau\, t\nu & \equiv & \tau + \not{E}_T + j_t + j \\ U_1U_1 & \to & t\nu\, t\nu & \equiv & \not{E}_T + 2j_t \end{array} \right\}. \tag{2.64}$$

Here, j_t corresponds to a fatjet originating from a hadronically decaying top quark. One can also consider the leptonically decaying top quark with a lower cross section. In Chapter 5, we show that by using sophisticated jet-substructure techniques, we can tag the boosted top-jets. This could improve the collider prospects of U_1 in the second and third channels. The symmetric $\not{E}_T + 2j_t$ channel (where both LQs decay to the same final states) has been considered in Refs. [58, 97]. The asymmetric channel (where the two LQs decay to different final states), the one with single τ, one top-jet, and missing energy ($\tau + \not{E}_T + j_t + b$), has started receiving attention [96]. This channel has a bigger cross section due to combinatorics. Hence, its unique final state might act as a smoking-gun signature for such scenarios (i.e., ones with non-negligible λ^L_{33}).

If only λ^R_{33} is nonzero, then U_1 entirely decays through the $U_1 \to b\tau$ mode and contributes to the $b\tau\, b\tau \equiv \tau\tau + 2j$ final state [93]. In this single coupling scenario, the U_1 cannot resolve the $R_{D^{(*)}}$ anomalies as the necessary couplings are not generated.

In multi-coupling scenarios such as Scenario RD2A, Scenario RD2B and Scenario RD3, there are many possible decay modes to investigate. Such investigation has been done in the context of sLQs [63]. For example, If one considers the two-coupling scenario Scenario RD2A (non-zero λ^L_{23} and λ^L_{33}), then one can obtain all the decay modes mentioned in Eqs. (2.63) and (2.64). In addition to this, we can also obtain the asymmetric decay channels such as,

$$pp \to \left\{ \begin{array}{lclcl} U_1U_1 & \to & s\tau\, b\tau & \equiv & \tau\tau + 2j \\ U_1U_1 & \to & s\tau\, t\nu & \equiv & \tau + \not{E}_T + j_t + j \\ U_1U_1 & \to & c\nu\, t\nu & \equiv & \not{E}_T + 2j_t \end{array} \right\}. \tag{2.65}$$

The strength of any particular channel depends on the couplings involved in production as well as the BRs involved.
In the case of $R_{K^{(*)}}$ scenarios, we have muons or neutrinos in the final states. Consider the single coupling scenario Scenario RK1A, where λ^L_{22} is the only nonzero coupling. Here, the pair production processes are given as,

$$pp \to \left\{ \begin{array}{lclcl} U_1U_1 & \to & s\mu\, s\mu & \equiv & \mu\mu + 2j \\ U_1U_1 & \to & s\mu\, c\nu & \equiv & \mu + \not{E}_T + 2j \\ U_1U_1 & \to & c\nu\, c\nu & \equiv & \not{E}_T + 2j \end{array} \right\} \tag{2.66}$$

We can use similar processes for Scenario RK1B. In the single coupling scenarios, Scenario RK1C (only λ^R_{22} nonzero) and Scenario RK1D (only λ^R_{32} nonzero), the BR of the $U_1 \to s\mu$ and $U_1 \to b\mu$ is 100%. Similarly, the two coupling $R_{K^{(*)}}$ scenarios have numerous interesting channels to explore, and the LHC is yet to perform searches for LQs in most of the asymmetric channels and some of the symmetric channels.

In Table 2.5, we have summarised the possible final states from U_1 pair production and the fraction of U_1 pairs producing the final states in the one- and two-coupling scenarios. The fractions depend on combinatorics and the relevant U_1 BRs. (Here, we have ignored the possible minor correction due to the mass differences between different final states, i.e., assumed all final state particles are much lighter than U_1). For example, in Scenario RD1A, since $\beta(U_1 \to s\tau) \approx \beta(U_1 \to c\nu) \approx 50\%$, only 25% of the produced U_1 pairs would decay to either $\tau\tau + 2j$ or $\not{E}_T + 2j$, whereas, as explained above, 50% of them would decay to the $\tau + \not{E}_T + 2j$ final state. Interestingly, we see that even in some two-coupling scenarios the fractions corresponding to the $\tau\tau/\mu\mu + 2j$ final states are constant irrespective of the relative magnitudes of the couplings, for example, it is 25%

Nonzero couplings	Signatures					
	$\tau\tau+2j$	$\tau+\not{E}_T+2j$	$\not{E}_T+2j$	$\tau+\not{E}_T+j_t+j$	$\not{E}_T+2j_t$	$\not{E}_T+j_t+j$
λ^L_{23} (Scenario RD1A)	0.25	0.50	0.25	–	–	–
λ^L_{33} (Scenario RD1B)	0.25	–	–	0.50	0.25	–
λ^R_{33}	1.00	–	–	–	–	–
$\lambda^L_{23},\lambda^L_{33}$ (Scenario RD2A)	0.25	ξ	ξ^2	$\frac{1}{2}-\xi$	$\left(\frac{1}{2}-\xi\right)^2$	$2\xi\left(\frac{1}{2}-\xi\right)$
$\lambda^L_{23},\lambda^R_{33}$ (Scenario RD2B)	$\left(\frac{1}{2}+\xi\right)^2$	$2\left(\frac{1}{4}-\xi^2\right)$	$\left(\frac{1}{2}-\xi\right)^2$	–	–	–
	$\mu\mu+2j$	$\mu+\not{E}_T+2j$	$\not{E}_T+2j$	$\mu+\not{E}_T+j_t+j$	$\not{E}_T+2j_t$	$\not{E}_T+j_t+j$
λ^L_{22} (Scenario RK1A)	0.25	0.50	0.25	–	–	–
λ^L_{32} (Scenario RK1B)	0.25	–	–	0.50	0.25	–
λ^R_{22} (Scenario RK1C)	1.00	–	–	–	–	–
λ^R_{32} (Scenario RK1D)	1.00	–	–	–	–	–
$\lambda^L_{22},\lambda^L_{32}$ (Scenario RK2A)	0.25	ξ	ξ^2	$\frac{1}{2}-\xi$	$\left(\frac{1}{2}-\xi\right)^2$	$2\xi\left(\frac{1}{2}-\xi\right)$
$\lambda^L_{22},\lambda^R_{32}$ (Scenario RK2B)	$\left(\frac{1}{2}+\xi\right)^2$	$2\left(\frac{1}{4}-\xi^2\right)$	$\left(\frac{1}{2}-\xi\right)^2$	–	–	–
$\lambda^R_{22},\lambda^L_{32}$ (Scenario RK2C)	$\left(\frac{1}{2}+\xi\right)^2$	–	–	$2\left(\frac{1}{4}-\xi^2\right)$	$\left(\frac{1}{2}-\xi\right)^2$	–
$\lambda^R_{22},\lambda^R_{32}$ (Scenario RK2D)	1.00	–	–	–	–	–

Table 2.5: Here, we show the effect of branching ratios on the pair production process of $U_1(pp \to U_1U_1)$ in various single and multi-coupling scenarios. We list the possible final states and the fraction of U_1 that decays to them, depending on the different coupling scenarios. The pair production contribution is calculated as the cross section of U_1 pair production multiplied by the appropriate branching fraction. Here, $0 \leq \xi \leq \frac{1}{2}$ is a free parameter. We ignored the mass differences between the final state particles.

in Scenario RD2A or 100% in Scenario RK2D. (This is interesting because, in the presence of two nonzero couplings, one normally expects the fraction corresponding to a particular final state to depend on their relative strengths. It happens because we sum over the possible flavours of the jets.) Moreover, we show that it is possible to parametrise all final states with just one free parameter (ξ). Such simple parametrisations could guide us in future U_1 searches at the LHC.

Single production

The second resonant mode of U_1 is the single production process. Here the U_1 is produced along with SM particle(s). There are two types of single productions of our interest: (a) where a U_1 is produced in association with a lepton, i.e., $U_1\mu$, $U_1\tau$ or $U_1\nu$ and (b) where a U_1 is produced with a lepton and a jet, i.e., $U_1\mu j$, $U_1\tau j$ or $U_1\nu j$. In process (b), the quark and the lepton can arise from the decay of an on-shell LQ; such a process should then be counted as pair production. To avoid double counting, we ensure that one of the LQs is off-shell while generating the single production events [98–100]. The single production process is model-dependent. Its contribution depends on κ [78] and λ. The single production channels for the single coupling scenario Scenario RD1A is given as,

$$pp \to \left\{ \begin{array}{lcccc} U_1\tau + U_1\tau j & \to & (s\tau)\tau + (s\tau)\tau j & \equiv & \tau\tau + n\,j \\ U_1\nu + U_1\nu j & \to & (c\nu)\nu + (c\nu)\nu j & \equiv & \not{E}_T + n\,j \\ U_1\tau + U_1\tau j & \to & (c\nu)\tau + (c\nu)\tau j & \equiv & \tau + \not{E}_T + n\,j \\ U_1\nu + U_1\nu j & \to & (s\tau)\nu + (s\tau)\nu j & \equiv & \tau + \not{E}_T + n\,j \end{array} \right\}. \tag{2.67}$$

The single production modes have the same final states as the pair production searches. The first and the second channels are symmetric, whereas the third and the fourth are asymmetric modes [63]. These modes have not been considered by the LHC in the search for LQs. For the $R_{K^{(*)}}$ motivated scenarios, the single production channels Scenario RK1A are as follows,

$$pp \to \left\{ \begin{array}{lcccc} U_1\mu + U_1\mu j & \to & (b\mu)\mu + (b\mu)\mu j & \equiv & \mu\mu + n\,j \\ U_1\mu + U_1\mu j & \to & (t\nu)\mu + (t\nu)\mu j & \equiv & \mu + \not{E}_T + j_t + n\,j \\ U_1\nu + U_1\nu j & \to & (b\mu)\nu + (b\mu)\nu j & \equiv & \mu + \not{E}_T + n\,j \\ U_1\nu + U_1\nu j & \to & (t\nu)\nu + (t\nu)\nu j & \equiv & \not{E}_T + j_t + n\,j \end{array} \right\}. \tag{2.68}$$

In case of Scenario RK1B, we could have interesting signatures such as boosted top quarks in the final states. In Scenario RK1C (Scenario RK1D), the $U_1 \to s(b)\mu$ decay has 100% BR.

2.6.1 Nonresonant production and interference

A U_1 can be exchanged in the t-channel and give rise to both dilepton and lepton+missing-energy final states [see e.g., Fig. 2.4d]. It is evident from Fig. 2.4d that the cross sections of the nonresonant production scales as λ^4. This channel becomes important for large values of the new couplings. At higher masses of U_1, this nonresonant mode of production overtakes the contributions from pair and single production processes. In addition to this, there is also a possibility of large interference of this nonresonant mode with the SM processes such as $pp \to \gamma/Z(W) \to \ell\ell\ (\ell + \not{E}_T)$. This interference contribution scales as λ^2, but the contribution can be significant due to the large SM backgrounds. For U_1, the interference is destructive in nature. The net nonresonant contribution from the λ^4 part and the destructive λ^2 part can be positive or negative. Thus, the cross section of the exclusive $pp \to \ell\ell\ (\ell + \not{E}_T)$ process can be bigger or smaller than the SM-only contribution [57] depending on the kinematic region we consider.

In Fig. 5.2, we show the parton-level cross sections of various production modes of U_1 as a function of M_{U_1}. In Figs. 2.5a and 2.5b the cross sections have been obtained by setting κ=0 and the relevant

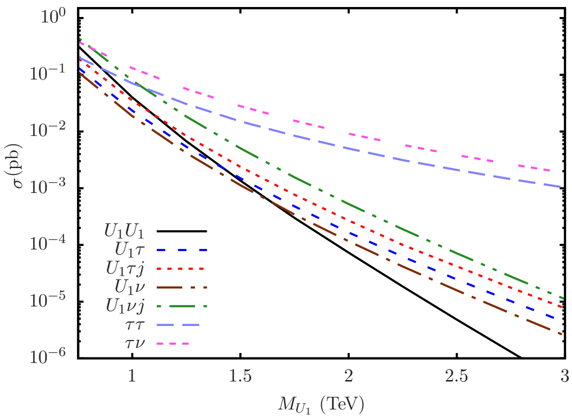

(a)

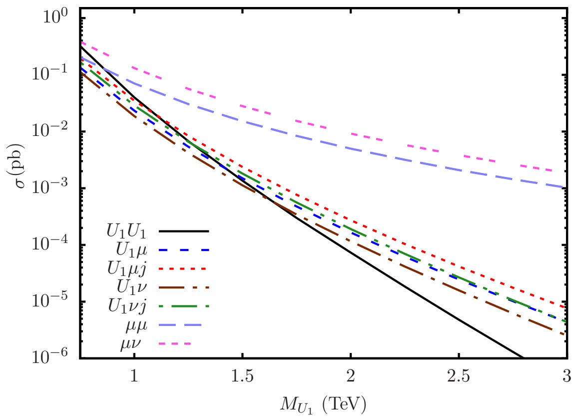

(b)

Figure 2.5: Here, we show the Parton-level cross sections of the various U_1 production modes as a function of their mass. We compute the cross section at the 13 TeV LHC. In (a), we consider the benchmark scenario with $\lambda^L_{23} = 1$ as the nonzero coupling, and in (b), we consider $\lambda^L_{22} = 1$. We set $\kappa = 0$ in both cases. We denote the light and the b jets as j. We apply a basic generational level cut of $p_T > 20$ GeV on the jets and leptons.

new coupling, λ^L_{23} or λ^L_{22}, to one, respectively. The pair production cross section is insensitive to the λ couplings; the major contribution comes from the QCD-mediated mode. The single production mode contributes more than the pair production mode for higher mass values. While generating processes like $U_1\tau$j, $U_1\mu$j, $U_1\nu$j, we make sure the one LQ remains off-shell so as to avoid contamination from the pair production process. The nonresonant LQ production cross section does not depend very strongly on the LQ mass. With nonzero λ^L_{23} and λ^L_{22}, we now have the possibility of producing U_1 (that couples to the third-generation fermions) through charm- and/or strange-initiated processes at the LHC.

2.7 Recast of dilepton data

The LHC dilepton searches, generally, do no put restrictions on the number of jets present in the final states, and hence, all the production modes of U_1 that lead to $\ell\ell$+jets in the final state can contribute to the exclusion bounds. It is non-trivial to obtain precise LHC bounds from the dilepton data, especially when multiple new couplings are involved. This is because different couplings lead to different topologies with the same final states. We provide an elaborate explanation of our approach for obtaining the bounds. We discuss the method in the context of the U_1 scenarios, but the method is generic and can be applied to other general cases (including other BSM ones) as well.

First, we take a quick look at the LHC dilepton searches we consider.

2.7.1 ATLAS $\tau\tau$ search

We consider the LHC search by the ATLAS Collaboration where they searched for a heavy particle decaying to a pair of τ's at the 13 TeV LHC with 139 fb^{-1} integrated luminosity [101]. In this search, they analysed events coming from two kinds of τ decays. Firstly, when both the τs decay hadronically ($\tau_{had}\tau_{had}$). Second, when one τ decays hadronically and the other decays leptonically ($\tau_{had}\tau_{lep}$). Below we list the basic event selection criteria for the $\tau\tau$ channel.

- The $\tau_{had}\tau_{had}$ channel has
  - at least two hadronically decaying τ's with no additional electrons or muons,
  - two τ_{had}'s with $p_{\mathrm{T}} > 65$ GeV. They should be oppositely charged and separated in the azimuthal plane by $|\Delta\phi(p_{\mathrm{T}}^{\tau_1}, p_{\mathrm{T}}^{\tau_2})| > 2.7$ rad.
  - p_{T} of leading τ must be > 85 GeV.
- The $\tau_{lep}\tau_{had}$ channel has one τ_{had} and only one $\ell = e$ or μ such that
  - the hadronic τ has $p_{\mathrm{T}} > 25$ GeV and $|\eta(\tau_{had})| < 2.5$(excluding $1.37 < |\eta| < 1.52$),
  - if $\ell = e$, then $|\eta| < 2.47$ (excluding $1.37 < |\eta| < 1.52$) and if $\ell = \mu$ then $|\eta| < 2.5$,
  - the lepton has $p_{\mathrm{T}}(\ell) > 30$ GeV with azimuthal separation from the τ_{had}, $|\Delta\phi(p_{\mathrm{T}}^{\ell}, p_{\mathrm{T}}^{\tau_{had}})|$ > 2.4.
  - the transverse mass on the selected lepton and missing transverse momentum, $m_{\mathrm{T}}(p_{\mathrm{T}}^{\ell}, \not{E}_{\mathrm{T}}) > 40$ GeV.
  - If $\ell = e$, to reduce the background from $Z \to ee$ events with an invariant mass for $\tau - \ell$ pair between 80 GeV and 110 GeV are rejected.

The transverse mass is defined as

$$m_{\mathrm{T}}(p_{\mathrm{T}}^{A}, p_{\mathrm{T}}^{B}) = \sqrt{2p_{\mathrm{T}}^{A}p_{\mathrm{T}}^{B}\left\{1 - \cos\Delta\phi(p_{\mathrm{T}}^{A}, p_{\mathrm{T}}^{B})\right\}}. \tag{2.69}$$

The analysis also made use of the total transverse mass defined as

$$m_{\mathrm{T}}^{tot}(\tau_1, \tau_2, \not{E}_{\mathrm{T}}) = \sqrt{m_T^2(p_{\mathrm{T}}^{\tau_1}, p_{\mathrm{T}}^{\tau_2}) + m_T^2(p_{\mathrm{T}}^{\tau_1}, \not{E}_{\mathrm{T}}) + m_T^2(p_{\mathrm{T}}^{\tau_2}, \not{E}_{\mathrm{T}})}, \tag{2.70}$$

Here, τ_2 in the $\tau_{lep}\tau_{had}$ channel represents the lepton. We use the distribution of the observed and the SM events with respect to m_{T}^{tot} presented in the analysis.

2.7.2 CMS $\mu\mu$ search

A search for nonresonant excesses in the dimuon channel was performed by the CMS experiment at a center-of-mass energy of 13 TeV corresponding to an integrated luminosity of 140 fb^{-1} [102]. The event selection criteria that we use in our analysis can be summarised as

- In the dimuon channel, the requirement is that both of the muons must have $|\eta| < 2.4$ and $p_{\mathrm{T}} > 53$ GeV. The invariant mass of the muon pair is $m_{\mu\mu} > 150$ GeV.

We implement the above cuts in our analysis to obtain the cut efficiencies. (Following Ref. [91], we have validated the above cuts with the efficiencies given in the experimental papers.) We use observed and the background distributions of the invariant mass of the muon pair, $m_{\mu\mu}$, to obtain the limits.

2.7.3 Cross section parametrisation for the $\ell\ell$ signal processes

■ **Pair production:** Although the dominant contribution to the pair production mode comes from the QCD-mediated process (See Fig. 2.4a), it is not entirely model-independent. It depends on the gluon-U_1-U_1 coupling κ given in the Eq. (2.14). There is also a contribution from the t-channel lepton exchange diagrams (Fig. 2.4b). These diagrams depend on the new coupling λ responsible for the $\ell q U_1$ interactions. If there are n different new couplings (λ_i with $i = \{1, 2, 3, \ldots n\}$) involved, then the total cross section for the process $pp \to U_1 U_1$ can be expressed as,

$$\sigma^{p}\left(M_{U_1}, \lambda\right) = \sigma^{p_0}\left(M_{U_1}\right) + \sum_{i}^{n} \lambda_i^2 \sigma_i^{p_2}\left(M_{U_1}\right) + \sum_{i \geq j}^{n} \lambda_i^2 \lambda_j^2 \sigma_{ij}^{p_4}\left(M_{U_1}\right) \tag{2.71}$$

where the sums go up to n. The σ^{p_x} terms depend only on the mass of U_1. The $\sigma^{p_0}(M_{U_1})$ term denotes the cross section of the QCD-mediated process. It doesn't depend on λ and can be obtained by setting $\lambda_i \to 0$. The $\sigma_i^{p_2}(M_{U_1})$ term originates from the interference between the QCD-mediated model-independent diagrams and the model dependent t-channel lepton exchange diagrams. The $\sigma_{ij}^{p_4}(M_{U_1})$ terms are from the pure t-channel lepton exchange diagrams.

We observe that for a particular M_{U_1}, there are n unknown $\sigma_i^{p_2}$ and $n(n+1)/2$ unknown $\sigma_{ij}^{p_4}$ functions that one needs to compute. For that, we compute σ^p for $n(n+3)/2$ different values of λ_i and solve the resulting linear equations. We repeat the same procedure for different mass points. We interpolate $\sigma^p(M_{U_1},\lambda)$ for any intermediate value of M_{U_1}.

In the presence of kinematic selection cuts, different $\sigma^{p_x}(M_{U_1})$ parts contribute differently to the surviving events. Hence, the overall cut efficiency for the pair production process ϵ^p depends on both M_{U_1} and λ. The total number of surviving events from the pair production process passing through some selection cuts can, therefore, be expressed as

$$\begin{aligned}\mathcal{N}^p &= \sigma^p \circ \epsilon^p\ (M_{U_1},\lambda) \times \mathcal{B}^2(M_{U_1},\lambda) \times L \\ &= \left\{ \sigma^{p_0} \times \epsilon^{p_0} + \sum_i^n \lambda_i^2 \sigma_i^{p_2} \times \epsilon_i^{p_2} + \sum_{i\geq j}^n \lambda_i^2\lambda_j^2 \sigma_{ij}^{p_4} \times \epsilon_{ij}^{p_4} \right\} \times \mathcal{B}^2(M_{U_1},\lambda) \times L \end{aligned} \tag{2.72}$$

where all ϵ^{p_x} depend only on M_{U_1}. Here L is the integrated luminosity, and $\mathcal{B}(M_{U_1},\lambda)$ is the relevant branching ratio (of the decay mode of U_1 that contributes to the signal) which can be obtained analytically. The $\epsilon^{p_x}(M)$ functions can be obtained by computing the fraction of events surviving the selection cuts while computing the $\sigma^{p_x}(M_{U_1})$ functions.

■ **Single production:** The contribution of the single production of U_1 comes from two processes—$pp \to U_1 q$ and $pp \to U_1 q \ell$. The amplitudes of $U_1 x$ type of processes are always proportional to λ. But $U_1 yz$ amplitudes can have both linear and cubic terms in λ. Therefore, the most generic form of the single production process $pp \to U_1 x + U_1 yz$ can be expressed as

$$\sigma^s(M,\lambda_i) = \sum_i^n \lambda_i^2 \sigma_i^{s_2}(M_{U_1}) + \sum_{i\geq j\geq k}^n \lambda_i^2\lambda_j^2\lambda_k^2 \sigma_{ijk}^{s_6}(M_{U_1}). \tag{2.73}$$

The $\sigma^{s_x}(M)$ functions can be obtained following the same method used for pair production. We can express the total number of single production events as

$$\begin{aligned}\mathcal{N}^s &= \sigma^s \circ \epsilon^s\ (M_{U_1},\lambda) \times \mathcal{B}(M_{U_1},\lambda) \times L \\ &= \left\{ \sum_i \lambda_i^2 \sigma_i^{s_2}(M_{U_1}) \times \epsilon_i^{s_2}(M_{U_1}) + \sum_{i\geq j\geq k} \lambda_i^2\lambda_j^2\lambda_k^2 \sigma_{ijk}^{s_6}(M_{U_1}) \times \epsilon_{ijk}^{s_6}(M_{U_1}) \right\} \\ &\quad \times \mathcal{B}(M_{U_1},\lambda_i) \times L. \end{aligned} \tag{2.74}$$

■ **Nonresonant production:** The nonresonant production contribution comes from the t-channel U_1 exchange and its interference with the SM background process. The cross section contribution from the t-channel U_1 exchange is proportional to λ^4 and the interference is proportional to λ^2.

Thus, the total cross section is given as,

$$\sigma^{nr}(M_{U_1},\lambda) = \sum_{i}^{n} \lambda_i^2 \sigma_i^{nr_2}(M_{U_1}) + \sum_{i\geq j}^{n} \lambda_i^2 \lambda_j^2 \sigma_{ij}^{nr_4}(M_{U_1}). \tag{2.75}$$

Note that $\sigma^{nr}(M_{U_1},\lambda)$ can be negative when the signal-background interference is destructive. Indeed, this is the case we observe for U_1. By introducing the $\epsilon(M_{U_1})$ functions, the total number of surviving events can be written as

$$\begin{aligned}
\mathcal{N}^{nr} &= \sigma^{nr} \circ \epsilon^{nr}\ (M_{U_1},\lambda) \times L \\
&= \left\{ \sum_{i}^{n} \lambda_i^2 \sigma_i^{nr_2}(M_{U_1}) \times \epsilon_i^{nr_2}(M_{U_1}) + \sum_{i\geq j}^{n} \lambda_i^2 \lambda_j^2 \sigma_{ij}^{nr_4}(M_{U_1}) \times \epsilon_{ij}^{nr_4}(M_{U_1}) \right\} \times L.
\end{aligned} \tag{2.76}$$

Notice, no BR appears in the above equation. A negative $\sigma^{nr}(M_{U_1},\lambda)$ makes $\mathcal{N}^{nr}$ a negative number as presented in Table 2.6.

2.7.4 Limits estimation: A χ^2 test

We perform χ^2 tests to estimate the limits on parameters from the transverse mass distribution of the $\tau\tau$ [101] and the invariant mass distribution of the $\mu\mu$ [102] data. The method is essentially an extension of the one used in Ref. [91] for S_1 LQ. The steps are as follows.

1. For each distribution, the statistic can be defined as

$$\chi^2 = \sum_i \left(\frac{\mathcal{N}_{\rm T}^i(M_{U_1},\lambda) - \mathcal{N}_{\rm D}^i}{\Delta \mathcal{N}^i} \right)^2 \tag{2.77}$$

   where the sum runs over the corresponding bins. Here, $\mathcal{N}_{\rm T}^i(M_{U_1},\lambda)$ stands for expected (theory) events, and $\mathcal{N}_{\rm D}^i$ is the number of observed events in the i^{th} bin. The number of theory events in the i^{th} bin can be expressed

$$\begin{aligned}
\mathcal{N}_{\rm T}^i(M_{U_1},\lambda) &= \mathcal{N}_{U_1}^i(M_{U_1},\lambda) + \mathcal{N}_{\rm SM}^i \\
&= \left[\mathcal{N}^p(M_{U_1},\lambda) + \mathcal{N}^s(M_{U_1},\lambda) + \mathcal{N}^{nr}(M_{U_1},\lambda) \right] + \mathcal{N}_{\rm SM}^i.
\end{aligned} \tag{2.78}$$

   Here, $\mathcal{N}_{U_1}^i$ and $\mathcal{N}_{\rm SM}^i$ are the total signal events from U_1 and the SM background in the i^{th} bin, respectively. The total signal events are composed of $\mathcal{N}^p$, $\mathcal{N}^s$, and $\mathcal{N}^{nr}$ from Eqs. (2.72), (2.74), and (2.76), respectively. The details on how to calculate $\mathcal{N}_{U_1}^i$ for different scenarios is sketched in Appendix 2.7.3. For the error $\Delta\mathcal{N}^i$, we use

$$\Delta \mathcal{N}^i = \sqrt{\left(\Delta \mathcal{N}_{stat}^i\right)^2 + \left(\Delta \mathcal{N}_{syst}^i\right)^2} \tag{2.79}$$

where $\Delta\mathcal{N}^i_{stat} = \sqrt{\mathcal{N}^i_D}$ and we assume a uniform 10% systematic error, i.e., $\Delta\mathcal{N}^i_{syst} = \delta^i \times \mathcal{N}^i_D$ with $\delta^i = 0.1$.

2. In every scenario, for some discrete benchmark values of $M_{U_1} = M^b_{U_1}$ we compute the minimum of χ^2 as $\chi^2_{min}(M^b_{U_1})$ by varying the couplings λ.

3. In one-coupling scenarios (like Scenario RD1A, Scenario RK1A, etc.), we obtain the 1σ and 2σ confidence level upper limits on the coupling at $M_{U_1} = M^b_{U_1}$ from the values of λ for which $\Delta\chi^2(M^b_{U_1}, \lambda) = \chi^2(M^b_{U_1}, \lambda) - \chi^2_{min}(M^b_{U_1}) = 1$ and 4, respectively.

   In two-coupling scenarios (like Scenario RD2A, Scenario RK2A, etc.), we do the same, except we obtain the 1σ and 2σ limits (contours) from the 2-parameter limits on $\Delta\chi^2$; i.e., we solve $\Delta\chi^2(M^b_{U_1}, \lambda_1, \lambda_2) = \chi^2(M^b_{U_1}, \lambda_1, \lambda_2) - \chi^2_{min}(M^b_{U_1}) = 2.30$ and 6.17, respectively.

   Similarly, we can obtain the limits for the scenarios with $n(\geq 2)$ free couplings by using the n-parameter ranges for $\Delta\chi^2$.

4. We obtain the limits for arbitrary values of M_{U_1} by interpolating the limits for the benchmark masses.

In Table 2.6, we show the production cross sections, cut efficiencies, and number of events surviving the cuts from different signal processes for the $R_{D^{(*)}}$-motivated and $R_{K^{(*)}}$-motivated one-coupling scenarios, respectively. We obtain these numbers by setting the concerned coupling to one. There are a few points to note here. The major contribution to pair production is insensitive to the new physics coupling; however, As expected, there is a minor contribution that comes from the λ-dependent t-channel lepton exchange diagram [see Fig. 2.4b]. In Scenario RD1A where only λ^L_{23} is nonzero, the pair production cross section is 40.87 fb for $M_{U_1} = 1$ TeV, whereas in Scenario RD1B, it is 35.67 fb. This is because the t-channel lepton exchange contribution is larger in Scenario RD1A. In the Scenario RD1A, the contribution comes from the s quark, and its PDF is more than the b PDF contributing in Scenario RD1B. Also, in the case of Scenario RD1A, there is a t-channel neutrino exchange diagram for the $cc \to U_1U_1$ process. Whereas, such a process is not possible in the Scenario RD1B. We observe a similar trend in the single production mode; the cross section is larger for scenarios where second generation quarks appear in the initial states. The cut efficiencies for different production modes for $R_{K^{(*)}}$ scenarios are generally much higher compared to $R_{D^{(*)}}$ scenarios. This is mainly because the selection efficiency of the τ in the final state is much lower compared to the μ. For example, in the $R_{K^{(*)}}$ scenarios, the efficiency for pair production processes ε^p can be as high as 71% for $M_{U_1} = 1$ TeV, whereas for $R_{D^{(*)}}$ scenarios, it is only $\sim 2\%$. The hadronic BR of τ is $\sim 64\%$, and the τ-tagging efficiency is about 60%. Combining just these two factors, we get a factor of $0.64^2 \times 0.6^2 \sim 1/7$ reduction in the efficiency for the two

Mass	Pair production			Single production			t-channel LQ			Interference		
(Tev)	σ^p	ϵ^p	$\mathcal{N}^p$	σ^s	ϵ^s	$\mathcal{N}^s$	σ^{nr4}	ϵ^{nr4}	$\mathcal{N}^{nr4}$	σ^{nr2}	ϵ^{nr2}	$\mathcal{N}^{nr2}$
Contribution to $\tau\tau$ signal [101]												
$\lambda^L_{23} = 1$ (Scenario RD1A)												
1.0	40.87	2.33	8.59	58.80	3.30	35.07	70.57	7.22	183.33	-232.63	3.17	-266.21
1.5	1.39	1.50	0.19	3.91	2.74	1.93	14.94	7.00	37.77	-104.31	3.34	-125.62
2.0	0.08	1.01	0.01	0.44	2.50	0.20	5.04	7.25	13.19	-58.79	3.28	-69.57
$\lambda^L_{33} = 1$ (Scenario RD1B)												
1.0	35.67	1.69	5.43	29.00	2.57	13.46	20.20	6.21	45.26	-75.02	3.08	-83.41
1.5	1.17	1.09	0.11	1.72	2.16	0.67	4.31	6.22	9.68	-33.62	2.88	-33.01
2.0	0.06	0.81	0.00	0.17	1.98	0.06	1.39	6.27	3.15	-18.97	2.88	-19.71
$\lambda^R_{33} = 1$												
1.0	35.67	1.74	22.45	29.18	2.43	25.62	20.17	6.45	46.97	-27.4	3.32	-32.83
1.5	1.17	1.10	0.46	1.69	1.88	1.15	4.31	6.47	10.06	-12.31	3.27	-14.54
2.0	0.06	0.84	0.02	0.17	1.57	0.10	1.39	6.33	3.18	-6.94	3.26	-8.17
Contribution to $\mu\mu$ signal [102]												
$\lambda^L_{22} = 1$ (Scenario RK1A)												
1.0	40.89	71.88	265.27	58.68	72.66	769.52	70.40	62.77	1595.21	-233.00	42.73	-3594.15
1.5	1.39	64.44	8.10	3.91	71.35	50.30	15.20	64.33	352.97	-105.00	42.59	-1614.37
2.0	0.08	52.62	0.36	0.44	70.15	5.60	5.00	64.22	115.92	-58.80	43.08	-914.54
$\lambda^R_{22} = 1$ (Scenario RK1B)												
1.0	38.91	71.74	1007.69	58.29	72.36	1522.36	70.43	62.69	1593.99	-82.52	49.17	-1464.79
1.5	1.32	64.18	30.64	3.81	68.62	94.40	15.21	64.20	352.5 7	-37.33	49.09	-661.52
2.0	0.07	52.50	1.36	0.42	63.79	9.78	5.00	64.53	116.48	-21.0	48.62	-368.53
$\lambda^L_{32} = 1$ (Scenario RK1C)												
1.0	35.67	71.59	230.45	28.93	72.74	379.76	20.00	63.49	458.17	-75.30	39.10	-1062.87
1.5	1.17	64.46	6.78	1.72	72.33	22.44	4.29	64.58	100.49	-33.70	39.82	-484.39
2.0	0.06	52.47	0.29	0.17	71.77	2.22	1.41	64.90	33.04	-19.00	40.12	-275.17
$\lambda^R_{32} = 1$ (Scenario RK1D)												
1.0	35.67	71.75	923.90	29.04	72.37	758.73	20.05	63.73	461.36	-26.29	45.77	-434.43
1.5	1.17	64.60	27.19	1.69	69.28	42.27	4.29	64.43	99.74	-11.84	46.32	-197.94
2.0	0.06	52.00	1.14	0.17	65.35	3.95	1.41	65.37	33.25	-6.69	46.64	-112.60

Table 2.6: In this table. we show the cross section (σ) in fb, efficiency (ϵ) in %, and the number of events ($\mathcal{N}$) surviving the cuts applied in the dilepton searches from various production processes. The number of events ($\mathcal{N}$) is calculated as ($\mathcal{N}$) = $\sigma \times \epsilon \times \mathcal{L}$. Where $\mathcal{L}$ is the luminosity. We explain the superscripts in detail in section 2.7.3. The negative signs in the interference contributions indicate destructive interference.

τ_{had}'s in the pair production final state. We can see from the table the pair, single productions, and the t-channel induced processes contribute positively. The signal-background interference has a negative sign indicating the destructive nature of the interference.

2.8 Computational tools for performing simulation and analysis

We use the software package `FeynRules` [103] for implementing the Lagrangian in section 2.12 in order to obtain the UFO model files. [104]. We generate signal events using the `MadGraph5` Monte-Carlo event generator [105] at the leading order (LO). The NNPDF2.3LO PDFs [106] are used with default dynamical scales.[2] We perform showering and hadronization using `Pythia6` [107] and matched up to two additional jets using the `MLM` matching scheme [108, 109] with virtuality-ordered PYTHIA showers to remove the double counting of the matrix element partons with parton showers. We simulate the detector environment using `Delphes` 3.4.2 [110] (with ATLAS and CMS cards). We cluster the jets using the anti-k_T algorithm [111] with the radius parameter $R = 0.4$.

2.9 Results

In Fig 2.6, we show the exclusion limits on the $R_{D^{(*)}}$ and $R_{K^{(*)}}$-motivated couplings taken one at a time. These are the LHC indirect limits obtained by recasting the dilepton data. These are the 95% (2σ) confidence level (CL) exclusion limits. The regions above the lines are excluded with 95% CL. To obtain the limits, we set the coupling under consideration to nonzero and the rest to zero. In Fig. 2.6a, we plot the exclusion limits for $R_{D^{(*)}}$ motivated couplings. The strongest limit comes from the λ^L_{23} coupling. This occurs because for a nonzero λ^L_{23} coupling, we get a s-quark initiated t-channel U_1 mediated process which interferes with the SM $ss \to \gamma^*/Z^* \to \tau\tau$ process. But in the case of a nonzero $\lambda^{L/R}_{33}$ coupling, the limits weaken because here the process is b quark initiated, and the b PDF is small as compared to s PDF. Similarly, in Fig. 2.6b, the limits on $\lambda^{L/R}_{22}$ is more severe than the ones on $\lambda^{L/R}_{32}$. The λ^R_{22} (λ^R_{32}) coupling has much stricter bounds than the λ^L_{22} (λ^L_{32}) because, in case of right-handed coupling, the BR is 100%. The four

[2]The NNPDF2.3LO PDF for the heavy quarks might have considerable uncertainties. However, the limits on the U_1 parameters are largely insensitive to these.

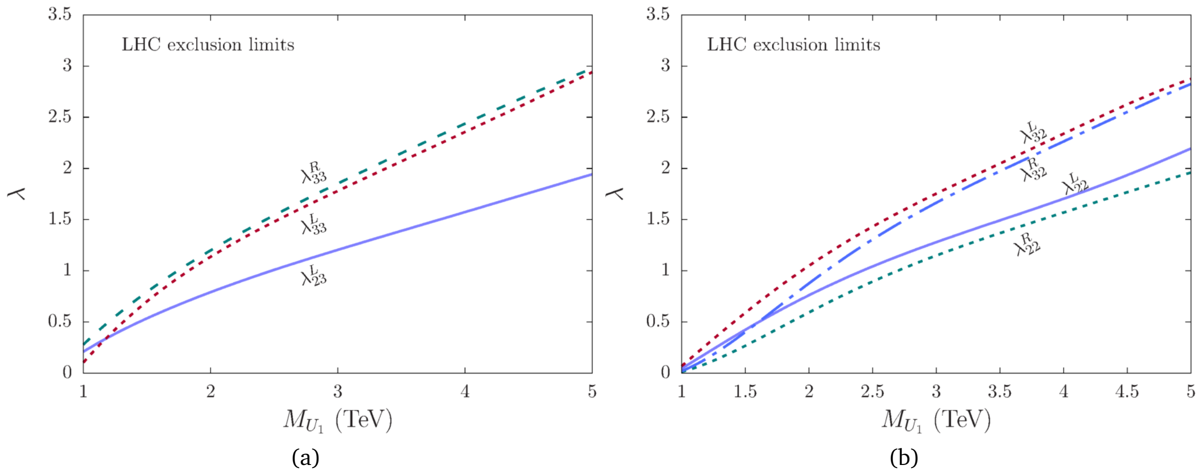

Figure 2.6: We show the 2σ LHC exclusion limits on the couplings relevant to the (a) $R_{D^{(*)}}$ and (b) $R_{K^{(*)}}$ scenarios. The regions above these lines are excluded. We obtain these exclusion limits by recasting the latest LHC dilepton data [101, 102] by combining all the U_1 production processes that contribute to dilepton in the final states.

modes of dilepton production contribute differently in different mass ranges to the exclusion limits. Fig. 2.7 shows the exclusion limits if one excludes the resonant production. From Fig. 2.6 and Fig. 2.7, it is clear that the resonant modes play crucial roles, especially in the lower mass regions, in making the limits tighter. This is an important point as often in the literature the resonant contributions are overlooked. Whereas, for high masses and $\lambda \gtrsim 1$, the nonresonant modes of production play a more determining role. At high masses, the contributions from resonant production are negligible, and hence the limits Fig. 2.6 and Fig. 2.7 converge.

In 2.8, we plot the LHC indirect exclusion limits along with the direct limits from the $jj + \not{E}_{\mathrm{T}}$ and $tt + \not{E}_{\mathrm{T}}$ channels [93] and the bounds from the $R_{D^{(*)}}$ scenarios for single and multi coupling scenarios. In addition to this, we also show the parameter space satisfying the relevant flavour observables in these plots. From Fig. 2.8a, we see the importance of the indirect limits for single coupling scenario λ^L_{23}. For instance, if one were to consider only the direct limits (shown in magenta), then one would conclude that a U_1 LQ can explain the $R_{D^{(*)}}$ scenarios (shown in yellow). But once we include the LHC indirect limits (shown in purple), we find that the entire $R_{D^{(*)}}$ favourable region is excluded by the LHC data. Here, FlavD is defined as

$$\text{FlavD} \equiv \text{the region allowed by } \left\{R_{D^{(*)}} + F_L(D^*) + P_\tau(D^*) + \mathscr{B}(B_{(c)} \to \tau\nu) + \mathscr{C}_9^{\text{univ}}\right\}, \quad (2.80)$$

and is in tension with the B_s-$\bar{B}_s$ mixing data (shown in orange) and is independently and entirely excluded by the LHC ditau search data. The tension between FlavD and the B_s-$\bar{B}_s$ mixing data arises

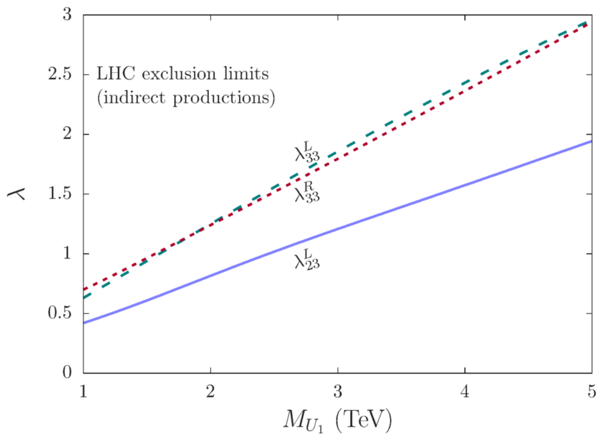

(a)

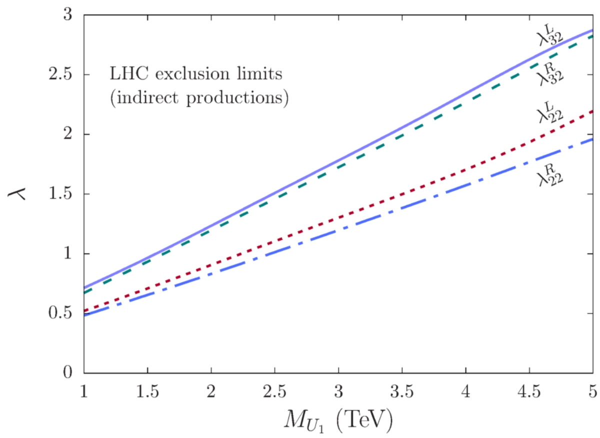

(b)

Figure 2.7: Similar to Fig. 2.6, we show 2σ LHC exclusion limits on the couplings to the relevant to the (a) $R_{D^{(*)}}$ and (b) $R_{K^{(*)}}$ scenarios. However, here we consider only contributions from the nonresonant modes while recasting the latest LHC dilepton searches. Contrary to 2.6, in the lower mass region, the bounds are loose. Hence, it is important to include the resonant modes of production to obtain tighter bounds. We find that in the higher mass regions, the limits mainly come from the nonresonant production and its interference with the SM background.

since the B_s-$\bar{B}_s$ mixing data favours a smaller $\mathscr{C}_{V_L}^{U_1}$ (via $\mathscr{C}_{box}^{U_1}$ which roughly goes as the square of $\mathscr{C}_{V_L}^{U_1}$) than the $R_{D^{(*)}}$ observables.

Fig. 2.8b shows parameter regions in Scenario RD1B. This scenario doesn't contribute to Eq. (2.26) and, thus, cannot accommodate a nonzero $\mathscr{C}_9^{\text{univ}}$. Here, FlavD$_9$ is defined as,

$$\text{FlavD}_9 \equiv \text{the region allowed by } \left\{R_{D^{(*)}} + F_L(D^*) + P_\tau(D^*) + \mathscr{B}(B_{(c)} \to \tau\nu)\right\}. \tag{2.81}$$

In Fig. 2.8b, we find that all but a minor region at high masses are excluded by the latest $\tau\tau$ data. Unlike Fig. 2.8a, the direct search limits in Fig. 2.8b show a slight model dependence since, in this case, the CMS analysis included the model-dependent single production in the signal [96]. The two-coupling scenarios show more promise. Fig. 2.8c and 2.8d correspond to Scenario RD2A and Scenario RD2B, respectively. In these plots, we show a slice of the three-dimensional parameter space of the two scenarios. In Fig. 2.8c, we vary the λ^L_{23} coupling and fix $\lambda^L_{33} = 0.5$. We observe that a good portion of the FlavD$_9$ region survives the LHC bounds but is in disagreement with the B_s-$\bar{B}_s$ mixing data. However, we note that a small region of FlavD$_9$ agrees with B_s-$\bar{B}_s$ mixing and survives the LHC bounds.

In Fig. 2.9, we show the bounds by varying the couplings and keeping the mass of U_1 fixed. Fig. 2.9a (Fig. 2.9c) corresponds to the two coupling scenario Scenario RD2A for a mass of $M_{U_1} = 1.5$ (2.0) TeV. The blue colour stands for the region allowed by the LHC bounds. As

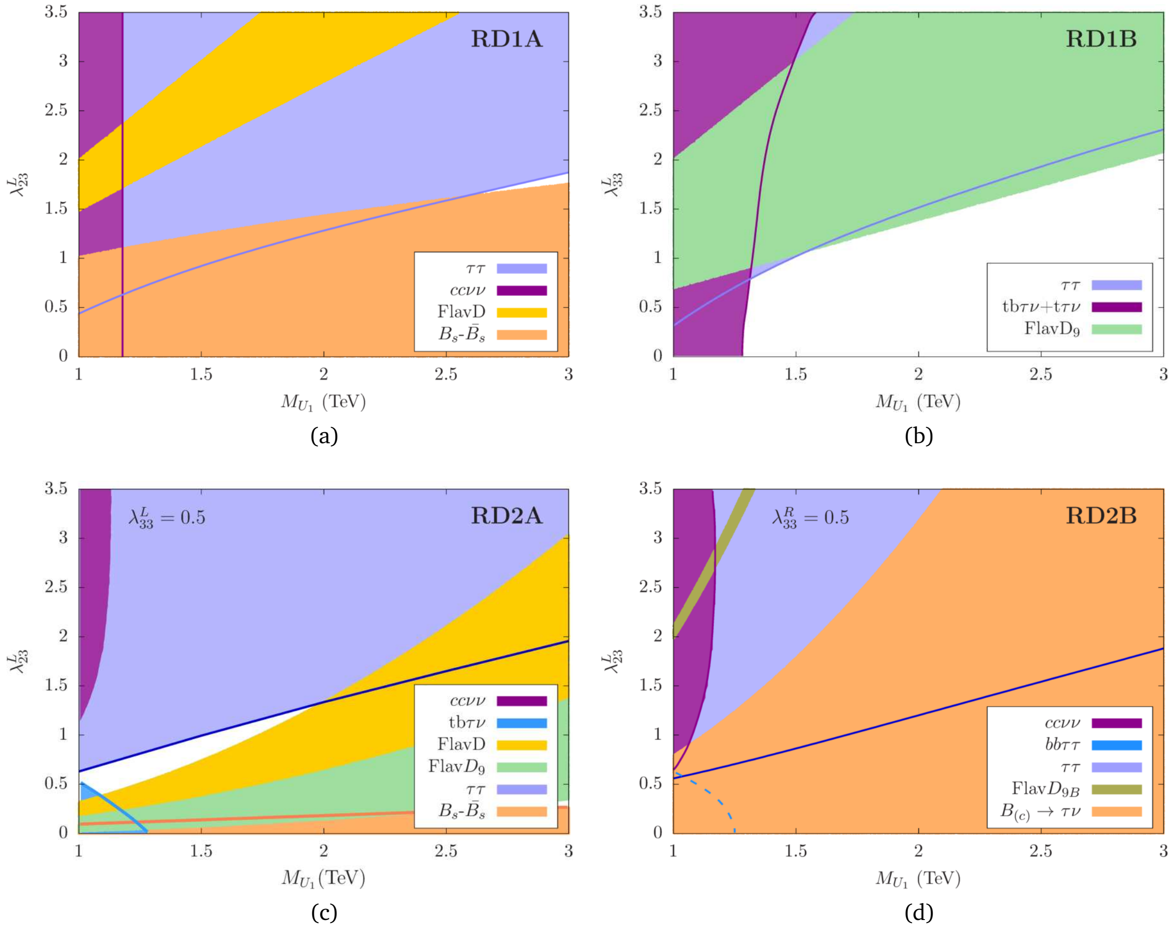

Figure 2.8: Here, we show the regions preferred by the flavour anomalies and the 2σ exclusion limits from the LHC. The purple color denotes the regions excluded by the LHC indirect limits by 2σ. The magenta and blue color denote the regions excluded by the LHC's direct limits (Search by search in the $cc\nu\nu$ channel [93]). (a) We consider only λ^L_{23} to be nonzero (Scenario RD1A). The yellow color denotes the regions favoured by the $R_{D^{(*)}}$ anomalies and is labeled as FlavD as explained in Eq. (2.80). The light orange region is favoured by B_s-$\bar{B}_s$ mixing. (b) In scenario RD1B, we consider only λ^L_{33} to be nonzero. The green-coloured region is allowed by the constraints in FlavD except for $\mathscr{C}_9^{\text{univ}}$ (See Eq. (2.27)). The magenta color depicts the limits from the recent CMS direct search in the $tb\tau\nu + t\tau\nu$ mode [96]. (c) In Scenario RD2A, we set $\lambda^L_{33} = 0.5$ and λ^L_{33} is the free parameter. The color scheme is the same as the previous plots. (d) In Scenario RD2B, we set $\lambda^R_{33} = 0.5$ (benchmark choice) and λ^L_{23} is free coupling parameter. The blue dashed line shows the limits from the ATLAS $bb\tau\tau$ direct search data [95]. The dashed line implies that the recast has been done from a scalar LQ direct search. The FlavD$_{9B}$ region (olive green), defined in Eq. (2.82), agrees with all the constraints in the FlavD$_9$ region without the constraints from the $B_{(c)} \to \tau\nu$ decays. The light orange colour shows the region preferred by $B_{(c)} \to \tau\nu$.

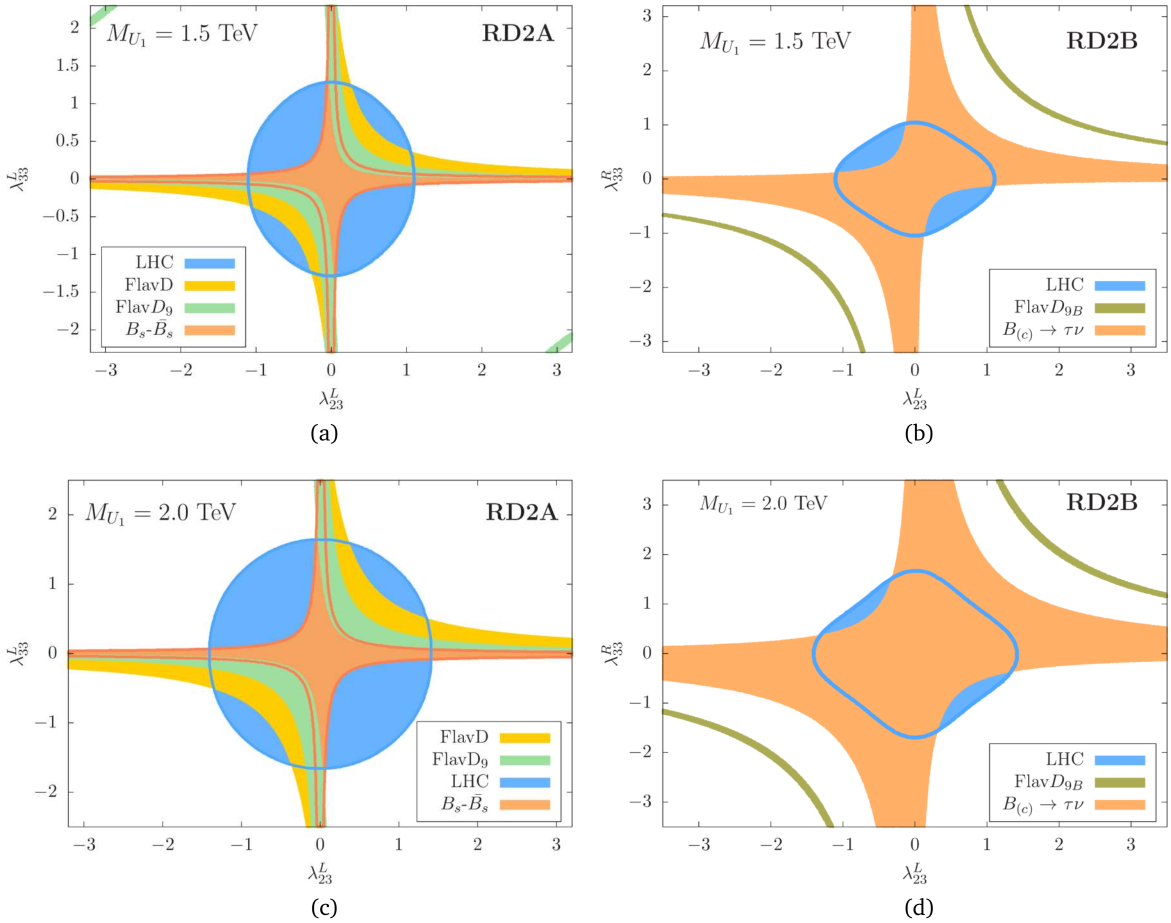

Figure 2.9: We show the two coupling scenarios for two benchmark mass values. We show the regions favoured by the flavour observables in yellow (FlavD), green(FlavD$_9$), and orange color (B_s-$\bar{B}_s$ mixing). The blue color denotes the regions allowed by the LHC data. In (a) and (c), we show the two-coupling scenario (Scenario RD2A) for masses $M_{U_1} = 1.5$ TeV and $M_{U_1} = 2.0$ TeV. In (b) and (d), we show the two-coupling scenario (Scenario RD2B) for masses $M_{U_1} = 1.5$ TeV and $M_{U_1} = 2.0$ TeV. The olive green color denotes the regions favoured by the flavour anomalies except for $\mathcal{O}_9^{\text{univ}}$ and the $B_{(c)} \to \tau\nu$ decay. We mark the regions preferred by the $B_{(c)} \to \tau\nu$ decay in light orange colour.

we can see, the blue region overlaps with the regions contributing to $R_{D^{(*)}}$ observables as well other relevant bounds. For higher masses, the LHC bounds become less strict. We plot similar limits for the Scenario RD2B in Figs. 2.9b and 2.9d. Here, the absence of λ^L_{33} makes it difficult to accommodate the allowed $\mathscr{C}_9^{\rm univ}$. Thus, there is no overlap between the regions favoured by the $R_{D^{(*)}}$ observable and the bounds from the $\mathscr{B}(B_{(c)} \to \tau\nu)$ constraint. The region FlavD_{9B} is defined as,

$$\text{FlavD}_{9B} \equiv \text{the region allowed by } \{R_{D^{(*)}} + F_L(D^*) + P_\tau(D^*)\}\,. \tag{2.82}$$

In Fig. 2.10, we plot the LHC exclusion limits (violet-coloured region) from the CMS $\mu\mu$ data [102] along with the regions favoured by the $R_{K^{(*)}}$ anomalies and allowed by the B_s-$\bar{B}_s$ mixing data (yellow coloured region) for the single coupling scenarios. Here, FlavK region is defined as,

$$\text{FlavK} \equiv \text{ the region favoured by } \left\{\text{the global fits to } b \to s\mu\mu \text{ data} + B_s\text{-}\bar{B}_s \text{ mixing}\right\} \tag{2.83}$$

However, in Fig. 2.10b (Scenario RD2B), we find that (as expected) λ^L_{32} alone cannot explain the $R_{K^{(*)}}$ anomalies, thus we plot only the regions allowed by the B_s-$\bar{B}_s$ mixing data. The magenta dashed lines are the bounds from the recent LHC pair production searches. We obtained the direct limits by recasting the recent ATLAS search for scalar LQ in the $\mu\mu + jj/bb$ channel obtained with 139 fb^{-1} of integrated luminosity [94]. Although the search was designed for a scalar LQ, we recast the limits assuming the (kinematic) selection efficiencies do not change when we switch from sLQ to U_1 LQ. We observe that the LHC exclusion limits from the $\mu\mu$ data are much less constraining than those from the $\tau\tau$ data. This happens because the magnitudes of these couplings required to explain the $R_{K^{(*)}}$ anomalies are much smaller than those in the $R_{D^{(*)}}$ scenarios. We also note that the direct search mass exclusion limits are weaker in the scenarios with left-type couplings (i.e., Scenario RK1A and Scenario RK1B) than those with right-type couplings (Scenario RK1C and Scenario RK1D). This is because the decay $U_1 \to \mu b/\mu j$ has 100% BR in the right-type coupling scenarios instead of the 50% in the left-type ones. The recast limits imply that all the two-coupling scenarios with a 1.5 TeV U_1 are ruled out.

We consider a 2 TeV U_1 in the two-coupling scenarios in Fig. 2.11. There we show the regions allowed by the LHC data along with the FlavK regions in Scenario RK2A and Scenario RK2D and FlavK_B regions in Scenario RK2B and Scenario RK2C. In the last two scenarios, the constraints from B_s-$\bar{B}_s$ mixing data are not applicable, and the FlavK_B regions are just the ones favoured by the global fit of $b \to s\mu\mu$ data

$$\begin{aligned} \text{FlavK}_B &\equiv \text{FlavK} + \text{the region exclusively disfavoured by } B_s\text{-}\bar{B}_s \text{ mixing} \\ &\equiv \text{the region favoured by the global fits to b} \to \text{s}\mu\mu \text{ data.} \end{aligned} \tag{2.84}$$

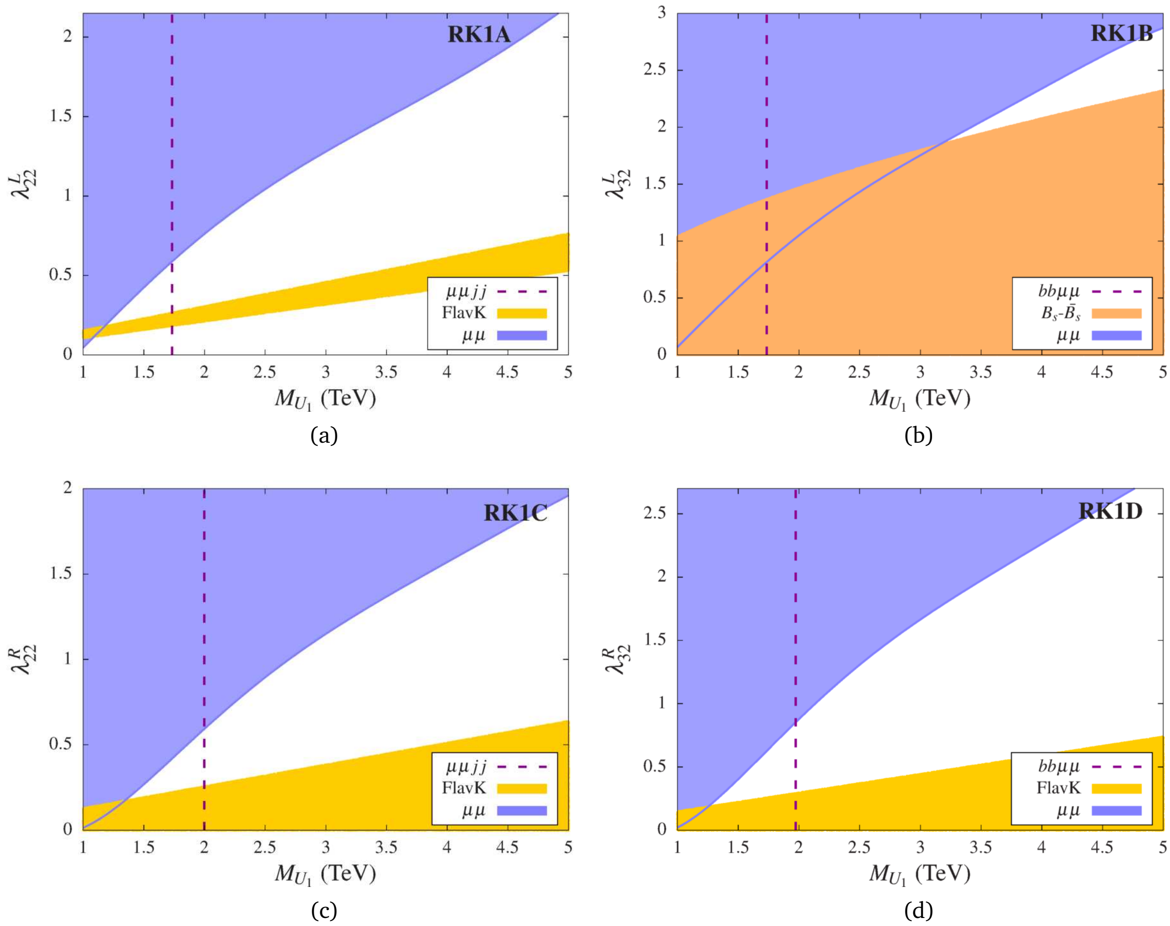

Figure 2.10: We show the 2σ excluded region by the LHC indirect limits in purple for the single coupling scenarios. We obtain it by recasting the latest CMS $\mu\mu$ search data [102]. The yellow color region (Defined as FlavK in Eq. (2.83)) is relevant to the global fits to the $\mathrm{b} \to \mathrm{s}\mu\mu$ and $\mathrm{B_s}$-$\mathrm{\bar{B}_s}$ mixing. We show the exclusion limits by recasting the ATLAS direct search for pair production of sLQs decaying to $\mu\mu + jj/bb$ channels [94] as magenta dashed lines. (a) We set λ_{22}^L (Scenario RK1A) to be nonzero. (b) Here, we set λ_{32}^L (Scenario RK1B) to be nonzero. Since λ_{32}^L alone cannot explain the $R_{K^{(*)}}$ anomalies, we only show the region allowed by the B_s-$\bar{B}_s$ mixing data. (c) we set λ_{22}^R (Scenario RK1C) to be nonzero. (d) Scenario RK1D: Only λ_{32}^R is nonzero.

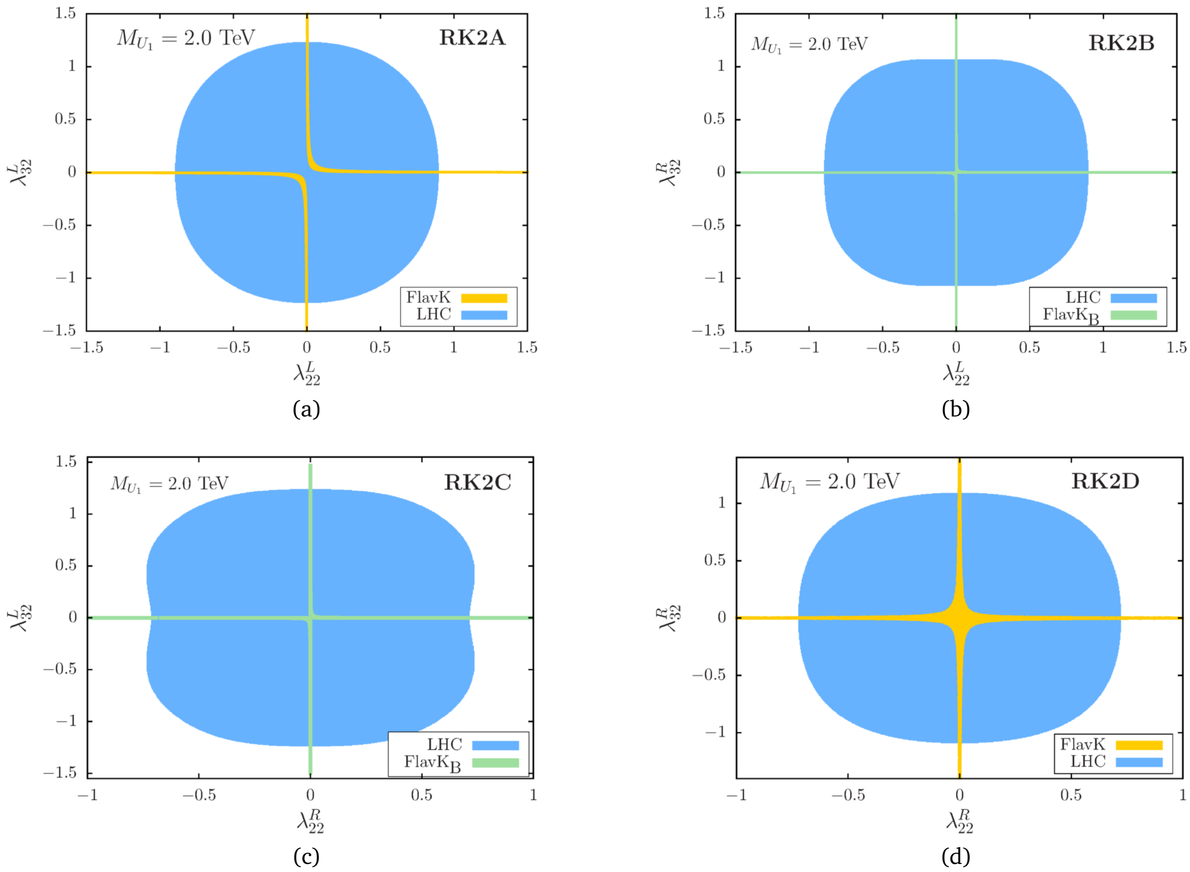

Figure 2.11: We show the regions favoured by the $R_{K^{(*)}}$ observables in yellow (FlavK as defined in Eq. 2.83) and green (FlavK$_B$ as define in Eq. 2.84). The blue colour denotes the regions allowed by the LHC indirect obtained by recasting the CMS $\mu\mu$ search data [102]. In (a) and (d), we show the two coupling scenarios—Scenario RK2A and Scenario RK2D and in (b) and (c) we show the Scenario RK2B and Scenario RK2C.

Before we move on, we make an interesting observation. A priori, it appears from the recast of the ATLAS scalar-search limits that a 1.5 TeV U_1 is ruled out by the LHC data. However, we show that a 1.5 TeV U_1 solution to $R_{D^{(*)}}$ and $R_{K^{(*)}}$ anomalies can still be viable with multiple new couplings. The presence of the extra couplings reduces the $\beta(U_1 \to \mu b/\mu j)$ below 0.25, bringing down the mass limit below 1.5 TeV. We consider the points $\lambda^L_{23} = 0.006$ and $\lambda^L_{33} = 0.93$ in Fig. 2.12. These points are relevant to the $R_{D^{(*)}}$ observables and satisfy the B_s-$\bar{B}_s$ mixing constraint and are allowed by the LHC limits. This result is interesting as we show four possible parameter choices for which a 1.5 TeV U_1 can account for both $R_{D^{(*)}}$ and $R_{K^{(*)}}$ anomalies. (A similar reduction in the mass limit can also be seen from Ref. [68], which studies LQ-mediated scalar productions at the LHC. There, a scalar LQ has six decay modes with roughly equal branching ratios ($\sim$ 1/6), bringing down the direct limit it below 1.5 TeV.)

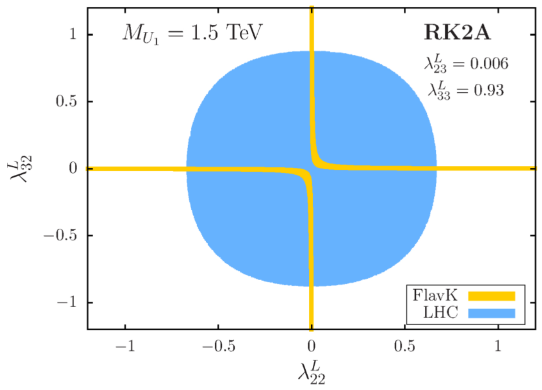

(a)

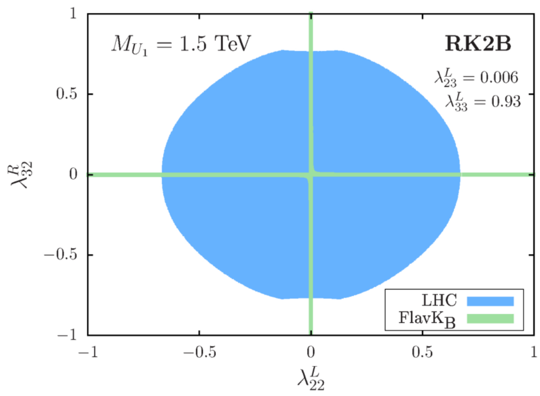

(b)

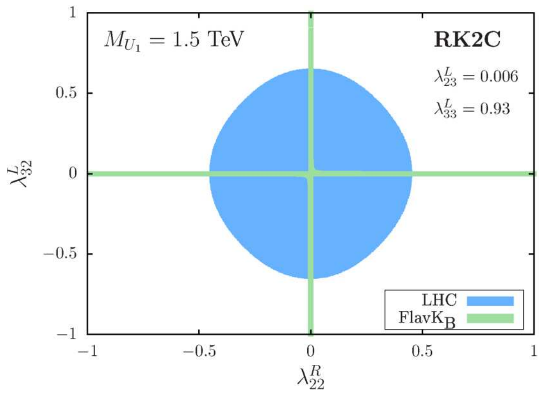

(c)

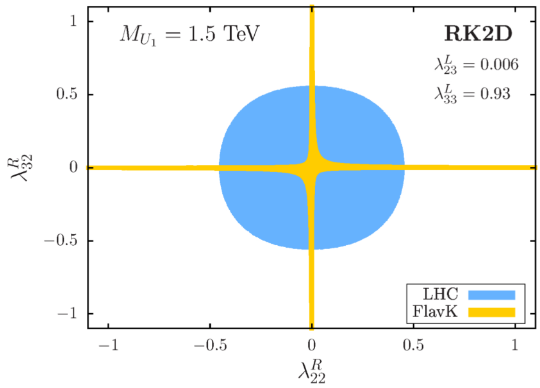

(d)

Figure 2.12: We show the regions in the parameter space of a 1.5 TeV U_1 surviving the LHC limits and tha can simultaneously explain the $R_{D^{(*)}}$ and $R_{K^{(*)}}$ anomalies. The FlavK (yellow), FlavK$_B$ (green) and the blue regions are identical to the ones in Fig. 2.11. We recast the ATLAS search in the $\mu\mu + bb/jj$ channels [94] and add the following couplings–$\lambda^L_{23} = 0.006$ and $\lambda^L_{33} = 0.93$ that are allowed by the LHC and flavour data (see Fig. 2.9a). This relaxes the exclusion limits and allows the otherwise excluded mass value in the R$_{K^{(*)}}$ two-coupling scenarios.

For an illustration, we show the observed $\mu\mu$ data [102] and the corresponding SM contributions in Fig. 2.13. We show the different signal components for $M_{U_1} = 1.5$ TeV and $\lambda^L_{22} = 1$ (Scenario RK1A) in the lower panel. Here, $\mathcal{N}^{p+s} = \mathcal{N}^p + \mathcal{N}^s$ denotes the total number of surviving events from the pair and single production processes, $\mathcal{N}^{\text{nr}_2}$ is for the SM-BSM interference, and $\mathcal{N}^{\text{nr}_4}$ denotes the number of pure-BSM nonresonant events. As the interference is destructive in nature and can be large, the total number of signal events can be positive or negative depending on the invariant mass of the muons.

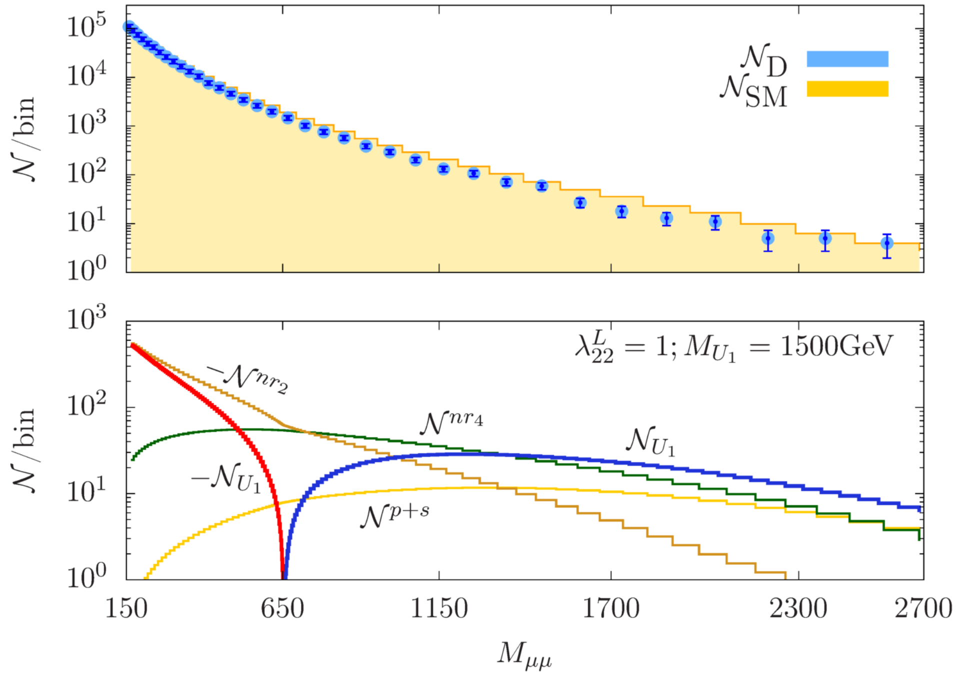

Figure 2.13: The observed $M_{\mu\mu}$ distribution and the corresponding SM contributions from Ref. [102]. We have obtained the errors using Eq. (2.79). (Lower Panel) We show the different signal components for a particular mass of $\hat{U}_1$ and benchmark scenario.

Chapter

3

Combined explanation of multiple anomalies in a singlet-triplet scalar leptoquark model

3.1 Overview

In the previous chapter, we showed that a 1.5 TeV U_1 LQ could address the anomalies in the $R_{K^{(*)}}$ and $R_{D^{(*)}}$ observables [15, 112–122][1]. However, there are more statistically significant experimental anomalies. For example, the experimental measurement of the anomalous magnetic moment of the muon, commonly referred to as $(g-2)_\mu$, performed by the Muon $g-2$ collaboration at Fermilab [123, 124] deviates from the SM value computed by the Muon g-2 Theory Initiative [125–160][2] by 4.2σ. Moreover, very recently, the CDF collaboration [163] at Fermilab observed a discrepancy of 7σ while measuring the mass of W boson. Various new-physics explanations of the W-boson mass anomaly have already been proposed in the literature [164–169, 169–204]. We know that various LQs can resolve different anomalies [31, 37, 45, 63, 205–213]. It is possible to resolve all these anomalies simultaneously if one considers models with more than one LQ. A

[1]Similar to chapter 2, we describe the anomalies as they were till Summer 2022. We discuss the changes due to the latest updates in Chapter 4.

[2]Note that if, instead of the $e^+e^- \to$ hadrons data-driven calculation by the Theory Initiative, the lattice-calculated value of hadronic vacuum polarisation from the BMW Collaboration [161] is used, the deviation reduces to only 1.6σ [162].

recent experiment at the LHCb detector strongly hints towards the existence of LQs [214] (also see Ref. [215]). In this chapter, we illustrate this point with a simple setup of two TeV-scale scalar Leptoquarks (sLQs)—a weak-singlet $S_1\left(\overline{\mathbf{3}},\mathbf{1},1/3\right)$ and a weak-triplet $S_3\left(\overline{\mathbf{3}},\mathbf{3},1/3\right)$—that can address all these anomalies simultaneously. Apart from being simple, this model is also economical as it requires only a few free parameters and is testable at the LHC.

3.2 The $S_1 + S_3$ model

Some of the $S_1 + S_3$ models have been studied in different contexts earlier [29, 216–228].The Yukawa part of the Lagrangian can be written as [9, 10]

$$\mathscr{L}_Y \supset x^L_{ij}\bar{Q}^{C\,i}_L S_1 \left(i\sigma_2\right) L^j_L + x^R_{ij}\bar{u}^{C\,i}_R S_1 \ell^j_R + y^L_{ij}\bar{Q}^{C\,i}_L \left(i\sigma_2\right)\left(\vec{\sigma}\cdot\vec{S}_3\right) L^j_L + \text{h.c.}, \tag{3.1}$$

where we have ignored the diquark interactions. The indices i and j denote the generations of the SM fermions, while $Q^{C\,i}_L$ and L^i_L are the ith-generation (charge-conjugated) quark and lepton doublets, respectively. The Pauli matrices are denoted by σ_k's. In general, the couplings x^L, x^R, and y^L are 3×3 complex matrices, but for simplicity, we assume all couplings are real. The triplet S_3 has three components with charges $-2/3$, $1/3$, and $4/3$.

3.2.1 Flavour ansatz

Following a similar approach as in the previous chapter, we make an economical flavour ansatz. We will elaborate on this particular choice of couplings in the following sections,

$$x^{L/R} = \begin{pmatrix} 0 & 0 & 0 \\ 0 & 0 & x^R_{23} \\ 0 & x^{L/R}_{32} & 0 \end{pmatrix};\; y^L = \begin{pmatrix} 0 & 0 & 0 \\ 0 & y^L_{22} & 0 \\ 0 & y^L_{32} & 0 \end{pmatrix}, \tag{3.2}$$

The $x^{L/R}$ coupling matrix corresponds to the singlet sLQ S_1 and the $y^{L/R}$ coupling matrix corresponds to the triplet sLQ S_3. We point out that the zeros in the coupling matrices are phenomenological and may not be strictly applicable in specific models [66, 71]. This leads to the following interaction

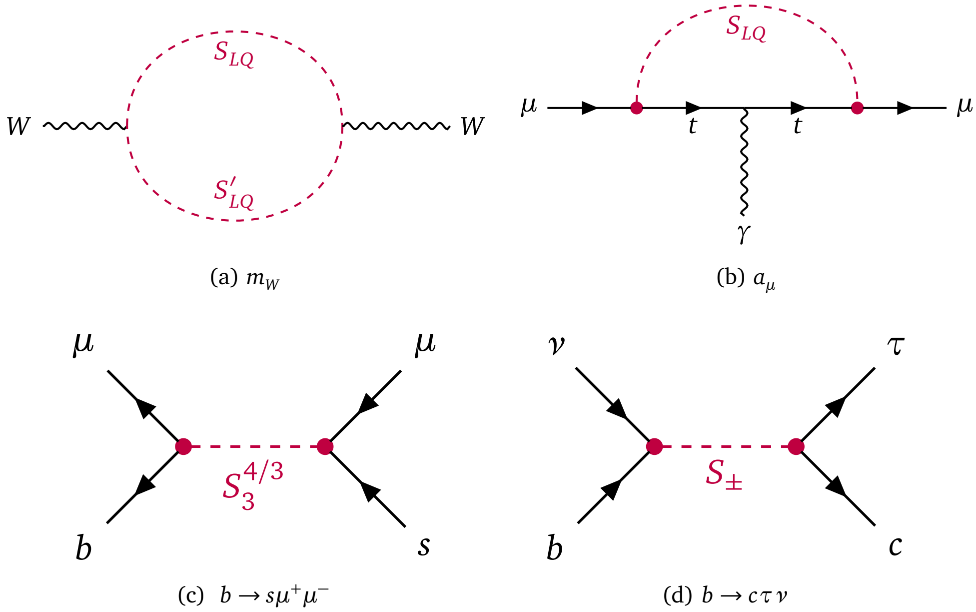

Figure 3.1: Here, we show the various diagrams that can contribute to the anomalies. S_{LQ} denotes a scalar LQ. The $q\ell LQ$ coupling is shown in red.

terms:

$$\begin{aligned}\mathscr{L} \supset &\Big[x^L_{32}\left(V_{td}\,\bar{u}^C_L\mu_L + V_{ts}\,\bar{c}^C_L\mu_L + V_{tb}\,\bar{t}^C_L\mu_L\right) - x^L_{32}\,\bar{b}^C_L\nu_{\mu_L} + x^R_{32}\,\bar{t}^C_R\mu_R + x^R_{23}\,\bar{c}^C_L\tau_L\Big]S_1 - \Big[y^L_{32}\left(\bar{b}^C_L\nu_{\mu_L}\right.\\ &\left.+ V_{td}\,\bar{u}^C_L\mu_L + V_{ts}\,\bar{c}^C_L\mu_L + V_{tb}\,\bar{t}^C_L\mu_L\right) + y^L_{22}\left(\bar{s}^C_L\nu_{\mu_L} + V_{cd}\,\bar{u}^C_L\mu_L + V_{cs}\,\bar{c}^C_L\mu_L + V_{cb}\,\bar{t}^C_L\mu_L\right)\Big]S_3^{1/3}\\ &+ \sqrt{2}\,y^L_{32}\left(V_{td}\,\bar{u}^C_L\nu_\mu + V_{ts}\,\bar{c}^C_L\nu_\mu + V_{tb}\,\bar{t}^C_L\nu_\mu\right)S_3^{-2/3} + \sqrt{2}\,y^L_{22}\left(V_{cd}\,\bar{u}^C_L\nu_\mu + V_{cs}\,\bar{c}^C_L\nu_\mu + V_{cb}\,\bar{t}^C_L\nu_\mu\right)S_3^{-2/3}\\ &- \sqrt{2}\left(y^L_{32}\,\bar{b}^C_L\mu_L + y^L_{22}\,\bar{s}^C_L\mu_L\right)S_3^{4/3}. \end{aligned} \tag{3.3}$$

Here, we have assumed the LQ interactions to be aligned with the down quarks and suppressed the neutrino-mixing matrix (since neutrino mixing would not affect the short-ranged experimental measurements of the low-energy observables).

3.3 Contribution to the anomalies

3.3.1 W mass

The recent CDF measurement puts the W-boson mass at $m_W^{\rm CDF} = 80.4335 \pm 0.0094$ GeV [163], about 7σ away from its SM value, $m_W^{\rm SM} = 80.361 \pm 0.006$ GeV [229]. The difference can be parameterised in terms of the Peskin-Takeuchi parameters (S, T, and U), of which the T parameter is the most sensitive. In Fig. 3.1a, we show the singlet-triplet model could contribute to the W-boson mass anomaly. A positive correction to the W-boson mass can come from the triplet scalar if there is a mass split among two of its components. In order to obtain the required mass split, we consider a Higg portal to mix different LQs which leads to a mass split after the electroweak symmetry breaking (EWSB) [230]. The relevant terms of the scalar potential are given as follows,

$$\mathscr{L}_S \supset -\sum_{i=1,3}\left[M_{S_i}^2 S_i^\dagger S_i + \lambda_{S_i}^H\left(H^\dagger H\right)\left(S_i^\dagger S_i\right) + \lambda_{S_i}\left(S_i^\dagger S_i\right)^2\right] - \left[\lambda H^\dagger\left(\vec{\sigma}\cdot\vec{S}_3\right)HS_1^* + \text{h.c.}\right]. \tag{3.4}$$

Here, H is the SM Higgs doublet, and $M_{S_i}^2$, $\lambda_{S_i}^H$, λ_{S_i}, and λ are positive quantities. The charge-$1/3$ components of the two SLQs (S_1 and $S_3^{1/3}$) mix in the presence of a nonzero λ after EWSB. We get the following mass matrix for the charge-$1/3$ fields:

$$\mathscr{M}^2 = \begin{pmatrix} M_1^2 & \lambda v^2/2 \\ \lambda v^2/2 & M_3^2 \end{pmatrix}, \tag{3.5}$$

where $M_i^2 = M_{S_i}^2 + \lambda_{S_i}^H v^2$. An orthogonal transformation can diagonalise it:

$$\begin{pmatrix} S_- \\ S_+ \end{pmatrix} = \begin{pmatrix} \cos\theta & \sin\theta \\ -\sin\theta & \cos\theta \end{pmatrix}\begin{pmatrix} S_1 \\ S_3^{1/3} \end{pmatrix} \tag{3.6}$$

where $S_\pm$ are the mass eigenstates with masses $m_\pm$, and θ is the mixing angle:

$$M_\pm^2 = \frac{1}{2}\left[M_3^2 + M_1^2 \pm \frac{1}{2}\sqrt{\left(M_3^2 - M_1^2\right)^2 + (\lambda v^2/2)^2}\right], \tag{3.7}$$

$$\theta = \frac{1}{2}\tan^{-1}\left(\frac{\lambda v^2/2}{M_1^2 - M_3^2}\right) \in [-\pi/4, \pi/4]. \tag{3.8}$$

Due to the $S_1 \leftrightarrow S_3^{1/3}$ mixing, a mass split is induced among the components of S_3. This shifts the T parameter and induces a shift in the W mass (the sLQ-induced corrections to the oblique parameters are studied in Ref. [231]). In the $S_1 + S_3$ model, the shift of the T parameter, ΔT, is given by

$$\Delta T = \frac{3}{4\pi s_W^2}\frac{1}{m_W^2}\left[F(M_3, M_-)c_\theta^2 + F(M_3, M_+)s_\theta^2\right], \tag{3.9}$$

where s_W is the sine of the Weinberg angle, $c_\theta = \cos(\theta)$ and $s_\theta = \sin(\theta)$. The function $F(m_a, m_b)$ is given as

$$F(m_a, m_b) = m_a^2 + m_b^2 - \frac{2m_a^2 m_b^2}{m_a^2 - m_b^2}\log\left(\frac{m_a^2}{m_b^2}\right). \tag{3.10}$$

It goes to zero in the limit $m_a = m_b$. The W-boson mass is connected to the oblique parameters through the following relation:

$$\Delta m_W^2 = \frac{\alpha_Z c_W^2 m_Z^2}{c_W^2 - s_W^2}\left[-\frac{\Delta S}{2} + c_W^2 \Delta T + \frac{c_W^2 - s_W^2}{4 s_W^2}\Delta U\right], \tag{3.11}$$

where α_Z is the fine-structure constant at the Z pole and $c_W^2 = 1 - s_W^2$. In our model, the S and U parameters do not shift significantly. The sign of $\Delta M = M_3 - M_1$ is important; we use $\Delta M > 0$ in our analysis. We find that a slight mass difference, $\Delta M = M_3 - M_1 \approx 25$ GeV, is necessary to explain the W-mass anomaly. The choice of the LQ mass will be explained later.

3.3.2 Anomalous magnetic moment of muon $(g-2)_\mu$

The recent experimental measurement of the anomalous magnetic moment of the muon– $(g-2)_\mu$ by the Muon $g-2$ collaboration at Fermilab and the earlier result by the E821 experiment at the Brookhaven Lab put it at $a_\mu^{\rm Exp} = 116592061(41) \times 10^{-11}$. The SM predicted value computed by the Muon (g-2) Theory initiative is given as, $a_\mu^{\rm SM} = 116591810(43) \times 10^{-11}$. Thus, this leads to a discrepancy of 4.2σ, $\Delta a_\mu = a_\mu^{\rm Exp} - a_\mu^{\rm SM} = (2.51 \pm 0.59) \times 10^{-9}$. In our model the $S_\pm$ and $S_3^{4/3}$ contribute to the $(g-2)_\mu$ (see Fig. 3.1b). From the flavour ansatz in Eq. (3.2), the following couplings can contribute: $x_{32}^{L/R}$, y_{32}^L, and $y_{22}^{L/R}$. Package-X [232] gives the total contribution to Δa_μ as,

$$
\begin{aligned}
\Delta a_\mu = \frac{N_c}{16\pi^2}\Bigg[& -\frac{m_\mu m_t}{M_+^2}\left\{\frac{7}{6}+\frac{2}{3}\ln\left(\frac{m_t^2}{M_+^2}\right)\right\}\left(2x_{32}^L x_{32}^R V_{tb} s_\theta^2 + x_{32}^R y_{32}^L V_{tb} s_{2\theta} + x_{32}^R y_{22}^L V_{cb} s_{2\theta}\right) \\
& + \frac{1}{6}\frac{m_\mu^2}{M_+^2}\left\{\left(|x_{32}^L|^2 V_t + |x_{32}^R|^2\right) s_\theta^2 + \left(|y_{32}^L|^2 V_t + |y_{22}^L|^2 V_c\right) c_\theta^2 + x_{32}^L y_{32}^L V_t s_{2\theta}\right\} \\
& - \frac{m_\mu m_t}{M_-^2}\left\{\frac{7}{6}+\frac{2}{3}\ln\left(\frac{m_t^2}{M_-^2}\right)\right\}\left(2x_{32}^L x_{32}^R V_{tb} c_\theta^2 - x_{32}^R y_{32}^L V_{tb} s_{2\theta} - x_{32}^R y_{22}^L V_{cb} s_{2\theta}\right) \\
& + \frac{1}{6}\frac{m_\mu^2}{M_-^2}\left\{\left(|x_{32}^L|^2 V_t + |x_{32}^R|^2\right) c_\theta^2 + \left(|y_{32}^L|^2 V_t + |y_{22}^L|^2 V_c\right) s_\theta^2 - x_{32}^L y_{32}^L V_t s_{2\theta}\right\} \\
& - \frac{2}{3}\frac{m_\mu^2}{M_3^2}\left(|y_{32}^L|^2 + |y_{22}^L|^2\right)\Bigg].
\end{aligned} \tag{3.12}
$$

Here, $V_t = |V_{td}|^2 + |V_{ts}|^2 + |V_{tb}|^2$ and $V_c = |V_{cd}|^2 + |V_{cs}|^2 + |V_{cb}|^2$. The terms contributing to the Δa_μ can be categorised into two types: 1) the chirality-preserving terms, where the chiralities of the initial and final muons are identical (these terms contribute as m_μ^2) and 2) the chirality-flipping terms where the initial and final muons have opposite chiralities and they contribute as $m_\mu m_q$ (q is the quark that runs in the loop). If we consider the quark running in the loop to be the top quark then, the muon $g-2$ discrepancy can be accommodated with perturbative couplings without conflicting with the current LHC data. We primarily consider the $x_{32}^{L/R}$ couplings of the S_1 for this purpose.

3.3.3 $R_{K^{(*)}}$ observables

In the previous chapter, we mentioned that in SM, the $b \to s\mu\mu$ decay occurs through loop diagrams. Similarly, the S_1 sLQ also contributes to the decay at the loop level. Thus, the S_1 would require large Yukawa couplings to resolve the $R_{K^{(*)}}$ anomalies. Such large couplings would either be ruled out or would be in tension with the LHC data. However, we find that the 4/3 component of S_3 ($S_3^{4/3}$) can contribute to the observables at the tree level (see Fig. 3.1c). We see that the required interactions are $b\mu S_3^{4/3}$ and $s\mu S_3^{4/3}$. Thus, in the flavour ansatz, we set the y_{32}^L and y_{22}^L couplings to nonzero. (It is possible to get the necessary interactions with only one of the couplings if the S_3 is aligned with the up-type quarks. The other coupling can then be generated through CKM mixing. However, since the CKM off-diagonal elements are small, the coupling must necessarily be large and hence will be in conflict with the LHC data.) The two non-zero couplings generate two Wilson operators, $\mathcal{O}_9 = (\bar{s}\gamma_\alpha P_L b)(\bar{\mu}\gamma^\alpha \mu)$ and $\mathcal{O}_{10} = (\bar{s}\gamma_\alpha P_L b)\big(\bar{\mu}\gamma^\alpha\gamma^5\mu\big)$, relevant for the $R_{K^{(*)}}$ observables. We express the corresponding coefficients in terms of the model parameters,

$$\mathscr{C}_9 = -\mathscr{C}_{10} = \frac{\pi v^2}{\alpha V_{tb} V_{ts}^*}\frac{y_{32}^L y_{22}^L}{M_3^2}. \tag{3.13}$$

The global fit for $\mathscr{C}_9 = -\mathscr{C}_{10}$ put them at $-0.39^{+0.07}_{-0.07}$ [233, 234]. . The negative value implies both the Yukawa couplings are either positive or negative since V_{ts} is also negative.

3.3.4 $R_{D^{(*)}}$ observables

In Fig. 3.1d, we show how the charge-1/3 components in the model, $S_\pm$, can contribute to the $R_{D^{(*)}}$ observables at the tree level via $b\nu S_1$ and $c\tau S_1$ couplings. These couplings are generated by nonzero x_{32}^L and x_{23}^R couplings. The product $x_{32}^L x_{23}^R$ needs to be $\mathcal{O}(1)$ for TeV-scale LQs to explain the $R_{D^{(*)}}$ anomalies. (One could also assume the coupling x_{23}^L to be nonzero. However, it would create a tension between the recent $R_K^{\nu\nu}$ measurements and the products $y_{32}^L x_{23}^L$ or $x_{32}^L x_{23}^L$. This can be mitigated by adding some constraints as done in [216].) Based on the interactions in Eq. (3.3), the coefficient of the operators $\mathcal{O}_{S_L} = (\bar{c}P_L b)(\bar{\tau}P_L\nu)$ and $\mathcal{O}_{T_L} = (\bar{c}\sigma^{\mu\nu}P_L b)\big(\bar{\tau}\sigma_{\mu\nu}P_L\nu\big)$ can be written as

$$\mathscr{C}_{S_L} = -4\rho\,\mathscr{C}_{T_L} = \frac{-1}{4\sqrt{2}V_{cb}G_F}\Big[\frac{x_{32}^L x_{23}^R c_\theta^2}{M_-^2} + \frac{x_{32}^L x_{23}^R s_\theta^2}{M_+^2} + \frac{y_{32}^L x_{23}^R c_\theta s_\theta}{M_-^2} - \frac{y_{32}^L x_{23}^R c_\theta s_\theta}{M_+^2}\Big]. \tag{3.14}$$

The $\rho = \rho(m_b, M_\pm)$ is the modification due to the running of the strong coupling [235]. In our model, the coupling x_{32}^L produces a second-generation neutrino in the $b \to c\tau\nu$ process. Whereas in the SM, the same process will produce a third-generation neutrino. Hence, the $\mathcal{O}_{S_L}$ and $\mathcal{O}_{T_L}$ in our model will not interfere with the corresponding SM operators. These operators contribute to the $R_{D^{(*)}}$ $F_L(D^*)$ and $P_\tau(D^*)$ observables (Refer to the 2 for the expressions and the values). They contribute to the $R_{D^{(*)}}$ observables as [18]

$$r_D \equiv \frac{R_D}{R_D^{\rm SM}} \approx\ 1+1.02\,|\mathscr{C}_{S_L}|^2+0.9\,|\mathscr{C}_{T_L}|^2+1.49\ \mathrm{Re}\big[\mathscr{C}_{S_L}\big]+1.14\ \mathrm{Re}\big[\mathscr{C}_{T_L}\big], \tag{3.15}$$

$$r_{D^*} \equiv \frac{R_{D^*}}{R_D^{\rm SM}} \approx\ 1+0.04\,|\mathscr{C}_{S_L}|^2+16.07\,|\mathscr{C}_{T_L}|^2-0.11\ \mathrm{Re}\big[\mathscr{C}_{S_L}\big]-5.12\ \mathrm{Re}\big[\mathscr{C}_{T_L}\big]. \tag{3.16}$$

The current averages are [63]

$$r_D = 1.137 \pm 0.101 \ \text{ and } r_{D^*} = 1.144 \pm 0.057. \tag{3.17}$$

The $\mathscr{O}_{S_L}$ and $\mathscr{O}_{T_L}$ operators also contribute to the $F_L(D^*)$ and $P_\tau(D^*)$ observables as,

$$\begin{aligned} f_L(D^*) \equiv \frac{F_L(D^*)}{F_L^{\rm SM}(D^*)} &\approx\ \frac{1}{r_{D^*}}\Big\{1+0.08\,|\mathscr{C}_{S_L}|^2+7.02\,|\mathscr{C}_{T_L}|^2 \\ &\qquad -0.24\ \mathrm{Re}\big[\mathscr{C}_{S_L}\big]-4.37\ \mathrm{Re}\big[\mathscr{C}_{T_L}\big]\Big\}, \qquad (3.18) \\ p_\tau(D^*) \equiv \frac{P_\tau(D^*)}{P_\tau^{\rm SM}(D^*)} &\approx\ \frac{1}{r_{D^*}}\Big\{1-0.07\,|\mathscr{C}_{S_L}|^2-1.86\times|\mathscr{C}_{T_L}|^2 \\ &\qquad +0.22\ \mathrm{Re}\big[\mathscr{C}_{S_L}\big]-3.37\ \mathrm{Re}\big[\mathscr{C}_{T_L}\big]\Big\}. \qquad (3.19) \end{aligned}$$

The couplings that play a role in explaining the B-anomalies can also contribute to the flavour-changing neutral-current (FCNC) process $b \to s\nu\nu$. In the SM, this process occurs via a loop and is suppressed by the Glashow-Iliopoulos-Maiani (GIM) mechanism. There are some ways to avoid a large contribution to $R_K^{\nu\nu}$ while generating the necessary contribution to the $R_{D^{(*)}}$ observables. For example, Ref. [216] imposes a discrete symmetry to control the couplings with the fermions. We don't follow such an approach here. In our model, the $R_K^{\nu\nu}$ observable receives the following correction [235]:

$$\begin{aligned} R_K^{\nu\nu} = 1 + \frac{\mathscr{A}^2}{3V_{tb}^2V_{ts}^2}\Bigg\{\Bigg(&\frac{y_{32}^Ly_{22}^Ls_\theta^2}{M_-^2}+\frac{y_{32}^Ly_{22}^Lc_\theta^2}{M_+^2}+\frac{x_{32}^Ly_{22}^Ls_\theta c_\theta}{M_-^2} \\ &-\frac{x_{32}^Ly_{22}^Ls_\theta c_\theta}{M_+^2}\Bigg)^2\Bigg\} - \frac{2\mathscr{A}}{3V_{tb}V_{ts}}\Bigg(\frac{y_{32}^Ly_{22}^Ls_\theta^2}{M_-^2}+\frac{y_{32}^Ly_{22}^Lc_\theta^2}{M_+^2} \\ &+\frac{x_{32}^Ly_{22}^Ls_\theta c_\theta}{M_-^2}-\frac{x_{32}^Ly_{22}^Ls_\theta c_\theta}{M_+^2}\Bigg) \end{aligned} \tag{3.20}$$

where $\mathscr{A} = \sqrt{2}\pi^2/(e^2G_F|C_L^{\rm SM}|)$ with $C_L^{\rm SM} \approx -6.38$ [235]. In the following section, we show that our choice of couplings does not create any tension between the $R_{D^{(*)}}$ observables and the $R_K^{\nu\nu}$ measurements.

Observable	Relevant couplings	Experimental bounds
$R_K^{\nu\nu}$	$x^L_{32}, y^L_{32}, y^L_{22}$ [235]	< 2.7 [236]
$\mathrm{BR}(\tau \to \mu\gamma)$	$x^R_{23}, x^{L\star}_{32}, y^{L\star}_{32}, y^L_{22}$ [227]	$< 4.4 \times 10^{-8}$[237]
$\mathrm{BR}(B_c \to \tau\bar{\nu})$	$x^L_{32}, x^R_{23}, y^L_{32}$ [235]	$\leq 10\%$ [79]
$f_L(D^*)$	$x^L_{32}, x^R_{23}, y^L_{32}$ [18]	1.277± 0.193 [238, 239]
$p_\tau(D^*)$	$x^L_{32}, x^R_{23}, y^L_{32}$ [18]	0.766± 1.093 [63]
$\delta g^Z_{\mu_L}(Z \to \mu\mu)$	$x^L_{32}, y^L_{32}, y^{L\star}_{22}$ [235]	$(0.3 \pm 1.1) \times 10^{-3}$ [240]
$\delta g^Z_{\mu_R}(Z \to \mu\mu)$	x^R_{32} [235]	$(0.2 \pm 1.3) \times 10^{-3}$ [240]
$\delta g^Z_{\tau_R}(Z \to \tau\tau)$	x^R_{23} [235]	$(0.66 \pm 0.66) \times 10^{-3}$ [240]
$\mathrm{BR}(D^0 \to \mu\mu)$	$x^{L\star}_{32}, y^{L\star}_{32}, y^{L\star}_{22}$[235]	$< 7.6 \times 10^{-9}$ [241]
$\mathrm{BR}(\tau \to \mu\mu\mu)$	$x^R_{23}, x^{L\star}_{32}, y^{L\star}_{32}, y^L_{22}$ [227]	$< 2.1 \times 10^{-8}$ [242]
$\mathrm{BR}(K \to \mu\nu)$	$x^{L\star}_{32}, y^{L\star}_{32}, y^L_{22}$ [235]	$(63.56 \pm 0.11)\%$ [243]
$\mathrm{BR}(D_s \to \mu\nu)$	$x^{L\star}_{32}, y^{L\star}_{32}, y^L_{22}$ [235]	$(0.543 \pm 0.015)\%$ [243]
$\mathrm{BR}(B \to \mu\nu)$	$x^{L\star}_{32}, y^{L\star}_{32}, y^{L\star}_{22}$ [235]	8.6×10^{-7} [243]
$\Delta m(B^0_s - \bar{B}^0_s)$	y^L_{32}, y^L_{22} [219, 227]	$(0.993 \pm 0.158)\Delta m^{\mathrm{SM}}_{B_s}$ [244, 245]

Table 3.1: Here, we list all the relevant low-energy observables sensitive to the new Yukawa couplings. $\mathrm{BR}(x \to y)$ denotes the branching ratio of the $x \to y$ decay. We use the "$\star$" symbol to denote the couplings that contribute through off-diagonal CKM terms.

3.4 Bounds

We show a comprehensive list of all the relevant low-energy experimental bounds that our model obeys in Table 3.1. In addition to being economical and providing a simultaneous solution to the relevant anomalies, we ensure that our model is testable at the LHC by considering the LQ mass around the TeV scale. We choose $M_1 = 1.5$ TeV and $M_3 = 1.525$ TeV. This gives us a mass difference of $\Delta M = M_3 - M_1 \approx 25$ GeV, which is necessary to explain the W-mass anomaly. Currently, there is no bound on the Higgs-portal coupling, λ, that controls the mixing between S_1 and S_3; we set it to 1. Below we explain our rationale for considering this mass value.

3.4.1 LHC bounds

As before, we systematically consider all the appropriate LHC bounds (direct [101, 102, 246–249] and indirect ones) on the $S_1 + S_3$ parameter space.

Direct bounds:

(a) Based on the flavour ansatz in Eq. (3.2) (i.e x^R_{23}, x^R_{32}, x^L_{32}, y^L_{32} and y^L_{22}), one obtains the following decay modes: $t\mu, b\nu, c\tau, s\nu$, and $c\mu$ for the charge-1/3 sLQs. Our analysis shows that the x^R_{32} coupling tends to be small in the favoured parameter regions (see the following Results section). Also, if we ignore the CKM-suppressed decay modes of the 1/3 sLQ, the left-handed couplings lead to two decay modes and the right-handed ones lead to a single decay mode. Hence, we can infer that these decay modes individually cannot have more than 50% BR. Among these final states, the $c\tau$ mode does not have a direct search limit. Whereas the strongest bound is obtained as 1.4 TeV in the $c\mu$ mode [249] with 50% BR.

(b) Based on the couplings, y^L_{32} and y^L_{22}, the limits on the $S_3^{-2/3}$ decaying mainly to $t\nu, c\nu$ final states are weak.

(c) We find that the strongest collider bound on our model setup comes from the direct limits on the charge-4/3 component of S_3 ($S_3^{4/3}$) decays to $b\mu$ and $s\mu$ decay modes via y^L_{32} and y^L_{22} couplings, respectively. The ATLAS Collaboration has put the lower limit on SLQs that decay to the $b\mu$ and μj final states with a 100% BR at 1721 and 1733 GeV [249] respectively. Now, for these direct limits to come down to our desired mass value of 1.5 TeV, we find that the branching ratio BR($S_3^{4/3} \to b(s)\mu) \lesssim 0.53$ (0.6). Since, the branching ratio BR($S_3^{4/3} \to b\mu$) + BR($S_3^{4/3} \to s\mu$) = 1, thus this leads to the couplings $|y^L_{32}|$ and $|y^L_{22}|$ be closer to each other in our case. We show this in Figs. 3.5b and 3.5c.

Indirect bounds: In the previous chapter, we highlighted the techniques and the importance of considering the indirect bounds from the LHC data. We explained that our methods were generic, and here we use it on the $S_1 + S_3$ model.

We obtain the indirect bounds on the coupling parameters recasting the latest high-p_T dilepton data [101, 102]. We systematically consider all the production modes [91, 250] of the LQs that lead to a pair of leptons in the final states. We show the various production modes of sLQ in Fig. 3.2. We briefly mention the various production modes here (for a detailed description, refer to Chapter 2). Since the high-p_T searches are agnostic about the number of associated jets, these production modes can contribute to the dilepton final states.

(a) The resonant production modes of sLQs comprises of pair production and single production processes. In the pair production mode, the sLQ decays to a lepton and a quark, and thus, we obtain dileptons and jets in the final state ($pp \to S_{LQ}S_{LQ} \to \ell\ell + 2j$). The pair production processes are mostly QCD-mediated (see Fig. 3.2a). Thus, the new couplings mainly feature in the BRs. In the case of the single production process, a LQ is produced along with a lepton

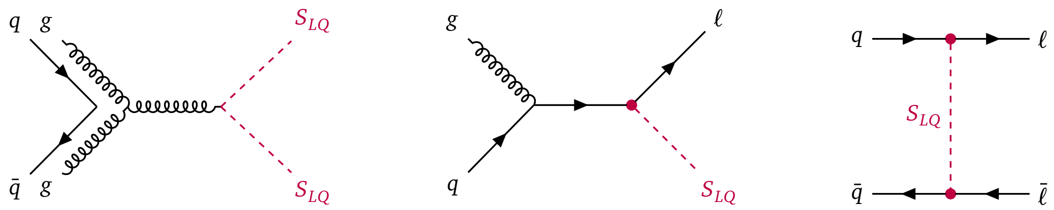

Figure 3.2: The Feynman diagrams for various production modes of the LQ at the LHC.

and/or a jet ($pp \to S_{LQ}\ell/S_{LQ}\ell j \to \ell\ell+$ jet(s)). The single production depends on the new coupling as λ^2 [98, 99].

(b) The nonresonant production modes of sLQs include the dilepton production from the t-channel LQ exchange (See Fig. 3.2c) and its interference with the SM dilepton production. For the t-channel and interference process, the new coupling contribution to the cross section scales as λ^4 and λ^2 respectively (also see Ref. [91]). Since we considered a 1.5 TeV sLQ for our analysis, we found that the resonant productions are suppressed than the nonresonant processes. The suppression is more in the case of sLQs than in the case of vLQs such as U_1. Hence, we consider only the nonresonant contributions to obtain the indirect limits on the new couplings.

We use publically available packages such as FeynRules [103] to generate the Universal FeynRules Output [104] files. We use MadGraph5 [105] to generate parton-level events from the nonresonant processes. These events are then passed through Pythia6 [107] for showering and hadronisation. We use Delphes v3 [110] to simulate the detector environments. Following what we did in chapter 2, we recast the Dilepton data from Refs. [101, 102] following the χ^2 fitting technique as shown in chapter 2 to obtain the indirect limits on the Yukawa couplings.

3.5 Results

The current LHC data prevent the sLQs to be lighter than about 1.5 TeV. Thus, in order to explain the W-mass anomaly, we consider $M_1 = 1.5$ TeV and $M_3 = 1.525$ TeV. This gives us a slight difference of $\Delta M = M_3 - M_1 \approx 25$ GeV required to explain the anomaly. We perform a parameter scan of the five nonzero couplings in order to obtain the parameter regions that can provide a simultaneous explanation. In addition to this, we also ensure that the parameter regions satisfy the relevant experimental constraints listed in Table 3.1. These parameter regions are shown in green color in Fig 3.3, Fig 3.4, and Fig 3.5. In these figures, the indirect bounds are shown with dot-dashed lines. The blue regions are the ones that can simultaneously explain the anomalies, satisfy the necessary experimental bounds, and are allowed by the LHC's direct and indirect limits. The number of couplings ensures that our model is minimal. The mass scale makes our model testable at the LHC. As one can see the current LHC bounds severely restrict the parameter space of the 1.5 TeV LQs. The LHC data do not allow the LQ mass scale to be smaller than ~ 1.5 TeV. It is evident from Figs. 3.5b and 3.5c that the $\mathscr{C}_9 = -\mathscr{C}_{10}$ global fit implies that both $|y^L_{32}|$ and $|y^L_{22}|$ cannot be large simultaneously; whereas the LHC direct limits on $S_3^{4/3}$ require $|y^L_{32}| \sim |y^L_{22}|$, severely constricting the parameter space. For a lighter LQ mass, the upper limit on $\text{BR}(S_3^{4/3} \to b(s)\mu)$ will be tighter and impossible to satisfy. One could always introduce new large couplings which would reduce the BR of the restrictive modes and reduce the direct limits on the mass scale. But introducing additional couplings makes the model appear less appealing and fine-tuned. One could also consider a heavier LQ which would enhance the allowed parameter regions as heavier LQs are less constrained by the low energy and LHC bounds. However, the trade-off is that they would require large couplings to accommodate the anomalies. We find that if we restrict all the couplings to the perturbative and add no additional couplings, then the upper bound on the LQ mass scale, i.e. the heaviest it can go is about 8 TeV. Our model also points to the exotic signatures the LHC could use to probe for LQs such as $c\tau$, $t\mu$ coming from the cross-generational couplings such as x^R_{23}, x^L_{32}.

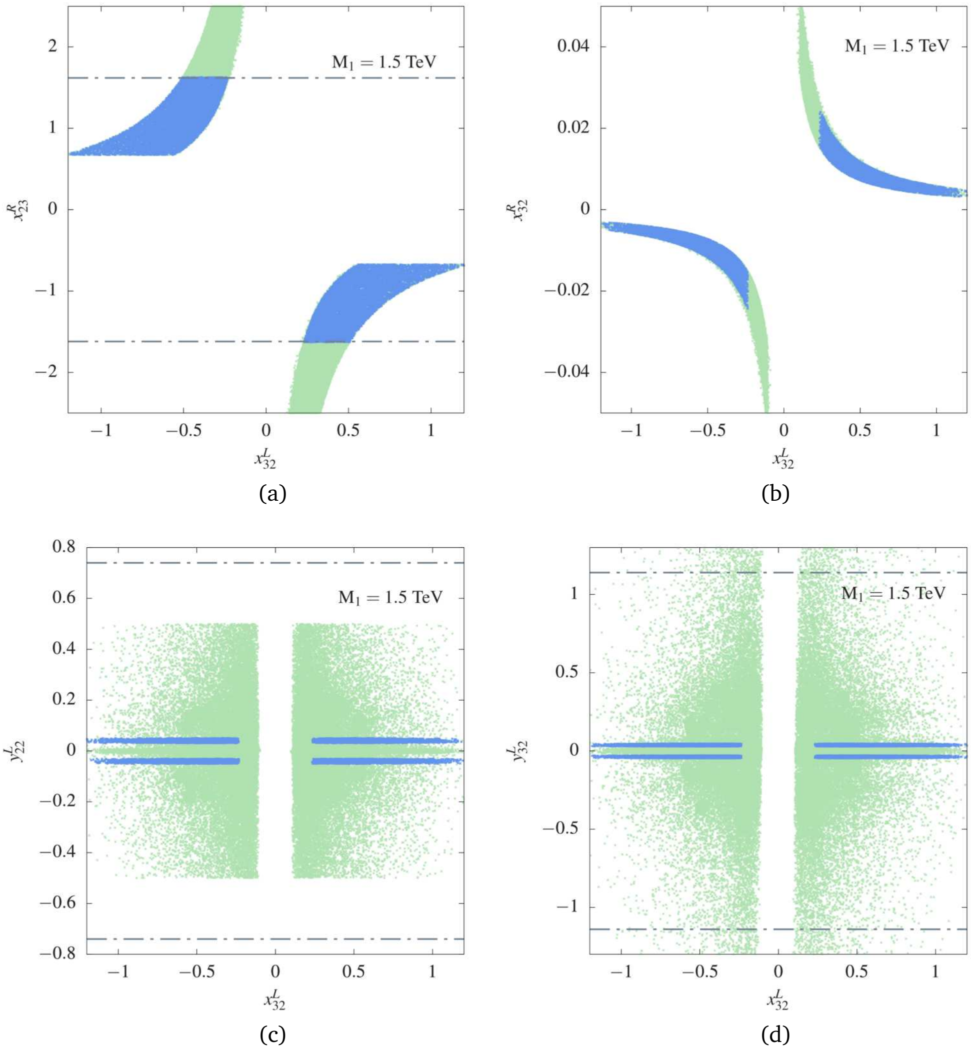

Figure 3.3: The light-green color denotes the regions that simultaneously explain the W-mass, muon $g-2$, $R_{K^{(*)}}$, and $R_{D^{(*)}}$ anomalies without violating the limits shown in Table 3.1. The blue color denotes the regions that explain the anomalies simultaneously and also is allowed by the LHC's direct and indirect searches. The dot-dashed lines described the bounds coming from the LHC's indirect limits—recasting the high-p_T dilepton data. These plots are self-explanatory.

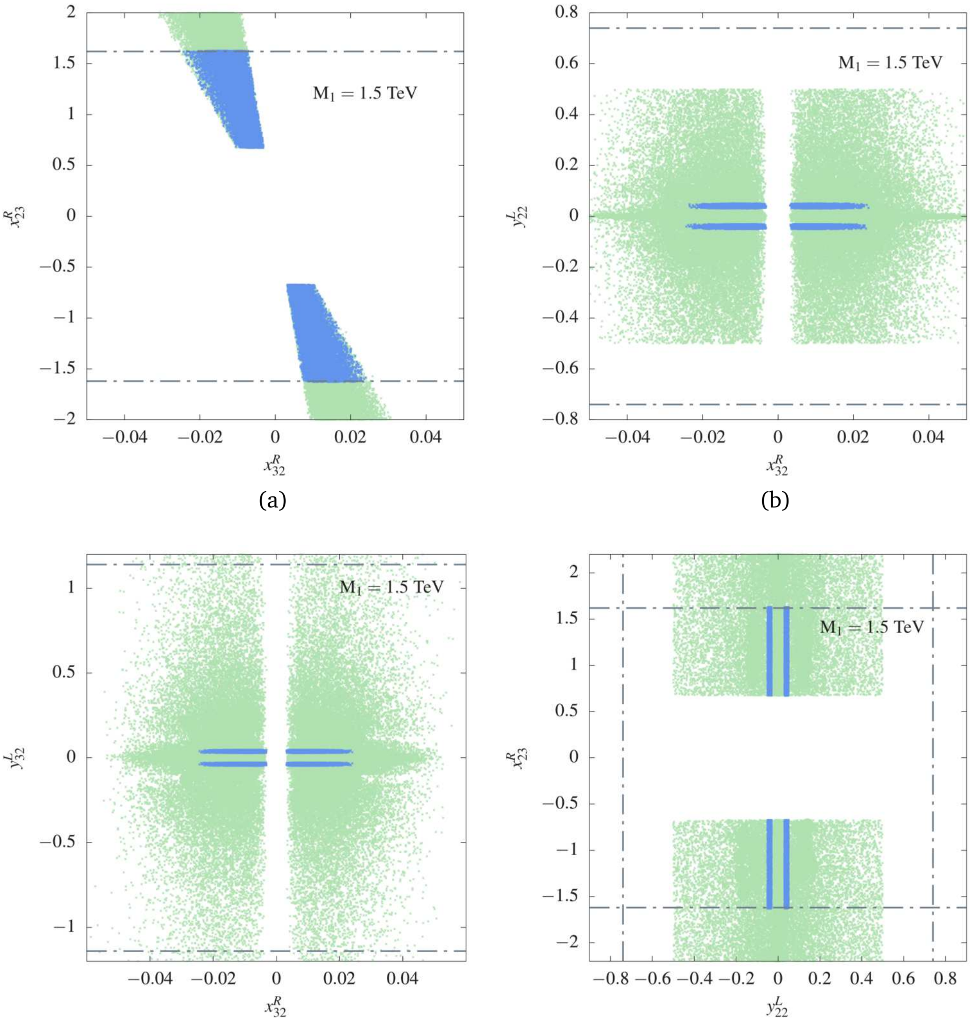

Figure 3.4: The description of the colored regions and the dashed lines is identical to Fig. 3.3.

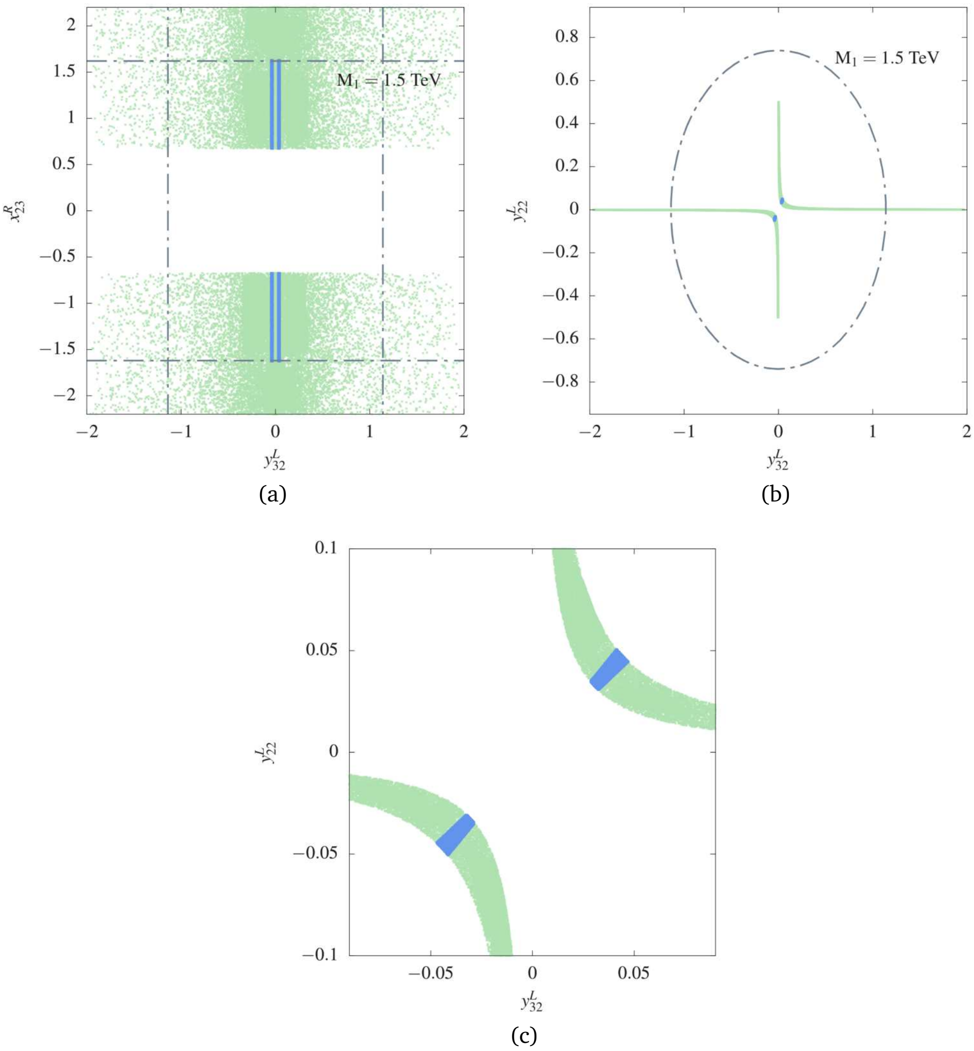

Figure 3.5: Here, Fig. 3.5c is the same as Fig. 3.5b with higher magnification. Rest of the description is same as Fig. 3.3.

Chapter

4

Status update on the B anomalies

The recent experiments at the LHCb have updated the measurements of the $R_{K^{(*)}}$ and $R_{D^{(*)}}$ observables. The $R_{K^{(*)}}$ numbers are as follows [251, 252],

$$\mathrm{low}-\mathrm{q}^2 \left\{ \begin{array}{ll} R_K & = 0.994^{+0.090}_{-0.082}\,(\mathrm{stat})^{+0.029}_{-0.027}\,(\mathrm{syst}), \\ R_{K^*} & = 0.927^{+0.093}_{-0.087}\,(\mathrm{stat})^{+0.036}_{-0.035}\,(\mathrm{syst}), \end{array} \right\}, \tag{4.1}$$

$$\mathrm{central}-\mathrm{q}^2 \left\{ \begin{array}{ll} R_K & = 0.949^{+0.042}_{-0.041}(\mathrm{stat})^{+0.022}_{-0.022}(\mathrm{syst}), \\ R_{K^*} & = 1.027^{+0.072}_{-0.068}(\mathrm{stat})^{+0.027}_{-0.026}(\mathrm{syst}), \end{array} \right\}. \tag{4.2}$$

These measurements are compatible with the SM predictions. In other words, the anomalies in the $R_{K^{(*)}}$ have vanished and their latest values should be treated as another bound on the relevant BSM models. Recent experiments have also updated the values of the $R_{D^{(*)}}$ [253]. The latest values stand as,

$$\left\{ \begin{array}{ll} R_{D^*} & = 0.284 \pm 0.013, \\ R_D & = 0.356 \pm 0.029 \end{array} \right\}. \tag{4.3}$$

The R_{D^*} and R_D values exceed the SM predictions by 2.0σ and 2.2σ, respectively. However, the combined $R_{D^{(*)}}$ still has a deviation of 3.3σ from the SM predicted value.

The change in the combined $R_{D^{(*)}}$ anomaly is not drastic, the tension between the experimental measurements and the SM values has decreased slightly. Hence, our analysis on the $R_{D^{(*)}}$ scenarios in chapter 2 are still valid—the LHC limits (the focus of our study) do not change but the relevant parameter spaces open up. For example, in Fig. 4.1, we show the updated favoured regions in some viable $R_{D^{(*)}}$ scenarios. Fig. 4.1a indicates that in Scenario RD1B, the high-p_T $\tau\tau$ limits still rule

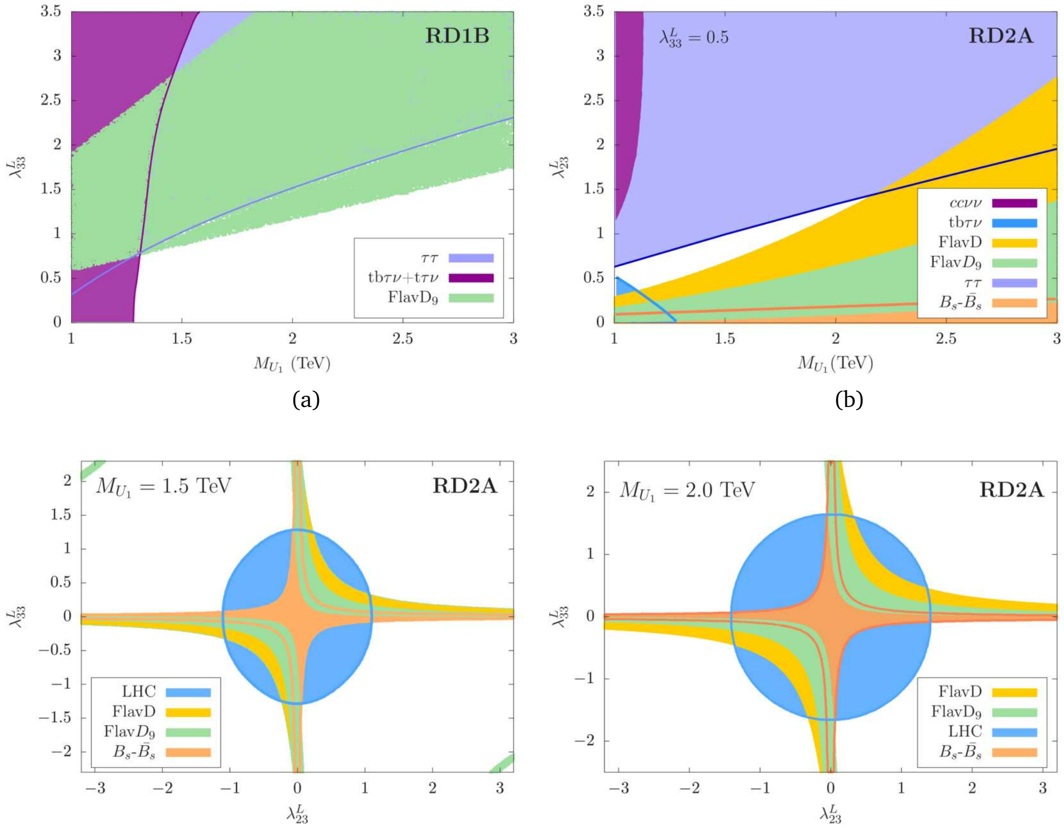

(a) (b)

(c) (d)

Figure 4.1: We show the updated figures for the $R_{D^{(*)}}$ motivated scenarios.

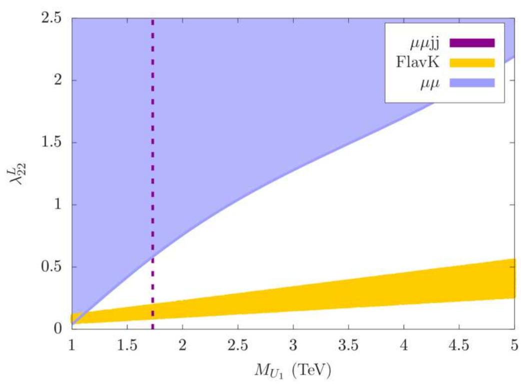

Figure 4.2: We show the updated flavour regions for the recent experimental update of the $R_{K^{(*)}}$ observables.

out most of the favoured region but the narrow strip that was allowed in Fig. 2.8b widens a little. (Scenario RD1A remains completely ruled out.) In the two-coupling scenarios, Scenario RD2A and Scenario RD2B, the changes in the flavour-favoured regions are minimal (see Figs. 4.1c and 4.1d).

However, with the $R_{K^{(*)}}$ anomalies disappearing, the immediate motivation behind the $R_{K^{(*)}}$ scenarios vanishes. Nevertheless, in the scenarios where the coupling(s) needed to address the anomalies were small or consistent with zero (see Figs. 2.10 and 2.11), the regions consistent with the low energy bounds (including the latest $R_{K^{(*)}}$) would not change drastically but contract towards the x axis. Hence, our conclusions will not be affected. Among the exceptions, we show the updated plot for Scenario RK1A in Fig. 4.2. We see that the FlavK region has come down (the B_s-$\bar{B}_s$ mixing data prevent it become zero). To obtain this, we have used the updated global fit for the scenarios satisfying $\mathscr{C}_9^{U_1} = -\mathscr{C}_{10}^{U_1}$ from Ref [254]. The corresponding two-coupling scenario, Scenario RK2A shows similar behaviour.

In Figs. 4.3, 4.4 and 4.5, we show the updated plots for the singlet-triplet scalar model described in chapter 3. The changes are minor and we observe that the blue-coloured regions (that explain the anomalies and survive the low-energy experimental and LHC bounds) decrease slightly. This implies that the updated measurements have reduced the scope for such a construction with 1.5 TeV LQs, although it still remains a valid and testable (and hence interesting) possibility to address the existing anomalies.

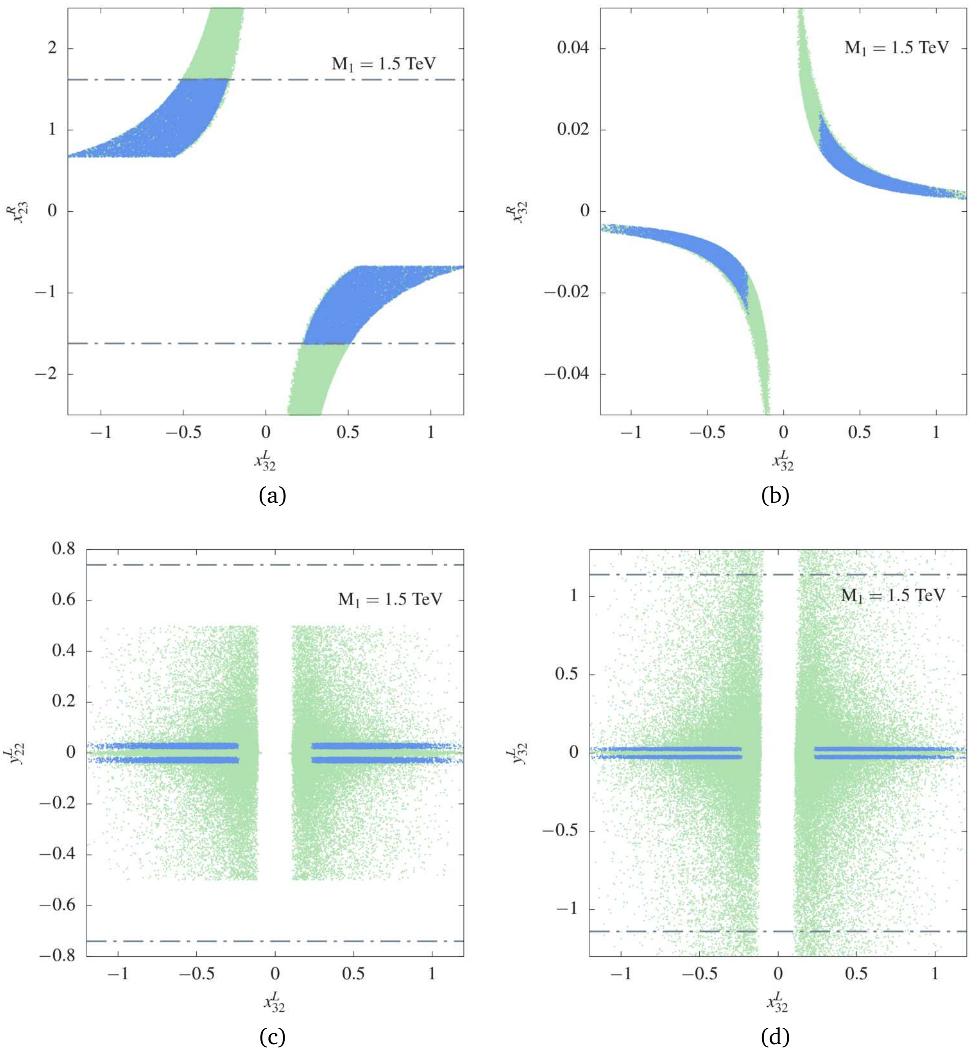

Figure 4.3: The light-green colour denotes the regions that simultaneously explain the W-mass, muon $g-2$, $R_{K^{(*)}}$, and $R_{D^{(*)}}$ anomalies without violating the limits shown in Table 3.1. The blue colour denotes the regions that explain the anomalies simultaneously and also is allowed by the LHC's direct and indirect searches. The dot-dashed lines described the bounds coming from the LHC's indirect limits—recasting the high-p_T dilepton data. These plots are self-explanatory.

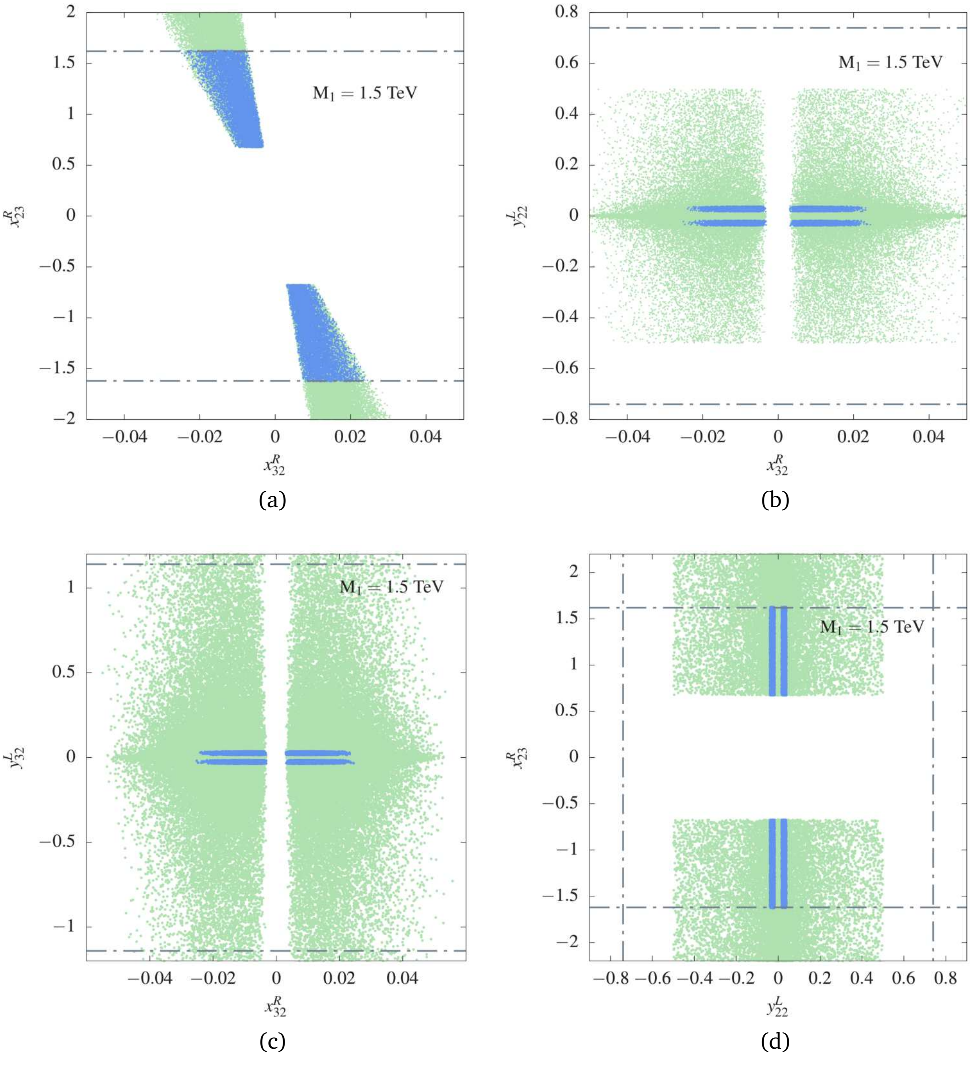

Figure 4.4: The description of the colored regions is identical to Fig. 4.3

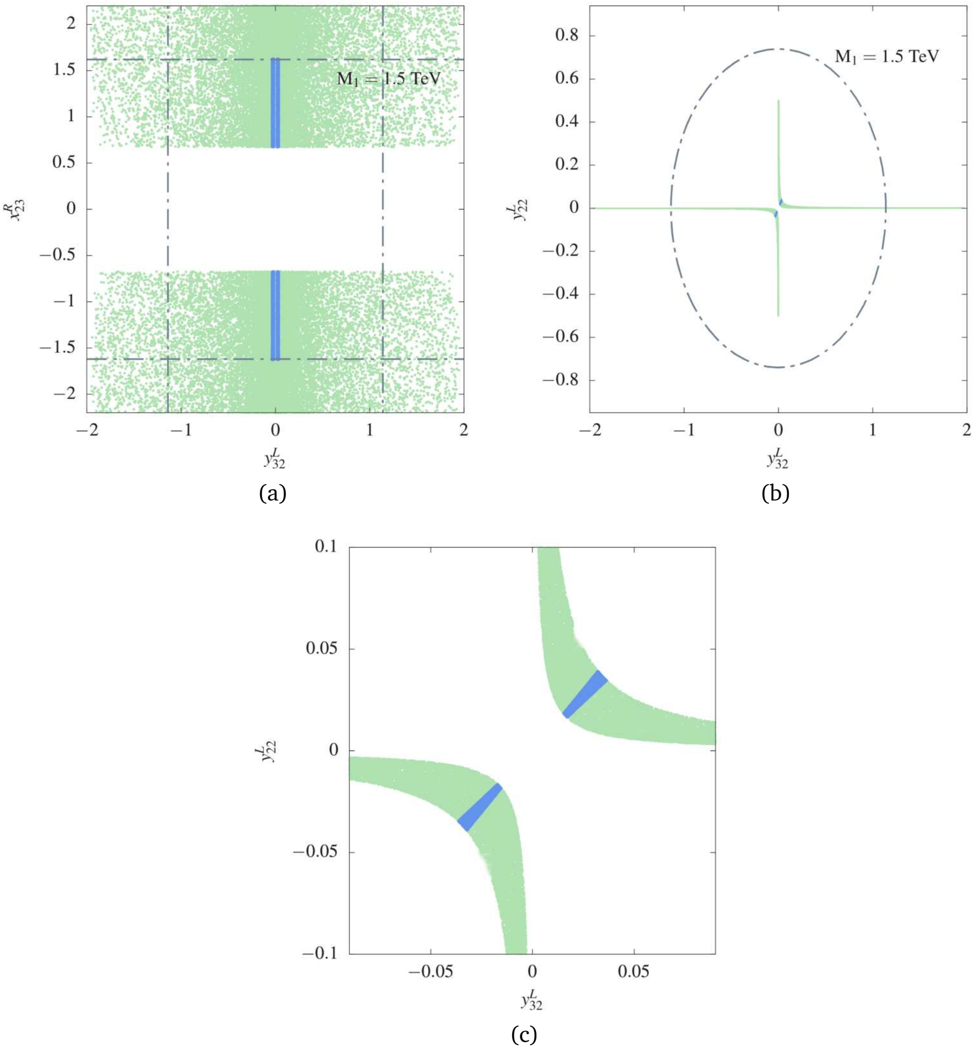

Figure 4.5: The description of the colored regions is same as Fig. 4.3

Part II

Prospects at the HL-LHC

Chapter

5

Searching for leptoquarks with boosted top quarks and high-p_T leptons

The LHC has been actively looking for LQs for a while now. In Chapter 2, we discussed the current searches for LQs in various final states [246, 248, 255–257] and listed the bounds on them. Here, we discuss the discovery prospects of LQs in the future run of the LHC, namely the High Luminosity LHC (HL-LHC). We investigate the prospects of all possible scalar and vector LQs decaying to top quarks and charged leptons. TeV-scale LQs decaying to a top quark and a charged lepton give rise to an exotic and interesting resonant system of a boosted top quark and a high-p_T lepton. In most prospect studies, one generally focuses on the pair production of LQs. However, the pair production mode is good for producing only low-mass LQs; as the masses go up, its contribution falls down rapidly due to phase-space suppression. Hence, we consider the contributions from model-dependent single production mode as well. The single production contribution scales as λ^2 (LQ-q-ℓ coupling). So for $\mathcal{O}(1)$ or larger couplings, the single production contribution becomes significant. We show that if one systematically combines the pair and single production events [64, 98–100], then one could significantly enhance the discovery/exclusion prospects of the LQs at the HL-LHC.

5.1 Scalar leptoquarks (sLQs)

We look at scalar Leptoquarks (sLQs) that decay to a top quark and a charged lepton ℓ. Below, we list the possible sLQs with charge-1/3, 2/3, and 5/3 (Ref. [9, 10, 76, 77]).

$S_1 = (\bar{\mathbf{3}}, \mathbf{1}, 1/3)$: The interaction Lagrangian of the sLQ S_1 which we encountered in Eq. (3.1) in chapter 3 can be written as follows:

$$\mathscr{L} \supset y^{LL}_{1\,ij} \bar{Q}^{C\,i}_L S_1 i\sigma^2 L^j_L + y^{RR}_{1\,ij} \bar{u}^{C\,i}_R S_1 \ell^j_R + \text{H.c.}, \tag{5.1}$$

where u_R and ℓ_R are a right-handed up-type quark and a charged lepton, respectively and Q_L and L_L are the left-handed quark and lepton doublets, respectively. The superscript C denotes charge conjugation, and σ^2 is the second Pauli matrix. The generation indices are denoted by $i, j = \{1,\ 2,\ 3\}$. We suppress the colour indices. The terms relevant to our analysis are given as (Following the notations of Ref. [10])

$$\mathscr{L} \supset y^{LL}_{1\,3j} \left(-\bar{b}^C_L \nu_L + \bar{t}^C_L \ell_L\right) S_1 + y^{RR}_{1\,3j}\ \bar{t}^C_R \ell_R S_1 + \text{H.c.} \tag{5.2}$$

We write the neutrinos as ν as the LHC is flavour blind.

$S_3 = (\bar{\mathbf{3}}, \mathbf{3}, 1/3)$: We show the interaction Lagrangian of a weak triplet sLQ S_3.

$$\mathscr{L} \supset y^{LL}_{3\,ij} \bar{Q}^{C\,i,a}_L \epsilon^{ab} (\ell^k S^k_3)^{bc} L^{j,c}_L + \text{H.c.} \tag{5.3}$$

Here, we denote the SU(2) indices by $a, b, c = \{1,\ 2\}$. We consider the terms relevant to our analysis.

$$\mathscr{L} \supset -y^{LL}_{3\,3j} \left[\left(\bar{b}^C_L \nu_L + \bar{t}^C_L \ell_L\right) S^{1/3}_3 + \sqrt{2}\left(\bar{b}^C_L \ell_L S^{4/3}_3 - \bar{t}^C_L \nu_L S^{-2/3}_3\right)\right] + \text{H.c.}$$

$R_2 = (\mathbf{3}, \mathbf{2}, 7/6)$: The Lagrangian terms for the R_2 sLQ is given as,

$$\mathscr{L} \supset -y^{RL}_{2\,ij} \bar{u}^i_R R^a_2 \epsilon^{ab} L^{j,b}_L + y^{LR}_{2\,ji} \bar{e}^j_R R^{a\,*}_2 Q^{i,a}_L + \text{h.c.}$$

On expanding we get,

$$\mathscr{L} \supset -y^{RL}_{2\,3j}\ \bar{t}_R \ell_L R^{5/3}_2 + y^{RL}_{2\,3j}\ \bar{t}_R \nu_L R^{2/3}_2 + y^{LR}_{2\,j3}\ \bar{\ell}_R t_L R^{5/3\,*}_2 + y^{LR}_{2\,j3}\ \bar{\ell}_R b_L R^{2/3\,*}_2 + \text{H.c.}$$

5.2 Vector leptoquarks (vLQs)

Similarly, we look at the vLQs that can decay to a top quark and a charged lepton.

$\underline{\tilde{U}_1 = (\mathbf{3},\mathbf{1},5/3)}$: The vLQ $\tilde{U}_1$ is charged 5/3. Thus, it couples only with the right-handed leptons.

$$\mathscr{L} \supset \tilde{x}_{1\ ij}^{RR} \bar{u}_R^i \gamma^\mu \tilde{U}_{1,\mu} \ell_R^j + \text{H.c.} \tag{5.4}$$

For our analysis, we have

$$\mathscr{L} \supset \tilde{x}_{1\ 3j}^{RR}\ \bar{t}_R \left(\gamma \cdot \tilde{U}_1\right) \ell_R + \text{H.c.} \tag{5.5}$$

$\underline{U_1 = (\mathbf{3},\mathbf{1},2/3)}$: As seen in Eq. (2.12), the required terms for the charge-2/3 U_1 vLQ is given as,

$$\mathscr{L} \supset x_{1\ ij}^{LL}\ \bar{Q}_L^i \gamma^\mu U_{1,\mu} L_L^j + x_{1\ ij}^{RR}\ \bar{d}_R^i \gamma^\mu U_{1,\mu} \ell_R^j + \text{H.c.} \tag{5.6}$$

Expanding it we get,

$$\mathscr{L} \supset x_{1\ 3j}^{LL} \left\{ \bar{t}_L \left(\gamma \cdot U_1\right) \nu_L + \bar{b}_L \left(\gamma \cdot U_1\right) \ell_L \right\} + x_{1\ 33}^{Rj}\ \bar{b}_R \left(\gamma \cdot U_1\right) \ell_R + \text{H.c.} \tag{5.7}$$

$\underline{V_2 = (\bar{\mathbf{3}},\mathbf{2},5/6)}$: For V_2, the Lagrangian is as follows:

$$\mathscr{L} \supset x_{2\ ij}^{RL}\ \bar{d}_R^{Ci} \gamma^\mu V_{2,\mu}^a \epsilon^{ab} L_L^{jb} + x_{2\ ij}^{LR}\ \bar{Q}_L^{Ci,a} \gamma^\mu \epsilon^{ab} V_{2,\mu}^b \ell_R^j + \text{H.c.} \tag{5.8}$$

Expanding the Lagrangian and writing the required terms, we get,

$$\mathscr{L} \supset -x_{2\ 3j}^{RL} \bar{b}_R^C \left\{ \left(\gamma \cdot V_2^{1/3}\right) \nu_L - \left(\gamma \cdot V_2^{4/3}\right) \ell_L \right\} + x_{2\ 3j}^{LR} \left\{ \bar{t}_L^C \left(\gamma \cdot V_2^{1/3}\right) - \bar{b}_L^C \left(\gamma \cdot V_2^{4/3}\right) \right\} \ell_R + \text{H.c.} \tag{5.9}$$

$\underline{\tilde{V}_2 = (\bar{\mathbf{3}},\mathbf{2},-1/6)}$: For $\tilde{V}_2$, the Lagrangian is given as,

$$\mathscr{L} \supset \tilde{x}_{2\ ij}^{RL} \bar{u}_R^{C\,i} \gamma^\mu \tilde{V}_{2,\mu}^b \epsilon^{ab} L_L^{j,a} + \text{H.c.} \tag{5.10}$$

The terms with the vLQs interacting with top quarks and leptons are given as,

$$\mathscr{L} \supset \tilde{x}_{2\ 3j}^{RL} \bar{t}_R^C \left\{ -\left(\gamma \cdot \tilde{V}_2^{1/3}\right) \ell_L + \left(\gamma \cdot \tilde{V}_2^{-2/3}\right) \nu_L \right\} + \text{H.c.} \tag{5.11}$$

$\underline{U_3 = (\mathbf{3},\mathbf{3},2/3):}$ The necessary interaction terms for the weak triplet U_3 are given as,

$$\mathcal{L} \supset x_{3\ ij}^{LL} \bar{Q}_L^{i,a} \gamma^\mu \left(\sigma^k U_{3,\mu}^k\right)^{ab} L_L^{j,b} + \text{H.c.} \tag{5.12}$$

The terms for the third-generation fermions can be written explicitly as,

$$\mathcal{L} \supset x_{3\ 3j}^{LL} \Big\{ -\bar{b}_L \left(\gamma \cdot U_3^{2/3}\right) \ell_L + \bar{t}_L \left(\gamma \cdot U_3^{2/3}\right) \nu_L + \sqrt{2}\, \bar{b}_L \left(\gamma \cdot U_3^{-1/3}\right) \nu_L + \sqrt{2}\, \bar{t}_L \left(\gamma \cdot U_3^{5/3}\right) \ell_L \Big\} + \text{H.c.} \tag{5.13}$$

As mentioned in chapter 2, the Lagrangian of the vLQs contain an additional gauge coupling, κ [10].

$$\mathcal{L} \supset -\frac{1}{2} \chi_{\mu\nu}^\dagger \chi^{\mu\nu} + M_\chi^2\ \chi_\mu^\dagger \chi^\mu - i g_s \kappa\ \chi_\mu^\dagger T^a \chi_\nu\ G^{a\mu\nu}, \tag{5.14}$$

where $\chi_{\mu\nu}$ is the field-strength tensor of generic vLQ, χ. The cross section of pair and single production processes get contribution from κ. We consider two benchmark values, $\kappa = 0$ and $\kappa = 1$.

5.3 Simplified phenomenological models

For our analysis, we propose some simplified Lagrangians that are easier to implement in collider searches:

$$
\begin{aligned}
\mathcal{L} &\supset \lambda_\ell \Big\{ \sqrt{\eta_L}\, \bar{t}^C_L \ell_L + \sqrt{\eta_R}\, \bar{t}^C_R \ell_R \Big\} \phi_1 + \lambda_\nu \bar{b}^C_L \nu_L \phi_1, \\
& +\text{H.c.}, && (5.15) \\
\mathcal{L} &\supset \hat{\lambda}_\ell \Big\{ \sqrt{\eta_L}\, \bar{b}_R \ell_L + \sqrt{\eta_R}\, \bar{b}_L \ell_R \Big\} \phi_2 + \hat{\lambda}_\nu \bar{t}_R \nu_L \phi_2 \\
& +\text{H.c.}, && (5.16) \\
\mathcal{L} &\supset \tilde{\lambda}_\ell \Big\{ \sqrt{\eta_L}\, \bar{t}_R \ell_L + \sqrt{\eta_R} \bar{t}_L \ell_R \Big\} \phi_5 + \text{H.c.}, && (5.17) \\
\mathcal{L} &\supset \Lambda_\ell \Big\{ \sqrt{\eta_R}\, \bar{t}^C_L (\gamma \cdot \chi_1) \ell_R + \sqrt{\eta_L}\, \bar{t}^C_R (\gamma \cdot \chi_1) \ell_L \Big\} \\
& + \Lambda_\nu\, \bar{b}^c_R (\gamma \cdot \chi_1)\, \nu_L + \text{H.c.}, && (5.18) \\
\mathcal{L} &\supset \hat{\Lambda}_\ell \Big\{ \epsilon_R \sqrt{\eta_R}\, \bar{b}_R (\gamma \cdot \chi_2) \ell_R + \sqrt{\eta_L}\, \bar{b}_L (\gamma \cdot \chi_2) \ell_L \Big\} \\
& + \hat{\Lambda}_\nu\, \bar{t}_L (\gamma \cdot \chi_2)\, \nu_L + \text{H.c.}, && (5.19) \\
\mathcal{L} &\supset \tilde{\Lambda}_\ell \Big\{ \sqrt{\eta_R}\, \bar{t}_R (\gamma \cdot \chi_5) \ell_R + \sqrt{\eta_L}\, \bar{t}_L (\gamma \cdot \chi_5) \ell_L \Big\} \\
& + \text{H.c.} && (5.20)
\end{aligned}
$$

Here, a charged 1/3, 2/3 and 5/3 sLQ is denoted as ϕ_1, ϕ_2 and ϕ_5 and similar charged vLQs are denoted as χ_1, χ_2 and χ_5 respectively. Here, η_L and $\eta_R = 1 - \eta_L$ are the charged lepton chirality fractions [64, 98]; thus, it tells us the fraction of leptons coming from LQ decays that left-handed and right-handed. In Eq. (5.19), ϵ_R is a parameter that can be used to obtain a relative sign between the left-handed and the right-handed terms. We consider real couplings for simplicity. Now, we introduce some benchmark scenarios based on the chirality of the leptons. The goal is to show that, in each scenario, one can map our simplified LQ models to the relevant LQ models within the Buchmüller-Rückl-Wyler classifications.

- **Left-handed couplings with the same sign (LCSS:)** For the scalar case, in Eq. (5.15), we set $\lambda_\ell = \lambda_\nu$ and $\eta_R = 0$. The ϕ_1 LQ couples to the left-handed ℓs. In this scenario, the ϕ_1 can be mapped to the sLQ $S_3^{1/3}$ and the coupling corresponds to $-y^{LL}_{3\,3j}$. The sLQ ϕ_1 decays to t-ℓ and b-ν with 50% branching ratios (BR). In case of vLQs, we set $\hat{\Lambda}_\ell = \hat{\Lambda}_\nu$ and $\eta_L = 1$ in Eq. (5.19). Here, χ_2 behaves as a U_1 vLQ with $\hat{\Lambda}_\ell = \hat{\Lambda}_\nu = x^{LL}_{13j}$. χ_2 decays to tν or bℓ with equal BR.

- **Left-handed couplings with opposite sign (LCOS):** This scenario is similar to above, except the couplings for the sLQs are set as $\lambda_\ell = -\lambda_\nu$ and in the case of vLQs, we consider $\hat{\Lambda}_\ell = -\hat{\Lambda}_\nu$. Here the ϕ_1 corresponds to the sLQ S_1 and the couplings are given as $y^{LL}_{1\,3j}$. Similar to the previous scenario, ϕ_1 decays to t-ℓ and b-ν with 50% BR. In this scenario, the vLQ χ_2

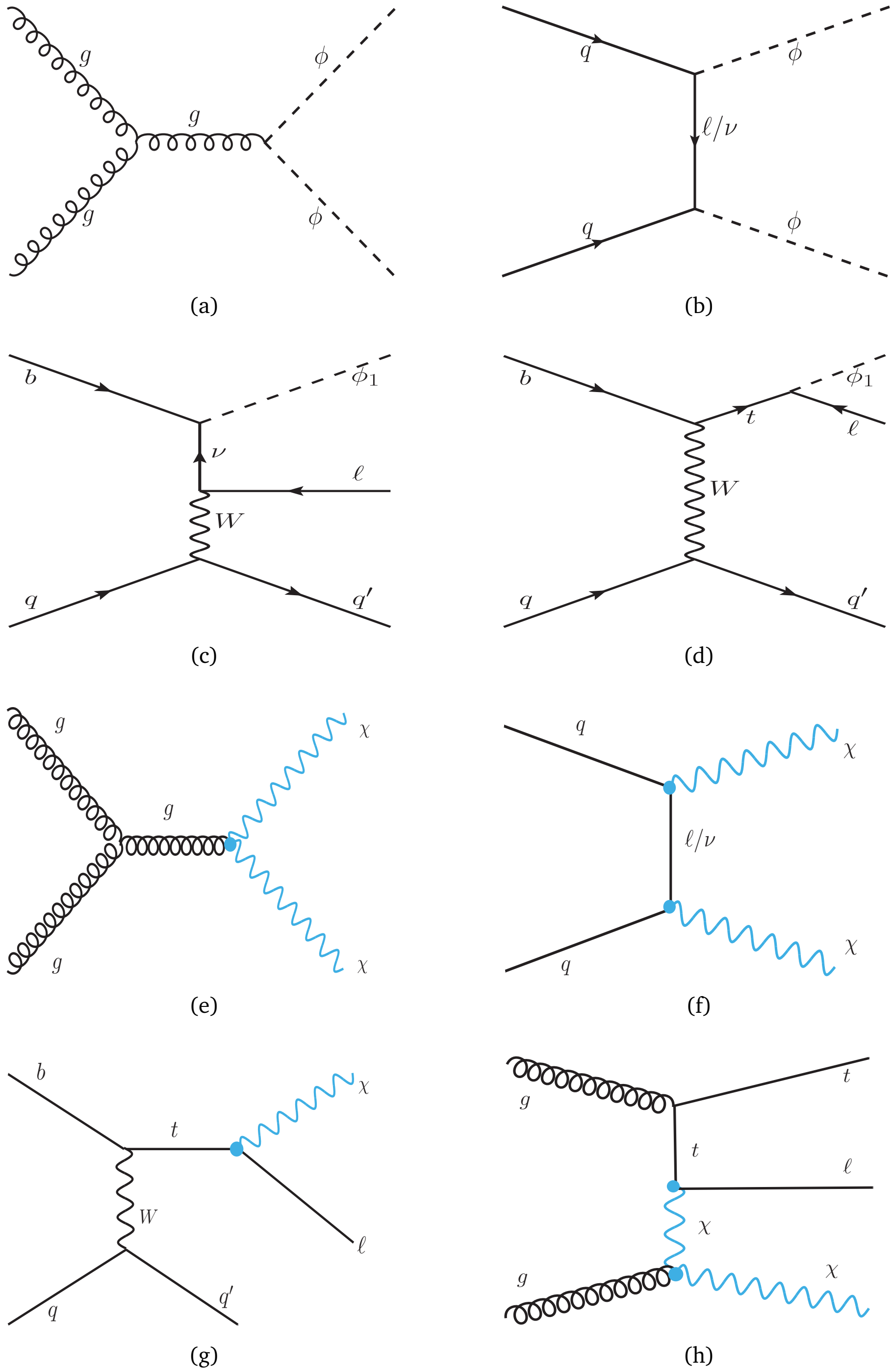

Figure 5.1: We show the various production processes of LQ at the LHC. (a) and (b) ((e) and (f)) show the pair production of the sLQs (vLQs). Similarly, (c) and (d) ((g) and (h)) show the single production of the sLQs (vLQs).

corresponds to $U_3^{2/3}$ and the corresponding coupling being $-x^{LL}_{33j}$. The branching ratio of χ_2 is the same as in the previous scenario.

- **Left Coupling (LC):** In this scenario, we set η_L in Eq. (5.17) to one. We look at the LQs exclusively couplings to left-handed leptons. Here, ϕ_2 maps to $\left(S_3^{-2/3}\right)^\dagger$ and $\hat{\lambda}_\nu$ maps to $\left(\sqrt{2}y^{LL}_{33j}\right)^*$. The sLQ ϕ_2 can also map to $R_2^{2/3}$ and $\hat{\lambda}_\nu$ maps to the coupling y^{RL}_{23j}. In both cases, ϕ_2 decays only to top and ν. In Eq. (5.17), the sLQ ϕ_5 maps to $R_2^{5/3}$ and the simplified coupling $\tilde{\lambda}_\ell$ maps to y^{RL}_{23j}. But here they decay to top and τ with 100% BR. In the case of vLQs, we set η_L in Eq. (5.18) and (5.20) to one. The vLQ χ_1 corresponds to $\tilde{V}_2^{1/3}$ and Λ_ℓ corresponds to the actual coupling $\tilde{x}^{RL}_{2\,3j}$. The charge-2/3 vLQ χ_2 maps to $\left(\tilde{V}_2^{-2/3}\right)^\dagger$ and the coupling $\hat{\Lambda}_\nu$ maps to $\left(\tilde{x}^{RL}_{2\,33}\right)^*$. In Eq. (5.20), χ_5 and coupling $\tilde{\Lambda}_\ell$ maps to vLQ $U_3^{5/3}$ and coupling $\sqrt{2}\,x^{LL}_{3\,3j}$, respectively. In this scenario, χ_1 and χ_5 decay to $t\tau$ with 100% BR and χ_2 decays to $t\,\nu$ with similar BR.

- **Right Coupling (RC):** In this scenario, we set $\eta_R = 1$ in Eq. 5.15 and 5.17 for the simplified sLQ models and in Eq. 5.18 and 5.20 for the vLQs. Here, the LQs exclusively couple to right-handed leptons as they have no weak charge. In the case of sLQs, ϕ_1 and ϕ_5 correspond to the standard LQs S_1 and $R_2^{5/3}$ respectively, and the simplified couplings—λ_ℓ and $\tilde{\lambda}_\ell$ map to $y^{RR}_{1\,3j}$ and $y^{RR}_{2\,3j}$ respectively. Both these sLQs decay to the $t\ell$ mode with 100% BR. The vLQs χ_1 and χ_5 map to $V_2^{1/3}$ and $\tilde{U}_1$ respectively. The simplified couplings Λ_ℓ and $\tilde{\Lambda}_\ell$ map to the actual coupling as $x^{LR}_{2\,3j}$ and $\tilde{x}^{RR}_{1\,3j}$. The decay mode and the BR are similar to the sLQs.

- **Right (lepton) left (neutrino) couplings with the same sign (RLCSS):** Here, we set $\hat{\lambda}_\ell = \hat{\lambda}_\nu$ and $\sqrt{\eta_R} = 1$ in Eq. (5.16). The ϕ_2 maps to $R_2^{2/3}$ and the coupling relation maps as $y^{RL}_{2\,33} = \left(y^{LR}_{2\,33}\right)^*$. Here, ϕ_2 decays to $t\,\nu$ and $b\ell$ with a branching ratio of 50%. Similarly, in the case of vLQs we consider $\sqrt{\eta_R} = 1$ and $\Lambda_\ell = \Lambda_\nu$. The generic vLQ χ_1 corresponds to the standard LQ $V_2^{1/3}$ and the coupling relation map as $x^{LR}_{2\,3j} = x^{RL}_{2\,3j}$. The decay modes of χ_1 are $t\ell$ and $b\,\nu$ with 50% BR.

- **Right (lepton) left (neutrino) couplings with the opposite sign (RLCOS):** This scenario is similar to the previous one, except that here the coupling relation is $\hat{\lambda}_\ell = -\hat{\lambda}_\nu$ in case of sLQ and $\Lambda_\ell = -\Lambda_\nu$ in case of vLQ. The generic LQs ϕ_2 and χ_1 map to the similar standard scalar and vector LQ from the previous scenario. Similar to the previous scenario, ϕ_2 decays to $t\,\nu$ and $b\ell$ with 50% BR and χ_1 decays to $t\ell$ and $b\,\nu$ with similar BR.

We summarise the mapping of the simplified Lagrangians to the standard LQ models in Table 5.1 with various benchmark scenarios. In Fig. 5.2, we show the parton-level cross sections of different production processes of sLQs. The single production processes are computed for

	Benchmark scenario	Possible charge(s)	Simplified models [Eqs. (5.15) – (5.20)]			LQ models [Eqs. (5.2) – (5.13)]		Decay mode(s)	Branching ratios(s) $\{\beta, 1-\beta\}$
			Type of LQ	Nonzero couplings equal to λ/Λ	Charged lepton chirality fraction	Type of LQ	Nonzero coupling equal to λ/Λ		
Scalar	LC	2/3	ϕ_2	$\hat{\lambda}_\nu$	—	$\left\{\left(S_3^{-2/3}\right)^\dagger, R_2^{2/3}\right\}$	$\left\{\sqrt{2}\left(y^{LL}_{3\,33}\right)^*, y^{RL}_{2\,33}\right\}$	$t\,\nu$	$\{100\%, 0\}$
		5/3	ϕ_5	$\tilde{\lambda}_\ell$	$\eta_L = 1$	$R_2^{5/3}$	$-y^{RL}_{2\,33}$	$t\ell$	
	LCSS LCOS	1/3	ϕ_1	$\lambda_\ell = \lambda_\nu$ $\lambda_\ell = -\lambda_\nu$	$\eta_L = 1$	$S_3^{1/3}$ S_1	$-y^{LL}_{3\,33}$ $y^{LL}_{1\,33}$	$\{t\ell,\, b\,\nu\}$	$\{50\%,\, 50\%\}$
	RC	1/3	ϕ_1	λ_ℓ	$\eta_R = 1$	S_1	$y^{RR}_{1\,33}$	$t\ell$	$\{100\%, 0\}$
		5/3	ϕ_5	$\tilde{\lambda}_\ell$	$\eta_R = 1$	$R_2^{5/3}$	$y^{LR}_{2\,33}$	$t\ell$	
	RLCSS* RLCOS*	2/3	ϕ_2	$\hat{\lambda}_\ell = \hat{\lambda}_\nu$ $\hat{\lambda}_\ell = -\hat{\lambda}_\nu$	$\eta_R = 1$	$R_2^{2/3}$ $R_2^{2/3}$	$y^{RL}_{2\,33} = \left(y^{LR}_{2\,33}\right)^*$ $y^{RL}_{2\,33} = -\left(y^{LR}_{2\,33}\right)^*$	$\{t\,\nu,\, b\ell\}$	$\{50\%,\, 50\%\}$
Vector	LC	1/3	χ_1	Λ_ℓ	$\eta_L = 1$	$\tilde{V}_2^{1/3}$	$\tilde{x}^{RL}_{2\,33}$	$t\ell$	$\{100\%, 0\}$
		2/3	χ_2	$\hat{\Lambda}_\nu$	—	$\left(\tilde{V}_2^{-2/3}\right)^\dagger$	$\left(\tilde{x}^{RL}_{2\,33}\right)^*$	$t\,\nu$	
		5/3	χ_5	$\tilde{\Lambda}_\ell$	$\eta_L = 1$	$U_3^{5/3}$	$\sqrt{2}\, x^{LL}_{3\,33}$	$t\ell$	
	LCSS* LCOS	2/3	χ_2	$\hat{\Lambda}_\ell = \hat{\Lambda}_\nu$ $\hat{\Lambda}_\ell = -\hat{\Lambda}_\nu$	$\eta_L = 1$	U_1 $U_3^{2/3}$	$x^{LL}_{1\,33}$ $-x^{LL}_{3\,33}$	$\{t\,\nu,\, b\ell\}$	$\{50\%,\, 50\%\}$
	RC	1/3 5/3	χ_1 χ_5	Λ_ℓ $\tilde{\Lambda}_\ell$	$\eta_R = 1$	$V_2^{1/3}$ $\tilde{U}_1$	$x^{LR}_{2\,33}$ $\tilde{x}^{RR}_{1\,33}$	$t\ell$	$\{100\%, 0\}$
	RLCSS* RLCOS*	1/3	χ_1	$\Lambda_\tau = \Lambda_\nu$ $\Lambda_\ell = -\Lambda_\nu$	$\eta_R = 1$	$V_2^{1/3}$ $V_2^{1/3}$	$x^{LR}_{2\,33} = x^{RL}_{2\,33}$ $x^{LR}_{2\,33} = -x^{RL}_{2\,33}$	$\{t\ell,\, b\,\nu\}$	$\{50\%,\, 50\%\}$

Table 5.1: Summary of the benchmark scenarios showing the map between the known sLQ and vLQ models and the simple models.

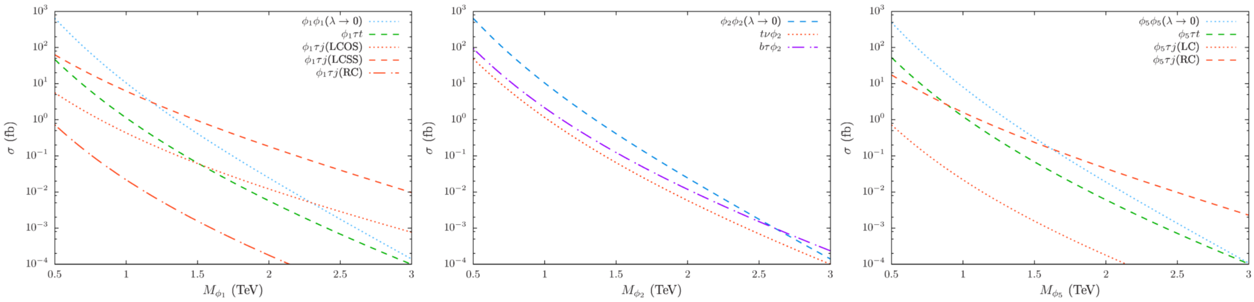

(a) (b) (c)

Figure 5.2: Here, we show the parton-level cross sections of the different production modes of sLQs (ϕ_1, ϕ_2 and ϕ_5) at the 14 TeV LHC as functions of M_{ϕ_n}. We compute the single production processes for a benchmark coupling $\lambda = 1$. We include both the $\phi_1 \tau j$ and $\phi_1 \tau t$ in the single production process. j includes all the light jets and b-jets. We generate these cross sections with a generational level cut on the transverse momentum of the jet, $p_{\mathrm{T}}^{j} > 20$ GeV.

$\lambda/\Lambda = 1$. We point out the role of single production processes at higher masses. With order one λ (or Λ), it is possible for some single production modes to have bigger cross sections than the pair production in the mass range of our interest. The single production process $[pp \to \phi_1 \ell j]$ in the LCOS scenario overcomes the pair production only for $M_\phi > 2.2$ TeV, whereas in the LCSS scenario, it overcomes at a much lesser mass $M_\phi \gtrsim 1$ TeV. This happens because, in the LCOS scenario, the diagrams 5.1c and 5.1d in the single production channel interfere destructively, and in the LCSS scenario, they interfere constructively. However, the cross section in both scenarios is the same for the single production channel $pp \to \phi_1 \ell t$. In the RC scenario, the single production channel $[(pp \to \phi_1 \ell j)]$ is smaller than the pair production process. The cross-section is small because ϕ_1 doesn't couple to a b quark or a left-handed top quark. Thus, the top quark cannot couple with the W boson and can do so only via chirality flipping. A similar situation arises in the case of ϕ_5 in the LC scenario. Here, the ϕ_5 couples exclusively to right-handed tops. Single production cross sections vary as the square of the new coupling λ or Λ. For the RLCOS and RLCSS scenarios, we show a ϕ_2 decaying to $t\nu$ and $b\ell$. From Fig. 5.2c, we can see that the single production channel doesn't overtake the pair production mode till $M_\phi \gtrsim 2.5$ TeV. In the LC scenario, $pp \to \chi_1 \tau j$ overtakes the pair production processes at 2.6 TeV for $\kappa = 1$ [Fig. 5.3g], but the cross section for the similar $\chi_1 \tau t$ process remains lower. In the RC scenario, we find that the $\sigma(pp \to \chi_1 \ell j)$ process is reduced by almost 2 orders of magnitude compared to that in the LC scenario. This happens because in the RC scenario, a χ_1 couples to a right-handed top that comes from another left-handed top generated in the charged-current interaction through a chirality flip. In the case of vLQs, the LCSS and LCOS scenarios are equivalent. The single production cross sections are the same, as there are no interfering diagrams. For χ_2, pair production $pp \to \chi_2 \chi_2$ always dominates over single production $pp \to \chi_2 t \nu$ up to a mass of 3 TeV with $\Lambda = 1$ coupling

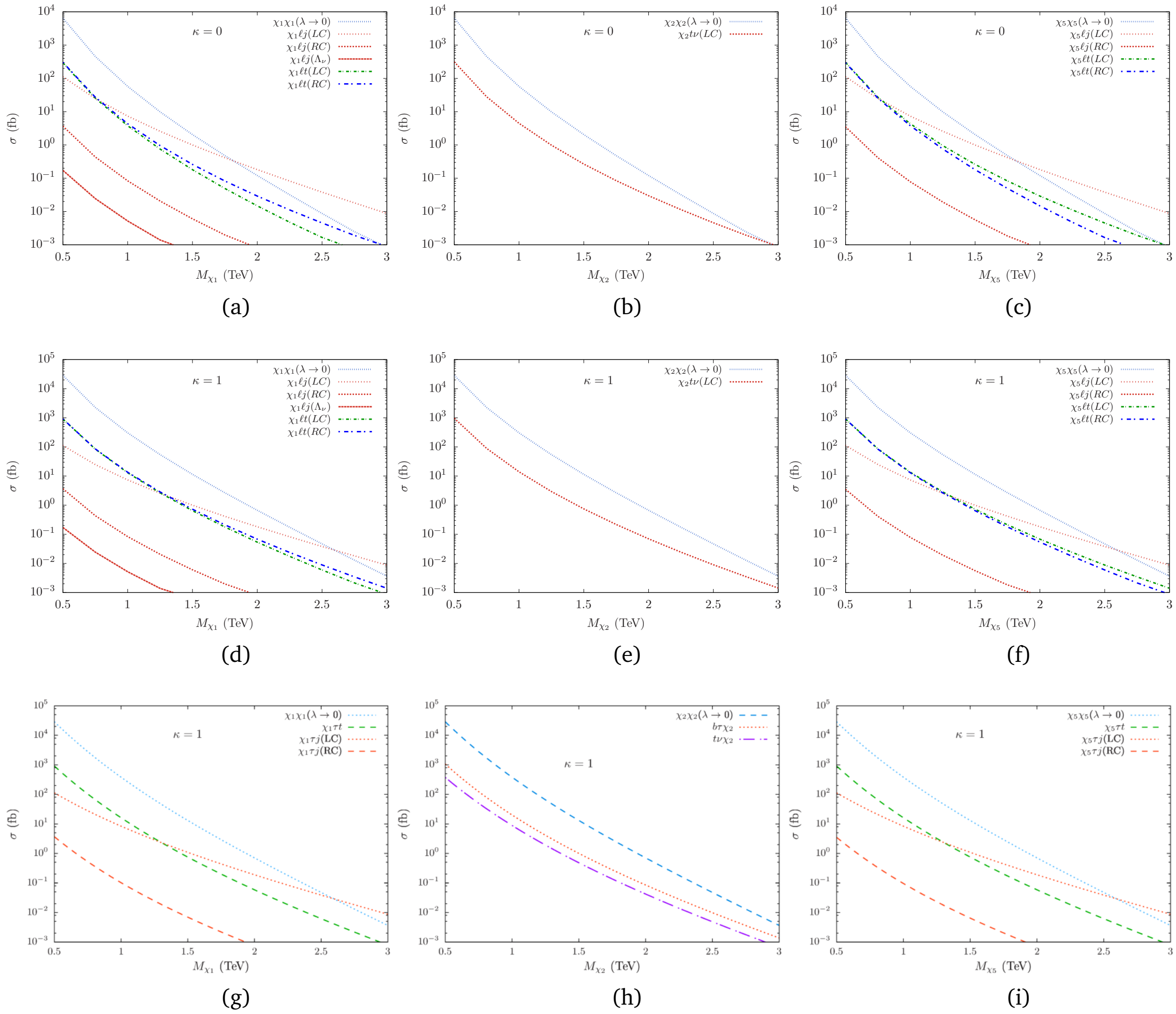

Figure 5.3: In (a), (b), and (c), we show the parton-level cross section of the different production modes of χ_1, χ_2, and χ_5, respectively for $\kappa = 0$ and in (d), (e), and (f), we show the production modes of χ_1, χ_2, and χ_5, respectively for $\kappa = 1$. In these Figures, ℓ denotes light leptons only. However, in Figs.(g), (h), and (i), we show the single production of χ_n along with a τ and a τj. The generation level cut includes a cut on the transverse momentum of the jet, $p_{\mathrm{T}}^{j} > 20$ GeV.

for both $\kappa = 0$ and $\kappa = 1$. In this case, we obtain a tt plus large $\not{E}_T$ signature which was analysed in Ref. [97]. The χ_5 vLQ is similar to the χ_1 and one obtains similar signatures at the colliders.

5.4 LHC phenomenology

We have discussed the publically available relevant computational packages in the previous chapters 2. The UFO model files are generated by encoding the simplified Lagrangians in FeynRules [103]. We generate signal and background events using MadGraph5 [105]. The next-to-leading order (NLO) QCD K-factor of 1.3 [51, 258] is available only for the pair production cross sections of sLQs. We use NNPDF2.3LO [106] parton distribution functions with dynamical renormalization and factorization scales set equal to the mass of the LQs. Showering and hadronization of the generated events are done using Pythia6 [107] and the detector simulation is done via Delphes3 [110].

5.4.1 Production at the LHC

We have discussed the various production modes of LQs in the previous chapters 2 and 3. Here, we consider their resonant modes of production— pair and single production. The pair production channels for the sLQs and vLQs are given as,

$$pp \to \left\{ \begin{array}{lcl} \phi_1\phi_1/\chi_1\chi_1 & \to & (t\ell)(t\ell)/(t\ell)(b\nu)/(b\nu)(b\nu) \\ \phi_2\phi_2/\chi_2\chi_2 & \to & (t\nu)(t\nu)/(t\nu)(b\ell)/(b\ell)(b\ell) \\ \phi_5\phi_5/\chi_5\chi_5 & \to & (t\ell)(t\ell) \end{array} \right\}. \tag{5.21}$$

In Eq. (5.21), we include the symmetric and asymmetric decay modes of the pair-produced scalar and vector LQs. In symmetric decay modes, the pair of LQs decay to the same final states—$\phi_1\phi_1 \to (t\ell)(t\ell)$. Whereas, in the asymmetric mode, they decay to different final states–$\phi_1\phi_1 \to (t\ell)(b\nu)$. We perform prospect study for symmetric and asymmetric decays modes of sLQs and vLQs decaying top quark and lepton (Ref. [64, 78, 259]). It is generally believed that the symmetric modes have good discovery prospects [260]. However, the asymmetric modes can be equally or more promising than the symmetric modes as their contributions becomes significant due to combinatorics. We ignore decay modes that do not contain a top quark or a lepton (ℓ) in the final state.

The possible symmetric and asymmetric single production modes are as follows,

$$pp \rightarrow \left\{ \begin{array}{lcl} \phi_1/\chi_1\; t\ell & \rightarrow & (t\ell)t\ell/(b\nu)t\ell \\ \phi_1/\chi_1\; b\nu & \rightarrow & (t\ell)b\nu/(b\nu)b\nu \\ \phi_1/\chi_1\; \ell j & \rightarrow & (t\ell)\ell j/(b\nu)\ell j \end{array} \right\}, \tag{5.22}$$

$$pp \rightarrow \left\{ \begin{array}{lcl} \phi_2/\chi_2\; t\nu & \rightarrow & (t\nu)t\nu/(b\ell)t\nu \\ \phi_2/\chi_2\; b\ell & \rightarrow & (t\nu)b\ell/(b\ell)b\ell \\ \phi_2/\chi_2\; \nu j & \rightarrow & (t\nu)\nu j/(b\ell)\nu j \end{array} \right\}, \tag{5.23}$$

$$pp \rightarrow \left\{ \begin{array}{lcl} \phi_5/\chi_5\; t\ell & \rightarrow & (t\ell)t\ell \\ \phi_5/\chi_5\; \ell j & \rightarrow & (t\ell)\ell j \end{array} \right\}. \tag{5.24}$$

The three-body single production process, where a sLQ/vLQ is produced along with a jet and a lepton, can have similar final states as the pair production process. Hence, we show that systematically combining contributions from the single production process can help achieve higher discovery reach.

5.5 Search strategy

5.5.1 Signal topologies

We consider scalar and vector LQs that mainly decay to boosted top quarks and high p_T leptons. Thus, we assume an interesting signal topology of a hadronically decaying top quark and exactly two high-p_{T} same-flavor-opposite-sign (SFOS) leptons in the final state. Since we analyze symmetric and asymmetric modes of production, we consider the following types of signatures,

1. **Signature A ($t_h\ell\ell$):** At least one hadronically decaying top quark forming a fatjet and exactly two high-p_{T} same-flavor-opposite-sign (SFOS) light leptons $t_h\ell^+\ell^-$. This signal is considered to analyse the collider prospect of vLQs (Refer to [78]).

2. **Signature B:** While investigating the collider prospects of sLQs and vLQs decaying to a top quark and τ (Ref [259]), we find the necessity to consider two distinct signal topologies because the τ decays hadronically and leptonically.

- **Signature B.1 ($t_h\tau_h\tau_h$ + $t_h\tau_h\tau_\ell$):** At least one hadronically-decaying top quark along with either two hadronically-decaying τ leptons ($t_h\tau_h\tau_h$) or a hadronically-decaying τ and a leptonically-decaying one ($t_h\tau_h\tau_\ell$),
- **Signature B.2 ($t_h\tau_h$+MET):** At least one hadronically-decaying top quark with only one τ decaying hadronically and some missing energy.

Our choice of signal topologies allows us to combine events from pair and single production modes and enhance our signal sensitivity. The final state $t\ell t\ell$ can come from pair-produced LQs decaying to a top and a lepton, or from a singly produced LQ along with a lepton and a top. Here, there is a possibility of double counting between events coming from single production and ones coming from pair production. Thus, to avoid this we ensure that χ/ϕ and $\chi^\dagger/\phi^\dagger$ are never on-shell simultaneously in any single production event [98].

5.5.2 SM background process

We discuss the main SM background processes for the signal topologies listed above. The SM background processes should have two high p_T leptons in their final state and a top-like jet. This top-like jet could either come from an actual top or could arise from other jets (for example, QCD jets). Processes with a single lepton can also contribute if the second lepton appears due to a jet misidentification. However, the jet misidentification rate is tiny, and thus these backgrounds contribute negligibly to the total background. There are some backgrounds that have a huge contribution, but we are interested in a specific kinematic region. Thus, we generate the background processes with strong generation-level cuts. This is done for better statistics and it saves computation time. We list some generational-level cuts and explain these background processes in detail.
Generation level cuts:

1. $p_{\mathrm{T}}(\ell_1) > 250$ GeV (For signature A); $p_{\mathrm{T}}(\ell_1) > 100$ GeV (For signature B),
2. the invariant mass of the lepton pair $M(\ell_1, \ell_2) > 110$ GeV (the Z-mass veto).

Here, ℓ_1 and ℓ_2 denote the leptons with the highest and the second highest p_{T}, respectively. We discuss the different background processes in more detail below.

1. $\underline{Z + jets}$: We simulate the Z background as $pp \to Z/\gamma^* + (0,1,2)$-$jets \to \ell\ell$+jets and we match up to two extra partons. For Signature A ($t_h\ell\ell$), the required two high p_T leptons can

be obtained from the leptonic decay of the Z boson. The top-like jet can arise from the QCD jets. This background is constrained by applying the Z-mass veto cut at the generation level.

This background process can also contribute to signatures B.1 ($t_h\tau_h\tau_h$ + $t_h\tau_h\tau_\ell$) and B.2 ($t_h\tau_h$+MET). The single lepton can come from the leptonic decay of Z. Small QCD jets can sometimes be mistagged as a hadronic tau (τ_h). Although the mistagging rate is small, the background cross section is large and it leads to a large number of background events surviving at the end.

2. $\underline{W + jets}$: We simulate this SM process as $pp \to W + (0,1,2)\text{-}jets \to \ell\nu + jets$ matched up to two extra partons. We can reconstruct the top-like jet from the QCD jets. Like $Z + jets$, the cross section of this background is also very high. But our signatures A and B.1 demand two high p_T opposite-sign dilepton, hence this background contribution comes down. However, since it can contain a single τ in the final state, it can contribute to signature B.2.

3. $\underline{WW + jets}$: The diboson processes that can mimic signature A are as follows, $W_\ell W_\ell$, $W_h Z_\ell$, and $Z_h Z_\ell$ plus additional QCD jets. The requirement for two opposite-sign dileptons can come from the leptonic decay of WW and the top-like jet can be reconstructed from the additional QCD jets. Similarly, in the $W_h Z_\ell$, and $Z_h Z_\ell$ modes, the dilepton can come from the leptonic decay of the Z boson and the top-like jet can be obtained from the hadronic decays of W and Z bosons.

   For signatures B.1 and B.2, the following diboson processes can contribute, $W_\ell W_h$, $W_\ell Z_h$, $Z_\ell Z_h$. The W_ℓ and Z_ℓ can decay to τs which can further hadronically decay giving us the desired background. The top-like jet can be reconstructed from the hadronic decay of the bosons. We find this background process to be subdominant.

4. $\underline{tt + jets}$: The SM top pair production is one of the most important background processes. We generate this background by matching up to two additional jets. In the case of signature A, we consider the leptonic decay of both the tops ($t_\ell t_\ell$). This gives us the required opposite-sign dilepton in the final state. The required top-like jet comes from reconstructing the additional QCD jets.

   In the case of Signature B.1 and B.2, we include the hadronic and semi-leptonic decays of the top quarks ($t_h t_\ell$ and $t_h t_h$) as well. The contribution from the semileptonic mode is dominant, followed by the leptonic and hadronic modes.

5. $\underline{ttV}$: The SM background of the pair produced top quarks along with a vector boson could act as a background process for our signatures. For signature A, one background could be $t_h t_h Z_\ell$. The leptonically decaying Z would give us the dilepton final state and the top-like fatjet comes from t_h. Secondly, $t_\ell t_\ell Z_h$ can also contribute as background to signature A.

For signature B.1, background processes such as a $t_h t_h Z_h$ and $t_h t_\ell Z_h$ could contribute. The top-like jet could come from one of the hadronically decaying top, and the pair of hadronically decaying τs can be obtained from the hadronic decay of the Z bosons. A lepton can come from the misidentification of the jet as a lepton or from the leptonic decay of the top quark. The $t_h t_\ell Z_h$ process can also contribute to signature B.2. However, the background processes have a small cross section and do not contribute much.

6. tV: The SM process of a top quark produced along a W/Z boson is one of the subdominant background processes. We add additional jets and match up to two jets. For signature A, the background process $t_\ell W_\ell$ would contribute as one could get the dilepton from the leptonic decay of the top and the W boson. The top-like jet could be obtained from the additional jets. Another background that can contribute to signature A is $t_h Z_\ell$. Here, the dilepton is obtained from the leptonic decay of the Z boson, and the top-like jet comes from the hadronic decay of the top quark.

   In signature B.1, the background process that can contribute is $t_h W_h$. The top-like jet comes from the hadronic top, and the jets from W_h can mimic the hadronic decay of the τs. A $t_h W_\ell$ can also contribute to signature B.1, the lepton coming from the W can mimic the leptonic decay of the τ, and the other hadronic decays can come from the hadronic top and additional jets. This background process could also be ideal for signature B.2.

We summarize all the relevant background processes in Table 5.2. They are computed at various orders of QCD, as mentioned in the literature. We scale the LO cross sections by their corresponding K-factors.

5.5.3 Selection cuts

We analyse the prospects of vLQs decaying to boosted tops and high p_T light leptons (in ref. [78]) and sLQs and vLQs decaying to a boosted top quark and a τ(in [259]). We use the anti-k_t jet clustering algorithm for both signatures. We analyse two kinds of jets based on the jet radius parameter R. We call jets with $R = 0.4$ "AK4-jets" and the jets with $R = 0.8$ ones as "AK8-fat jets". The AK4-jets are used to identify τ_h- and b-tagged jets. We utilise information from the Delphes tower objects to construct the AK8-fatjets. In the following sections, we apply some conditions on these AK8-fatjets to identify the hadronic top. We sequentially apply the analysis level cuts on the signal (See 5.5.1) and background processes.

Background processes		σ (pb)	QCD order
$V+$ jets [261, 262]	$Z+$ jets	6.33×10^4	N^{2}LO
	$W+$ jets	1.95×10^5	NLO
$VV+$ jets [263]	$WW+$ jets	124.31	NLO
	$WZ+$ jets	51.82	NLO
	$ZZ+$ jets	17.72	NLO
Single t [264]	tW	83.10	N^{2}LO
	tb	248.00	N^{2}LO
	tj	12.35	N^{2}LO
tt [265]	$tt+$ jets	988.57	N^{3}LO
ttV [266]	ttZ	1.05	NLO+N^{2}LL
	ttW	0.65	NLO+N^{2}LL

Table 5.2: Cross-sections of the major background processes without any cut. The higher-order cross-sections are taken from the literature; the corresponding QCD orders are shown in the last column. We use these cross-sections to compute the K factors to incorporate the higher-order effects.

5.5.3.1 Cuts for signature A ($t_h\ell\ell$)

$\mathscr{C}_1$: (a) We demand at least one top jet, which we tag using the sophisticated tagging algorithm HEPTOPTAGGER with a transverse momentum $p_{\rm T}(t_h) > 135$ GeV.

(b) We demand exactly two same flavor opposite sign (SFOS) leptons with $p_{\rm T}(\ell_1) > 400$ GeV and $p_{\rm T}(\ell_2) > 200$ GeV and pseudorapidity $|\eta(\ell)| < 2.5$. For the electron, we consider the barrel-end cap cut on η between 1.37 and 1.52.

(c) The invariant mass of the lepton pair should be greater than 120 GeV [$M(\ell_1, \ell_2) > 120$ GeV] to minimize the dilepton background coming from Z boson.

(d) We consider the missing energy $\not{E}_T < 200$ GeV.

$\mathscr{C}_2$: The scalar sum of the transverse p_T of all visible objects, $S_T > 1.2 \times \text{Min}\left(M_\chi, 1750\right)$ GeV.

$\mathscr{C}_3$: We consider the invariant mass of the reconstructed top jet and lepton cut as $\text{Max}(M(\ell_1, t)$ OR $M(\ell_2, t)) > 0.8 \times \text{Min}\left(M_\chi, 1750\right)$ GeV.

For Signature B, we do not use the tagging algorithm HEPTOPTAGGER but rather cluster the jets using the anti-k_t algorithm and apply the following conditions to tag the hadronic top among them. These conditions are common to both signatures B.1 and B.2.

– We demand that the mass of the AK8-fatjet, $M_{fj} > 120$ GeV and the transverse momentum $p_{\mathrm{T}} > 200$ GeV.

– The subjettiness parameter τ_N tells us the about the number of subjets in a fatjet. If τ_N assumes small values, then the fatjet contains N subjets. Here, we apply the subjettiness ratios $\tau_{32} < 0.81$ and $\tau_{21} > 0.35$ where $\tau_{ij} \equiv \tau_i/\tau_j$.

5.5.3.2 Cuts for signature B.1

1. Leptons and jet selection: We demand leptons with transverse momentum $p_{\mathrm{T}}(\ell) > 100$ GeV and pseudorapidity $|\eta_\ell| < 2.5$. We exclude the parameter region $1.37 < |\eta_e| < 1.52$. Similarly, the transverse momentum of the jet $p_{\mathrm{T}}(j) > 30$ GeV and the pseudorapidity $|\eta_j| < 5.0$. We demand $p_{\mathrm{T}}(\tau_h) > 150$ GeV. After the basic cuts on the p_T of the leptons, we demand there be at least one high p_T lepton with $p_{\mathrm{T}}(\hat{\ell}) > 250$ GeV.

2. Number of leptons or jets: We demand exactly two hadronically decaying τ leptons ($N(\tau_h) = 2$) or one hadronically τ lepton and one leptonically decaying τ ($N(\tau_h) = N(\ell) = 1$). We require atleast one b-tagged AK4-jet ($N(b) > 0$).

3. Mass cuts: We demand that the invariant mass of the hadronic ditau $M(\tau_{h_1}\tau_{h_2}) > 250$ GeV. And we require that the transverse mass of the single hadronic τ and leptonic τ $M_{\mathrm{T}}(\tau_h, \not{E}_{\mathrm{T}}) > 300$ GeV.

4. Top quark identification: The top decay as fatjets. The transverse momentum of the fatjet– $p_{\mathrm{T}}(\text{fatjet}) > 200$ GeV. The mass of the fatjet is $M(\text{fatjet}) > 120$ GeV. The subjettiness parameters are assumed to be $\tau_{32} < 0.81$, $\tau_{21} > 0.35$. The fatjet-lepton radius cuts are $\Delta R(\text{fatjet}, \hat{\ell}_1)$, $\Delta R(\text{fatjet}, \hat{\ell}_2) > 0.8$. Finally we apply the cut the scalar sum of tranverse momenta–$S_{\mathrm{T}} > 1300$ GeV.

5.5.3.3 Cuts for signature B.2

1. Leptons and jet selection: Here, the basic level leptons and jets p_T and pseudorapidity η cuts are the same as above. The only difference is that we demand $p_{\mathrm{T}}(\tau_h) > 250$ GeV.

2. Number of leptons or jets: We demand only one hadronically decaying τ ($N(\tau_h) = 1$) and at least one b-tagged AK4-jet ($N(b) > 0$).

3. Mass/Energy cuts: Here, we demand that the missing energy $\not{E}_{\mathrm{T}} > 300$ GeV and we require that the transverse mass of the single hadronic τ and the missing energy $M_{\mathrm{T}}(\tau_h, \not{E}_{\mathrm{T}}) > 300$ GeV.

4. Top quark identification: The cuts are the same as the ones given in Signature A with minor differences such as–$\Delta R(\text{fatjet}, \tau_h) > 0.8$ and $S_{\mathrm{T}} > 1100$ GeV.

The transverse mass M_{T} is defined as,

$$M_{\mathrm{T}}^2(A,B) = 2p_{\mathrm{T}}^A p_{\mathrm{T}}^B \left\{1 - \cos\Delta\phi(p_{\mathrm{T}}^A, p_{\mathrm{T}}^B)\right\}, \tag{5.25}$$

$$M_{\mathrm{T}}^2(A,B,\not{E}_{\mathrm{T}}) = M_{\mathrm{T}}^2(A,B) + M_{\mathrm{T}}^2(A,\not{E}_{\mathrm{T}}) + M_{\mathrm{T}}^2(B,\not{E}_{\mathrm{T}}). \tag{5.26}$$

A few remarks highlight the motivation behind the cuts. We demand at least one b-tagged AK4-jet as it reduces the single vector boson plus jets background drastically. We demand that the fatjet and τ_h are radially separated while tagging a top so as to avoid overlap. The invariant mass cut on the pair of τ_h in signature A is to avoid the Z+jets background.

5.6 HL-LHC prospects

We use the following definition of statistical significance $\mathscr{Z}$ [267],

$$\mathscr{Z} = \sqrt{2\,(N_S + N_B)\ln\left(\frac{N_S + N_B}{N_B}\right) - 2N_S}\,, \tag{5.27}$$

where N_S and N_B are the numbers of the signal and background events, respectively, surviving the selection cuts as mentioned in Section 5.5.3:

$$N_S = (\sigma_{\text{pair}}(M_{\phi/\chi})\epsilon_{\text{pair}} + \lambda^2\sigma_{\text{single}}(\lambda = 1, M_{\phi/\chi}) \times \epsilon_{\text{single}}) \times \mathscr{L} \tag{5.28}$$

$$N_B = \sigma_{\mathrm{B}} \times \epsilon_B \times \mathscr{L}, \tag{5.29}$$

where σ_{pair} is the cross section from the pair production mode, σ_{single} is the cross section from the single production channel, σ_{B} is the cross section of the background process, ϵ_x denotes the fraction of events surviving the cuts mentioned above and $\mathscr{L}$ is the luminosity of the HL-LHC which is 3000 fb^{-1}.

5.6.1 Results: signature A

Here, we present the results for signature A. We show the signal significance as a function of the mass of the LQ. We plot these for 14 TeV LHC with 3000 fb^{-1} of integrated luminosity. We have considered $\Lambda = 1$ while calculating the significance for the combined signal (pair and single production mode) for vLQs decaying to top and light leptons. In 5.4, we show the significance vs mass plot for the vLQs χ_1 and χ_5 and for the scenarios $\kappa = 0$ and $\kappa = 1$ (See Figs. 5.4a,5.4b,5.4c,5.4d). Here, the χ decays to a top quark and a light lepton. The three horizontal dotted lines in the figures are the 2σ, 3σ, and 5σ significance. The Pair100 or Pair50 curve denotes the significance as a function of mass when one considers contributions from the pair production mode only. The curves labeled LC50, LC100, RC50, and RC100 involve contributions from both pair and single production modes. The 50 and 100 denote the branching ratio (BR) of $\chi \to t\ell$ as 50% and 100% respectively. Some key observations are as follows,

- Assuming $\kappa = 0$, for χ_1, the discovery mass reach with pair production search only pair100(50) is about 2.05 (1.80) TeV. If one considers the contribution from the single production mode as well then the discovery reach goes as high as 2.35 (2.10) TeV in the case of LC100 (50). However, the enhancement in the RC scenario is minimal as the $\sigma(pp \to \chi_1 \ell j)$ is small in the RC scenario.
- For $\kappa = 1$, the discovery reach enhances as the cross section goes up due to additional diagrams coming from the $g\chi\chi$ coupling. For pair100 (50), the reach goes up to 2.36(2.10) TeV and once you consider the combined signal then the reach enhances to 2.51 (2.26) TeV. We obtain similar numbers for χ_5 as well.
- In the absence of discovery, we also show the heaviest LQ one can exclude with 95% confidence limit (CL). In the case of pair100 (50), for $\kappa = 0$ one can exclude a vLQ up to a mass of 2.23 (1.97) TeV. On combining the single production process, the exclusion limit goes as high as 2.64 (2.1) TeV in the LC100 (RC100). For $\kappa = 1$, the numbers go up.

For completeness, we also show a previous study [64], where the decay of sLQs (ϕ_1 and ϕ_5) to top quarks and light leptons (See Fig. 5.5) was analysed. We have summarized the discovery reaches and exclusion limits for χ_1 and χ_5 in Tables. 5.3 and 5.4 for benchmark scenario $\kappa = 0$ and $\kappa = 1$ respectively.

In Fig. 5.11 and 5.7, we obtained the discovery reach and exclusion limits by setting $\Lambda = 1$. We recast these significance plots in terms of Λ and M_χ. In Fig. 5.11, we show the discovery curves

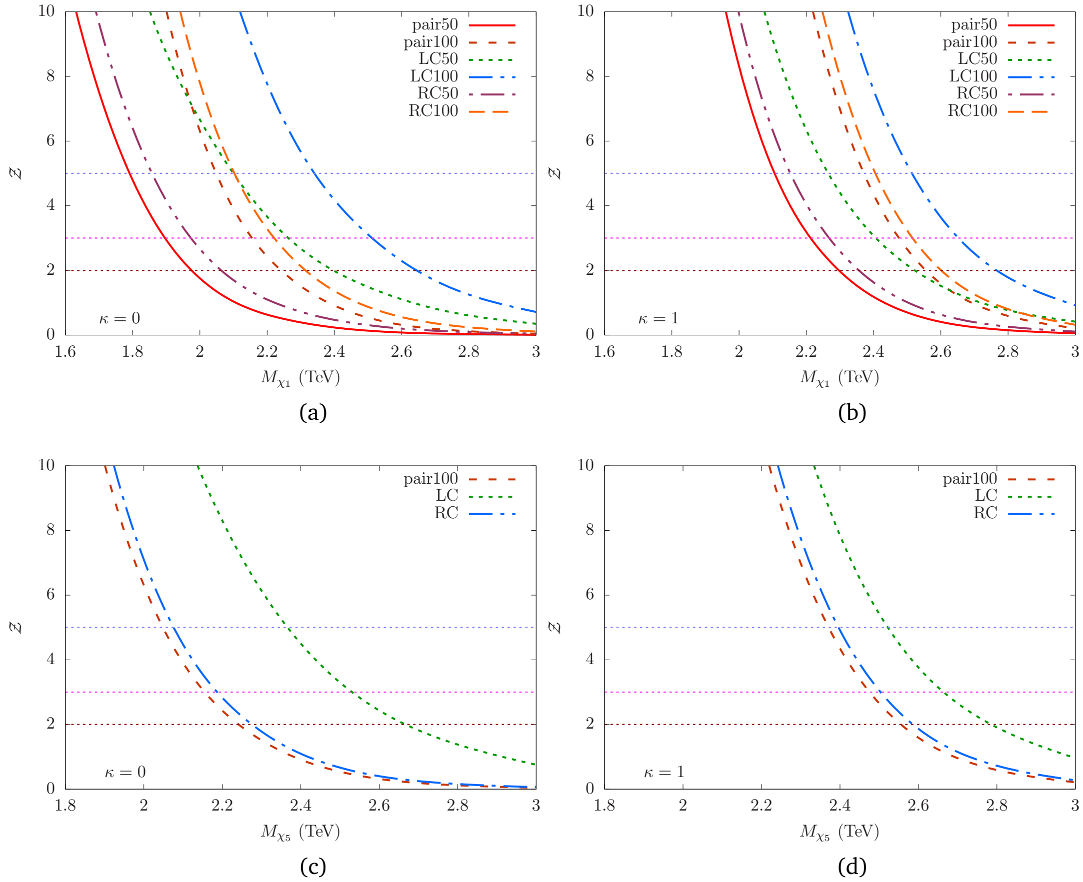

Figure 5.4: We show the χ_1 significance for (a)[$\kappa = 0$],(b)[$\kappa = 1$] and χ_5(c)[$\kappa = 0$],(d)[$\kappa = 1$] signals over the SM backgrounds. We plot them as a function of their masses M_{χ_n} for 3 ab^{-1} of integrated luminosity at the 14 TeV HL-LHC for different coupling scenarios in the light lepton modes. We show the pair production significance for 50% and 100% BRs in the $\chi \to t\ell$ decay mode. We set the benchmark coupling $\Lambda = 1$ while generating the signal.

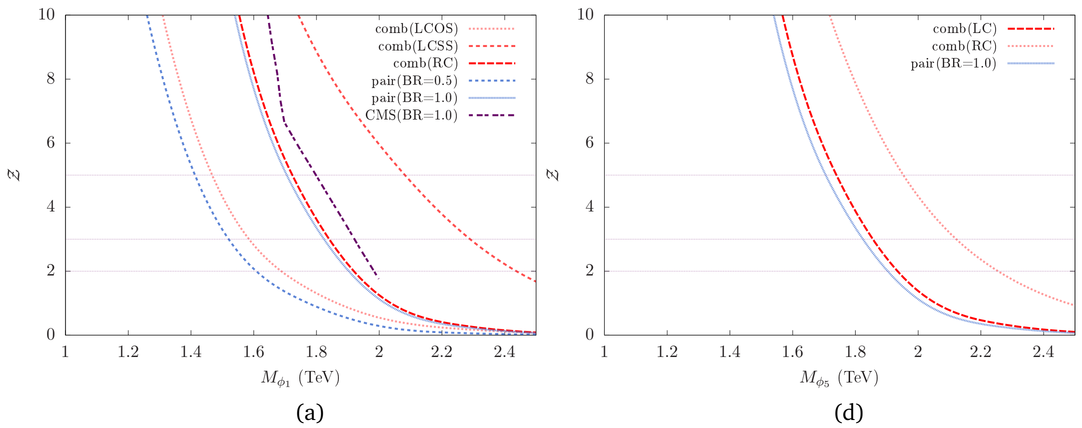

Figure 5.5: For completeness, we also show the expected significance for observing ϕ_1/ϕ_5 based on the study [64].

Signif. $\mathscr{Z}$	Limit on M_χ (TeV) $\kappa = 0$								
	χ_1						χ_5		
	Combined				Pair		Combined		Pair
	LC50	LC	RC50	RC	BR=0.5	BR=1	LC	RC	BR=1
5	2.10	2.34	1.85	2.10	1.79	2.05	2.36	2.07	2.04
3	2.25	2.51	1.97	2.22	1.89	2.15	2.52	2.18	2.15
2	2.39	2.64	2.06	2.31	1.97	2.23	2.66	2.27	2.23

Table 5.3: We show the mass limits for χ_1 and χ_5 at $\kappa = 0$. The 5σ significance corresponds to discovery reach and the 3σ and 2σ correspond to the exclusion limits for observing the sLQs signals over background at 3 ab^{-1} integrated luminosity at the 14 TeV LHC. Here, we combine the signal events from pair and single production processes. Here, LC (RC) denotes LC100 (RC100).

Signif. $\mathscr{Z}$	Limit on M_χ (TeV) $\kappa = 1$								
	χ_1						χ_5		
	Combined				Pair		Combined		Pair
	LC50	LC	RC50	RC	BR=0.5	BR=1	LC	RC	BR=1
5	2.26	2.51	2.14	2.40	2.10	2.36	2.52	2.39	2.36
3	2.40	2.65	2.26	2.51	2.21	2.47	2.66	2.50	2.47
2	2.52	2.76	2.35	2.59	2.29	2.55	2.78	2.58	2.55

Table 5.4: Here, we show the mass limits for χ_1 and χ_5 for $\kappa = 1$. The rest of the description is the same as Table. 5.3

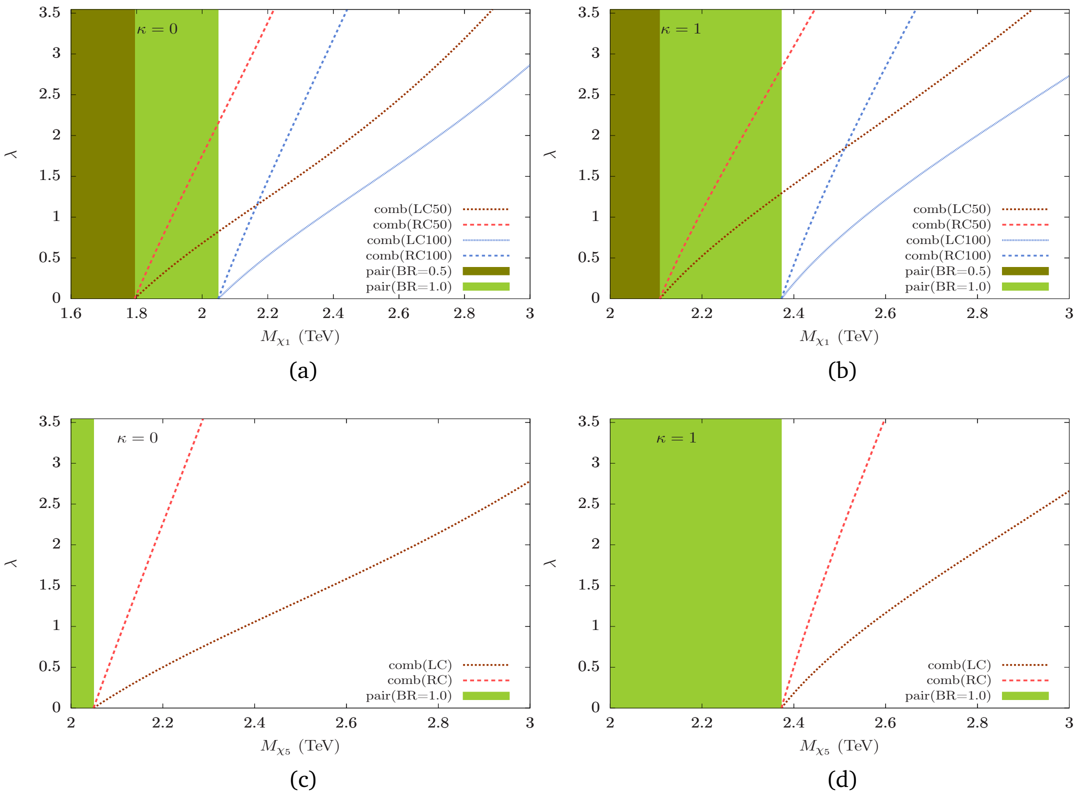

Figure 5.6: We show the 5σ discovery reach as a function of λ-M_χ for χ_1 with (a) $\kappa = 0$ and (b) $\kappa = 1$ and for χ_5 with (c) $\kappa = 0$ and (d) $\kappa = 1$. Here, we show the smallest value of new coupling λ required to observe a χ_1/χ_5 signal with 5σ significance for different values of M_χ with 3 ab^{-1} of integrated luminosity. The shades of green colour denote the pair-production-only regions for 50% and 100% BRs in the $\chi \to t\ell$ decay mode. The pair production mode is insensitive to λ thus one can get 5σ even with a small value of coupling in the green region.

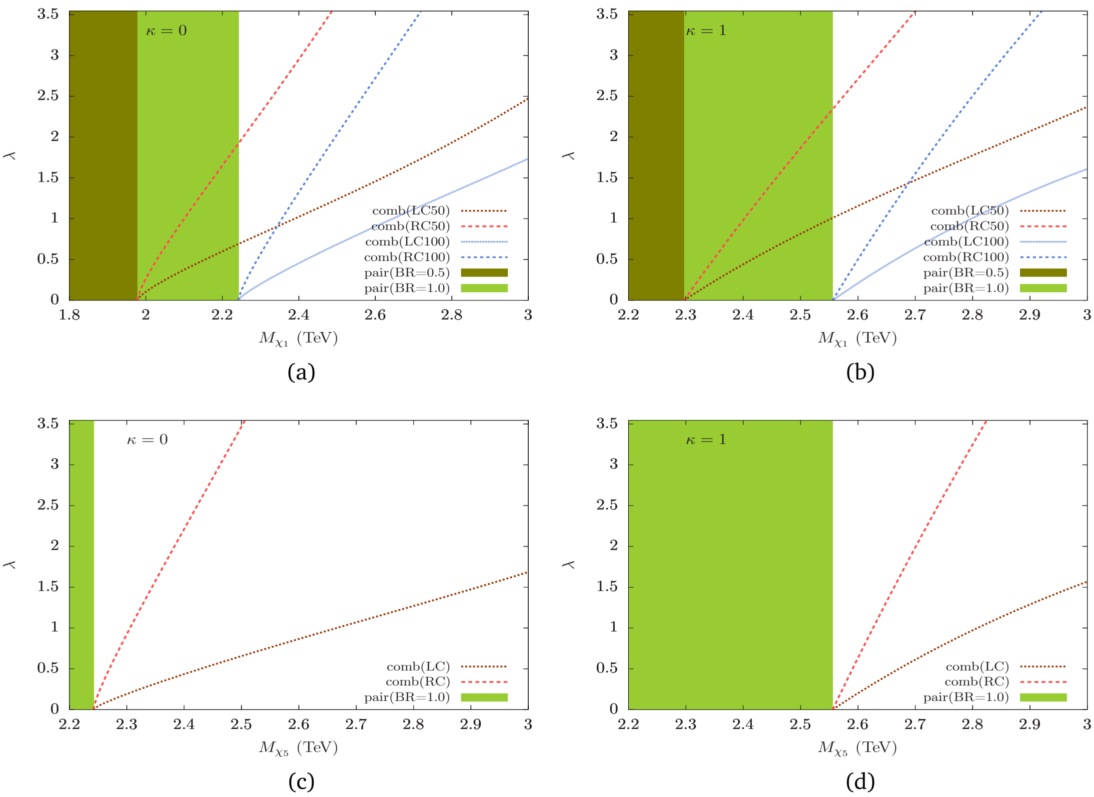

Figure 5.7: Here, similar to the previous figure, we show the 2σ exclusion limits in the λ-M_χ planes for χ_1 with (a) $\kappa = 0$ and (b) $\kappa = 1$ and for χ_5 with (c) $\kappa = 0$ and (d) $\kappa = 1$. These plots show the smallest λ that can be excluded by the HL-LHC with 3 ab^{-1} of integrated luminosity. The pair-production-only regions for 50% and 100% BRs in the $\chi \to t\ell$ decay mode are shown with green shades.

while the 2σ exclusion curves are displayed in Fig. 5.7. These plots show the lowest value of λ required to observe the vLQ signal for a varying M_χ with 5σ confidence level for discovery. For the exclusion plots, all points above the curves can be excluded at the 95% confidence level at the HL-LHC.

5.6.2 Results: signature B

Here, we discuss the results for signatures B.1 ($t_h\tau_h\tau_h$ + $t_h\tau_h\tau_\ell$) and B.2 ($t_h t_\tau$+ MET). In Fig. 5.8, we plot the significance as a function of the mass of sLQ and vLQ for $\lambda/\Lambda = 1$. In the case of vLQs we have shown only the scenario with $\kappa = 1$. 'Pair' implies contributions are from the pair production channel only and 'comb' means contributions from pair and single production processes. LC50 and RC50 denote the left and right-handed coupling scenarios (See section 5.3), where LQs decay to $t\tau$ with 50% BR. We highlight some key results as follows,

1. Signature B.1

   – In Fig. 5.8a, if one considers the pair-only searches with BR 50% for $\phi_1 \to t\tau$ mode, the discovery limit can go up to 0.96 TeV. However, one can probe higher M_{ϕ_1} values in the combined LCSS scenario (1.07 TeV) than the combined LCOS scenario (0.99 TeV) even though the decays $\phi_1 \to t\tau$ and $\phi_1 \to b\nu$ share 50% BR each in both scenarios. This difference occurs due to the destructive interference in single production diagrams in the case of LCOS and constructive interference in the LCSS scenario. In the RC scenario, ϕ_1 has 100% BR in the $\phi_1 \to t\tau$ decay mode. In the scenario, the single production contribution is small, thus the improvement in reach from the pair-only search (1.31 TeV) to the combined search (1.33 TeV) is marginal. The expected significance for ϕ_5 is shown in Fig. 5.8c.

   – In Fig. 5.8b, we show the significance for the vLQ χ_1 with $\kappa = 1$. There are no LCOS and LCSS scenarios here. Here, the LC50 and RC50 represent the scenarios where the BR of $\chi_1 \to t\tau$ mode is 50%. Such scenarios occur only if there are other decay modes whose only role is to modify the BR. We show these scenarios to outline the variation of the significance with respect to the BR. The discovery reach numbers for vLQ χ_5 are similar to that of χ_1 (See Fig. 5.8d).

2. Signature B.2

   – In Fig. 5.9, we plot the expected significance $\mathscr{Z}$ as a function of M_{ϕ_n/χ_n}. CMS performed an analysis of the signature $tb\tau\nu + t\tau\nu$ in [96] for charge-2/3 vLQ (χ_2) or the charge-

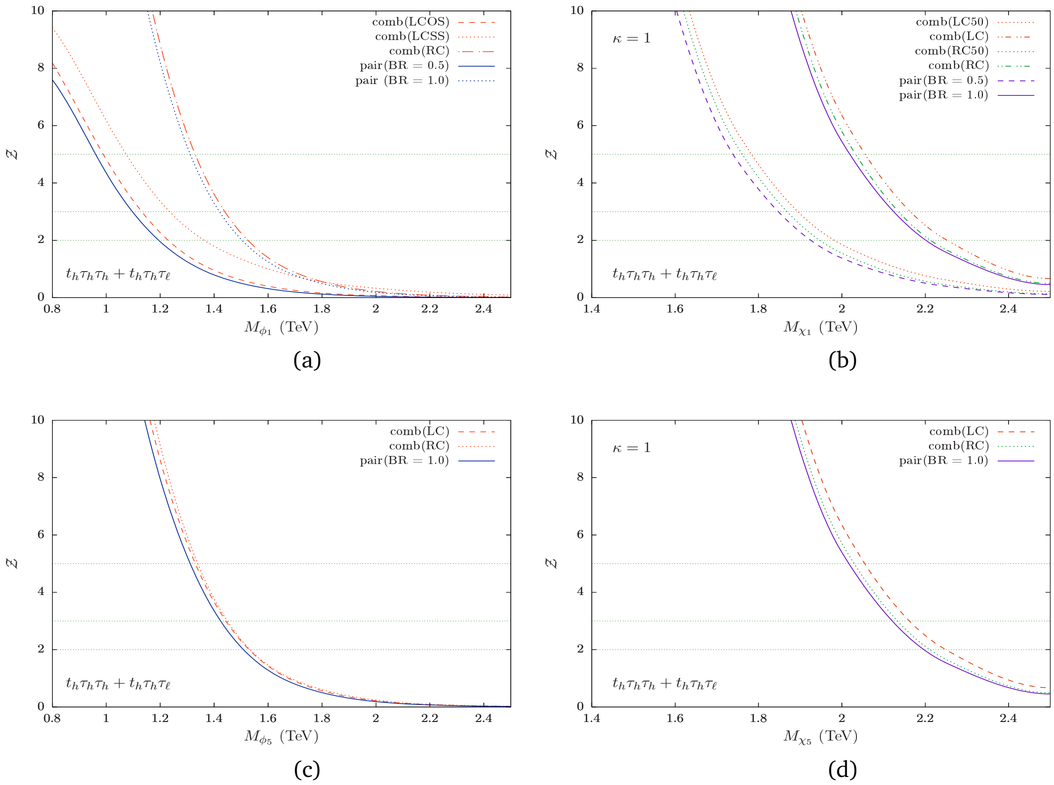

Figure 5.8: We show the expected significance $\mathscr{Z}$ for observing ϕ_n [(a) and (c)] and χ_n [(b) and (d)] for the signal signature A ($t_h\tau_h\tau_h + t_h\tau_h\tau_\ell$) as a function of their masses for 3 ab^{-1} of integrated luminosity at the 14 TeV HL-LHC. We plot for different coupling scenarios. The 'comb' denotes combined events from pair and single production processes. For the pair production process, we show significance with BR = 50% and BR = 100%. We consider λ, $\Lambda = 1$ when computing the signals.

1/3 sLQ (ϕ_1). Considering this analysis as a motivation we show that a charge-2/3 sLQ (ϕ_2) or a charge-1/3 vLQ (χ_1) can lead to the same final state. In Fig. 5.9a, we show the significance vs mass plot for ϕ_1. Here, there are no interference effects for ϕ_1. Thus, we combine the LCOS and LCSS scenarios and denote it as LC50. Thus, for this signature, the discovery reach for the pair-only (with BR= 50%) searches is 1.10 TeV, and once we add the single production–comb(LC50) the reach goes up to 1.16 TeV. Similarly, in the case of ϕ_2, we club the RLCOS and RLCSS and write it as RLC50. The discovery reach in the pair-only mode and the combined(LC50) mode is given as 1.09 TeV and 1.13 TeV respectively. We have summarized the discovery reach and exclusion limits for all the LQs and their scenarios and for each signature in Tables. 5.3, 5.4, 5.5, 5.6, 5.7, 5.8, and 5.9.

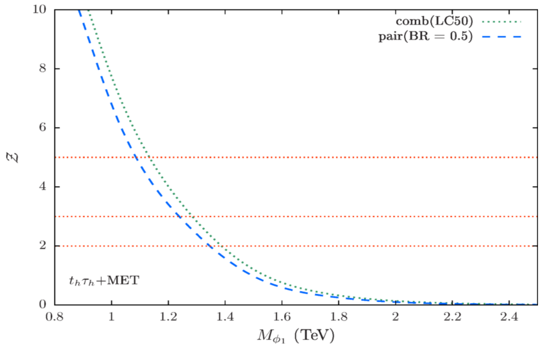

(a)

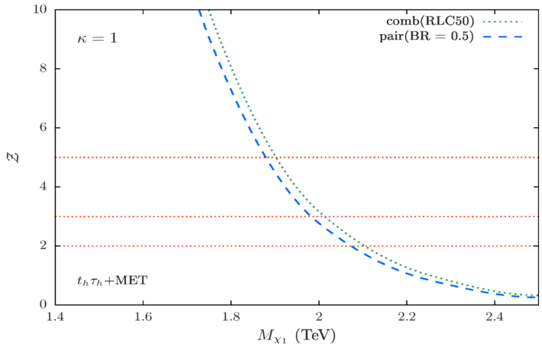

(b)

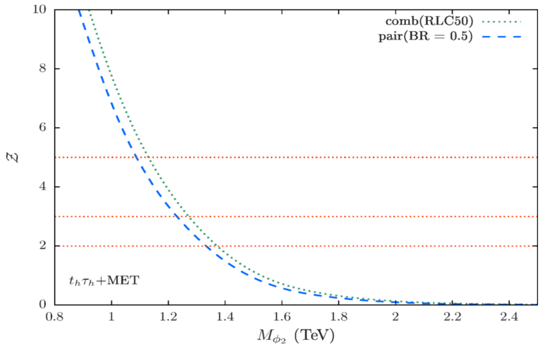

(c)

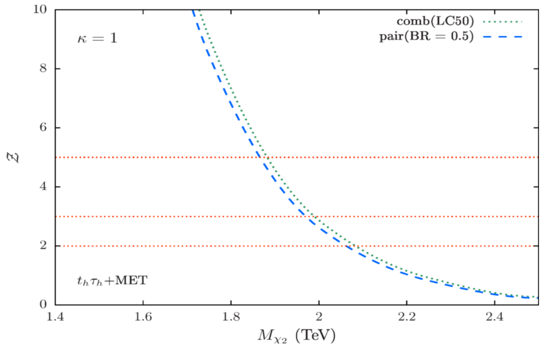

(d)

Figure 5.9: Similar to the Fig. 5.8, we plot the expected significance $\mathscr{Z}$ for observing ϕ_n [(a) and (c)] and χ_n [(b) and (d)] for the signal signature B ($t_h\tau_h$ + MET)

Comb. $\mathscr{Z}$	Limit on M_ϕ (TeV) $t_h\tau_h\tau_h + t_h\tau_h\tau_\ell$							
	ϕ_1					ϕ_5		
	Combined			Pair		Combined		Pair
	LCOS	LCSS	RC	BR=0.5	BR=1	LC	RC	BR=1
5	0.99	1.07	1.33	0.96	1.31	1.33	1.34	1.31
3	1.13	1.23	1.44	1.10	1.23	1.44	1.45	1.42
2	1.23	1.36	1.52	1.19	1.50	1.53	1.53	1.51

Table 5.5: We show the 5σ discovery limits and $2\sigma/3\sigma$ exclusion bounds on ϕ_n for signature B.1 ($t_h\tau_h\tau_h + t_h\tau_h\tau_\ell$). We show limits for pair only and combined signals computed for 3 ab^{-1} integrated luminosity at the 14 TeV LHC.

Comb. $\mathscr{X}$	Limit on M_ϕ (TeV) $t_h\tau_h$+MET			
	ϕ_1		ϕ_2	
	Combined	Pair	Combined	Pair
	LCSS	BR=0.5	RLCSS	BR=0.5
5	1.16	1.10	1.13	1.09
3	1.32	1.24	1.27	1.23
2	1.42	1.34	1.37	1.33

Table 5.6: We show the 5σ discovery limits and $2\sigma/3\sigma$ exclusion bounds on ϕ_n for signature B.2 ($t_h\tau_h$+MET). We show limits for pair only and combined signals computed for 3 ab^{-1} integrated luminosity at the 14 TeV LHC.

Comb. $\mathscr{X}$	Limit on M_χ (TeV) (Signature: $t_h\tau_h\tau_h + t_h\tau_h\tau_\ell$) $\kappa = 0$								
	χ_1						χ_5		
	Combined				Pair		Combined		Pair
	LC50	LC	RC50	RC	BR=0.5	BR=1	LC	RC	BR=1
5	1.49	1.75	1.43	1.69	1.41	1.68	1.75	1.69	1.68
3	1.60	1.87	1.53	1.80	1.51	1.78	1.87	1.80	1.78
2	1.69	1.96	1.61	1.88	1.59	1.86	1.96	1.88	1.86

Table 5.7: We show the 5σ discovery limits and $2\sigma/3\sigma$ exclusion bounds on χ_n for signature B.1 ($t_h\tau_h\tau_h + t_h\tau_h\tau_\ell$) for $\kappa = 0$. We show limits for pair only and combined signals computed for 3 ab^{-1} integrated luminosity at the 14 TeV LHC.

Comb. $\mathscr{X}$	Limit on M_χ (TeV) (Signature: $t_h\tau_h\tau_h + t_h\tau_h\tau_\ell$) $\kappa = 1$								
	χ_1						χ_5		
	Combined				Pair		Combined		Pair
	LC50	LC	RC50	RC	BR=0.5	BR=1	LC	RC	BR=1
5	1.78	2.05	1.76	2.03	1.74	2.02	2.05	2.03	2.01
3	1.90	2.16	1.87	2.13	1.85	2.12	2.16	2.13	2.12
2	1.98	2.25	1.95	2.21	1.92	2.20	2.25	2.21	2.20

Table 5.8: We show the 5σ discovery limits and $2\sigma/3\sigma$ exclusion bounds on χ_n for signature B.1 ($t_h\tau_h\tau_h + t_h\tau_h\tau_\ell$) for $\kappa = 1$. We show limits for pair only and combined signals computed for 3 ab^{-1} integrated luminosity at the 14 TeV LHC.

Comb. $\mathscr{L}$	Limit on M_χ (TeV) (Signature: $t_h\tau_h$+MET)							
	$\kappa=0$				$\kappa=1$			
	χ_1		χ_2		χ_1		χ_2	
	Combined	Pair	Combined	Pair	Combined	Pair	Combined	Pair
	RLC50	BR=0.5	LCSS	BR=0.5	RLC50	BR=0.5	LC50	BR=0.5
5	1.58	1.53	1.56	1.53	1.90	1.88	1.88	1.87
3	1.69	1.64	1.66	1.63	2.01	1.98	1.99	1.97
2	1.79	1.72	1.74	1.71	2.10	2.07	2.08	2.06

Table 5.9: We show the 5σ discovery limits and $2\sigma/3\sigma$ exclusion bounds on χ_n for signature B.2 ($t_h\tau_h$+MET). We show limits for pair only and combined signals computed for 3 ab^{-1} integrated luminosity at the 14 TeV LHC.

In Figs. 5.10 and 5.11d, we show the 5σ (2σ) discovery (exclusion) reaches for signature B.1 as a function of λ-M_{ϕ_n} and Λ-M_{χ_n}, respectively. And in Figs. 5.12 and 5.13, we show the 5σ (2σ) discovery (exclusion) reaches for signature B.2 as a function of λ-M_{ϕ_n} and Λ-M_{χ_n}, respectively. These plots show the lowest values of LQ-q-ℓ couplings needed to observe the LQ signatures as functions of LQ masses with 5σ confidence level for discovery. For the exclusion plots, all points above the curves can be excluded with 95% confidence level at the HL-LHC. These plots are significant from the perspective of the B-meson anomalies. For example, the λ in the LCOS curves in Figs. 5.10a and 5.10b represent the $y_{1\,33}^{LL}$ coupling of S_1 or the Λ in the LC50 curves in Figs. 5.13c and 5.13d is the $x_{1\,33}^{LL}$ coupling of U_1. Hence, these plots show how far the LHC can probe the couplings required to explain the anomalies.

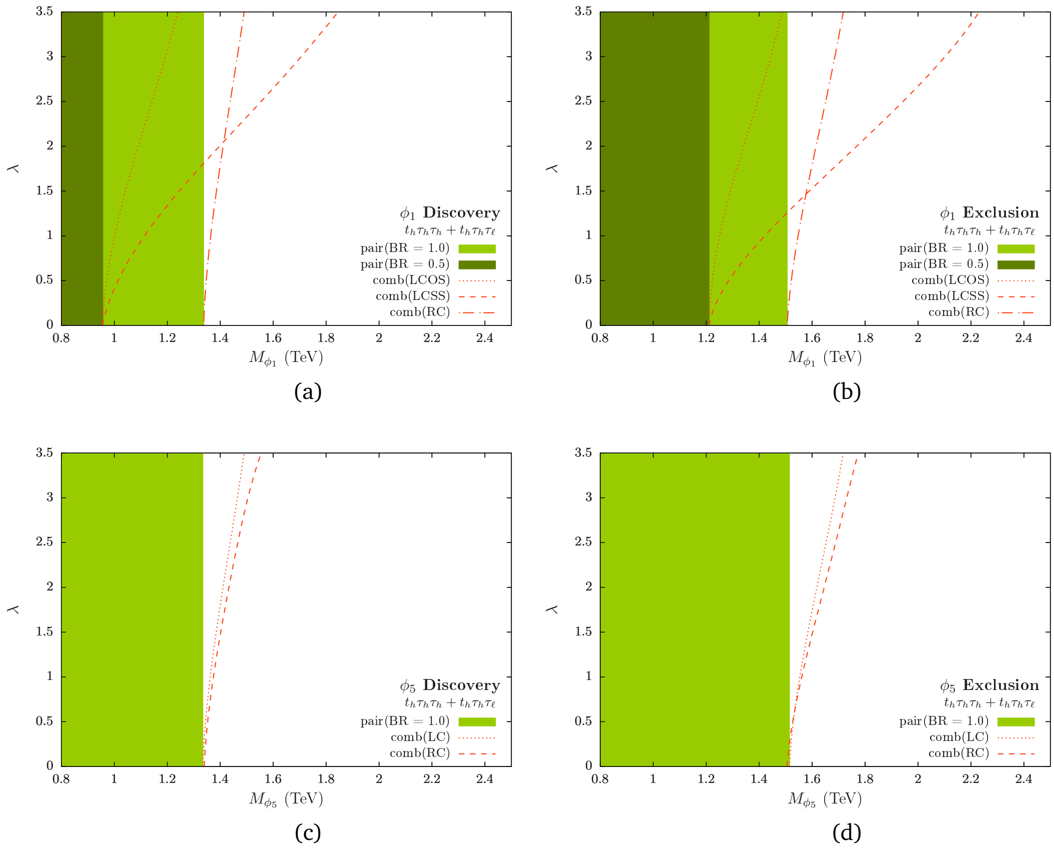

Figure 5.10: The 5σ (2σ) discovery (exclusion) reaches the mass-coupling plane for signature B.1. These plots describe the lowest values of couplings needed to observe LQ signals with 5σ and 2σ significance as functions of M_{ϕ_n} with 3 ab^{-1} of integrated luminosity. The pair-production-only regions for 50% and 100% BRs in the $\chi/\phi \to t\tau$ decay mode are shown in green. The pair production processes are insensitive to the new couplings.

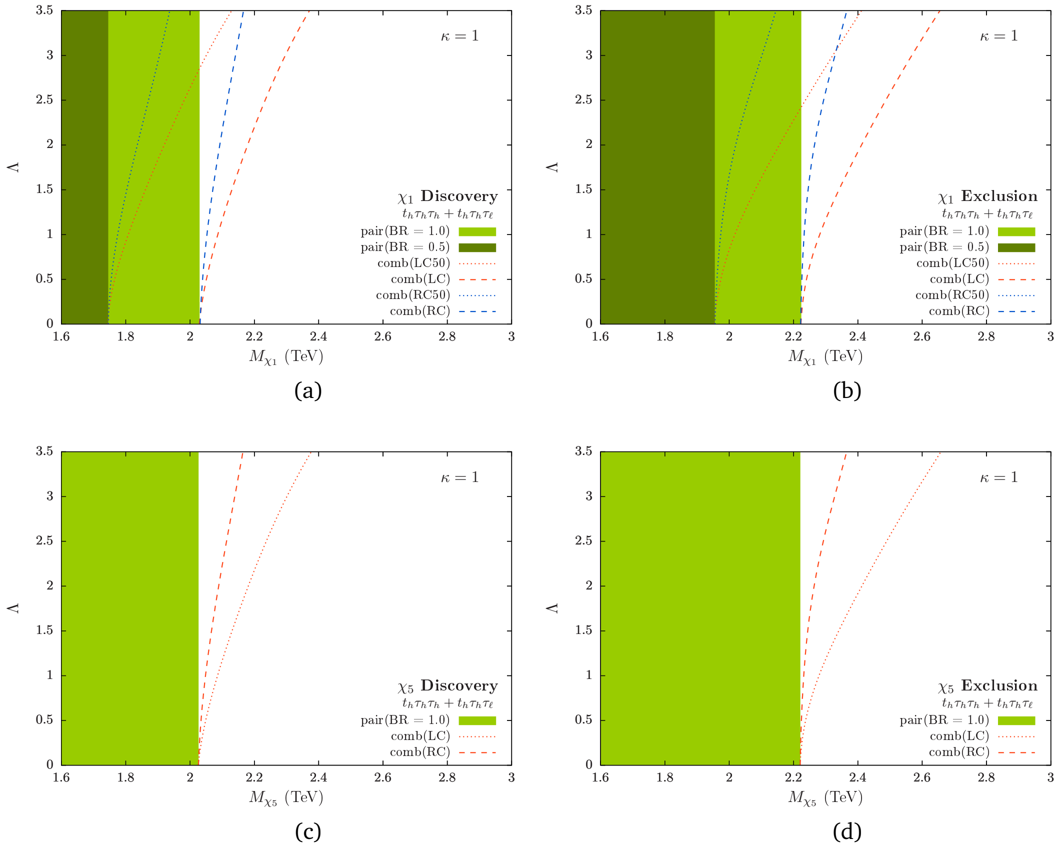

Figure 5.11: Same as Fig. 5.10 but for χ_n.

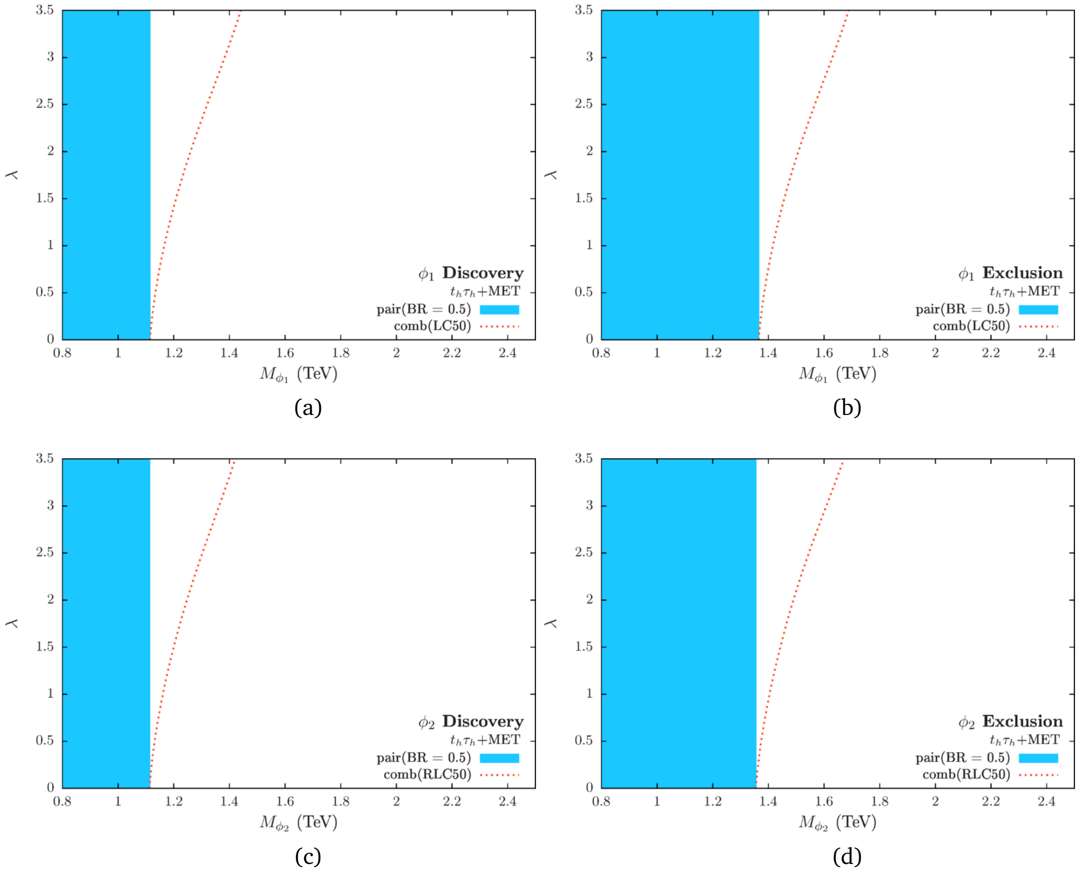

Figure 5.12: Same as Fig. 5.10 but for the $t_h\tau_h$ + MET channel. The pair-production-only regions for 50% BRs in the $\phi \to t\tau$ and $b\nu$ decay mode are shown in blue.

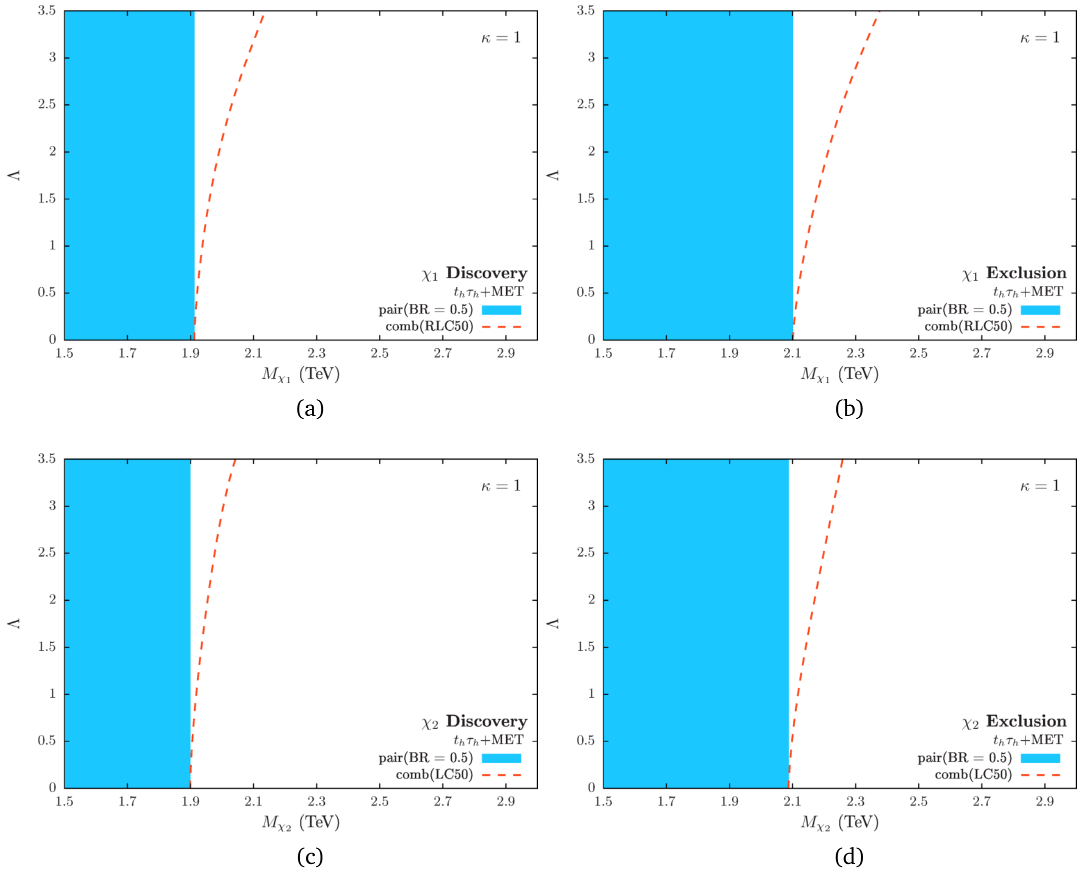

Figure 5.13: Same as Fig. 5.12 but for χ_n.

Chapter

6

Hunting for right-handed neutrinos from leptoquark productions

In this chapter, we study the discovery prospects of LQs exclusively decaying to quarks and right-handed neutrinos (RHNs). Such decays are possible if the RHNs are lighter than the LQs. Sub-TeV RHNs are realisable in models where the neutrinos acquire masses through a process like the inverse seesaw mechanism. Experimentally, it is an unexplored channel and phenomenologically, it is an interesting decay mode as there are no direct experimental bounds on the coupling of LQs, quarks, and RHNs. It opens up the possibility of producing the RHNs abundantly at the LHC, which is otherwise a challenging task. In this chapter, we investigate the signatures at the LHC from the LQs decaying dominantly to second-generation quarks (for reasons we explain later) and RHNs. For completeness, we also study the RHN pair production through a t-channel LQ exchange. For our analysis, we consider the dilepton and monolepton final states to estimate the discovery and exclusion prospects at the HL-LHC. Similar to the previous case (See Refs, [68, 268–271])), we consider simple phenomenological models covering all possible scalar and vector LQs that can give us the desired final states.

6.1 Inverse seesaw mechanism

Neutrino oscillations observed in various experiments (e.g., solar neutrino experiments, KamLAND) have established that neutrinos carry tiny nonzero masses. Various mechanisms have been proposed to explain these observations. The seesaw mechanism [272, 273] offers a natural explanation for the smallness of the neutrino mass. In the seesaw mechanism, one includes a heavy right-handed neutrino N_R for each generation. The RHNs are colour and weak singlets and are electromagnetically neutral. The seesaw mechanism follows from the neutrino mass matrix of the form,

$$M_\nu = \begin{pmatrix} 0 & \mathrm{M_D} \\ \mathrm{M_D}^\mathrm{T} & \mathrm{M_R} \end{pmatrix}, \tag{6.1}$$

Here, $\mathrm{M_D}$ is the Dirac mass and is of the order of the electroweak scale and $\mathrm{M_R}$ is the mass of the heavy right-handed neutrino. On diagonalising the mass matrix, we get two eigenvalues, λ_1 and λ_2. Since the determinant of the matrix is $-M_D^2$, if one of the eigenvalues goes up, the other has to come down, hence the name seesaw mechanism. Since $\mathrm{M_R}$ is much heavier than the electroweak scale, $\lambda_1 \approx \mathrm{M_R}$ and $\lambda_2 \approx -\mathrm{M_D}/\mathrm{M_R}$. For λ_2 to be in the eV-scale neutrino mass range, $\mathrm{M_R}$ needs to be around the GUT scale. This elegant solution to the neutrino mass problem is however not directly testable at the LHC as the GUT scale lies way beyond its reach. Thus, from a collider perspective, a more testable model would need to contain TeV-range RHNs. For our purpose, we look at an ingenious mechanism known as the inverse seesaw mechanism (ISM) [274, 275].

The ISM is a variation of the standard seesaw mechanism. It extends the original idea by introducing three additional singlet neutral fermions S_{iL} ($i = 1, 2, 3$ is the generation index) to the particle spectrum. These fermions are known as the sterile neutrinos. Due to these extra fermions, the mass matrix becomes 3×3 (for each generation) and gains an extra eigenvalue. This allows the RHNs to have (sub-)TeV-range masses. The interaction Lagrangian is given as,

$$\mathscr{L} \supset -\bar{\nu}_L m_D N_R - \bar{S}_L M N_R - \frac{1}{2}\bar{S}_L\, \nu S_L^C + \text{H.c.} \tag{6.2}$$

Here, we have suppressed the generation indices but otherwise, m_D, M, and μ are all 3×3 matrices. These 3×3 mass matrices can be arranged as a 9×9 neutrino mass matrix in the basis (ν_L, N_L^C, S_L):

$$M_\nu = \begin{pmatrix} 0 & m_D^T & 0 \\ m_D & 0 & M^T \\ 0 & M & \mu \end{pmatrix}; \tag{6.3}$$

For $\mu \ll m_D \ll M$, we get the effective neutrino mass matrix after diagonalising the 9×9 mass matrix. The masses of the SM neutrinos are given as, $m_\nu = \; m_D^T (m^T)^{-1} \mu \, M^{-1} m_D$. Thus, there is a double suppression that allows another scale below the GUT scale. If m_D at the electroweak scale, M at the TeV scale, and μ at the KeV scale, then one can get SM neutrinos at the sub-eV scale (see, e.g., Ref. [276]).

We consider the parameter regions where the RHNs are lighter than LQs so they can decay exclusively through the RHN+jet decay mode. For the LHC to detect their signatures, the RHNs should not be long-lived and decay to SM particles within the detectors. Generally, the strongest collider bounds on the RHNs come from the searches for the same-sign dilepton pairs, the signature of the Majorana nature of the RHNs. However, these bounds do not affect our analysis as the RHNs are pseudo-Dirac types in ISM. They decay mainly through the $\nu_R \to W^\pm \ell^\mp$ and $\nu_R \to Z/h\ \nu_\ell$ processes in roughly 2 : 1 : 1 ratio [276, 277].

6.2 Scalar and vector leptoquark models

Generally, a quark and a neutrino of different generations can simultaneously couple with a LQ. Below, we list the scalar and vector LQs which couple to the RHNs and light quarks [10].

6.2.1 Scalar LQs

■ $\tilde{R}_2 = (\overline{\mathbf{3}}, \mathbf{2}, 1/6)$: The interaction of $\tilde{R}_2$ can be written as follows,

$$\mathcal{L} \supset \tilde{y}_{2\,ij}^{\overline{LR}}\ \bar{Q}_L^{i,a} \tilde{R}_2^a \nu_R^j + \text{H.c.}, \tag{6.4}$$

where $\bar{Q}_L$ denotes the left-handed quark doublet, $a, b = 1, 2$ are the $SU(2)$ indices, and $\epsilon = i\sigma^2$. The terms relevant to our analysis are

$$\mathcal{L} \supset \tilde{y}_{2\ ii}^{\overline{LR}}\ \bar{u}_L^i\ \nu_R^i \tilde{R}_2^{2/3} + \tilde{y}_{2\ ii}^{\overline{LR}}\ \bar{d}_L^i\ \nu_R^i \tilde{R}_2^{-1/3} + \text{H.c.} \tag{6.5}$$

Since we consider the interactions with second-generation quarks and leptons, the Lagrangian simplifies as,

$$\mathcal{L} \supset \tilde{y}_{2\ 22}^{\overline{LR}}\ \bar{c}_L^i\ \nu_R^2 \tilde{R}_2^{2/3} + \tilde{y}_{2\ 22}^{\overline{LR}}\ \bar{s}_L^i\ \nu_R^2 \tilde{R}_2^{-1/3} + \text{H.c.} \tag{6.6}$$

Here, ν_R^2 denotes the second generation RHN.

■ $S_1 = (\overline{\mathbf{3}}, \mathbf{1}, 1/3)$: The interaction Lagrangian of S_1 coupling exclusively to RHN and quark is given as,

$$\mathcal{L} \supset -\bar{y}_{1\,ii}^{RR}\ \bar{d}_R^{C\ i} S_1 \nu_R^i + \text{H.c.} \tag{6.7}$$

The relevant interactions are,

$$\mathcal{L} \supset -\bar{y}_{1\,22}^{RR}\ \bar{s}_R^{C\ i} S_1 \nu_R^2 + \text{H.c.} \tag{6.8}$$

■ $\underline{\bar{S}_1 = (\overline{\mathbf{3}}, \mathbf{1}, -2/3)}$: The relevant term is

$$\mathscr{L} \supset +\bar{y}^{\overline{RR}}_{1\,22}\,\bar{c}^{C\ i}_{R}\bar{S}_1\,\nu^2_R + \text{H.c.} \tag{6.9}$$

6.2.2 Vector LQs

■ $\underline{\tilde{V}_2 = (\overline{\mathbf{3}}, \mathbf{2}, -1/6)}$: The RHN interaction of $\tilde{V}_2$ can be written as

$$\mathscr{L} \supset \tilde{x}^{\overline{LR}}_{2\,ij}\bar{Q}^{C\ i,a}_{L}\gamma^{\mu}\epsilon^{ab}\tilde{V}^{b}_{2,\mu}\,\nu^j_R + \text{H.c.}, \tag{6.10}$$

which gives us the terms relevant to our analysis:

$$\mathscr{L} \supset \tilde{x}^{\overline{LR}}_{2\ ii}\ \bar{u}^{C\ i}_{L}\gamma^{\mu}\,\nu^i_R\tilde{V}^{-2/3}_{2,\mu} -\ \tilde{x}^{\overline{LR}}_{2\ ii}\ \bar{d}^{C\ i}_{L}\gamma^{\mu}\,\nu^i_R\tilde{V}^{-1/3}_{2,\mu} + \text{H.c.} \tag{6.11}$$

■ $\underline{\bar{U}_1 = (\overline{\mathbf{3}}, \mathbf{1}, -1/3)}$: The only relevant term for $\bar{U}_1$ is as follows,

$$\mathscr{L} \supset \bar{x}^{\overline{RR}}_{1\,ii}\ \bar{d}^i_R\gamma^{\mu}\bar{U}_{1,\mu}\,\nu^i_R + \text{H.c.} \tag{6.12}$$

■ $\underline{U_1 = (\overline{\mathbf{3}}, \mathbf{1}, 2/3)}$: The relevant term for U_1 is as follows,

$$\mathscr{L} \supset \bar{x}^{\overline{RR}}_{1\,ii}\ \bar{u}^i_R\gamma^{\mu}\bar{U}_{1,\mu}\,\nu^i_R + \text{H.c.} \tag{6.13}$$

As mentioned in chapters 3 and 6, the vLQs have an additional parameter κ in the Lagrangian. Here, we consider two benchmark values, $\kappa = 0$ and $\kappa = 1$.

For our study, we will focus on the second-generation interactions, i.e., we will consider the cases where LQs mostly decay to a second-generation quark and a second-generation RHN (which produces a muon in the final state). This is mainly to obtain a conservative estimate of this channel's prospects (the first-generation interactions will lead to better prospects owing to the larger PDFs, and the third-generation interactions will produce third-generation fermions, which require separate analysis strategies) and make use of the superior muon-detection efficiency than those for the other leptons. However, the second-generation case is interesting for another reason. So far, while studying the LHC phenomenology of LQs, we have ignored the effect of quark mixing. However, if a LQ directly couples with a left-handed quark of a particular generation, it gets coupled with the quarks of the other two generations through the CKM matrix. Hence, even if we start with only second-generation interactions, the LQs will couple to the first-generation quarks enhancing the production cross sections. This effect is most prominent in the second-generation case.

6.2.3 Phenomenological models

As we did in the cases with LQs decaying to a top and a lepton [64, 78, 259], we introduce simple phenomenological Lagrangians which can be mapped to the LQ models:

$$\mathscr{L} \supset \lambda_1 \bar{s}_L \nu_R \phi_1 + \lambda_2 \bar{c}_L \nu_R \phi_2 + \text{H.c.}, \tag{6.14}$$

$$\mathscr{L} \supset \Lambda_1 \bar{s}_R (\gamma \cdot \chi_1) \nu_R + \Lambda_2 \bar{c}_R (\gamma \cdot \chi_2) \nu_R + \text{H.c.} \tag{6.15}$$

Here, ϕ_n denotes a charge $n/3$ sLQ and χ_n denotes a charge-$n/3$ vLQ. For the interactions with the right-handed quarks (i.e., for the weak-singlet LQs), there is no quark mixing and hence, it is easy to map the above Lagrangians to the models. For instance, the ϕ_1 term in Eq. (5.15) can be mapped to $S_1(\overline{\mathbf{3}}, \mathbf{1}, 1/3)$ with $\lambda_1 = -\bar{y}^{RR}_{1ii}$ (in this case, the s_L in the phenomenological Lagrangian actually represents the charge-conjugate state of a right-handed s quark). Similarly, the χ_2 term in Eq. (5.18) maps to $U_1 = (\overline{\mathbf{3}}, \mathbf{1}, 2/3)$ with $\Lambda_2 = \bar{x}^{\overline{RR}}_{1ii}$. To map the interactions of the doublet LQs ($\tilde{R}_2$ or $\tilde{V}_2$), we can set $\lambda_1 = \lambda_2$ (or $\Lambda_1 = -\Lambda_2$) and replace s_L by $[V_{\text{CKM}}]_{2j} d^j_L$ (where d^j is a down-type quark of generation j) if the LQ is aligned with the up-type quarks or c_L by $[V^\dagger_{\text{CKM}}]_{2j} u^j_L$ (where V_{CKM} is the CKM quark-mixing matrix) if the LQ is aligned with the down-type quark basis. We assume all couplings to be real for simplicity.

6.3 LHC phenomenology

In the above models, both pair and single productions of LQs lead to a pair of RHNs and high-p_T jets. Then there is also the $qq \to \nu_R \nu_R$ process via a t-channel LQ exchange. As we saw earlier, the single production depends on the LQ-q-ν_R coupling as λ^2 and the t-channel process as λ^4. This coupling (and the parameter space in general) remains unexplored. Hence, if it is large [i.e., $\mathcal{O}(1)$], both single and t-channel processes are relevant, especially for the higher LQ masses. In fact, for a very heavy LQ, the t-channel process directly producing a RHN pair (which we can also think of as the indirect production of the LQ) becomes the leading one. We show the dependence of the cross section of each production mode on the mass of the LQ in Fig. 6.1.

The figures marked as up- or down-aligned correspond to the cases when the LQ is aligned with the left-handed up-type or down-type quarks, respectively (if the LQ couples with the right-handed s or c quark, quark mixing does not affect our analysis). As explained above, the cross sections are generally larger in the presence of quark mixing (see, e.g., Figs. 6.1a and 6.1b) since, in that case, the first-generation quarks can also contribute to the initial states. This can also be

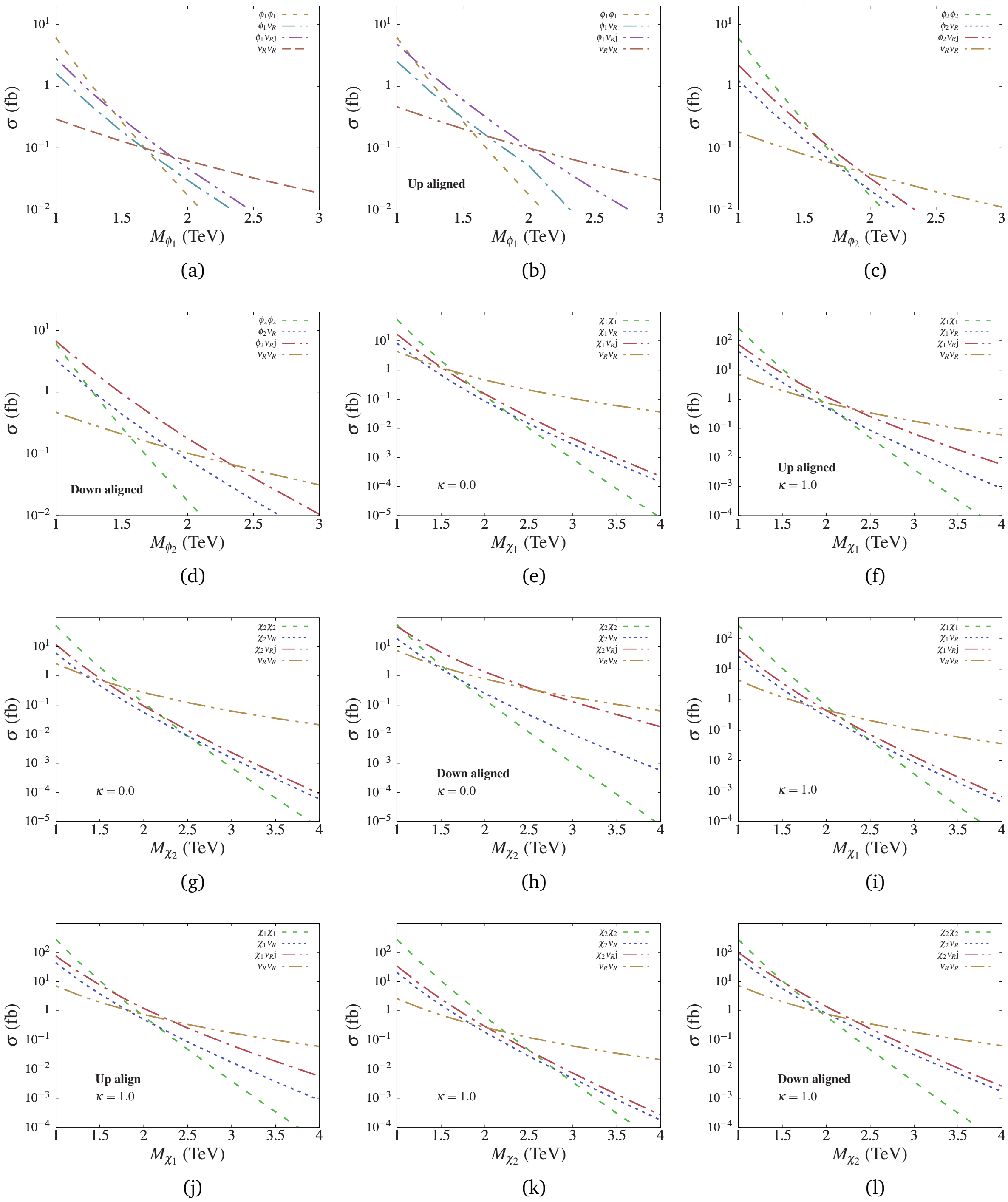

Figure 6.1: Cross-sections of different production modes of sLQs [(a) – (d)] and vLQs with $\kappa = 0$ [(e) – (h)] and $\kappa = 1$ [(i) – (l)]. We also show the cross-section of RHN pair production through t-channel LQ exchange. The LQ single productions and RHN pair production process are computed for $\lambda(\Lambda) = 1$.

inferred from the fact the cross sections are significantly larger in the up-aligned cases, especially for the single LQ production and t-channel process.

In principle, LQs decaying exclusively through RHN can be lighter than a TeV since there are no direct experimental bounds on them. Here, however, we mainly look at the $M_{\rm LQ} \geq 1$ TeV and $M_{\nu_R} \sim 500$ GeV region. In the case of RHNs coming from vLQs we consider the scenarios with extra gauge coupling $\kappa = 0$ and $\kappa = 1$ [10].

6.3.1 RHN decay modes

The RHN neutrino can decay to a W boson and a charged ℓ a Z boson and a neutrino, or a H boson and a neutrino. For our study, we consider the first two decay modes (Sophisticated techniques such as machine learning would be better suited to study the RHN neutrino decay to a H boson and a neutrino). Hence, a pair of RHNs would lead to two charged leptons and at least one boosted W boson or a single charged lepton and missing energy and a boosted Z boson. We classify the RHN pair production in terms of the charged leptons in the final state as follows,

(a) **Monolepton final state**: Here, we consider one of the RHNs to decay to a W boson and a muon and the other to decay to a Z boson and a neutrino. The different production and decay modes of RHNs with monolepton final state are as follows,

  – Pair Production mode

$$pp \;\to\; \phi\phi/\chi\chi \to (j\,\nu_R)(j\,\nu_R) \to \mu^{\pm}\, W_h^{\mp}\, Z_h\, \nu_L + \text{jet(s)} \tag{6.16}$$

  – Single Production mode

$$pp \;\to\; \phi/\chi\;\nu_R\;(+j) \to (j\,\nu_R)(j\,\nu_R) \to \mu^{\pm}\, W_h^{\mp}\, Z_h\, \nu_L + \text{jet(s)} \tag{6.17}$$

  – RHN Pair Production via t-channel LQ

$$pp \;\to\; \nu_R\,\nu_R\;(+j) \;\to \nu_R\,\nu_R\;(+j) \to \mu^{\pm}\, W_h^{\mp}\, Z_h\, \nu_L + \text{jet(s)} \tag{6.18}$$

(b) **Dilepton final state**: Here, both the RHNs decay to a W boson and a muon. We consider only oppositely charged muons in the final state. Thus, we obtain dimuon in the final state and a couple of fatjets. Another way to obtain dimuon in the final state is to decay both the RHNs to a Z boson and a neutrino. Then, we can obtain the pair of oppositely-charged muons from the leptonic decay of one Z boson, and the other decays hadronically to a fatjet.

However, we do not consider this mode because as one applies the Z-veto cut to suppress the large Drell-Yan dilepton background, the signal events from the leptonic decays of Z are also cut out.

The different production and decay modes are as follows,

- Pair Production mode

$$pp \;\rightarrow\; \phi\phi/\chi\chi \rightarrow (j\,\nu_R)(j\,\nu_R) \rightarrow \left\{ \begin{array}{l} \mu^\pm\mu^\mp\, W_h^\pm W_h^\mp + \text{jet(s)} \\ \nu_L\,\nu_L Z_h Z_\mu + \text{jet(s)} \end{array} \right\} \tag{6.19}$$

- Single Production mode

$$pp \;\rightarrow\; \phi/\chi\;\nu_R\;(+j) \rightarrow (j\,\nu_R)(j\,\nu_R) \rightarrow \left\{ \begin{array}{l} \mu^\pm\mu^\mp\, W_h^\pm W_h^\mp + \text{jet(s)} \\ \nu_L\,\nu_L Z_h Z_\mu + \text{jet(s)} \end{array} \right\} \tag{6.20}$$

- RHN Pair Production via t-channel LQ

$$pp \;\rightarrow\; \nu_R\nu_R\;(+j) \;\rightarrow \nu_R\,\nu_R\;(+j) \rightarrow \left\{ \begin{array}{l} \mu^\pm\mu^\mp\, W_h^\pm W_h^\mp + \text{jet(s)} \\ \nu_L\,\nu_L Z_h Z_\mu + \text{jet(s)} \end{array} \right\} \tag{6.21}$$

One could also get more than two muons in the final state, by considering the leptonic decays of the W and Z bosons. However since the leptonic branching ratios of these heavy gauge bosons is smaller than their hadronic decays, we do not consider final states with more than two muons. The subscripts h and μ denote the hadronic and leptonic decays of vector bosons, respectively.

6.4 Search strategy

Keeping in spirit with our previous studies [98, 99] where we showed how one could systematically combine pair and single production processes leading to the same final states without double counting. Later, in Refs. [64, 78, 100, 259], we further demonstrated the usefulness of it. Here, we extend this strategy to the pair production of RHNs.

6.4.1 Signal selection

We discuss signal selection criteria for monolepton and dilepton events as follows:

(a) A monolepton event must have contain exactly one high-p_T muon. This muon comes from the decay of the heavy RHN to a W and a muon and hence would possess high-p_T. It should have at least one high-p_T AK4 jet. This AK4 jet comes from a TeV scale LQ decaying to a RHN and a jet, hence the high-p_T (see chapter 5 for the definitions of AK4 and AK8 jets.)

(b) In the case of dilepton events, we demand the signal to contain a pair of opposite-sign muons and one of them should have a high-p_T. In addition to this, we demand at least one high-p_T AK4 jet and at least one AK8 fatjet.

6.4.2 Background channels

Below We list the background proceeses relevant to the dilepton and monolepton final state seperately. These background processes have been generated with some basic generation-level cuts to save computation time.

1. Monolepton final state :
   - W_ℓ $(+2j)$
   - $W_\ell Z_h$ $(+2j)$
   - Z_ℓ $(+2j)$
   - $W_\ell W_h$ $(+2j)$
   - $t_h W_\ell + t_\ell W_h$
   - $t_\ell + b/j$
2. Dilepton final state :
   - $W_h Z_\ell$ $(+2j)$
   - $W_\ell W_\ell$ $(+2j)$
   - $t_\ell W_\ell$ $(+2j)$
   - $t_\ell t_\ell$ $(+2j)$

h denotes hadronic decay mode and ℓ denotes leptonic decays. While generating the processes with very high cross-sections, we apply some basic generational-level cuts to save computation time. We list only those processes which contribute For the dilepton final state, the W_ℓ+jets process can act as a background since a jet can be misidentified as a lepton. In fact, it is one of the major backgrounds for the RHN searches with same-sign dilepton final states. Since we consider only opposite-sign lepton pairs, in our case, the contribution is not important as the jet-faking-lepton efficiency is very small, $\sim 10^{-4}$ [278].

6.4.3 Signal and background cuts

We sequentially apply the following analysis level cuts on our monolepton and dilepton signals and their corresponding background process.

(a) **Cuts on dilepton final state**:

- Selection of high p_{T} Leptons and jets ($\mathfrak{C}_1$) : $p_{\mathrm{T}}(\mu) > 220$ GeV, $p_{\mathrm{T}}(j_1) > 200$ GeV, No b-tagged jet
- Identification of fatjet ($\mathfrak{C}_2$) : $p_{\mathrm{T}}(\mathrm{fj}_{\phi(\chi)}) > 120\ (180)$ GeV,
  $\tau_{21} < 0.3$,
  $65 < M(\mathrm{fj}) < 100$ GeV,
  $\Delta R(\mathrm{fj}, \mu) > 0.8$
- Dilepton invariant mass ($\mathfrak{C}_3$) : $M(\mu, \mu) > 150$ GeV
- Scalar cuts ($\mathfrak{C}_4$) : $S_{\mathrm{T}} > 1400$ GeV, $\mathrm{fj}_{\mathrm{H_T}} > 600$ GeV

(b) **Cuts on monolepton final state**:

- Selection of high p_{T} Leptons and jets ($\mathfrak{C}_1$) : $p_{\mathrm{T}}(\mu) > 200$ GeV,
  $p_{\mathrm{T}}(j_1) > 200$ GeV,
  No b-tagged jet
- Identification of fatjet ($\mathfrak{C}_2$) : $p_{\mathrm{T}}(\mathrm{fj}) > 80$ GeV,
  $\tau_{21} < 0.3$,
  $65 < M(\mathrm{fj}) < 100$ GeV,
  $\Delta R(\mathrm{fj}, \mu) > 1.0$
- Dilepton invariant mass ($\mathfrak{C}_3$) : –
- Scalar cuts ($\mathfrak{C}_4$) : $S_{\mathrm{T}} > 1200$ GeV, $\not{E}_T > 150$ GeV, $\mathrm{fj}_{\mathrm{H_T}} > 600$ GeV

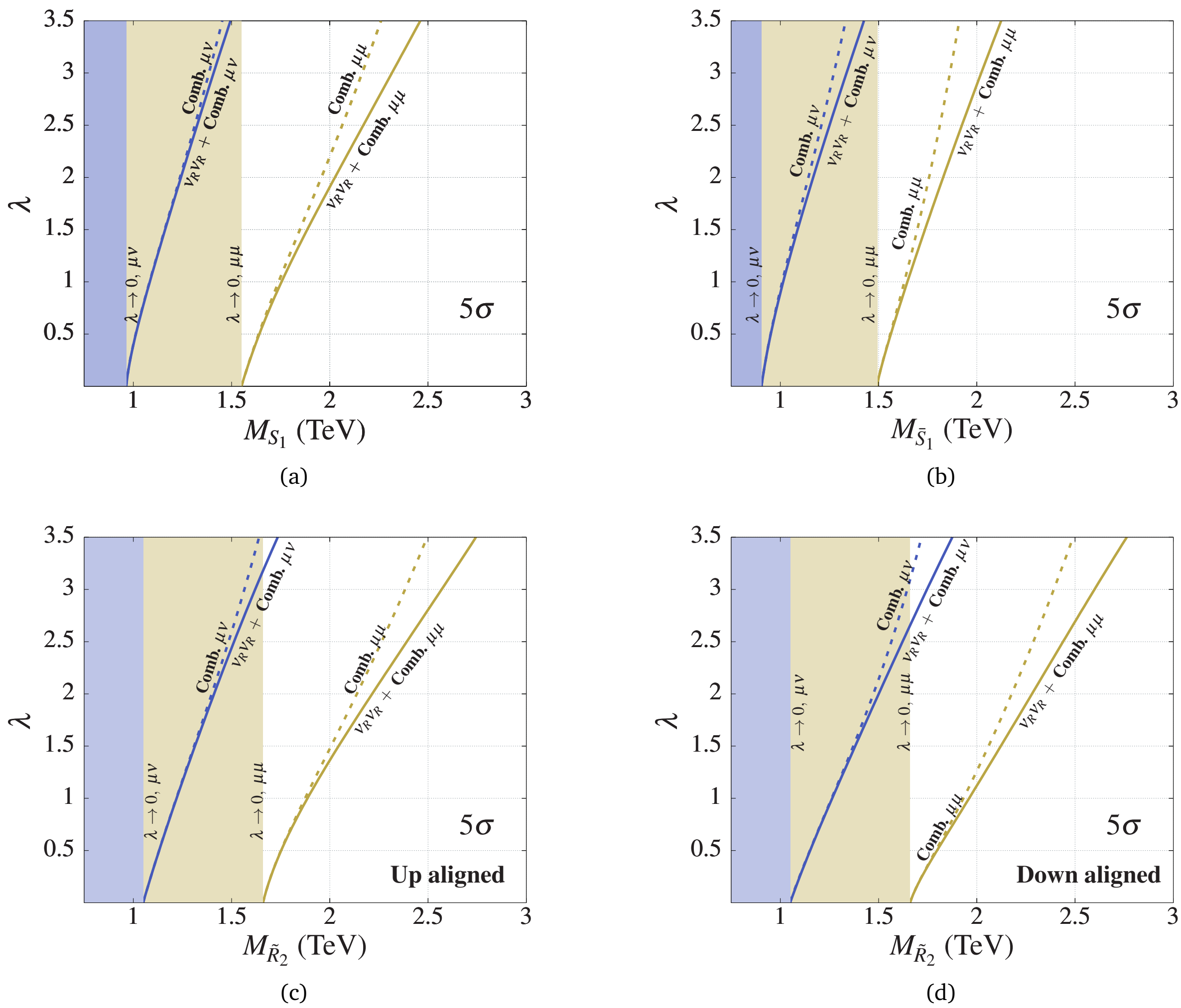

Figure 6.2: We show the least value of new coupling λ needed to observe the signals with 5σ significance as a function of mass at the HL-LHC. These plots are generated for $M_{\nu_R} = 500$ GeV. The QCD regions ($\lambda \to 0$; dominated by LQ pair productions) in the monolepton and dilepton channels are shown with solid colours; the dashed lines are obtained by combining the LQ pair and single production events. Combining single-production events with pair-production events enhances the prospects. However, the prospects improve even further for high couplings since the RHN pair production via LQ exchange also contributes to the signals and enhances the significance (solid lines).

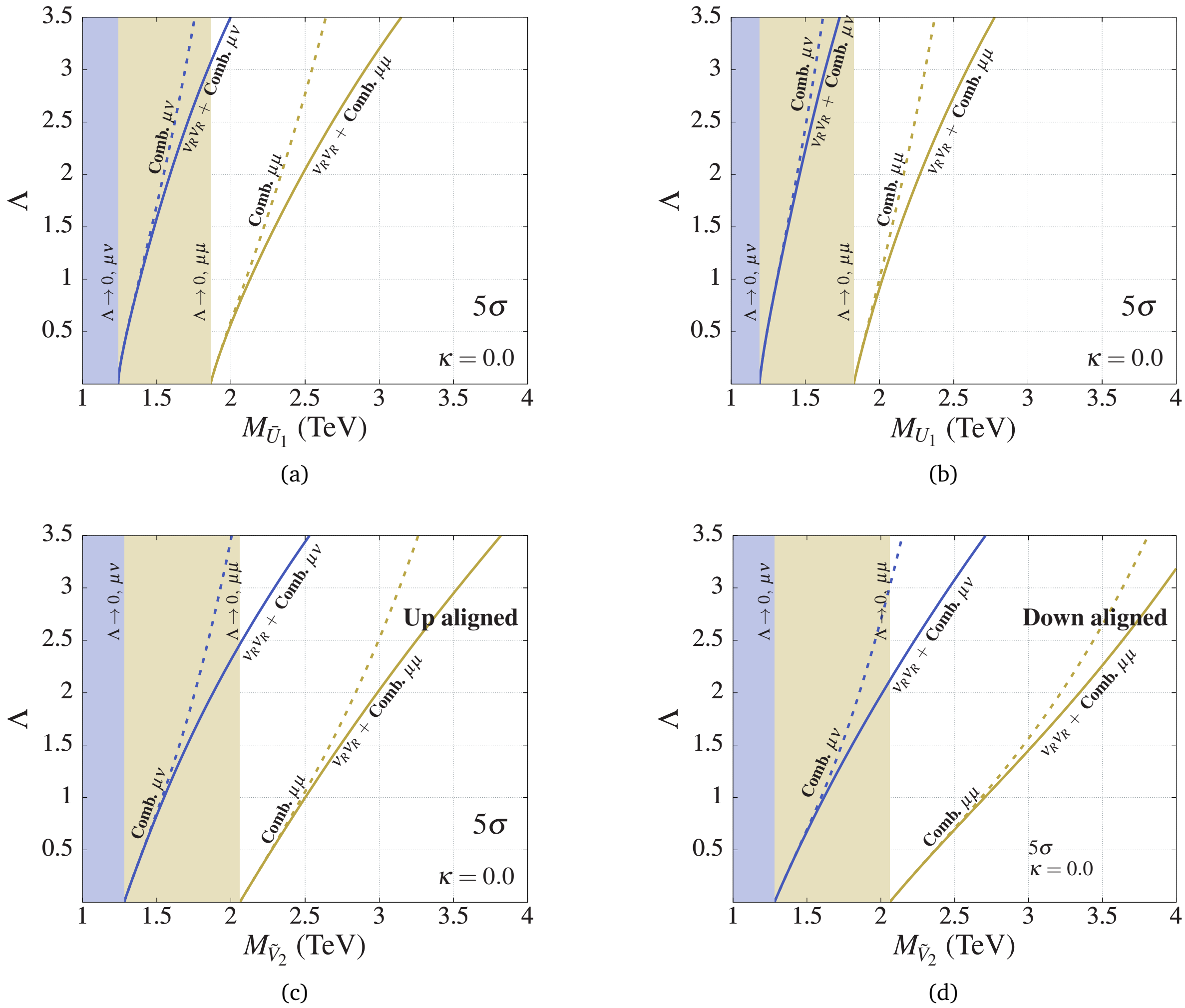

Figure 6.3: Similar to Fig. 6.2, but here we show the 5σ significance as function of Λ and M_χ for $\kappa = 0$.

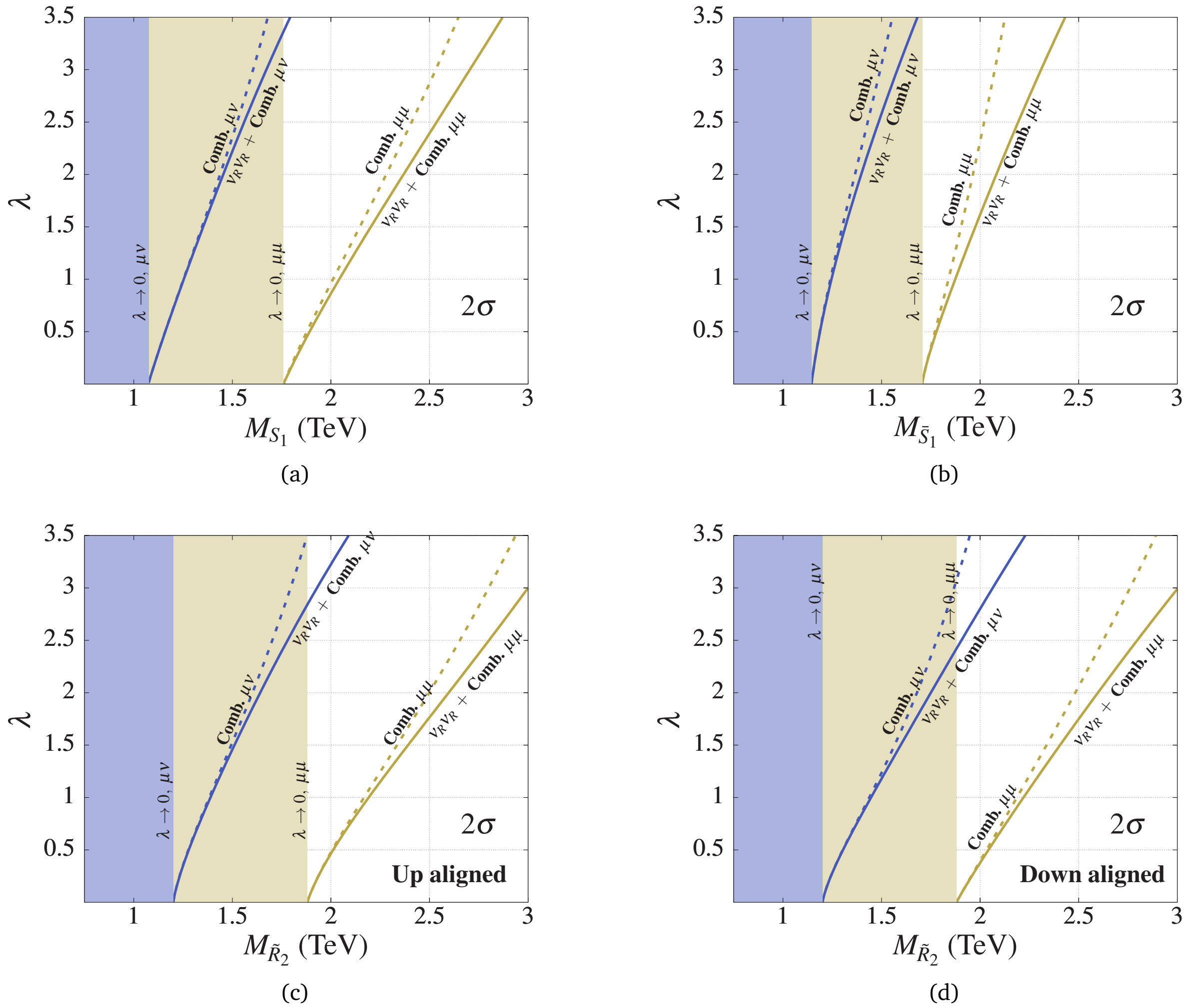

Figure 6.4: The least values of the new coupling λ needed to observe the signals with 2σ significances as functions of masses at the HL-LHC. Rest are same as Fig. 6.2.

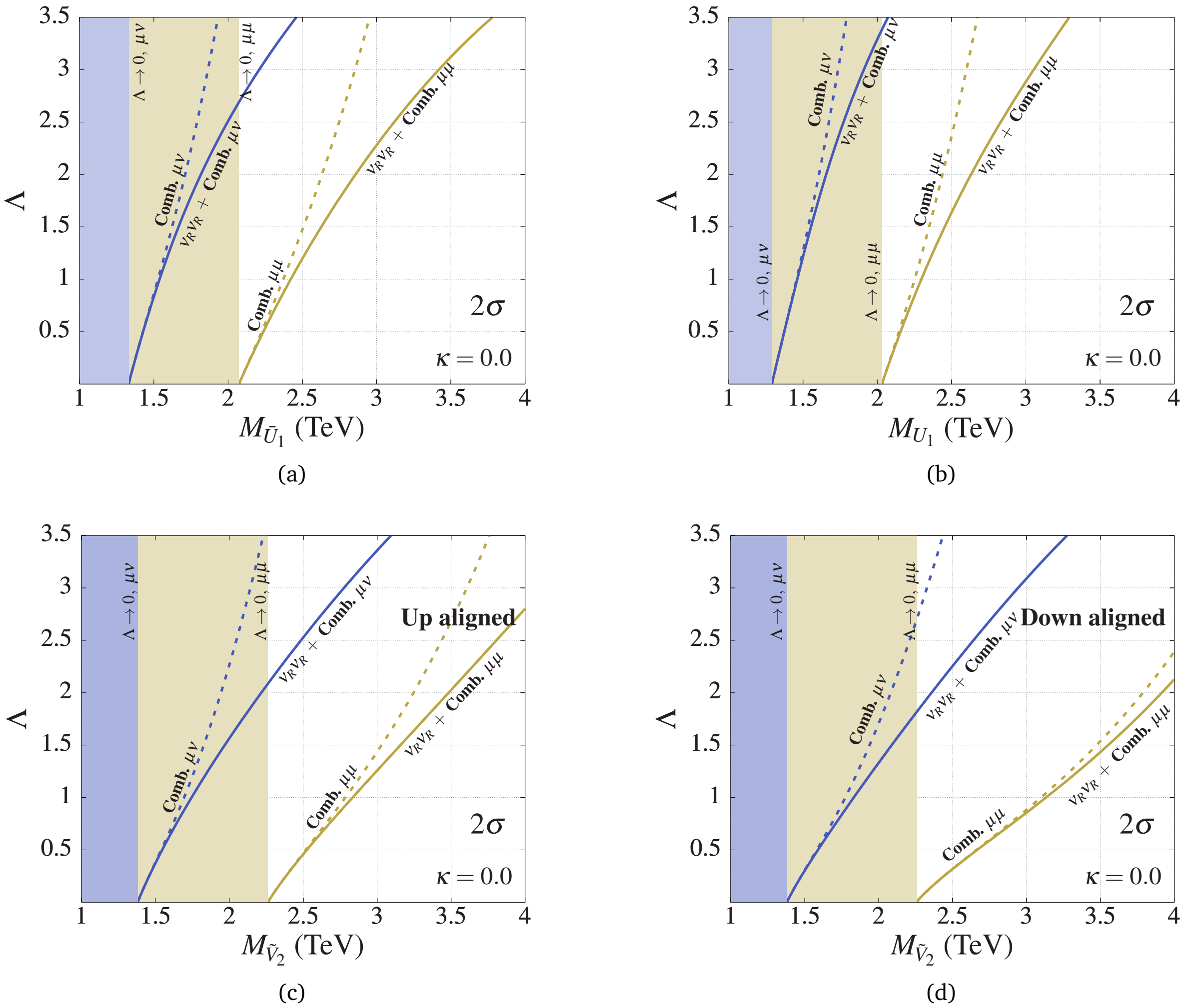

Figure 6.5: The least values of the new coupling Λ needed to observe the signals with 2σ significances as functions of masses at the HL-LHC. Rest are same as Fig. 6.2.

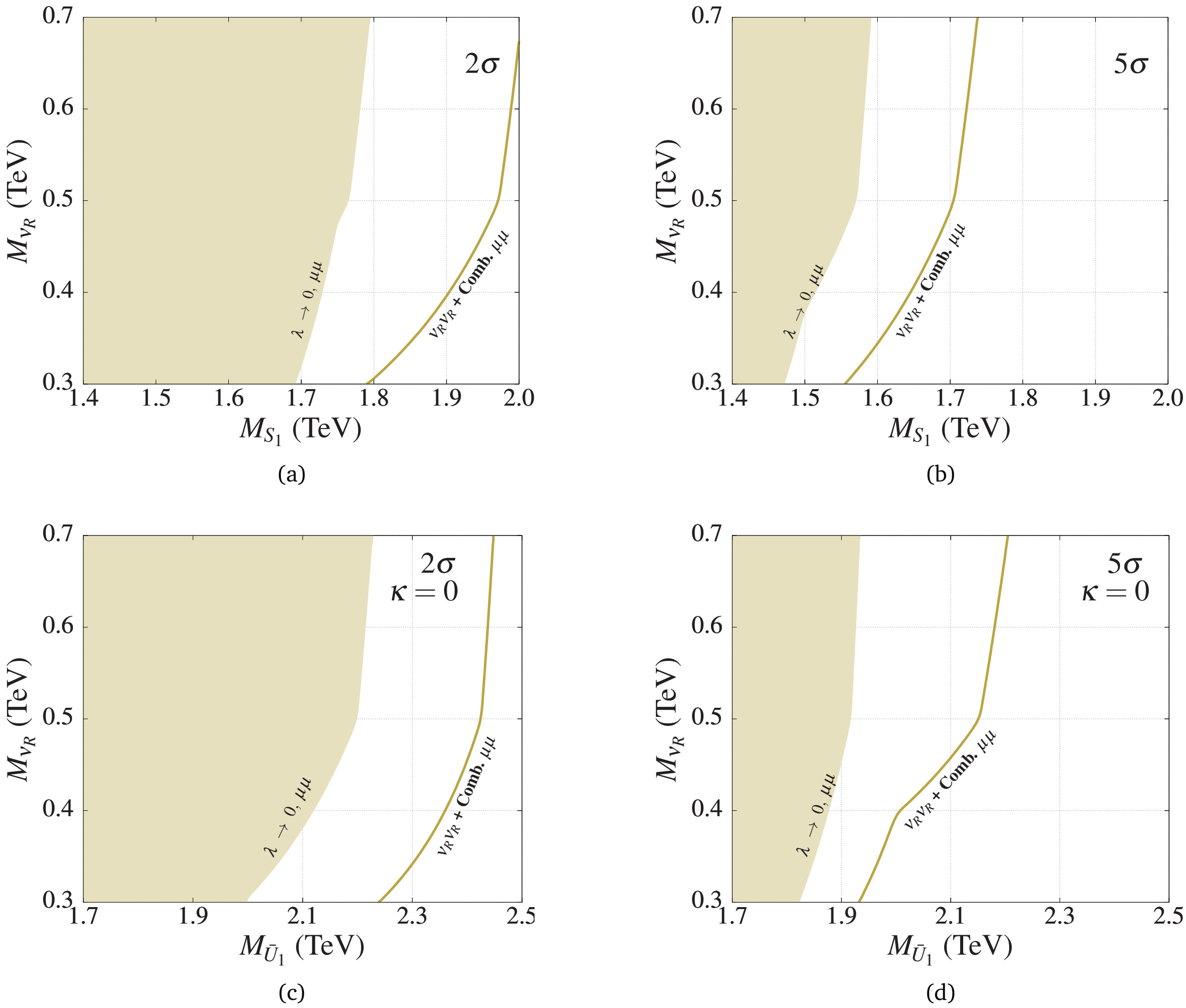

Figure 6.6: The [(a), (c)] 2σ and [(b), (d)] 5σ contours in the dilepton mode on the $M_{S_1}/M_{\tilde{U}_1}$–M_{ν_R} plane. The combined contours are obtained for $\lambda, \Lambda = 1$.

6.5 Results

We use the same computation packages as in previous chapters to generate the model files, event generation, showering, and detector simulations. We estimate the signal significance from the binned data using the Liptak-Stouffer (weighted) $\mathscr{Z}$-score method. We explain it in detail in appendix A. We now discuss the important results and offer some key insights.

We plot the 5σ (discovery) significance contours on the $M_{\rm LQ}$–λ/Λ planes for the sLQs and vLQs in Figs. 6.2 and 6.3 respectively. These plots show the minimum coupling required to obtain 5σ significance for a given mass of the LQ. We show similar plots for the 2σ exclusion limits in Figs. 6.4 and 6.5 for the sLQs and vLQs, respectively. We fix the mass of the RHN at $M_{\nu_R} = 500$ GeV. The olive colour denotes the dilepton final state and the violet colour denotes the monolepton final state. The solid regions denote the discovery reaches or exclusion limits obtained with only the pair production mode; $\lambda/\Lambda \to 0$ implies a coupling small enough to suppress the single productions and the t-channel LQ exchange but not enough to form displaced vertices. The dashed contour lines denote the 5σ reaches or the 2σ limits when one considers events from the pair and single production modes. Whereas, the solid lines indicate the 5σ reach or the 2σ limits when one considers events from the pair, single, and t-channel LQ-induced RHN pair production modes. We see that the minimum values of coupling needed to obtain the required significance come down when all production modes are combined.

The 5σ discovery reaches for the charge-1/3 S_1 and the charge-2/3 $\bar{S}_1$ go as high as 1.6 and 1.5 TeV, respectively, in the dilepton channel with the pair-only signal. Once we include the single production and the t-channel LQ-exchange contributions, the reaches go up to 1.8 and 1.6 TeV, respectively, for $\lambda = 1$. The reach is higher in the case of S_1 because, in this case, the quark-initiated single and RHN pair production process can come from a s quark whereas for $\bar{S}_1$ these are c-initiated processes. Hence, the contribution is higher as we know the s quark PDF is more than the c quark PDF.

In the case of vector LQs we obtain similar results. For the charge 1/3 vLQ ($\bar{U}_1$) and the charge 2/3 (U_1), the 5σ reaches in the pair-only mode are about 1.9 and 1.8 TeV, respectively. For $\lambda = 1$, the same RHN mass and $\kappa = 0$, once we combine the single production and the t-channel events, the reach enhances to 2.1 and 2.0 TeV. These numbers can go up if we include the additional $g\chi\chi$ coupling–κ. Setting $\kappa = 1$, the 5σ reaches for $\bar{U}_1$ and U_1 go to about 2.2 and 2.1 TeV, respectively, in the pair-only mode. On including single and t-channel mode with $\Lambda = 1$, the reach enhances to 2.4 and 2.2 TeV. In the absence of discovery, we provide the 2σ

exclusion limits. For $M_{\nu_R} = 500$ GeV, the HL-LHC can exclude up to 2.0 and 1.9 TeV in the cases of S_1 and $\bar{S}_1$, respectively. The exclusion limits for $\bar{U}_1$ and U_1 for $\kappa = 0$ are 2.4 and 2.3 TeV, respectively in the dilepton mode. For $\kappa = 1$, the 2σ limits change to 2.6 and 2.5 TeV, respectively in the combined mode. The enhancement occurs because as we show in Fig. 6.1, for a nonzero κ, we get additional diagrams in the pair and single production modes and the cross-section goes up.

We find the results for the doublet model more promising for two reasons. The doublet LQ contains two components of different charges. The selection criteria we proposed doesn't depend on the charge of the LQ. It is specific to the final state. Thus, we can systematically combine individual components leading to enhancement in the signal. Secondly, we show that in the sLQ $\tilde{R}_2$, one component couples with the first generation quark through the CKM mixing. This could be either of the two charged components–1/3 or 2/3, depending on how the LQ is aligned. This enhances the cross-sections. In Fig. 6.2c and Fig. 6.2d, we show the 5σ discovery contour for the pair-only (solid regions) and combined modes (solid and dashed lines) for the dilepton (yellow) and monolepton (violet) for $\tilde{R}_2$ aligned with up-type and down-types quarks respectively. It is evident from the figures that since the CKM mixing leads to enhancement in the cross-section, this leads to that fact now, for a given mass of LQ, one can obtain 5σ discovery for a lower new coupling value. A similar trend can be seen for the vLQ $\tilde{V}_2$ in Figs. 6.3c and 6.3d. In Fig. 6.6, We show the 2σ and 5σ contours on the $M_{S_1,\bar{U}_1}$–M_{ν_R} planes to demonstrate how the signal significance varies with M_{ν_R}. Since the RHNs appear only in the decay, we do not expect any significant dependence on M_{ν_R} (we only show the $S_1, \bar{U}_1$ plots for illustration). We observe a drop in the sensitivity in the $M_{\nu_R} \ll M_{LQ}$ region. If the $M_{LQ} - M_{\nu_R}$ mass gap is large, the RHN becomes highly boosted, and the decay products of RHN become very collimated, making it difficult to isolate the W-like fatjet from the selected muon. This requires a different strategy, and has been discussed in Ref. [279].

Chapter

7

Summary and conclusions

Leptoquarks are special types of BSM scalars or vector bosons that simultaneously couple to leptons and quarks. They appear in various BSM theories. They are currently popular in the literature as they can explain experimental anomalies like the recent CDF measurement of the W boson mass, the magnetic moment of the muon $(g-2)_\mu$, and the B-anomalies, etc. In this thesis, we have studied some anomalies-motivated LQ models by scrutinising the relevant parts of the parameter spaces that survive the relevant experimental constraints. We have looked at various low-energy bounds and obtained precise, competitive and complementary bounds from the latest LHC data, thus bridging a gap between the B-physics literature and the LHC studies on LQ models. We have also looked at the discovery and exclusion prospects of all possible LQs in some interesting channels.

- We started with a U_1 vLQ model that could explain the $R_{D^{(*)}}$ and $R_{K^{(*)}}$ anomalies simultaneouly. We introduced some simple flavour ansatzes to generate the required $c\nu U_1$, $b\tau U_1$, $s\mu U_1$, and $b\mu U_1$ interactions. Adopting a minimalist approach, we looked for possibilities with only a few unknown couplings. We listed the possible single and multi-coupling scenarios in a bottom-up manner. These scenarios may appear similar from an effective-field-theory approach but their LHC perspectives (hence, the limits on them) are very different, as the production processes and decay modes differ with different new coupling(s). Based on the different final states, we considered an exhaustive list of bounds from the recent direct searches. We found that the direct bounds did not show the complete picture—one needed to consider the indirect LHC bounds on these models because they contain one or more order-one (i.e., large) coupling(s). For instance, in the case of the $R_{D^{(*)}}$-motivated single coupling scenarios, one could wrongly conclude that the LHC allows the relevant regions if one considered the direct bounds only. However, the indirect limits essentially rule out those regions.

- We recast the latest high-p_T $\tau\tau$ and $\mu\mu$ searches by systematically combining the events from all production modes of U_1 that lead to dilepton final states to obtain the indirect limits. The production modes consist of the resonant pair and single production modes and the nonresonant dilepton production via a t-channel U_1 exchange and its interference with the SM dilepton production process. We found that, in the regions of interest, the number of events from the interference term contributes the most and, since it is destructive in nature, leads to a decrease in the overall number of events. We obtain the 2σ exclusion bounds by performing a χ^2 fit on the latest $\tau\tau$ and $\mu\mu$ search data. For the lower masses of LQs, the pair production mode is majorly QCD-mediated and contributes more as compared to the nonresonant mode. But as we move over to the higher masses, the nonresonant contributions, especially the interference part, take over. Thus, it is essential to systematically combine all production modes to obtain precise bounds. We showed this quantitatively in the exclusion limits for the single coupling scenarios.

- We analysed all possible one and two-coupling scenarios of U_1. We found that in the two coupling scenarios, there were considerable overlaps between the regions relevant to the observables and the regions allowed by the LHC's direct and indirect bounds. The LHC's indirect limits are less restrictive on the $R_{K^{(*)}}$ scenarios since the $R_{K^{(*)}}$ anomalies require smaller couplings than those needed for the $R_{D^{(*)}}$ anomalies. We found that the LHC's direct bounds rule out a U_1 of mass 1.5 TeV in the $R_{K^{(*)}}$ single-coupling scenarios. However, we showed that with multiple new couplings, it is possible to obtain a 1.5 TeV U_1 that is allowed by the LHC data and can simultaneously explain the $R_{D^{(*)}}$ and $R_{K^{(*)}}$ anomalies.

- We considered a multi-component model containing a combination of a singlet and a triplet ($S_1 + S_3$) sLQ for a simultaneous explanation of the discrepancy in CDF W boson mass measurement, $(g-2)_\mu$ anomaly, and the anomalies in the $R_{D^{(*)}}$ and $R_{K^{(*)}}$ observables. The model is simple and economical, requiring only a few new couplings ($\sim$ a minimal set). Based on the assumed couplings, we considered an exhaustive list of the relevant low-energy experimental constraints and the bounds from the LHC direct searches. We found that the LHC data allowed the sLQs in our model to be about 1.5 TeV. Hence, the model is testable at the LHC. We showed that if all the couplings were perturbative, the heaviest the sLQs could become would be about 8 TeV without any additional new couplings.

- Recent experimental updates from the LHCb put the $R_{K^{(*)}}$ observables within the SM expectations. Similarly, the tension between the experimental and the SM value of R_{D^*} came down slightly in the recent experimental update. The combined measurement of the $R_{D^{(*)}}$ observable still deviated from the SM value by 3.2σ. We updated our analysis with the new values. We observed that almost all LQ models we considered remained valid possibilities. The LHC limits we obtained are unaffected by the updates.

- We also studied the prospects of LQs through boosted top quarks and high-p_T leptons at the HL-LHC. Considering all possible scalar and vector LQs that decay to a top quark and a charged lepton, we designed simple phenomenological Lagrangians suitable for experimental searches. These simple models can be easily mapped to all the scalar and vector LQ models that give us the desired final states. Often, the prospect studies focus on the LQ pair production process, which is mainly QCD-mediated and contributes more at low masses. But its contribution decreases rapidly at high masses due to phase space suppression. We devised a strategy to systematically combine the pair-production signal with the (model-dependent) single-production signal to address this shortcoming. The contribution from the single production process scales as λ^2; thus, at higher masses and for $\mathcal{O}(1)$ coupling or more, the single production contribution becomes significant. We quantitatively showed that the inclusion of single production significantly enhanced the discovery or exclusion reaches of the LQs at the HL-LHC. We found that the HL-LHC can discover a ~ 2 TeV sLQ and a ~ 2.5 TeV in the modes we considered.

- We also performed a similar prospect study for the LQs decaying exclusively to RHNs and (second-generation) quarks. This is an experimentally unexplored interesting channel as there are no direct experimental bounds on the couplings responsible for such interactions. If a LQ is heavier than the RHN, a pair of RHNs can come from the decay of the LQ (produced singly or in pairs) or via a t-channel LQ exchange. The nonresonant contribution scales as λ^4. Hence, if the unknown coupling is large enough, the nonresonant mode can contribute significantly. We considered two signal topologies producing dilepton and monolepon final states. We found that for perturbative new couplings and 500 GeV RHN, the discovery reaches for the sLQs could go as high as 3 TeV and about 4 TeV for the vLQs.

To summarise, we have performed a detailed phenomenological investigation of the TeV-scale LQ models. We have looked at their current status and future prospects. Our analyses are exhaustive and systematic and our methods are generic. They can be easily applied to other BSM scenarios (including other LQ models) as well. While our analyses are precise and sophisticated and our results are promising, more advanced computational techniques such as machine learning or multivariate analysis can improve them further. One could also investigate LQ decays to first/third-generation RHNs and quarks. One could also study the prospect of these models at other future colliders (such as the muon collider).

Appendix

A

Systematics errors

In experiments at the LHC, one has to account for the systematics. In our study of sLQs and vLQs decaying to the top and τ [259], we find our estimates get affected by systematic uncertainties. We consider two benchmark choices of 5% and 10% systematics on our background estimations. In the presence of total systematic error σ_B, Eq. (5.27) generalises to

$$\mathscr{Z} = \sqrt{2}\left((N_S + N_B)\ln\left[\frac{(N_S+N_B)(N_B+\sigma_B^2)}{N_B^2+(N_S+N_B)\sigma_B^2}\right] - \left(\frac{N_B}{\sigma_B^2}\right)^2 \ln\left[1+\frac{\sigma_B^2 N_S}{N_B(N_B+\sigma_B^2)}\right]\right)^{1/2}, \tag{A.1}$$

whose approximated form is perhaps more familiar,

$$\mathscr{Z} \approx \frac{N_S}{\sqrt{N_B+\sigma_B^2}}. \tag{A.2}$$

We find that the Eq. (A.1) severely affects the estimation of our mass limits, especially for the sLQs as their cross sections are smaller than the vLQs [280]. To overcome these effects due to systematic errors, we estimate the mass limits from binned data. We estimate the signal significance from the binned data using the Liptak-Stouffer (weighted) $\mathscr{Z}$-score method. The Metascore or the combined significance is given as,

$$\mathscr{Z} = \frac{\sum_{i=1}^{N} w_i \mathscr{Z}_i}{\sqrt{\sum_{i=1}^{N} w_i^2}}. \tag{A.3}$$

Here, $\mathscr{Z}_i$ denotes the signal significance in the i^{th} bin ($i \in \{1,2,3,\ldots,N\}$) computed from Eq. (A.1) and w_i is the corresponding weight, which is taken to be equal to the inverse of the variance in that bin. We have set the w_i's equal to the inverse of the square of the total errors, i.e.,

Comb. $\mathscr{L}$	Limit on M_{ϕ_1} (TeV)											
	(Signature: $t_h\tau_h\tau_h + t_h\tau_h\tau_\ell$)								(Signature: $t_h\tau_h$ + MET)			
	LCSS-Comb.		Pair (BR=0.5)		RC-Comb.		Pair (BR=1)		LCSS-Comb.		Pair (BR=0.5)	
	5%	10%	5%	10%	5%	10%	5%	10%	5%	10%	5%	10%
5	1.06	0.94	0.84	0.75	1.42	1.37	1.40	1.36	1.19	1.11	1.15	1.05
3	1.34	1.26	1.12	1.04	1.56	1.51	1.54	1.49	1.37	1.30	1.32	1.24
2	1.53	1.47	1.27	1.22	1.67	1.65	1.66	1.63	1.47	1.43	1.44	1.38

Table A.1: The mass limits for some sample scenarios, with 5% and 10% systematic uncertainties.

w_i^{-1} = (statistical error)^2 + (systematic error)^2 $= N_B^i + (\sigma_B^i)^2$. In Fig. A.1, we show the binned distribution for the sLQ ϕ_1 for a benchmark mass point. In Figs. A.1a and A.1b, we plot the number of signal and background events at $\mathscr{L} = 3000\text{fb}^{-1}$ as a function of the binning parameter transverse mass $[m_T(\tau, \ell, \not{E}_T)]$ for signature A. A similar figure is given for Signature B in Figs. A.1c and A.1d, with the binning variable–missing transverse energy (MET). We show the mass limits for the sLQ ϕ_1 with benchmark systematic uncertainties 5% and 10% in Table A.1.

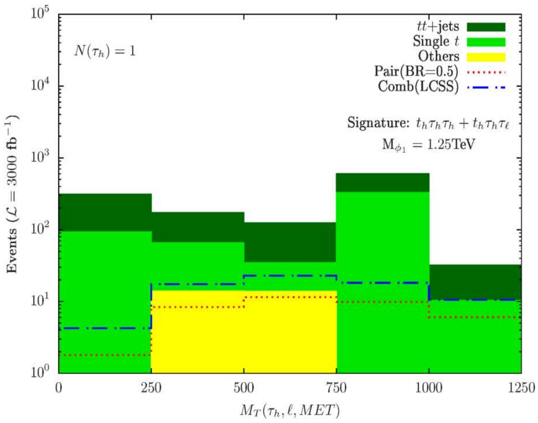

(a)

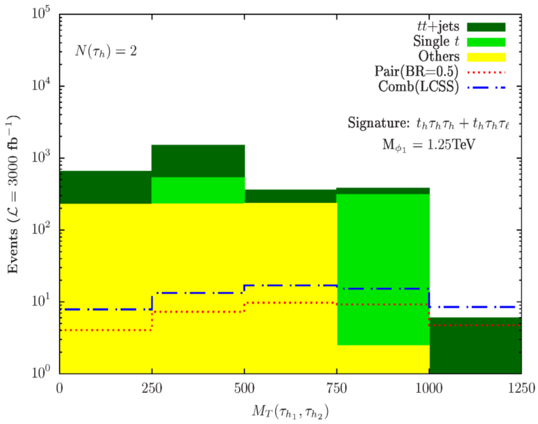

(b)

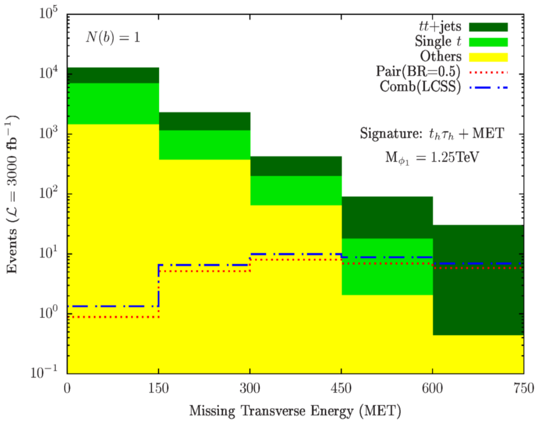

(c)

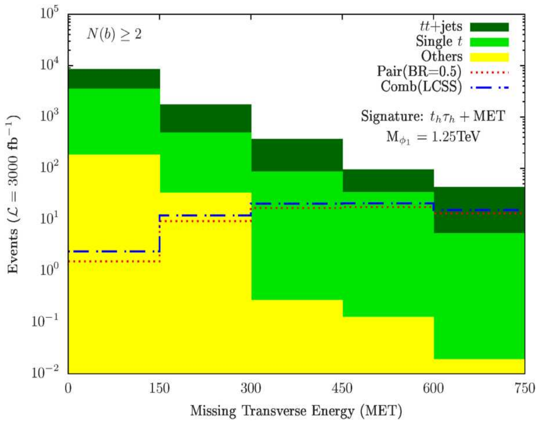

(d)

Figure A.1: The bins show the number of signal and background events in the $t_h\tau_h\tau_h + t_h\tau_h\tau_\ell$ channel [(a) and (b)] and the $t_h\tau_h$+ MET channel [(c) and (d)]. The events are obtained applying all the cuts in Sections 5.5.3.2 and 5.5.3.3, except the ones on the variables used for binning, i.e., $N(\tau_h)$ and M_T in the $t_h\tau_h\tau_h + t_h\tau_h\tau_\ell$ channel and $N(b)$ and MET in the $t_h\tau_h$+ MET channel.

Bibliography

[1] 'Standard model of elementary particles,' https://commons.wikimedia.org/wiki/File:Standard_Model_of_Elementary_Particles.svg.

[2] R. Barbier *et al.*, Phys. Rept. **420**, 1 (2005), arXiv:hep-ph/0406039 .

[3] B. Schrempp and F. Schrempp, Phys. Lett. **B153**, 101 (1985).

[4] J. C. Pati and A. Salam, Phys. Rev. **D10**, 275 (1974), [Erratum: Phys. Rev.D11,703(1975)].

[5] H. Georgi and S. L. Glashow, Phys. Rev. Lett. **32**, 438 (1974).

[6] M. Kohda, H. Sugiyama, and K. Tsumura, Phys. Lett. B **718**, 1436 (2013), arXiv:1210.5622 [hep-ph] .

[7] C. T. Hill and E. H. Simmons, Phys. Rept. **381**, 235 (2003), [Erratum: Phys.Rept. 390, 553–554 (2004)], arXiv:hep-ph/0203079 .

[8] B. Abbott *et al.* (D0), Phys. Rev. Lett. **79**, 4321 (1997), arXiv:hep-ex/9707033 .

[9] W. Buchmuller, R. Ruckl, and D. Wyler, Phys. Lett. **B191**, 442 (1987), [Erratum: Phys. Lett.B448,320(1999)].

[10] I. Doršner, S. Fajfer, A. Greljo, J. F. Kamenik, and N. Košnik, Phys. Rept. **641**, 1 (2016), arXiv:1603.04993 [hep-ph] .

[11] D. Bigi and P. Gambino, Phys. Rev. **D94**, 094008 (2016), arXiv:1606.08030 [hep-ph] .

[12] F. U. Bernlochner, Z. Ligeti, M. Papucci, and D. J. Robinson, Phys. Rev. **D95**, 115008 (2017), [erratum: Phys. Rev.D97,no.5,059902(2018)], arXiv:1703.05330 [hep-ph] .

[13] D. Bigi, P. Gambino, and S. Schacht, JHEP **11**, 061 (2017), arXiv:1707.09509 [hep-ph] .

[14] S. Jaiswal, S. Nandi, and S. K. Patra, JHEP **12**, 060 (2017), arXiv:1707.09977 [hep-ph] .

[15] Y. Amhis *et al.* (HFLAV), Eur. Phys. J. **C77**, 895 (2017), we have used the Spring 2019 averages from https://hflav-eos.web.cern.ch/hflav-eos/semi/spring19/html/RDsDsstar/RDRDs.html. For regular updates see https://hflav.web.cern.ch/content/semileptonic-b-decays., arXiv:1612.07233 [hep-ex] .

[16] M. Tanaka and R. Watanabe, Phys. Rev. D **87**, 034028 (2013), arXiv:1212.1878 [hep-ph] .

[17] F. Feruglio, P. Paradisi, and O. Sumensari, JHEP **11**, 191 (2018), arXiv:1806.10155 [hep-ph] .

[18] S. Iguro, T. Kitahara, Y. Omura, R. Watanabe, and K. Yamamoto, JHEP **02**, 194 (2019), arXiv:1811.08899 [hep-ph] .

[19] C. Bobeth, M. Misiak, and J. Urban, Nucl. Phys. B **574**, 291 (2000), arXiv:hep-ph/9910220 .

[20] C. Bobeth, A. J. Buras, F. Kruger, and J. Urban, Nucl. Phys. B **630**, 87 (2002), arXiv:hep-ph/0112305 .

[21] R. Alonso, B. Grinstein, and J. Martin Camalich, JHEP **10**, 184 (2015), arXiv:1505.05164 [hep-ph] .

[22] L. Calibbi, A. Crivellin, and T. Ota, Phys. Rev. Lett. **115**, 181801 (2015), arXiv:1506.02661 [hep-ph] .

[23] S. Fajfer and N. Košnik, Phys. Lett. B **755**, 270 (2016), arXiv:1511.06024 [hep-ph] .

[24] R. Barbieri, G. Isidori, A. Pattori, and F. Senia, Eur. Phys. J. C **76**, 67 (2016), arXiv:1512.01560 [hep-ph] .

[25] D. Bečirević, N. Košnik, O. Sumensari, and R. Zukanovich Funchal, JHEP **11**, 035 (2016), arXiv:1608.07583 [hep-ph] .

[26] S. Sahoo, R. Mohanta, and A. K. Giri, Phys. Rev. **D95**, 035027 (2017), arXiv:1609.04367 [hep-ph] .

[27] B. Bhattacharya, A. Datta, J.-P. Guévin, D. London, and R. Watanabe, JHEP **01**, 015 (2017), arXiv:1609.09078 [hep-ph] .

[28] M. Duraisamy, S. Sahoo, and R. Mohanta, Phys. Rev. **D95**, 035022 (2017), arXiv:1610.00902 [hep-ph] .

[29] D. Buttazzo, A. Greljo, G. Isidori, and D. Marzocca, JHEP **11**, 044 (2017), arXiv:1706.07808 [hep-ph] .

[30] N. Assad, B. Fornal, and B. Grinstein, Phys. Lett. B **777**, 324 (2018), arXiv:1708.06350 [hep-ph] .

[31] L. Calibbi, A. Crivellin, and T. Li, Phys. Rev. D **98**, 115002 (2018), arXiv:1709.00692 [hep-ph] .

[32] M. Blanke and A. Crivellin, Phys. Rev. Lett. **121**, 011801 (2018), arXiv:1801.07256 [hep-ph] .

[33] A. Greljo and B. A. Stefanek, Phys. Lett. B **782**, 131 (2018), arXiv:1802.04274 [hep-ph] .

[34] S. Sahoo and R. Mohanta, J. Phys. **G45**, 085003 (2018), arXiv:1806.01048 [hep-ph] .

[35] J. Kumar, D. London, and R. Watanabe, Phys. Rev. D **99**, 015007 (2019), arXiv:1806.07403 [hep-ph] .

[36] A. Crivellin, C. Greub, D. Müller, and F. Saturnino, Phys. Rev. Lett. **122**, 011805 (2019), arXiv:1807.02068 [hep-ph] .

[37] A. Angelescu, D. Bečirević, D. Faroughy, and O. Sumensari, JHEP **10**, 183 (2018), arXiv:1808.08179 [hep-ph] .

[38] J. Aebischer, A. Crivellin, and C. Greub, Phys. Rev. D **99**, 055002 (2019), arXiv:1811.08907 [hep-ph] .

[39] B. Chauhan and S. Mohanty, Phys. Rev. D **99**, 095018 (2019), arXiv:1812.00919 [hep-ph] .

[40] B. Fornal, S. A. Gadam, and B. Grinstein, Phys. Rev. D **99**, 055025 (2019), arXiv:1812.01603 [hep-ph] .

[41] M. J. Baker, J. Fuentes-Martín, G. Isidori, and M. König, Eur. Phys. J. C **79**, 334 (2019), arXiv:1901.10480 [hep-ph] .

[42] C. Hati, J. Kriewald, J. Orloff, and A. Teixeira, JHEP **12**, 006 (2019), arXiv:1907.05511 [hep-ph] .

[43] C. Cornella, J. Fuentes-Martin, and G. Isidori, JHEP **07**, 168 (2019), arXiv:1903.11517 [hep-ph] .

[44] L. Da Rold and F. Lamagna, JHEP **12**, 112 (2019), arXiv:1906.11666 [hep-ph] .

[45] K. Cheung, Z.-R. Huang, H.-D. Li, C.-D. Lü, Y.-N. Mao, and R.-Y. Tang, (2020), arXiv:2002.07272 [hep-ph] .

[46] P. Bhupal Dev, R. Mohanta, S. Patra, and S. Sahoo, Phys. Rev. D **102**, 095012 (2020), arXiv:2004.09464 [hep-ph] .

[47] S. Kumbhakar and R. Mohanta, (2020), arXiv:2008.04016 [hep-ph] .

[48] S. Iguro, M. Takeuchi, and R. Watanabe, (2020), arXiv:2011.02486 [hep-ph] .

[49] C. Hati, J. Kriewald, J. Orloff, and A. Teixeira, (2020), arXiv:2012.05883 [hep-ph] .

[50] J. Alda, J. Guasch, and S. Penaranda, (2020), arXiv:2012.14799 [hep-ph] .

[51] T. Mandal, S. Mitra, and S. Seth, Phys. Rev. **D93**, 035018 (2016), arXiv:1506.07369 [hep-ph] .

[52] D. Das, C. Hati, G. Kumar, and N. Mahajan, Phys. Rev. D **94**, 055034 (2016), arXiv:1605.06313 [hep-ph] .

[53] P. Bandyopadhyay and R. Mandal, Phys. Rev. **D95**, 035007 (2017), arXiv:1609.03561 [hep-ph] .

[54] U. K. Dey, D. Kar, M. Mitra, M. Spannowsky, and A. C. Vincent, Phys. Rev. **D98**, 035014 (2018), arXiv:1709.02009 [hep-ph] .

[55] P. Bandyopadhyay and R. Mandal, Eur. Phys. J. **C78**, 491 (2018), arXiv:1801.04253 [hep-ph] .

[56] U. Aydemir, D. Minic, C. Sun, and T. Takeuchi, JHEP **09**, 117 (2018), arXiv:1804.05844 [hep-ph] .

[57] S. Bansal, R. M. Capdevilla, A. Delgado, C. Kolda, A. Martin, and N. Raj, Phys. Rev. D **98**, 015037 (2018), arXiv:1806.02370 [hep-ph] .

[58] A. Biswas, D. Kumar Ghosh, N. Ghosh, A. Shaw, and A. K. Swain, J. Phys. **G47**, 045005 (2020), arXiv:1808.04169 [hep-ph] .

[59] R. Mandal, Eur. Phys. J. **C78**, 726 (2018), arXiv:1808.07844 [hep-ph] .

[60] A. Biswas, A. Shaw, and A. K. Swain, LHEP **2**, 126 (2019), arXiv:1811.08887 [hep-ph] .

[61] J. Roy, (2018), arXiv:1811.12058 [hep-ph] .

[62] A. Alves, O. J. P. Éboli, G. Grilli Di Cortona, and R. R. Moreira, Phys. Rev. **D99**, 095005 (2019), arXiv:1812.08632 [hep-ph] .

[63] U. Aydemir, T. Mandal, and S. Mitra, Phys. Rev. **D101**, 015011 (2020), arXiv:1902.08108 [hep-ph] .

[64] K. Chandak, T. Mandal, and S. Mitra, Phys. Rev. **D100**, 075019 (2019), arXiv:1907.11194 [hep-ph] .

[65] W.-S. Hou, T. Modak, and G.-G. Wong, Eur. Phys. J. **C79**, 964 (2019), arXiv:1909.00403 [hep-ph] .

[66] M. Bordone, O. Catà, and T. Feldmann, JHEP **01**, 067 (2020), arXiv:1910.02641 [hep-ph] .

[67] R. Padhan, S. Mandal, M. Mitra, and N. Sinha, Phys. Rev. D **101**, 075037 (2020), arXiv:1912.07236 [hep-ph] .

[68] A. Bhaskar, D. Das, B. De, and S. Mitra, Phys. Rev. D **102**, 035002 (2020), arXiv:2002.12571 [hep-ph] .

[69] P. Bandyopadhyay, S. Dutta, and A. Karan, (2020), arXiv:2003.11751 [hep-ph] .

[70] L. Buonocore, U. Haisch, P. Nason, F. Tramontano, and G. Zanderighi, Phys. Rev. Lett. **125**, 231804 (2020), arXiv:2005.06475 [hep-ph] .

[71] M. Bordone, O. Cata, T. Feldmann, and R. Mandal, (2020), arXiv:2010.03297 [hep-ph] .

[72] A. Greljo and N. Selimovic, (2020), arXiv:2012.02092 [hep-ph] .

[73] U. Haisch and G. Polesello, (2020), arXiv:2012.11474 [hep-ph] .

[74] P. Bandyopadhyay, S. Dutta, and A. Karan, (2020), arXiv:2012.13644 [hep-ph] .

[75] A. Crivellin, D. Müller, and L. Schnell, (2021), arXiv:2101.07811 [hep-ph] .

[76] J. Blumlein, E. Boos, and A. Pukhov, Mod. Phys. Lett. **A9**, 3007 (1994), arXiv:hep-ph/9404321 [hep-ph] .

[77] J. Blumlein, E. Boos, and A. Kryukov, Z. Phys. **C76**, 137 (1997), arXiv:hep-ph/9610408 [hep-ph] .

[78] A. Bhaskar, T. Mandal, and S. Mitra, Phys. Rev. D **101**, 115015 (2020), arXiv:2004.01096 [hep-ph] .

[79] A. Akeroyd and C.-H. Chen, Phys. Rev. D **96**, 075011 (2017), arXiv:1708.04072 [hep-ph] .

[80] M. Tanabashi *et al.* (Particle Data Group), Phys. Rev. D **98**, 030001 (2018).

[81] M. Bona (UTfit), PoS **CKM2016**, 096 (2017).

[82] S. Hirose *et al.* (Belle), Phys. Rev. Lett. **118**, 211801 (2017), arXiv:1612.00529 [hep-ex] .

[83] S. Hirose *et al.* (Belle), Phys. Rev. **D97**, 012004 (2018), arXiv:1709.00129 [hep-ex] .

[84] S. Bhattacharya, S. Nandi, and S. Kumar Patra, Eur. Phys. J. C **79**, 268 (2019), arXiv:1805.08222 [hep-ph] .

[85] K. Adamczyk (Belle, Belle-II), in *10th International Workshop on the CKM Unitarity Triangle* (2019) arXiv:1901.06380 [hep-ex] .

[86] T. Inami and C. S. Lim, Prog. Theor. Phys. **65**, 297 (1981), [Erratum: Prog.Theor.Phys. 65, 1772 (1981)].

[87] L. Di Luzio, M. Kirk, and A. Lenz, Phys. Rev. D **97**, 095035 (2018), arXiv:1712.06572 [hep-ph] .

[88] M. Algueró, B. Capdevila, A. Crivellin, S. Descotes-Genon, P. Masjuan, J. Matias, M. Novoa-Brunet, and J. Virto, Eur. Phys. J. C **79**, 714 (2019), [Addendum: Eur.Phys.J.C 80, 511 (2020)], arXiv:1903.09578 [hep-ph] .

[89] J. Aebischer, W. Altmannshofer, D. Guadagnoli, M. Reboud, P. Stangl, and D. M. Straub, Eur. Phys. J. C **80**, 252 (2020), arXiv:1903.10434 [hep-ph] .

[90] M. Algueró, B. Capdevila, S. Descotes-Genon, J. Matias, and M. Novoa-Brunet, in *55th Rencontres de Moriond on Electroweak Interactions and Unified Theories* (2021) arXiv:2104.08921 [hep-ph] .

[91] T. Mandal, S. Mitra, and S. Raz, Phys. Rev. **D99**, 055028 (2019), arXiv:1811.03561 [hep-ph] .

[92] W. Altmannshofer, C. Niehoff, P. Stangl, and D. M. Straub, Eur. Phys. J. C **77**, 377 (2017), arXiv:1703.09189 [hep-ph] .

[93] A. M. Sirunyan *et al.* (CMS), Phys. Rev. **D98**, 032005 (2018), arXiv:1805.10228 [hep-ex] .

[94] G. Aad *et al.* (ATLAS), JHEP **10**, 112 (2020), arXiv:2006.05872 [hep-ex] .

[95] M. Aaboud *et al.* (ATLAS), JHEP **06**, 144 (2019), arXiv:1902.08103 [hep-ex] .

[96] A. M. Sirunyan *et al.* (CMS), (2020), arXiv:2012.04178 [hep-ex] .

[97] N. Vignaroli, Phys. Rev. **D99**, 035021 (2019), arXiv:1808.10309 [hep-ph] .

[98] T. Mandal, S. Mitra, and S. Seth, JHEP **07**, 028 (2015), arXiv:1503.04689 [hep-ph] .

[99] T. Mandal and S. Mitra, Phys. Rev. **D87**, 095008 (2013), arXiv:1211.6394 [hep-ph] .

[100] T. Mandal, S. Mitra, and S. Seth, Phys. Lett. **B758**, 219 (2016), arXiv:1602.01273 [hep-ph] .

[101] G. Aad *et al.* (ATLAS), Phys. Rev. Lett. **125**, 051801 (2020), **HEPData** link: `https://www.hepdata.net/record/ins1782650.`, arXiv:2002.12223 [hep-ex] .

[102] A. M. Sirunyan *et al.* (CMS), (2021), **HEPData** link: `https://www.hepdata.net/record/ins1849964.`, arXiv:2103.02708 [hep-ex] .

[103] A. Alloul, N. D. Christensen, C. Degrande, C. Duhr, and B. Fuks, Comput. Phys. Commun. **185**, 2250 (2014), arXiv:1310.1921 [hep-ph] .

[104] C. Degrande, C. Duhr, B. Fuks, D. Grellscheid, O. Mattelaer, and T. Reiter, Comput. Phys. Commun. **183**, 1201 (2012), arXiv:1108.2040 [hep-ph] .

[105] J. Alwall, R. Frederix, S. Frixione, V. Hirschi, F. Maltoni, O. Mattelaer, H. S. Shao, T. Stelzer, P. Torrielli, and M. Zaro, JHEP **07**, 079 (2014), arXiv:1405.0301 [hep-ph] .

[106] R. D. Ball *et al.*, Nucl. Phys. **B867**, 244 (2013), arXiv:1207.1303 [hep-ph] .

[107] T. Sjostrand, S. Mrenna, and P. Z. Skands, JHEP **05**, 026 (2006), arXiv:hep-ph/0603175 [hep-ph] .

[108] M. L. Mangano, M. Moretti, F. Piccinini, and M. Treccani, JHEP **01**, 013 (2007), arXiv:hep-ph/0611129 [hep-ph] .

[109] S. Hoeche, F. Krauss, N. Lavesson, L. Lonnblad, M. Mangano, A. Schalicke, and S. Schumann, in *HERA and the LHC: A Workshop on the implications of HERA for LHC physics: Proceedings Part A* (2006) arXiv:hep-ph/0602031 [hep-ph] .

[110] J. de Favereau, C. Delaere, P. Demin, A. Giammanco, V. Lemaître, A. Mertens, and M. Selvaggi (DELPHES 3), JHEP **02**, 057 (2014), arXiv:1307.6346 [hep-ex] .

[111] M. Cacciari, G. P. Salam, and G. Soyez, JHEP **04**, 063 (2008), arXiv:0802.1189 [hep-ph] .

[112] J. P. Lees *et al.* (BaBar), Phys. Rev. Lett. **109**, 101802 (2012), arXiv:1205.5442 [hep-ex] .

[113] J. P. Lees *et al.* (BaBar), Phys. Rev. D **88**, 072012 (2013), arXiv:1303.0571 [hep-ex] .

[114] R. Aaij *et al.* (LHCb), Phys. Rev. Lett. **113**, 151601 (2014), arXiv:1406.6482 [hep-ex] .

[115] R. Aaij *et al.* (LHCb), Phys. Rev. Lett. **115**, 111803 (2015), [Erratum: Phys.Rev.Lett. 115, 159901 (2015)], arXiv:1506.08614 [hep-ex] .

[116] R. Aaij *et al.* (LHCb), JHEP **08**, 055 (2017), arXiv:1705.05802 [hep-ex] .

[117] R. Aaij *et al.* (LHCb), Phys. Rev. Lett. **120**, 171802 (2018), arXiv:1708.08856 [hep-ex] .

[118] R. Aaij *et al.* (LHCb), Phys. Rev. D **97**, 072013 (2018), arXiv:1711.02505 [hep-ex] .

[119] M. Huschle *et al.* (Belle), Phys. Rev. D **92**, 072014 (2015), arXiv:1507.03233 [hep-ex] .

[120] Y. Sato *et al.* (Belle), Phys. Rev. D **94**, 072007 (2016), arXiv:1607.07923 [hep-ex] .

[121] S. Hirose *et al.* (Belle), Phys. Rev. Lett. **118**, 211801 (2017), arXiv:1612.00529 [hep-ex] .

[122] S. Hirose *et al.* (Belle), Phys. Rev. D **97**, 012004 (2018), arXiv:1709.00129 [hep-ex] .

[123] G. W. Bennett *et al.* (Muon g-2), Phys. Rev. D **73**, 072003 (2006), arXiv:hep-ex/0602035 .

[124] B. Abi *et al.* (Muon g-2), Phys. Rev. Lett. **126**, 141801 (2021), arXiv:2104.03281 [hep-ex] .

[125] T. Aoyama *et al.*, Phys. Rept. **887**, 1 (2020), arXiv:2006.04822 [hep-ph] .

[126] T. Aoyama, M. Hayakawa, T. Kinoshita, and M. Nio, Phys. Rev. Lett. **109**, 111808 (2012), arXiv:1205.5370 [hep-ph] .

[127] T. Aoyama, T. Kinoshita, and M. Nio, Atoms **7**, 28 (2019).

[128] M. Davier, A. Hoecker, B. Malaescu, and Z. Zhang, Eur. Phys. J. C **77**, 827 (2017), arXiv:1706.09436 [hep-ph] .

[129] A. Keshavarzi, D. Nomura, and T. Teubner, Phys. Rev. D **97**, 114025 (2018), arXiv:1802.02995 [hep-ph] .

[130] G. Colangelo, M. Hoferichter, and P. Stoffer, JHEP **02**, 006 (2019), arXiv:1810.00007 [hep-ph] .

[131] M. Hoferichter, B.-L. Hoid, and B. Kubis, JHEP **08**, 137 (2019), arXiv:1907.01556 [hep-ph] .

[132] M. Davier, A. Hoecker, B. Malaescu, and Z. Zhang, Eur. Phys. J. C **80**, 241 (2020), [Erratum: Eur.Phys.J.C 80, 410 (2020)], arXiv:1908.00921 [hep-ph] .

[133] A. Keshavarzi, D. Nomura, and T. Teubner, Phys. Rev. D **101**, 014029 (2020), arXiv:1911.00367 [hep-ph] .

[134] A. Kurz, T. Liu, P. Marquard, and M. Steinhauser, Phys. Lett. B **734**, 144 (2014), arXiv:1403.6400 [hep-ph] .

[135] B. Chakraborty *et al.* (Fermilab Lattice, LATTICE-HPQCD, MILC), Phys. Rev. Lett. **120**, 152001 (2018), arXiv:1710.11212 [hep-lat] .

[136] S. Borsanyi *et al.* (Budapest-Marseille-Wuppertal), Phys. Rev. Lett. **121**, 022002 (2018), arXiv:1711.04980 [hep-lat] .

[137] T. Blum, P. A. Boyle, V. Gülpers, T. Izubuchi, L. Jin, C. Jung, A. Jüttner, C. Lehner, A. Portelli, and J. T. Tsang (RBC, UKQCD), Phys. Rev. Lett. **121**, 022003 (2018), arXiv:1801.07224 [hep-lat] .

[138] D. Giusti, V. Lubicz, G. Martinelli, F. Sanfilippo, and S. Simula, Phys. Rev. D **99**, 114502 (2019), arXiv:1901.10462 [hep-lat] .

[139] E. Shintani and Y. Kuramashi (PACS), Phys. Rev. D **100**, 034517 (2019), arXiv:1902.00885 [hep-lat] .

[140] C. T. H. Davies *et al.* (Fermilab Lattice, LATTICE-HPQCD, MILC), Phys. Rev. D **101**, 034512 (2020), arXiv:1902.04223 [hep-lat] .

[141] A. Gérardin, M. Cè, G. von Hippel, B. Hörz, H. B. Meyer, D. Mohler, K. Ottnad, J. Wilhelm, and H. Wittig, Phys. Rev. D **100**, 014510 (2019), arXiv:1904.03120 [hep-lat] .

[142] C. Aubin, T. Blum, C. Tu, M. Golterman, C. Jung, and S. Peris, Phys. Rev. D **101**, 014503 (2020), arXiv:1905.09307 [hep-lat] .

[143] D. Giusti and S. Simula, PoS **LATTICE2019**, 104 (2019), arXiv:1910.03874 [hep-lat] .

[144] K. Melnikov and A. Vainshtein, Phys. Rev. D **70**, 113006 (2004), arXiv:hep-ph/0312226 .

[145] P. Masjuan and P. Sanchez-Puertas, Phys. Rev. D **95**, 054026 (2017), arXiv:1701.05829 [hep-ph] .

[146] G. Colangelo, M. Hoferichter, M. Procura, and P. Stoffer, JHEP **04**, 161 (2017), arXiv:1702.07347 [hep-ph] .

[147] M. Hoferichter, B.-L. Hoid, B. Kubis, S. Leupold, and S. P. Schneider, JHEP **10**, 141 (2018), arXiv:1808.04823 [hep-ph] .

[148] A. Gérardin, H. B. Meyer, and A. Nyffeler, Phys. Rev. D **100**, 034520 (2019), arXiv:1903.09471 [hep-lat] .

[149] J. Bijnens, N. Hermansson-Truedsson, and A. Rodríguez-Sánchez, Phys. Lett. B **798**, 134994 (2019), arXiv:1908.03331 [hep-ph] .

[150] G. Colangelo, F. Hagelstein, M. Hoferichter, L. Laub, and P. Stoffer, JHEP **03**, 101 (2020), arXiv:1910.13432 [hep-ph] .

[151] V. Pauk and M. Vanderhaeghen, Eur. Phys. J. C **74**, 3008 (2014), arXiv:1401.0832 [hep-ph] .

[152] I. Danilkin and M. Vanderhaeghen, Phys. Rev. D **95**, 014019 (2017), arXiv:1611.04646 [hep-ph] .

[153] F. Jegerlehner, *The Anomalous Magnetic Moment of the Muon*, Vol. 274 (Springer, Cham, 2017).

[154] M. Knecht, S. Narison, A. Rabemananjara, and D. Rabetiarivony, Phys. Lett. B **787**, 111 (2018), arXiv:1808.03848 [hep-ph] .

[155] G. Eichmann, C. S. Fischer, and R. Williams, Phys. Rev. D **101**, 054015 (2020), arXiv:1910.06795 [hep-ph] .

[156] P. Roig and P. Sanchez-Puertas, Phys. Rev. D **101**, 074019 (2020), arXiv:1910.02881 [hep-ph] .

[157] G. Colangelo, M. Hoferichter, A. Nyffeler, M. Passera, and P. Stoffer, Phys. Lett. B **735**, 90 (2014), arXiv:1403.7512 [hep-ph] .

[158] T. Blum, N. Christ, M. Hayakawa, T. Izubuchi, L. Jin, C. Jung, and C. Lehner, Phys. Rev. Lett. **124**, 132002 (2020), arXiv:1911.08123 [hep-lat] .

[159] A. Czarnecki, W. J. Marciano, and A. Vainshtein, Phys. Rev. D **67**, 073006 (2003), [Erratum: Phys.Rev.D 73, 119901 (2006)], arXiv:hep-ph/0212229 .

[160] A. Crivellin and M. Hoferichter, JHEP **07**, 135 (2021), arXiv:2104.03202 [hep-ph] .

[161] S. Borsanyi *et al.*, Nature **593**, 51 (2021), arXiv:2002.12347 [hep-lat] .

[162] L. Di Luzio, A. Masiero, P. Paradisi, and M. Passera, Phys. Lett. B **829**, 137037 (2022), arXiv:2112.08312 [hep-ph] .

[163] T. Aaltonen *et al.* (CDF), Science **376**, 170 (2022).

[164] Y.-Z. Fan, T.-P. Tang, Y.-L. S. Tsai, and L. Wu, (2022), arXiv:2204.03693 [hep-ph] .

[165] K. Cheung, W.-Y. Keung, and P.-Y. Tseng, Phys. Rev. D **106**, 015029 (2022), arXiv:2204.05942 [hep-ph] .

[166] K. I. Nagao, T. Nomura, and H. Okada, (2022), arXiv:2204.07411 [hep-ph] .

[167] S. Kanemura and K. Yagyu, Phys. Lett. B **831**, 137217 (2022), arXiv:2204.07511 [hep-ph] .

[168] J. Kawamura, S. Okawa, and Y. Omura, (2022), arXiv:2204.07022 [hep-ph] .

[169] Y. H. Ahn, S. K. Kang, and R. Ramos, (2022), arXiv:2204.06485 [hep-ph] .

[170] P. Mondal, (2022), arXiv:2204.07844 [hep-ph] .

[171] T. A. Chowdhury, J. Heeck, S. Saad, and A. Thapa, (2022), arXiv:2204.08390 [hep-ph] .

[172] J. de Blas, M. Pierini, L. Reina, and L. Silvestrini, (2022), arXiv:2204.04204 [hep-ph] .

[173] J. M. Yang and Y. Zhang, (2022), arXiv:2204.04202 [hep-ph] .

[174] A. Strumia, (2022), arXiv:2204.04191 [hep-ph] .

[175] K.-Y. Zhang and W.-Z. Feng, (2022), arXiv:2204.08067 [hep-ph] .

[176] P. Fileviez Perez, H. H. Patel, and A. D. Plascencia, (2022), arXiv:2204.07144 [hep-ph] .

[177] M.-D. Zheng, F.-Z. Chen, and H.-H. Zhang, (2022), arXiv:2204.06541 [hep-ph] .

[178] X.-F. Han, F. Wang, L. Wang, J. M. Yang, and Y. Zhang, (2022), arXiv:2204.06505 [hep-ph] .

[179] M. Endo and S. Mishima, (2022), arXiv:2204.05965 [hep-ph] .

[180] Y. Heo, D.-W. Jung, and J. S. Lee, (2022), arXiv:2204.05728 [hep-ph] .

[181] K. S. Babu, S. Jana, and V. P. K., (2022), arXiv:2204.05303 [hep-ph] .

[182] J. Gu, Z. Liu, T. Ma, and J. Shu, (2022), arXiv:2204.05296 [hep-ph] .

[183] L. Di Luzio, R. Gröber, and P. Paradisi, (2022), arXiv:2204.05284 [hep-ph] .

[184] H. Bahl, J. Braathen, and G. Weiglein, (2022), arXiv:2204.05269 [hep-ph] .

[185] H. M. Lee and K. Yamashita, (2022), arXiv:2204.05024 [hep-ph] .

[186] K. Sakurai, F. Takahashi, and W. Yin, (2022), arXiv:2204.04770 [hep-ph] .

[187] M. Blennow, P. Coloma, E. Fernández-Martínez, and M. González-López, (2022), arXiv:2204.04559 [hep-ph] .

[188] T.-P. Tang, M. Abdughani, L. Feng, Y.-L. S. Tsai, J. Wu, and Y.-Z. Fan, (2022), arXiv:2204.04356 [hep-ph] .

[189] G. Cacciapaglia and F. Sannino, (2022), arXiv:2204.04514 [hep-ph] .

[190] X. K. Du, Z. Li, F. Wang, and Y. K. Zhang, (2022), arXiv:2204.04286 [hep-ph] .

[191] C.-T. Lu, L. Wu, Y. Wu, and B. Zhu, (2022), arXiv:2204.03796 [hep-ph] .

[192] C.-R. Zhu, M.-Y. Cui, Z.-Q. Xia, Z.-H. Yu, X. Huang, Q. Yuan, and Y. Z. Fan, (2022), arXiv:2204.03767 [astro-ph.HE] .

[193] G.-W. Yuan, L. Zu, L. Feng, Y.-F. Cai, and Y.-Z. Fan, (2022), arXiv:2204.04183 [hep-ph] .

[194] J. Fan, L. Li, T. Liu, and K.-F. Lyu, (2022), arXiv:2204.04805 [hep-ph] .

[195] H. Song, W. Su, and M. Zhang, (2022), arXiv:2204.05085 [hep-ph] .

[196] P. Asadi, C. Cesarotti, K. Fraser, S. Homiller, and A. Parikh, (2022), arXiv:2204.05283 [hep-ph] .

[197] P. Athron, M. Bach, D. H. J. Jacob, W. Kotlarski, D. Stöckinger, and A. Voigt, (2022), arXiv:2204.05285 [hep-ph] .

[198] J. J. Heckman, (2022), arXiv:2204.05302 [hep-ph] .

[199] X. K. Du, Z. Li, F. Wang, and Y. K. Zhang, (2022), arXiv:2204.05760 [hep-ph] .

[200] A. Ghoshal, N. Okada, S. Okada, D. Raut, Q. Shafi, and A. Thapa, (2022), arXiv:2204.07138 [hep-ph] .

[201] A. Crivellin, M. Kirk, T. Kitahara, and F. Mescia, (2022), arXiv:2204.05962 [hep-ph] .

[202] D. Borah, S. Mahapatra, D. Nanda, and N. Sahu, (2022), arXiv:2204.08266 [hep-ph] .

[203] O. Popov and R. Srivastava, (2022), arXiv:2204.08568 [hep-ph] .

[204] P. Athron, A. Fowlie, C.-T. Lu, L. Wu, Y. Wu, and B. Zhu, (2022), arXiv:2204.03996 [hep-ph] .

[205] M. Bauer and M. Neubert, Phys. Rev. Lett. **116**, 141802 (2016), arXiv:1511.01900 [hep-ph] .

[206] X.-Q. Li, Y.-D. Yang, and X. Zhang, JHEP **08**, 054 (2016), arXiv:1605.09308 [hep-ph] .

[207] G. Hiller, D. Loose, and K. Schönwald, JHEP **12**, 027 (2016), arXiv:1609.08895 [hep-ph] .

[208] G. D'Amico, M. Nardecchia, P. Panci, F. Sannino, A. Strumia, R. Torre, and A. Urbano, JHEP **09**, 010 (2017), arXiv:1704.05438 [hep-ph] .

[209] G. Hiller and I. Nisandzic, Phys. Rev. D **96**, 035003 (2017), arXiv:1704.05444 [hep-ph] .

[210] D. Bečirević, I. Doršner, S. Fajfer, N. Košnik, D. A. Faroughy, and O. Sumensari, Phys. Rev. D **98**, 055003 (2018), arXiv:1806.05689 [hep-ph] .

[211] A. Crivellin, D. Mueller, and F. Saturnino, Phys. Rev. Lett. **127**, 021801 (2021), arXiv:2008.02643 [hep-ph] .

[212] I. Doršner, S. Fajfer, and S. Saad, Phys. Rev. D **102**, 075007 (2020), arXiv:2006.11624 [hep-ph] .

[213] U. Aydemir, T. Mandal, S. Mitra, and S. Munir, (2022), arXiv:2209.04705 [hep-ph] .

[214] R. Aaij *et al.* (LHCb), Nature Phys. **18**, 277 (2022), arXiv:2103.11769 [hep-ex] .

[215] A. Carvunis, A. Crivellin, D. Guadagnoli, and S. Gangal, Phys. Rev. D **105**, L031701 (2022), arXiv:2106.09610 [hep-ph] .

[216] A. Crivellin, D. Müller, and T. Ota, JHEP **09**, 040 (2017), arXiv:1703.09226 [hep-ph] .

[217] S.-M. Choi, Y.-J. Kang, H. M. Lee, and T.-G. Ro, JHEP **10**, 104 (2018), arXiv:1807.06547 [hep-ph] .

[218] H. Yan, Y.-D. Yang, and X.-B. Yuan, Chin. Phys. C **43**, 083105 (2019), arXiv:1905.01795 [hep-ph] .

[219] A. Crivellin, D. Müller, and F. Saturnino, JHEP **06**, 020 (2020), arXiv:1912.04224 [hep-ph] .

[220] H. M. Lee, Phys. Rev. D **104**, 015007 (2021), arXiv:2104.02982 [hep-ph] .

[221] S.-L. Chen, W.-w. Jiang, and Z.-K. Liu, (2022), arXiv:2205.15794 [hep-ph] .

[222] L. Da Rold and F. Lamagna, Phys. Rev. D **103**, 115007 (2021), arXiv:2011.10061 [hep-ph] .

[223] D. Marzocca, JHEP **07**, 121 (2018), arXiv:1803.10972 [hep-ph] .

[224] V. Gherardi, D. Marzocca, and E. Venturini, JHEP **07**, 225 (2020), [Erratum: JHEP 01, 006 (2021)], arXiv:2003.12525 [hep-ph] .

[225] D. Marzocca, S. Trifinopoulos, and E. Venturini, Eur. Phys. J. C **82**, 320 (2022), arXiv:2106.15630 [hep-ph] .

[226] A. Greljo, P. Stangl, and A. E. Thomsen, Phys. Lett. B **820**, 136554 (2021), arXiv:2103.13991 [hep-ph] .

[227] S. Saad, Phys. Rev. D **102**, 015019 (2020), arXiv:2005.04352 [hep-ph] .

[228] V. Gherardi, D. Marzocca, and E. Venturini, JHEP **01**, 138 (2021), arXiv:2008.09548 [hep-ph] .

[229] C. Patrignani *et al.* (Particle Data Group), Chin. Phys. C **40**, 100001 (2016).

[230] I. Doršner, S. Fajfer, and O. Sumensari, JHEP **06**, 089 (2020), arXiv:1910.03877 [hep-ph] .

[231] A. Crivellin, D. Müller, and F. Saturnino, JHEP **11**, 094 (2020), arXiv:2006.10758 [hep-ph] .

[232] H. H. Patel, Comput. Phys. Commun. **197**, 276 (2015), arXiv:1503.01469 [hep-ph] .

[233] W. Altmannshofer and P. Stangl, Eur. Phys. J. C **81**, 952 (2021), arXiv:2103.13370 [hep-ph] .

[234] A. Carvunis, F. Dettori, S. Gangal, D. Guadagnoli, and C. Normand, JHEP **12**, 078 (2021), arXiv:2102.13390 [hep-ph] .

[235] Y. Cai, J. Gargalionis, M. A. Schmidt, and R. R. Volkas, JHEP **10**, 047 (2017), arXiv:1704.05849 [hep-ph] .

[236] J. Grygier *et al.* (Belle), Phys. Rev. D **96**, 091101 (2017), [Addendum: Phys.Rev.D 97, 099902 (2018)], arXiv:1702.03224 [hep-ex] .

[237] B. Aubert *et al.* (BaBar), Phys. Rev. Lett. **104**, 021802 (2010), arXiv:0908.2381 [hep-ex] .

[238] M. Bordone, M. Jung, and D. van Dyk, Eur. Phys. J. C **80**, 74 (2020), arXiv:1908.09398 [hep-ph] .

[239] A. Abdesselam *et al.* (Belle), *10th International Workshop on the CKM Unitarity Triangle*, (2019), arXiv:1903.03102 [hep-ex] .

[240] S. Schael *et al.* (ALEPH, DELPHI, L3, OPAL, SLD, LEP Electroweak Working Group, SLD Electroweak Group, SLD Heavy Flavour Group), Phys. Rept. **427**, 257 (2006), arXiv:hep-ex/0509008 .

[241] R. Aaij *et al.* (LHCb), Phys. Lett. B **725**, 15 (2013), arXiv:1305.5059 [hep-ex] .

[242] K. Hayasaka *et al.*, Phys. Lett. B **687**, 139 (2010), arXiv:1001.3221 [hep-ex] .

[243] R. L. Workman (Particle Data Group), PTEP **2022**, 083C01 (2022).

[244] M. Bona *et al.* (UTfit), Phys. Rev. Lett. **97**, 151803 (2006), arXiv:hep-ph/0605213 .

[245] M. Tanabashi *et al.* (Particle Data Group), Phys. Rev. D **98**, 030001 (2018).

[246] A. M. Sirunyan *et al.* (CMS), Phys. Rev. D **98**, 032005 (2018), arXiv:1805.10228 [hep-ex] .

[247] A. M. Sirunyan *et al.* (CMS), Phys. Rev. Lett. **121**, 241802 (2018), arXiv:1809.05558 [hep-ex] .

[248] M. Aaboud *et al.* (ATLAS), JHEP **06**, 144 (2019), arXiv:1902.08103 [hep-ex] .

[249] G. Aad *et al.* (ATLAS), JHEP **10**, 112 (2020), arXiv:2006.05872 [hep-ex] .

[250] A. Bhaskar, D. Das, T. Mandal, S. Mitra, and C. Neeraj, Phys. Rev. D **104**, 035016 (2021), arXiv:2101.12069 [hep-ph] .

[251] LHCb (LHCb Collaboration), (2022), arXiv:2212.09152 [hep-ex] .

[252] LHCb (LHCb Collaboration), (2022), arXiv:2212.09153 [hep-ex] .

[253] https://hflav-eos.web.cern.ch/hflav-eos/semi/summer23/html/RDsDsstar/RDRDs.html.

[254] M. Algueró, A. Biswas, B. Capdevila, S. Descotes-Genon, J. Matias, and M. Novoa-Brunet, Eur. Phys. J. C **83**, 648 (2023), arXiv:2304.07330 [hep-ph] .

[255] A. M. Sirunyan *et al.* (CMS), Eur. Phys. J. C **78**, 707 (2018), arXiv:1803.02864 [hep-ex] .

[256] M. Aaboud *et al.* (ATLAS), Eur. Phys. J. C **79**, 733 (2019), arXiv:1902.00377 [hep-ex] .

[257] G. Aad *et al.* (ATLAS), JHEP **2306**, 188 (2023), arXiv:2210.04517 [hep-ex] .

[258] M. Kramer, T. Plehn, M. Spira, and P. M. Zerwas, Phys. Rev. D **71**, 057503 (2005), arXiv:hep-ph/0411038 .

[259] A. Bhaskar, T. Mandal, S. Mitra, and M. Sharma, Phys. Rev. D **104**, 075037 (2021), arXiv:2106.07605 [hep-ph] .

[260] B. Diaz, M. Schmaltz, and Y.-M. Zhong, JHEP **10**, 097 (2017), arXiv:1706.05033 [hep-ph] .

[261] S. Catani, L. Cieri, G. Ferrera, D. de Florian, and M. Grazzini, Phys. Rev. Lett. **103**, 082001 (2009), arXiv:0903.2120 [hep-ph] .

[262] G. Balossini, G. Montagna, C. M. Carloni Calame, M. Moretti, O. Nicrosini, F. Piccinini, M. Treccani, and A. Vicini, JHEP **01**, 013 (2010), arXiv:0907.0276 [hep-ph] .

[263] J. M. Campbell, R. K. Ellis, and C. Williams, JHEP **07**, 018 (2011), arXiv:1105.0020 [hep-ph] .

[264] N. Kidonakis, *Proceedings, 23rd International Workshop on Deep-Inelastic Scattering and Related Subjects (DIS 2015): Dallas, Texas, USA, April 27-May 01, 2015*, PoS **DIS2015**, 170 (2015), arXiv:1506.04072 [hep-ph] .

[265] C. Muselli, M. Bonvini, S. Forte, S. Marzani, and G. Ridolfi, JHEP **08**, 076 (2015), arXiv:1505.02006 [hep-ph] .

[266] A. Kulesza, L. Motyka, D. Schwartländer, T. Stebel, and V. Theeuwes, Eur. Phys. J. **C79**, 249 (2019), arXiv:1812.08622 [hep-ph] .

[267] G. Cowan, K. Cranmer, E. Gross, and O. Vitells, Eur. Phys. J. C **71**, 1554 (2011), [Erratum: Eur.Phys.J.C 73, 2501 (2013)], arXiv:1007.1727 [physics.data-an] .

[268] D. Das, K. Ghosh, M. Mitra, and S. Mondal, Phys. Rev. **D97**, 015024 (2018), arXiv:1708.06206 [hep-ph] .

[269] S. Mandal, M. Mitra, and N. Sinha, Phys. Rev. **D98**, 095004 (2018), arXiv:1807.06455 [hep-ph] .

[270] G. Cottin, O. Fischer, S. Mandal, M. Mitra, and R. Padhan, JHEP **06**, 168 (2022), arXiv:2104.13578 [hep-ph] .

[271] A. Bhaskar, D. Das, B. De, S. Mitra, A. K. Nayak, and C. Neeraj, Phys. Lett. B **833**, 137341 (2022), arXiv:2205.12210 [hep-ph] .

[272] P. Minkowski, Phys. Lett. B **67**, 421 (1977).

[273] R. N. Mohapatra and G. Senjanovic, Phys. Rev. Lett. **44**, 912 (1980).

[274] R. N. Mohapatra, Phys. Rev. Lett. **56**, 561 (1986).

[275] R. N. Mohapatra and J. W. F. Valle, Phys. Rev. D **34**, 1642 (1986).

[276] M. Thomas Arun, T. Mandal, S. Mitra, A. Mukherjee, L. Priya, and A. Sampath, Phys. Rev. D **105**, 115007 (2022), arXiv:2109.09585 [hep-ph] .

[277] M. T. Arun, A. Chatterjee, T. Mandal, S. Mitra, A. Mukherjee, and K. Nivedita, Phys. Rev. D **106**, 095035 (2022), arXiv:2204.02949 [hep-ph] .

[278] D. Curtin, J. Galloway, and J. G. Wacker, Phys. Rev. D **88**, 093006 (2013), arXiv:1306.5695 [hep-ph] .

[279] M. Mitra, R. Ruiz, D. J. Scott, and M. Spannowsky, Phys. Rev. D **94**, 095016 (2016), arXiv:1607.03504 [hep-ph] .

[280] E. Gross, in *PHYSTAT-LHC Workshop on Statistical Issues for LHC Physics* (2007) pp. 205–212.